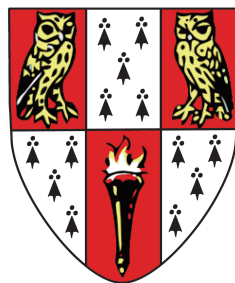




UNIVERSITY OF
CAMBRIDGE

Exotic Stars and Thorne-Żytkow Objects



Alexander J. Hackett

Supervisors:
Prof. Christopher A. Tout
Dr. Anna N. Żytkow

Institute of Astronomy
University of Cambridge

This dissertation is submitted for the degree of
Doctor of Philosophy

Hughes Hall

July 2023

Declaration

I hereby declare that except where specific reference is made to the work of others, the contents of this dissertation are original and have not been submitted in whole or in part for consideration for any other degree or qualification in this, or any other university. This dissertation is my own work and contains nothing which is the outcome of work done in collaboration with others, except as specified in the text and Acknowledgements. This dissertation contains fewer than 60,000 words subject to the conditions as outlined by the Institute of Astronomy and the University Degree Committee.

- Chapter 6 is based in part on my contributions to the work of Bhattacharya M., Hackett A. J., Gupta A. Tout C. A., 2022, *Evolution of Highly Magnetic White Dwarfs by Field Decay and Cooling: Theory and Simulations*, ApJ, 925, 2.

Alexander J. Hackett

Supervisors:
Prof. Christopher A. Tout
Dr. Anna N. Źytkow
July 2023

Abstract

Exotic Stars and Thorne-Żytkow Objects

Alexander Jan Hackett

The concept of a hybrid star, a stellar object that has some sort of atypical internal structure, particularly in regards to its energy budget, has been around for over a century. Arguably the pre-Gamow explanations offered for the source of luminosity for all stars correspond to a form of hybrid star models, from Kelvin's thermal explanation, to Landau's suggestion that the sun harboured a neutron degenerate core. This dissertation focuses on the study of exotic stellar objects, both a class of hybrid stars with a neutron core known as Thorne-Żytkow Objects (TŻOs), and highly magnetized, super-Chandrasekhar mass white dwarfs. A Thorne-Żytkow Object may form as a result of a Common Envelope Evolution (CEE) event between a giant or supergiant star with a neutron star companion. It consists of a large, diffuse giant envelope surrounding a neutron degenerate core. We investigate the structure and evolution of these objects here. Focusing on the central degenerate component of these objects themselves leads to the study of exotic compact objects in their own right, in this case, white dwarfs that harbour intense magnetic fields, which provide sufficient magnetic pressure support for them at masses above the Chandrasekhar mass, making them possible progenitors of overly luminous Type Ia supernovae.

In Chapter 1, I provide a brief introduction to the venerable field of stellar evolution to provide the necessary context for the following Chapters of this work. In Chapter 2, I present an introduction to the physics, structure and evolution of Thorne-Żytkow Objects, the canonical models thereof as they exist in the literature and the challenges and some of the approaches taken to overcome them. I also discuss the formation and death of TŻOs. In Chapter 3, I provide a similar introduction to the study of highly magnetized compact objects, white dwarfs (B-WDs) and neutron stars (B-NS / magnetars) as well as the relevant microphysics that we must consider to study these objects. In particular I discuss the mechanisms by which thermal neutrinos can be produced in such objects. This is essential to understanding their cooling.

In Chapter 4 I introduce and explain the numerical techniques and codes used throughout

this dissertation, specifically the STARS and MESA Henyey-style one-dimensional stellar evolution codes. I also explain the modifications made to the codes in question to model the exotic objects I study.

In Chapter 5 I present a novel series of solutions for envelopes of T $\ddot{\text{O}}$ s which, while qualitatively similar to those of the canonical T $\ddot{\text{O}}$ models that I discussed in Chapter 2, differ in a few key ways. The solutions resemble the canonical supergiant-like solutions, dominated by nuclear burning, even for masses that admit a giant-like solution, dominated by accretion on to the neutron core, in these earlier models. I have investigated the thermodynamic consistency of these models and how robust the qualitative structure of the solutions is to changing accretion rates and other boundary conditions. I found that our use of revised, updated tables of thermal neutrino loss rates compared those used in the canonical work serves to explain the majority of the structural differences between our models. I also present a series of hybrid-AGB models, in which the core exists in a state between that of a neutron star and a white dwarf, and is modelled in full. Anomalous surface chemical abundances in these models indicate a method by which T $\ddot{\text{O}}$ s could be identified observationally.

In Chapter 6, I investigate the structure and evolution of super-Chandrasekhar mass B-WDs, finding that solutions do exist at masses above the Chandrasekhar mass, given a sufficiently large magnetic field permeating the object. I also present a modified field prescription that addresses an issue regarding non-physical current sheaths in the B-WDs, by means of a saturation radius. This was shown to replicate the previous results and suggests that highly magnetized supermassive white dwarfs could indeed serve as progenitors for overly luminous Type Ia supernovae.

In Chapter 7 I summarize the content of this dissertation, contextualising and expanding upon the results and providing a short review of possible future avenues for related research.

For Mieczysław Brandyk, who, but for a misfortune befalling his supervisor, would have had
the chance to produce a work like this of his own.

Acknowledgements

“Somewhere in the world there is defeat for everyone. Some are destroyed by defeat, and some made small and mean by victory. Greatness lives in one who triumphs equally over defeat and victory.”

John Steinbeck,
The Acts of King Arthur and His Noble Knights

It is more than a little surreal to be sitting here and writing acknowledgements for a Ph.D. dissertation, and actually getting to this point has been possible only with the support, encouragement, mentorship and most importantly, friendship, of almost too many people to count. I'll try to cover you all here, but if I do leave anyone out, please feel free to take the hardbound copy of this dissertation out from the University Library and write your name in pen somewhere in this section (Please don't do this to the copy in the IoA library, as I assume Mark would be very upset with me).

First of all, I'd like to thank Chris Tout and Anna Źytkow. It might be a clichéd thing to say, but this body of work very simply would not exist without them. I'd like to thank you both for your continued guidance, advice, patience, thoroughness and most importantly, passion for research that has transferred inexorably to me. Any attempt at a Ph.D. during the time period containing that particular phase of *viral unpleasantness* was always going to be especially challenging, and I have no doubt that your support made it possible. I'd likewise wish to thank all the other people I've had the distinct pleasure of sharing membership in the Stars group with over these last years, Holly Preece, Tom Comerford, Arnab Sakar, Hongwei Ge, Boyuan Liu, Sverre Aarseth, Douglas Gough, as well as Natalie Rees and Rob Izzard. Thank you also to David H. and Arman A. for making me feel very welcome at your group meetings and for taking such an interest in my work. Thanks to you all, along with Chris and Anna, for creating a wonderful and exciting environment to work in. Also, if you, the person reading this right at this moment, are, in fact, Arnab, then I regret to inform you that any material/layout *etc.* that you might find useful for your own dissertation is unfortunately not located here in the acknowledgments, apologies, and good luck!

A special thanks goes out to the wonderful denizens of O35 whose wonderful company I have had the pleasure of enjoying over the last four years, many thanks to, in no particular

order, Erik Rosenberg, Andy Buchan, Holly Preece, Aneesh Naik, Marc Brouwers, Hannah Petrovic and Frances Rigby, who wanted me to note in writing here that I think that she and Hannah are “quite nice really”. Of course, I have made countless friends at the IoA since starting here, and I owe so very much to your friendship and support. Many thanks to Andrew, Annabelle, Chiara, Jonny, Sam, Sam and Sam, Steve, Jess, Laura, Clay, Amy, Savvas, Stefan, and Payton, thanks to Aoife for helping me keep going and to Jamie for presumably doing the same for her, thanks to Maggie for being the other TCD person to come across the water, to Jake, Adam, Adam, Tom, Steve, and Matt for the astrohouse tradition that we carried on, and to the amazing residents of the astrohouse that have been such incredibly lovely people to live with. Thanks to Sam, Erik, Júlia, Carolina, Stefan, Annabelle and Zofia, the most esteemed honorary member of the house, and owner of the couch.

I really can’t be grateful enough for having you in my life, Zofia. Without you I would have certainly gone insane (the bad kind...), particularly over these last few months. Thank you for being the most wonderful person in the world.

I’d like to thank the CUGCR, and in particular Sam Johnson and Jonathan Shanklin for teaching me how to ring and to Greg, Kate and Kirsten for serving as Masters during my time here. Thanks also to Thomas for so often joining me in ringing at St. Andrews in Chesterton, and to all those in the regular bands at St. Andrews in Cherry Hinton, StAG, Great St. Mary’s and St. Bene’t’s.

I owe much thanks to Chris, Clare and Rob for providing references for a multitude of job applications.

I’d like to thank Brian Espey, Paul Eastham, José Groh, Aline Vidotto, Cormac McGuinness and Simon Jeffery for mentoring and inspiring me during my time in TCD. Thanks to my colleagues Mukul B. and Bani M., with whom was written a paper that I am proud to have contributed to, and the sections of which I wrote serve as a partial basis for chapter 6 of this dissertation. Many thanks also to Ross Church and Warrick Ball for much technical help and inspiration.

A great deal of thanks is owed to my friends at home and around the world that have always supported and encouraged me, thanks to Sally-Ann, Kate, Molly, Éanna, Andrew, Malek, Peter, Richard, Jack, Jack, Ian and countless others.

Many thanks to my wonderful and supportive family, who have always been there for me. I’d like to thank my grandparents, aunts and uncles, cousins, Mum, Dad and Anna, I couldn’t have done this without you.

Contents

Declaration	iii
Abstract	v
Dedication	vii
Acknowledgements	ix
Table of Contents	xiv
1 An Introduction to Stellar Evolution	1
1.1 An Introduction to this Dissertation	1
1.2 Perspective and the STARS Code	3
1.3 The Mathematical Treatment of Stellar Evolution	5
1.3.1 Conservation of Mass	6
1.3.2 Gravitation	6
1.3.3 Hydrostatic Equilibrium	7
1.3.4 Energy Generation	8
1.3.5 Energy Transport	9
1.4 Convection	11
1.4.1 Mixing Length Theory	12
1.4.2 Convective Overshooting	15
2 Thorne-Żytkow Objects: background and existing literature	21
2.1 Introduction	21
2.2 Canonical Structure Solutions of TŻOs	23
2.2.1 Canonical models: Thorne & Żytkow 1977	23
2.2.2 Canonical models: Cannon et al. 1992, 1993	25
2.3 Nuclear energy generation, nucleosynthesis and the irp process	26

2.4	Hydrodynamic Evolution of T \ddot{Z} Os	28
2.4.1	Formation pathways for T \ddot{Z} Os	29
2.4.2	Final Fates of T \ddot{Z} Os	31
3	Highly Magnetized Compact Objects: B-WDs and B-NSs	33
3.1	Highly magnetized neutron stars	33
3.2	Highly magnetized white dwarfs: background and introduction	34
3.3	Thermal neutrino generation processes	36
3.3.1	Pair annihilation	39
3.3.2	The photoneutrino process	40
3.3.3	The plasmon decay process	40
4	Stellar Evolution Codes	43
4.1	Henyey Implicit Integration Approach	43
4.2	The Cambridge Stellar Evolution Code (STARS)	46
4.2.1	Custom matrix inversion algorithm	50
4.2.2	The STARS Equation of State	53
4.2.2.1	The core-envelope interaction artifice	62
4.2.2.2	Modifications made to the STARS code for the purposes of modelling T \ddot{Z} Os and B-WDs	66
4.2.2.2.1	Opacity	67
4.2.2.2.2	Modified Electron Mass	69
4.2.2.2.3	Neutron Opacity	70
4.2.2.2.4	Magnetic Fields	71
4.2.2.2.5	Convergence Aids	71
4.3	Modules for Experiments in Stellar Astrophysics (MESA)	74
4.3.1	Overview of code developed for MESA	75
5	A new equilibrium model for supergiant-like Thorne-\dot{Z}ytkow Objects	77
5.1	Construction of Model Grid	78
5.1.1	General Relativistic Corrections	79
5.1.2	The Core-Envelope Interface Artifice	82
5.2	Fiducial Relaxed Core Models	83
5.2.1	Fiducial Relaxed Core Model Results	85
5.2.1.1	Surface Properties	86
5.2.1.2	Internal Structure Properties	95
5.2.1.3	Effects of GR corrections	97

5.2.1.4	Fiducial model results in the UV plane	98
5.2.2	Fiducial Relaxed Core Models: Sensitivity to central radius boundary condition	99
5.2.3	Fiducial Relaxed Core Models with extended hydrogen burning network	102
5.2.4	Fiducial Relaxed Core Models with varying accretion rate	108
5.2.4.1	Static accretion rate models in the UV plane	111
5.3	TŻO Structure Investigations with STARS	113
5.3.1	Structural Results	114
5.3.2	Nucleosynthesis Results	121
5.4	Discussion	122
5.4.1	Comparison with models of TŻ and Cannon et al	125
5.4.2	Explaining the internal structure differences between the canonical models and our own	126
5.4.3	Limitations and caveats	133
5.5	Conclusions	134
6	Highly Magnetised White Dwarfs	137
6.1	Implementation	138
6.2	Simulation Results	141
6.2.1	Summary of simulation results	147
6.3	The Magnetic Field Plateau — magnetised white dwarf models with a field saturation radius	147
6.4	Models & Results	147
6.4.1	Overview of Models with Plateau Central Magnetic Fields	148
6.4.2	Super-Chandrasekhar Mass B-WD Model Results	149
6.4.3	Super-Chandrasekhar Mass Fiducial Model Results	154
6.5	Summary & Conclusions	159
7	Conclusions	163
7.1	Literature assessment and details of computational methodologies	163
7.2	New equilibrium structures for Thorne-Żytkow Objects	165
7.3	Super-Chandrasekhar mass, highly magnetized white dwarfs: possible over-luminous SNe Ia progenitors	168
7.4	Potential avenues for future work	169
7.4.1	TŻOs and other hybrid stars	169
7.4.2	Highly magnetized and supermassive compact objects	171

Bibliography	173
Appendix A Analytical Derivations	185
A.1 Contact between relativistic and standard stellar structure equations in the Newtonian limit	185
A.2 Magnetic field decay mechanisms for B-WDs	188
Appendix B Nuclear reaction networks	191
B.1 Networks – STARS	191
B.1.1 The structural network	191
B.1.2 Post-processing nuclear reaction network	193
B.2 Networks – MESA	194
B.2.1 Heger 2002-like adaptive nuclear network	196
Appendix C Commentary on Farmer et al. (2023)	199
C.1 A brief overview of work in question	199
C.1.1 A discussion of the modelling of TŻOs	199
C.1.2 Concerns regarding placing the inner boundary above the radiative zone	201
C.2 A point-by-point comparison of conclusions derived	203

Chapter 1

An Introduction to Stellar Evolution

Fred once started a talk by saying,
‘Oh, Ooh, basically a star is a pretty
simple thing.’

And from the back of the room was
heard the voice of R. O. Redman,
saying,

‘Well, Fred, you’d look pretty
simple too, from ten parsecs!’

John Faulkner,
Red giants: then and now,
The Scientific Legacy of Fred Hoyle,
2005

We begin with a brief but essential introduction to the enormous and enormously significant field of stellar evolution as it pertains to the research presented in this dissertation. Particular attention is devoted to the equations of stellar structure, the construction of numerical solutions to which is the principle methodology by which this research was conducted.

1.1 An Introduction to this Dissertation

This work will focus in depth on the numerical study of stars with some sort of non-standard internal structure. These will include Thorne-Żytkow Objects, a class of hypothetical hybrid stars consisting of a giant diffuse stellar envelope surrounding a neutron-star core, and supermassive white dwarfs, electron degenerate objects that are supported above the Chandrasekhar mass by the presence of an internal magnetic field with an extremely large field density, and hence contribution to pressure support.

Cowling (1966a) made a special point in the opening lines of his Presidential Address to mention that, in his opinion, otherwise promising research students in stellar astrophysics were often “lamentably ignorant” of the history of this subject. Here we shall attempt to avoid the error of these students. He goes on to briefly recount the history of stellar evolution from its earliest inception up to the state-of-the-art up to that point. Worth noting is his mention of Lane (1870) and his theory of polytropic spheres of gas. From this point up to our modern understanding of stellar interiors is quite a remarkable journey. Eddington (1920)’s proposal that nuclear fusion of hydrogen into helium was the primary energy source for stars is our most prominent trail marker along the path (Although Perrin, Jean (1919),

William D. Harkins, Hans A. Bethe and Carl F. von Weizsäcker all have valid claims to at least some portions of this theory). Understanding the exact mechanics of this fusion process, and further fusion processes (from hydrogen fusion all the way up to the fusion of silicon in highly evolved stars) in the interiors of stars is the grand vista at the pinnacle of the journey, but the objects studied and discussed in this dissertation have some of their roots in the branching paths that broke off from the main trail towards hydrostatic, thermally self-regulating proton-proton and CNO cycle fusion.

The most basic structural description of a Thorne-Żytkow Object (TŻO), where a (giant) stellar envelope surrounds a neutron-star core may have been first described explicitly by [Thorne & Żytkow \(1975\)](#) and [Thorne & Żytkow \(1977\)](#) but the idea of a core of neutron degenerate matter existing inside a stellar envelope was initially proposed by [Landau \(1938\)](#). Landau speculated that all stars (above some very low cut-off mass of around $0.001 M_{\odot}$) harboured a core of what he dubbed “pathological” material, wherein it is energetically favourable for inverse beta decay to occur, forming neutrons from the protons and electrons. The principle energy source of stars could then be, according to Landau, the contraction of stellar material onto this neutron core. Landau’s life was incredibly eventful and very shortly after the publication of this work, he was imprisoned for a year (his close friend Pyotr Leonidovich Kapitsa wrote to Stalin himself on the day Landau was arrested and cited this very paper as evidence that Landau was too famous and too prolific a scientist to jail). As [Yakovlev et al. \(2013\)](#) states, by the time of Landau’s release from prison, works such as that by [Bethe \(1939\)](#) had made quite clear that stars, at least those on the main-sequence, were powered by the fusion of hydrogen into helium in their cores. As one reads through chapters 2 and 5 of this dissertation, it becomes remarkable clear how much the internal structure for all stars as proposed by [Landau \(1938\)](#) has in common with the proposed structures of TŻOs that [Thorne & Żytkow \(1977\)](#); [Bisnovatyi-Kogan & Lamzin \(1984\)](#); [Eich et al. \(1989\)](#); [Cannon et al. \(1992\)](#); [Podsiadlowski et al. \(1995\)](#) and this work discuss. Our motivation for continuing the research into TŻOs has to do with building upon this long line of research, that stretches back to the early days of stellar evolution.

Chapters 3 and 6 of this work will deal with the study of another kind of exotic stellar object; super-Chandrasekhar mass, highly magnetised white dwarfs (B-WDs). These are white dwarfs, objects usually held up by electron degeneracy pressure, that exist above the maximum mass for this kind of object, the Chandrasekhar mass. The presence of large magnetic fields in the interiors of these objects provide the necessary pressure support to keep them from collapsing. These sorts of object correspond to yet more interesting side-paths on the trail of stellar evolution. Our motivation for wishing to study B-WDs comes from the study of overluminous type-Ia supernovae ([Chornock et al., 2013](#)). A very natural explanation

for these supernovae would be to suggest that the detonating progenitors in question are simply exploding at masses above the Chandrasekhar mass. There are a number of other possible underlying physical phenomena that could provide the pressure support needed to allow white dwarfs to exist above the Chandrasekhar mass, spinning the objects right up to the threshold breakup, for example.

The primary tools of our trade are stellar evolution codes, which solve the equations of stellar structure, as described in this chapter, by using the Henyey relaxation technique, as discussed in chapter 4. In that chapter, we discuss also the modifications that I have made to two of these codes, STARS and MESA, for the purposes of incorporating the additional physics required to adequately describe the exotic objects that we are interested in investigating.

With some of the background to this dissertation now briefly introduced, we can lay out the broad aims of this dissertation. After providing an introduction to the equations of stellar structure in the remainder of this chapter, and the existing literature regarding T $\ddot{\text{Z}}$ Os and B-WDs in chapters 2 and 3, we discuss the two Henyey codes we employed in chapter 4. This includes both a detailed overview of the features and the inner workings of both codes, as well as a description of the modifications we made in order to incorporate the physics necessary to simulate the exotic objects in which we are interested, as well as the myriad other miscellaneous modifications made in order to allow the models to converge. In chapters 5 and 6, we aim to present and explain how the modified codes as discussed were used in order to improve upon the state of the art in the study of T $\ddot{\text{Z}}$ Os and B-WDs. The series of structure solutions we produced for supergiant-like T $\ddot{\text{Z}}$ Os act much like those by Cannon et al. (1992), but with significant quantitative structural differences, that we explain primarily due to the differences in the thermal neutrino luminosity tables we have used, compared to those used in earlier works. Our study of B-WDs serves to explain a possible mechanism by which white dwarfs could be supported at masses above the Chandrasekhar mass, allowing them to act as progenitors of overly luminous SNe-Ia. By invoking a magnetic field saturation radius mechanism, we can now construct such models without the risk of requiring a sheath supporting an unphysically large current at small radii, removing one of the major obstacles to the validity of these models.

To conclude the dissertation, we summarize all the work performed in the prior chapters, and explore possible avenues for expanding upon the research presented.

1.2 Perspective and the STARS Code

Stars are the fundamental observable constituent of the Universe. Stars produce essentially all the visible light in the night sky and, fortuitously, they are excellent laboratories for a

diverse range of physics. The formation, structure and evolution of stars are governed by the laws of nuclear physics, atomic processes, particle physics, opacity, convection, radiative transfer, degenerate and solid state physics and thermodynamics. As observational units, stars allow us to constrain models of galaxy formation and evolution, cosmology and dynamics. With that in mind, to produce a realistic stellar model requires a detailed understanding of all the underlying input physics. The more realistically the physics is treated, the more realistic and useful the models become. To this end, a number of stellar evolution codes have been written. These codes generally have a number of things in common, particularly the use of the Henyey relaxation technique to solve the equations of stellar structure. There are three main points that separate the STARS code from other such codes. First STARS uses an adaptive non-Lagrangian mesh. This means that the points at which the structure and composition equations are solved are distributed neither evenly nor statically in mass (as in a Lagrangian code), but rather they are distributed by means of an eigenfunction, that is, evenly in a chosen mesh spacing function of the structure. This function is pre-selected and its coefficients can be varied from model to model. As such, the mesh point locations vary over the course of the evolution of the model. In this way, the code can successfully solve for models through a wide variety of evolutionary stages, with a minimal number of mesh points (Eggleton, 1971). A typical Lagrangian code, GENEC for example, requires 10^3 mesh points for MS evolution and 10^5 to well-resolve such phases as thermally pulsing AGB evolution (Eggenberger et al., 2008). STARS can typically produce a good MS model with just 199 mesh points and a well-resolved AGB model with even a 500 point viscous mesh (Stancliffe et al., 2004). This allows STARS models to be run quickly in comparison to other codes even on modest hardware. Secondly, the code solves both the equations of stellar structure and stellar composition simultaneously and implicitly. As such, phases of stellar evolution where composition changes very rapidly, causing rapid changes in structure are dealt with more accurately than in a code where the implicit solutions of structure equations are used as input for explicit solutions of composition equations. Finally, the STARS source code is short compared to many other stellar evolution codes, with just a few thousand lines of functional FORTRAN. Therefore, STARS is well suited to the sort of considerable modification needed to produce models of Thorne-Żytkow Objects (TŻOs), the exotic hybrid stars consisting of a giant, diffuse envelope surrounding a neutron degenerate core that shall comprise a considerable portion of the rest of this dissertation, in particular in Chapters 2 and 5. The STARS routines that set up variables for the implicit equation solver and the routines that compute the equation of state and the opacity are particularly well suited to heavy modification and are implemented in a modular fashion. In addition the equation of state is solved explicitly, as opposed to being interpolated from a set of tables and, as

such, can give first and second derivatives for many thermodynamic variables (Pols et al., 1995). Hence, the code can be easily modified to deal with extremely dense or sparse stellar material, as well as extremely high or low temperatures. These are all particularly useful features when it comes to using the code to model exotic stellar objects.

1.3 The Mathematical Treatment of Stellar Evolution

At its simplest, every stellar evolution model begins with producing numerical solutions to the equations of stellar structure. To describe the structure of an isolated (not evolving in a binary system), slowly rotating star, four differential equations must be solved with sensible boundary conditions. These are the conservation of mass, the conservation of energy, the equation of hydrostatic equilibrium and the equation of energy transport. The model must also consider the equation of state for the stellar material, the opacity of the stellar material and the energy generation rates inside the star (MacDonald, 2015). Finally, because the STARS code is a hydrostatic code, it must rely only on solving models in hydrostatic equilibrium. There exist hydrodynamic codes that fully simulate 3D MHD in a star, DJEHUTY (Bazán et al., 2003) for example, but these are unsuited to modelling stellar evolution because of the time-scales on which they run. We need to cover evolution on nuclear time-scales whereas these simulations cover only dynamical time-scales (Arnett et al. 2018; 2018b). Requiring the condition of a slowly rotating star allows us to make the assumption of spherical symmetry throughout. When rotating at a negligible fraction of the critical (break-up) velocity, we can assume that a star is pulled by its self-gravity into a perfect sphere. Hence, we can reduce all equations into one dimension, where we consider only the radial direction in the star. At larger rotational velocities, (assuming a fluid-like response) the star is rotationally flattened, bulging at the equator and flattening at the poles¹, requiring an additional spatial dimension to describe.

¹The most simple way that this can be demonstrated is via coordinate transform to a co-rotating reference frame. This will alter the expression for the acceleration at (former) equipotentials along the star as $\mathbf{g} = \mathbf{g}_{\text{grav}} + \mathbf{g}_c$, where \mathbf{g}_{grav} is the gravitational acceleration, and \mathbf{g}_c the centrifugal acceleration, which has a magnitude (in spherical coordinates) $r \sin\theta \Omega^2$, directed away from the axis of rotation. Hence, we can write an effective centrifugal potential χ , analogous to the gravitational potential ψ , as $\chi(r, \theta) = \frac{1}{3} \Omega^2 r^2 (P_2(\cos\theta) - 1)$, where P_2 is the third Legendre polynomial. Hence, assuming a fluid-like response, that is, that our star is to be composed of material unable to withstand shear stress, we can compute the ellipticity, the difference between the polar and equatorial radii, from the rotation rate.

1.3.1 Conservation of Mass

We define m to be the mass of the star interior to the radius of a shell at radius r , then m , r and the density ρ are related by imposing the condition that mass is conserved. For a thin shell of radius r and thickness dr inside the star, the volume of the shell is $dV = 4\pi r^2 dr$ and so

$$\frac{dm}{dr} = 4\pi r^2 \rho(r). \quad (1.1)$$

Equation 1.1 is the *Eulerian* equation of mass conservation, because the independent variable is the radius of the shell inside the star. With m as the independent variable instead we have the *Lagrangian* equation of mass conservation

$$\frac{dr}{dm} = \frac{1}{4\pi r^2 \rho}. \quad (1.2)$$

In order to derive equation 1.2 from equation 1.1 the Eulerian to Lagrangian transformation

$$\left(\frac{\partial}{\partial m} \right)_t = \frac{1}{4\pi r^2 \rho} \left(\frac{\partial}{\partial r} \right)_t \quad (1.3)$$

is applied. We note here that time is to be held constant during this coordinate transform. With equation 1.3 the Eulerian equations of stellar structure can be converted into the more useful, both for simulation and for analysis, Lagrangian equations of stellar structure. A set of boundary conditions can be placed on equation 1.2 by asserting that $r \rightarrow 0$ as $m \rightarrow 0$, so there is no mass located within a shell of zero radius at the very centre of the star, and that $r \rightarrow R_*$ as $m \rightarrow M_*$, and all of the star's mass is contained within a sphere with a radius equal, or larger, to the radius of the star.

1.3.2 Gravitation

Stars are self-gravitating bodies. Poisson's equation for the gravitational field is

$$\nabla^2 \phi = 4\pi G \rho, \quad (1.4)$$

where ϕ is the gravitational potential and $G \approx 6.673 \times 10^{-8} \text{ dyn cm}^2 \text{ g}^{-2}$ is Newton's gravitational constant. Because the stellar models are spherically symmetric, the radial spherical

coordinate can be utilized, ($\phi = \phi(r)$ only) giving an equation of the form

$$\frac{1}{r^2} \left(\frac{\partial}{\partial r} \right)_t \left(r^2 \left(\frac{\partial \phi}{\partial r} \right)_t \right) = 4\pi G\rho. \quad (1.5)$$

As in equation 1.3, these derivatives taken with respect to the spatial coordinate are total derivatives in space alone. They are partial derivatives with respect to the spatial coordinate when time is kept fixed. We then define the gravitational acceleration vector as that derivative of the gravitational potential, as,

$$\mathbf{g} = -\nabla\phi, \quad (1.6)$$

where $g = |\mathbf{g}|$. Equation 1.5 then has a solution

$$g = \frac{Gm}{r^2} \quad (1.7)$$

in the spherically symmetric case. For extremely massive stars ($M_* > 1000M_\odot$) or compact objects such as neutron stars, Newtonian gravity is no longer sufficient and Poisson's equation may no longer be useful. Codes that simulate such objects must be modified² to account for effects arising from general relativity (see [Heger et al. \(2002\)](#); [Marigo, P. et al. \(2003\)](#); [Woods et al. \(2017\)](#) and [Haemmerlé et al. \(2018\)](#) for discussions of recent such code implementations). Again, as for the Possionian case, the gravitational field of the star goes to 0 as $r \rightarrow \infty$. The potential itself is uniquely described up to a constant, and therefore for convenience is typically chosen such that $\phi \rightarrow 0$ as $r \rightarrow \infty$.

1.3.3 Hydrostatic Equilibrium

Again describing a shell of material inside the star of radius r , thickness dr , one identifies two central forces acting on the shell, gravitational acceleration ($-4g\pi r^2\rho\Delta r$) and pressure difference ($\Delta P = \frac{\partial P}{\partial r}\Delta r$). The force is $4\pi r^2\Delta P$. The condition that the shell of material remains static, gives another equation of stellar structure

$$\frac{\partial P}{\partial r} = -\frac{Gm}{r^2}\rho. \quad (1.8)$$

This can be converted to a Lagrangian form with equation 1.3 to give

$$\frac{\partial P}{\partial m} = -\frac{Gm}{4\pi r^4}. \quad (1.9)$$

²For a discussion of how we modify the equation of gravitational potential, amongst others, with regards to the, specifically, the MESA code, for the purposes of modelling such exotic objects, the reader is directed to sections 5.1.1 & A.1.

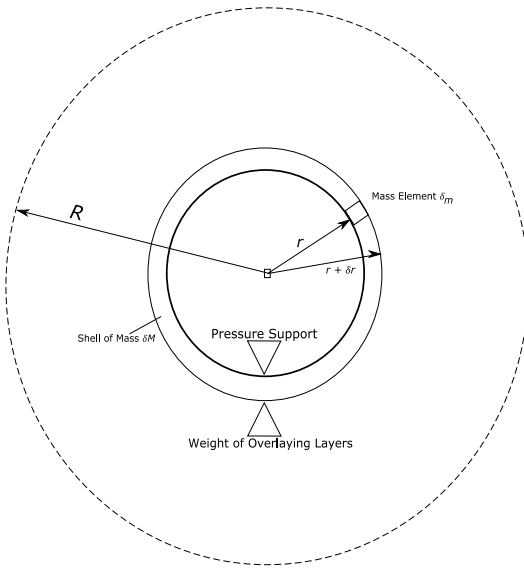


Figure 1.1 Simple sketch of mass conservation and hydrostatic equilibrium in a stellar model.

STARS imposes a set of boundary conditions (BCs) on the equations of stellar structure at the surface and the centre of the star. The BCs at the surface mesh point are chosen physically, applying BCs at optical depth $\tau = \frac{2}{3}$ (corresponding to a standard definition of the stellar photosphere, hence neglecting the mass and the radius of the stellar atmosphere. At this point, our equations could be coupled to a stellar atmosphere code, if needed.), mass chosen such to conform to the computed mass-loss rate *etc*. Owing to the implicit nature of the STARS solver, setting luminosity, mass and radius to zero at the central point of the star would result in singularities. Instead, Taylor expansions around the central, previous and anteprevious meshpoints in L_r (the total luminosity at radius r), m and r are utilized. This can be done implicitly, because the code solves by relaxation of all equations at all meshpoints simultaneously.

1.3.4 Energy Generation

Owing to the small mean free paths of the photons and the particles in the stellar interior, it follows that a good model of a star is in local thermodynamic equilibrium. Energy in a star can be generated through nuclear burning, gravitational contraction or other, more uncommon transient events such as accretion or merging. In the isolated case, the energy generated per unit time per unit mass may be written as ε . Because the contribution to the total luminosity of the star from any one shell is dependent on the energy generated in that

shell, the equation for energy generation in the Eulerian form is

$$\frac{\partial L}{\partial r} = 4\pi r^2 \rho \varepsilon, \quad (1.10)$$

where L is the luminosity and this can be expressed simply in Lagrangian coordinates as

$$\frac{\partial L}{\partial m} = \varepsilon. \quad (1.11)$$

Here, we have chosen, for the sake of clarity, to include all forms of energy generation or loss in ε . In practice, this term includes three main significant contributions. The first, and usually largest is the energy released from nuclear burning, ε_{nuc} . This term shall include the energy lost from the system as a result of neutrinos created in the nuclear burning processes free-streaming out of the star. We also consider ε_v , which is the energy loss due to the production of thermal (that is, via non-nuclear burning processes) neutrinos. We discuss the processes that generate such neutrinos and the implications therein in section 3.3. Finally, the term shall include the energy gained or lost through thermal processes, that is, the contraction or expansion of a region of the star, such as during the inflation of the stellar envelope as a star transitions across the Hertzsprung Gap from the end of the main sequence to the first ascent of the giant branch. The energy liberated/consumed in such a process is given as $\varepsilon_{\text{therm}} = -T \frac{ds}{dt}$.

1.3.5 Energy Transport

Here radiative and conductive energy transport in stellar models are summarized. Radiative energy transport is the movement of energy from the nuclear burning regions of the star out through the envelope by scattering, absorption and re-emission of photons. Diffusion of energy out from the core of a star can be described by the Eddington equation for radiative equilibrium

$$\frac{\partial T}{\partial r} = -\frac{3\kappa\rho L_r}{16acT^3\pi r^2}, \quad (1.12)$$

where T is the temperature, $a = \frac{4\sigma}{c}$ is the radiation constant, σ is the Stefan-Boltzmann constant, κ is the opacity and L_r is the luminosity at radius r . Again, this provides an Eulerian description of the radiation transport. A more general description of the energy transport equation that includes the effects of convective and radiative transport requires switching from an Eulerian radial coordinate, not to a Lagrangian mass coordinate, but instead a hydrostatic

³Although in practical terms the implementation into an evolution code, e.g. MESA is usually of the form $\varepsilon_{\text{therm}} = -TC_P \left[(1 - \nabla_{\text{ad}}\chi T) \frac{d\ln T}{d\ln t} - \nabla_{\text{ad}}\chi \rho \frac{d\ln \rho}{dt} \right]$

pressure coordinate P . This requires rewriting the equation of hydrostatic equilibrium as

$$\frac{\partial P}{\partial m_P} = -\frac{GM_P}{4\pi r_P^4}, \quad (1.13)$$

where P is the pressure, m_P the mass interior to the pressure P and r_P the radius at that given pressure coordinate. This transformation allows the energy transport equation to be formulated as

$$\frac{\partial \ln T}{\partial m_P} = -\frac{Gm_P}{4\pi r_P^4} \nabla_{\text{rad}}. \quad (1.14)$$

This provides a description of energy transport via radiation, where

$$\nabla_{\text{rad}} = \frac{3}{16\pi acG} \frac{\kappa L_r P}{m T^4}. \quad (1.15)$$

The opacities, in particular, are challenging to determine and STARS relies on tables of opacities. It uses the opacity tables from the OPAL (Opacity Project at Livermore) group ([Iglesias & Rogers, 1996a](#)). At lower temperatures however, it becomes possible to form molecules in the stellar plasma, and as such, we also make use of a table of molecular opacities by [Ferguson et al. \(2005b\)](#). The OPAL tables are computed and compiled tables of Rosseland mean opacity for a wide range of densities, temperatures and compositions. Although very detailed, these tables of course do not cover every possible combination as required by STARS. As such an interpolation is performed in order to compute the needed κ . There are currently three methods to determine opacity that we use. The first interpolates linearly in a table of opacities ([Pols et al., 1995](#)). This is generally not used anymore, however, can be useful in regions of temperature–density space where the tables are particularly sparse, and as such where the potential of the cubic spline to overfit is undesirable. The second performs a cubic spline interpolation in temperature and density but is still linear in composition since the electron scattering opacity κ_{es} is proportional to $1 + X$ where X is the hydrogen mass fraction. Finally, the third performs a full 5D interpolation in an opacity table in a set of such tables that all make provisions for non-constant ratios of carbon to oxygen, as explained by [Eldridge & Tout \(2004\)](#). Generally, cubic spline interpolation is used across temperature and density, while linear interpolation is used in composition. This reflects the underlying physics regarding the rates of changes of opacity with these properties. To model the more extreme conditions in stellar materials in TŻOs, the standard opacity tables are modified to cover considerably increased ranges of temperature and density. Convective regions are regions where either the chosen convection criterion indicates a convective instability, or are regions where the convective overshooting parameter permits mixing by convection despite the region being stable against convection according to the selected convective criterion.

In the first case, convection rapidly becomes the dominant energy transport mechanism owing to its increased efficiency compared to radiative transport. However STARS does not transport energy by convection in overshooting regions. It only mixes the compositions. In the non-overshooting convective regions, equation 1.14 could be modified to

$$\frac{\partial \ln T}{\partial M} = -\frac{GM_P}{4\pi r_P^4} \nabla_{\text{ad}}, \quad (1.16)$$

where

$$\nabla_{\text{ad}} = \frac{T\delta}{P\rho C_P} = \left(\frac{\partial \ln T}{\partial \ln P} \right)_S, \quad (1.17)$$

C_P is the heat capacity at constant pressure, $\delta = -\left(\frac{\partial \ln \rho}{\partial \ln T}\right)_{P,\mu} = \frac{T}{V} \left(\frac{\partial V}{\partial T}\right)_{P,\mu}$, S is the entropy and μ is the mean molecular mass of the stellar material. This description serves perfectly well as an illustrative definition, but one encounters problems when attempting to use it directly. If we want a (somewhat) consistent approach, we make use of a formalism known as Mixing Length Theory that uses a series of empirical, but observationally motivated assumptions in order to create a spherically symmetric convective energy transport formalism that is capable of well reproducing observations. We shall discuss these assumptions in section 1.4, but shall note here that convection and convective energy transport is a fundamentally chaotic, scale-dependent, time-dependent and above all, three dimensional problem, to which any one dimensional description is necessarily incomplete.

1.4 Convection

In stars of high ($M > 1.7M_\odot$) and very low ($M < 0.3M_\odot$) initial mass, convection is a vitally important energy transfer mechanism in the core of the star. In the first case, the higher temperature gradient, characteristic of a CNO burning dominated main-sequence energy generation, drives a convective core while in the second case the entire star becomes convective while on the MS, leading to a single convective region reaching from the core of the star to the atmosphere. For more massive stars, their characteristics are dominated by the properties of the convective core. In order to model the core (as well as burning shell, deep envelope and subsurface) convection, a stellar evolution code must apply a convective criterion in order to determine the extent of the convective zone. The Schwarzschild criterion for convection, while more commonly used, is strictly speaking, only valid in a chemically homogeneous region (e.g. in a completely convective low-mass star). The criterion states

that a region of the star or stellar core is stable against convection if and only if

$$\nabla_{\text{rad}} < \nabla_{\text{ad}}, \quad (1.18)$$

where the adiabatic temperature gradient, $\nabla_{\text{ad}} = \left(\frac{\partial \ln T}{\partial \ln P} \right)_S = \frac{P\delta}{C_P \rho T}$ is the interior temperature gradient in a moving fluid element when the element does not exchange heat with its surroundings and the radiative temperature gradient, $\nabla_{\text{rad}} = \frac{3}{16\pi acG} \frac{\kappa L_P}{mT^4}$ is the thermal gradient required to carry the entire flux by radiation only. If this condition is violated, then convection becomes the most efficient form of energy transport outside of electron thermal conduction, which only occurs in extremely dense core material, such as a white dwarf or giant's core ([Hubbard & Lampe, 1969a](#)) and as such begins to dominate energy transport, driving a region of core, shell or envelope convection. Another commonly used convective stability criterion is the Ledoux criterion, which is valid in a region with a chemical gradient, unlike the Schwarzschild criterion. Under the Ledoux criterion, a region is stable against convection when

$$\nabla_{\text{rad}} < \nabla_{\text{ad}} + \frac{\phi}{\delta} \nabla_{\mu}. \quad (1.19)$$

For a generic equation of state for the stellar material, $\rho = \rho(P, T)$ and internal energy $u = u(\rho, T)$. We write the first law of thermodynamics in terms of heat per unit mass, $dq = du + PdV$, where dq is the differential increment of heat added to the system per unit mass, and the variables ϕ and δ are defined as

$$\phi = \left(\frac{\partial \ln \rho}{\partial \ln \mu} \right)_{P,T} \quad (1.20)$$

and

$$\delta = - \left(\frac{\partial \ln \rho}{\partial \ln T} \right)_{P,\mu} = \frac{T}{V} \left(\frac{\partial V}{\partial T} \right)_{P,\mu}, \quad (1.21)$$

where $\nabla_{\mu} = \frac{\partial \ln \mu}{\partial \ln P}$, in equation 1.19, is the chemical gradient. STARS utilizes the Schwarzschild Criterion to determine convective instability but allows for a form of semi-convection by treating convective mixing as chemical diffusion. In particular, we allow mixing by one mesh point beyond a Schwarzschild boundary.

1.4.1 Mixing Length Theory

In order to actually compute the convective heat flow based only on the local properties of the star, we make use of Mixing Length Theory (MLT) ([Böhm-Vitense, 1958](#)). If we have heat being transported by a bubble of material travelling upwards through a star, then the

bubble will rise adiabatically until it has dissipated and mixed with the surrounding material, transporting net heat upwards. Here, the star has (locally) some temperature gradient which is larger (more negative) than the adiabatic temperature gradient. So once the bubble has risen a distance dr , the surrounding gas will have cooled by,

$$dT^s = \frac{dT}{dr} dr, \quad (1.22)$$

the bubble of course, is rising adiabatically, so it will have cooled,

$$dT^b = \left(\frac{dT}{dr} \right)_{ad} dr, \quad (1.23)$$

and as such, the difference in temperature between the bubble and the surroundings is,

$$\delta T = \delta \frac{dT}{dr} dr. \quad (1.24)$$

Naturally this serves to indicate how superadiabatic the stellar material is. If the bubble travels some distance l before dissipating then the energy per unit volume of convective material that is transferred to the surrounding material is just,

$$\delta q = \rho c_P \delta T = \rho c_P \delta \left(\frac{dT}{dr} \right) l. \quad (1.25)$$

Unfortunately this is only the heat transferred per unit volume per single bubble. The total heat transport is actually,

$$F = \rho c_P \delta \left(\frac{dT}{dr} \right) l \bar{v}_c (4\pi r^2), \quad (1.26)$$

where l is the characteristic distance that bubbles travel before dissipating and \bar{v}_c is the characteristic (local) velocity at which bubbles rise. As stated earlier, a self-consistent theory for computing these values is not possible in one dimension, and as such, we rely on MLT to get from the above equation to a working one dimensional implementation of convective heat transport. The first assumption of MLT is to state that the characteristic length that convective bubbles travel before dissipating depends on the pressure change, such that as the bubble expands as it rises to remain in pressure equilibrium. We assume that once the bubble is required to approximately double in volume, then we might expect it to dissipate. We shall parameterize this as the distance traveled before the change in pressure dP is of order of the pressure, P , such that,

$$1 \approx \frac{dP}{P} = \frac{1}{P} \frac{dP}{dr} dr = -\frac{\rho g}{P} dr. \quad (1.27)$$

Defining the inverse quantity $\frac{P}{\rho g}$ as the pressure scale height, H_P , we define l , the characteristic convective length scale in MLT to be,

$$l = \alpha H_P = \alpha \frac{P}{\rho g}, \quad (1.28)$$

where we have introduced an additional factor of order unity, α which allows us to tune the model to reproduce observations of the Sun. In order to compute the heat flux due to convection, we now need some method to approximate the characteristic velocity of convective motion, \bar{v}_c . Starting from the equation of motion that one might expect for such a convective bubble,

$$\frac{d^2}{dt^2} dr = A g dr, \quad (1.29)$$

which is SHM with the amplitude as,

$$A = \left(\frac{\gamma_{ad} - 1}{\gamma_{ad}} \right) \frac{1}{P} \frac{dP}{dr} - \frac{1}{T} \frac{dT}{dr} = \frac{1}{T} \left(\left(\frac{dT}{dr} \right)_{ad} - \frac{dT}{dr} \right) = \frac{1}{T} \delta \left(\frac{dT}{dr} \right). \quad (1.30)$$

The acceleration of the convective material is then,

$$a = \frac{g}{T} \delta \left(\frac{dT}{dr} \right) dr. \quad (1.31)$$

MLT then makes the very simple assumption that the characteristic acceleration of convective material is just equal to the instantaneous acceleration at the halfway point, i.e. $\frac{l}{2}$. The final velocity of the convective material at the point where it dissipates is then,

$$v = \sqrt{2al} = \alpha \frac{\mathcal{R} T}{\mu g} = \alpha \frac{\mathcal{R}}{\mu} \sqrt{\left(\frac{T}{g} \delta \left(\frac{dT}{dr} \right) \right)}. \quad (1.32)$$

If we take the initial velocity to be zero, and reason that the mean velocity must be some value between zero and the final velocity, we can add a term β , of order unity, which can again be tuned as needed, to get the mean velocity. We can now write, and implement in our codes, the convective heat flow as a function of local properties of the star only, alongside two empirical factors that must be fit to observations,

$$F = 4\pi r^2 \rho c_P \left(\frac{\mathcal{R}}{\mu} \right)^2 \left(\frac{T}{g} \right)^{3/2} \alpha^2 \sqrt{\beta} \left(\delta \frac{dT}{dr} \right)^{3/2}. \quad (1.33)$$

1.4.2 Convective Overshooting

One issue with the computation modelling of a convective system is the phenomenon of convective overshooting. In actual physical systems, most familiarly in clouds in the troposphere, a region of material unstable against convection does not stop instantly upon reaching the boundary of the unstable region as defined by a convective stability criterion, instead, the material overshoots the boundary by some distance as determined by its inertia. This phenomenon was discussed extensively, in the context of stellar evolution, beginning in the 1950s by [Unno \(1957\)](#); [Schwarzschild & Härm \(1958\)](#); [Böhm \(1963\)](#); [Shaviv & Salpeter \(1973\)](#) and more recently in works by, for example, [Roxburgh \(1998\)](#); [Griffin et al. \(2016\)](#). In an atmospheric system, overshooting can be observed by noting that the base of a tropospheric cloud is generally flat. The upper surface often consists of regions of overshoot material protruding from the bulk of the cloud. A very similar concept of overshooting can be applied to stellar modelling. Although some of the earliest work done on overshooting largely dismissed its effects on the outcomes of stellar models, ([Saslaw & Schwarzschild, 1965](#)), more recent work has suggested that it can, in fact, alter basic properties of stellar model outputs, such as central temperature and density during the MS and He burning phases ([Yong-quan & Ru-feng, 1996](#)), convective mixing and even complete chemical homogeneity of the star ([Jie et al., 2015](#)). Of interest then, is the implementation of variables that dictate overshooting as free parameters in a stellar evolution model. Convection and convective overshooting are generally implemented, and implemented in the Geneva code in particular, as a 1-D mixing length theory (MLT) problem ([Eggenberger et al., 2008](#); [Arnett et al., 2018b](#)).

[Marques et al. \(2006\)](#) describe qualitatively in figure 1.2, the behaviour of the temperature gradient in an overshooting model, where CZ is the pure convective zone, as defined by the criterion of Schwarzschild or Ledoux, d_{ov} is $\alpha \mathcal{H}$, as shall be described in equation 1.34, where \mathcal{H} is the pressure scale height, that is, the increase in radial coordinate for which the pressure of the stellar material decreases by a factor of e . Mixing Zone (MZ) is the full zone over which mixing can occur. This is important when considering the chemical composition, chemical gradient and chemical homogeneity of the model. BMZ marks the Boundary of the Mixing Zone, where in a rotating model, differential rotation and shearing effects become important. ∇_{MLT} describes the convective temperature gradient which, as prescribed by standard Mixing Length Theory, is driven towards the adiabatic gradient to a high degree of accuracy in the completely convective case ([Böhm-Vitense, 1958](#)), ∇_{ov} describes the overshooting region temperature gradient. This allows the material to cool as if the convective condition were not being met, (strictly, this is the case) while still allowing energy transport to be convection dominated, ∇_{rad} is the radiative temperature gradient (equation 1.15), and ∇_{ad} is the adiabatic temperature gradient (equation 1.17). This can

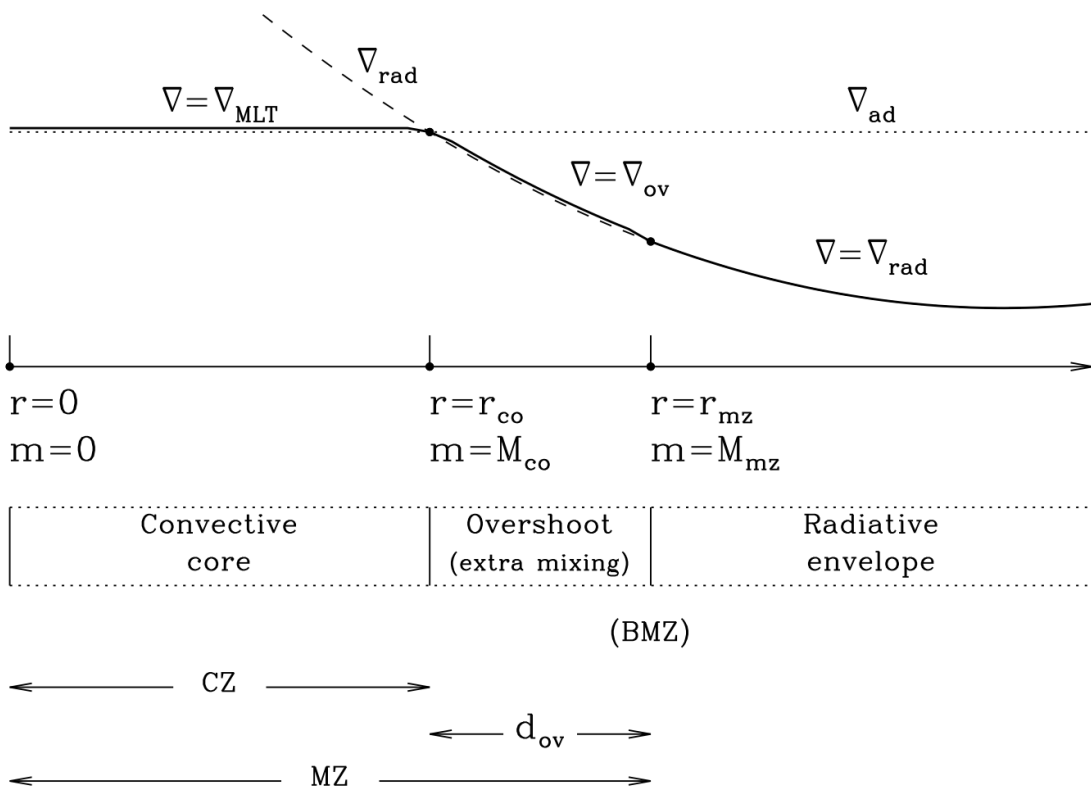


Figure 1.2 Qualitative description of the behaviour of the temperature gradient inside a $2M_\odot$ (very low mass for our purposes) star where convective overshooting is utilized, by Marques et al. (2006). Convective overshooting at this mass produces a smooth profile for the temperature gradient moving from the fully convective (by the Schwarzschild criterion) core to the overshooting region, and on to a fully radiative envelope. In GENEC, sub-surface convection is additionally modelled at higher masses.

approximate closely the MLT gradient, particularly for core convective regions. However, in the case of an envelope convective region, such as that in the Sun, the superadiabatic gradient can be critical, which will determine the adiabat on which the rest of the convective envelope lies. [Renzini \(1987\)](#) produced an original critique of 1D MLT as implemented in 1D stellar evolution codes, stating that full 3D hydrodynamic or MHD calculations were the best way to completely capture and treat overshooting and convection as a whole. Recently, [Arnett et al. \(2018a\)](#) investigated the critique of MLT as offered by Renzini and concluded that full, self-consistent 3D MHD (magnetohydrodynamics) simulations would be needed for a complete description of convection, particularly at the boundaries between convective and non-convective regions. In a follow-up publication [Arnett et al. \(2018b\)](#) concluded that there were certain features of convection, such as turbulent boundary zones at the base of convective regions that the full MHD approach described but which were not captured in an MLT approach. In addition they concluded that MLT convective models, while largely valid in a weak stratification case (such as core convection), would need significant modification to describe convection accurately in the strongly stratified case (such as stellar atmosphere and upper envelope convection). Given the complex convective structure of a post-main sequence massive star and the computational time required to produce such a simulation ([Arnett et al., 2018a](#)), it is clear that computing such a detailed simulation of convection at every timestep of a stellar evolution model is unfeasible. As is made clear from figure 1.3, even a very small snapshot of a star, both in time and in space, in a very late stage of burning, is extremely computationally intensive to generate. Attempting to produce a full hydrodynamic simulation of the core of a star on the MS, or even the helium or hydrogen burning shells of the later phases of stellar evolution, is hindered by the laws of fluid mechanics themselves, because the lower energy generation rates results in a lower Mach number and lower Reynolds number ([Cristini et al., 2017](#)) in the simulation. This greatly increases the convective turnover time. This results in a simulation that would require billions of hours of CPU time to produce just a few convective turnover times worth of simulation, and this problem is only exacerbated by the relatively larger physical regions of the star which would have to be considered, particularly in the MS core simulation example. As such, convective overshooting remains necessary as an engineered implementation which produces a sufficiently accurate simulation (with regards to the consistency of these models when compared to observations, particularly observations of the Sun). There is also some degree of observational evidence (although not, of course, for Population III stars), that some convective overshooting is required in order to produce accurate stellar models, although these investigations have only been performed for Galactic open clusters ([Woo & Demarque, 2001](#)), and as such is sampling somewhat lower masses and higher metallicities than expected

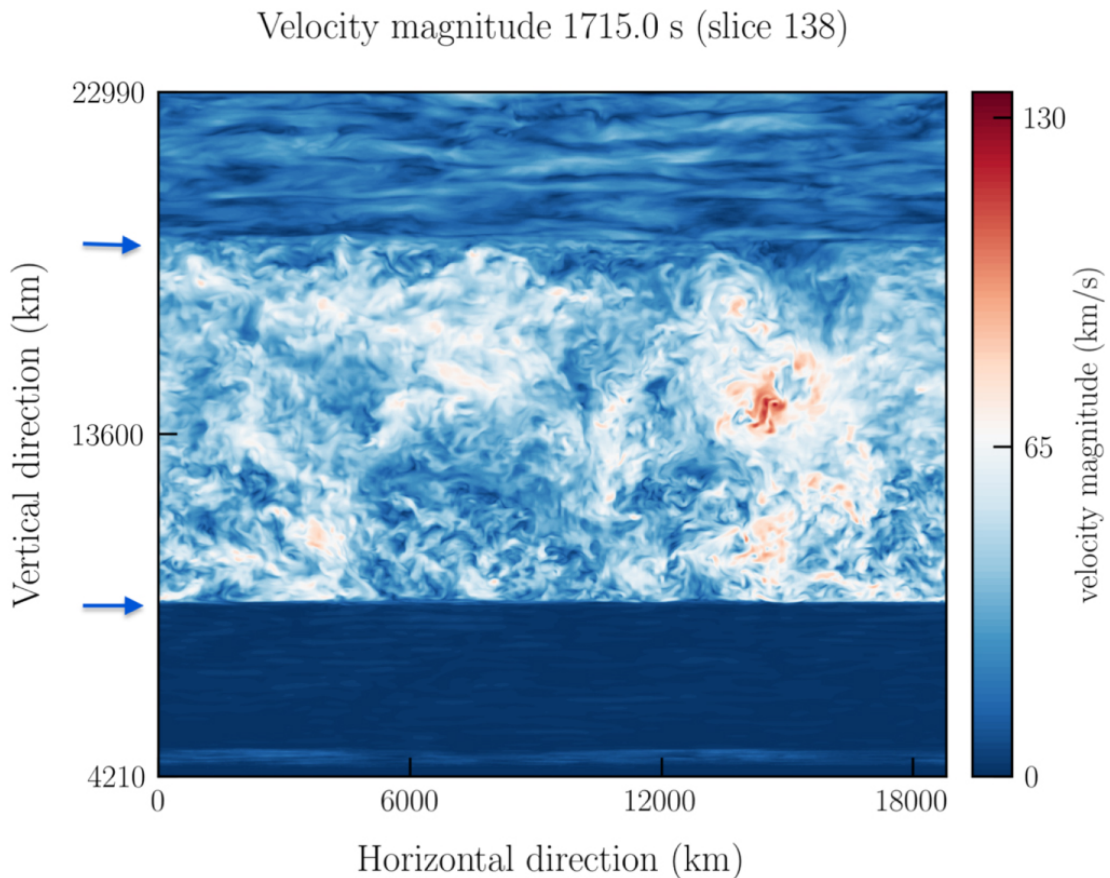


Figure 1.3 Slice of a full, 3D MHD simulation of the carbon burning shell of a $15M_{\odot}$ star with 1024^3 grid points from [Cristini et al. \(2017\)](#) provided by [Arnett et al. \(2018b\)](#) as an example of a 3D MHD model capable of capturing detail missed in a simple 1D MLT treatment of convection, such as radial g-mode waves in the radiative regions above and below the shell, as well as the complex turbulent behaviour of the material in the shell itself.

for a typical PopIII (zero metalicity) stellar population. They placed an observational upper limit on the convective overshooting parameter for low mass (less than $1.2M_{\odot}$) and high metalicity ($Z \approx Z_{\odot}$) stars. The overshooting parameter, β describes the fraction of the pressure scale height at the convective boundary of the core (or burning shell) that a bubble of convective material travels above the boundary of the convective zone under its own inertia.

$$z = \beta \mathcal{H}_P \quad (1.34)$$

where \mathcal{H}_P is the pressure scale height at the boundary of the convective region, defined as,

$$\mathcal{H}_P = \frac{P}{\left| \frac{dP}{dr} \right|} \quad (1.35)$$

This detail becomes relevant because there are different methods by which the pressure scale height can be calculated, and GENEC and MESA utilize different methods ([Eggenberger et al., 2008](#); [Paxton et al., 2018a](#)).

Chapter 2

Thorne-Żytkow Objects: background and existing literature

‘An’, as it blowed an’ blowed, I
often looked up at the sky an’ assed
meself the question—
what is the stars, what is the stars?’
‘Ah, that’s the question, that’s the
question—
what is the stars?’

Seán O’ Casey,
Juno and the Paycock, 1924

In this chapter, I shall introduce the concept of a Thorne-Żytkow Object (TŻO), a form of proposed hybrid star, and describe the structural models of these objects as described in the literature, specifically those by [Thorne & Żytkow \(1975\)](#); [Thorne & Żytkow \(1977\)](#); [Eich et al. \(1989\)](#); [Cannon et al. \(1992\)](#) and [Cannon \(1993b\)](#). I shall discuss the proposed nuclear energy generation processes in these objects, as well as their proposed formation pathways, final fates, and observational prospects thereof.

2.1 Introduction

Thorne-Żytkow Objects (TŻOs, [Thorne & Żytkow \(1977\)](#), from hereon, TŻ) are proposed hybrid stars consisting of a giant or supergiant star with a core of neutron degenerate matter. A TŻO may be thought of as a giant star envelope with a neutron star as a core, in much the same way that a giant star may be thought of as an envelope with a white dwarf as a core. A proposed formation mechanism for TŻOs involves a neutron star in a binary with a giant or supergiant companion. As discussed by [Podsiadlowski \(2007\)](#), the orbit of a neutron-star red-giant binary shrinks initially owing to the emission of gravitational radiation or the transport of angular momentum by the accretion of winds, depending on the exact evolutionary state of the companion, and then by tidal interactions, until the neutron star spirals into the envelope of the giant star in a period of common envelope evolution (CEE), wherein it experiences dynamical friction, which causes it to settle at the centre of

the giant star, merging with its core. If the time-scale for this orbital decay is shorter than the time-scale for mass loss from the common envelope, as [Terman et al. \(1995\)](#) suggests, then all X-ray binaries consisting of neutron stars and giants could eventually form TŻOs. We distinguish between two categories of TŻOs, low-mass (envelope mass $M_{\text{env}} \lesssim 8M_{\odot}$) TŻOs and high-mass (envelope mass $M_{\text{env}} > 14M_{\odot}$) TŻOs (assuming fixed core masses and radii, see fig. 4 of TŻ). These are distinguished by their primary energy source. Low-mass TŻOs are powered by Eddington-limited accretion, while high-mass TŻOs are, in addition, powered by a shell of nuclear burning material. As [Podsiadlowski \(2007\)](#) points out, the burning regions of this class of TŻOs contain very little fuel (about $10^{-11}M_{\odot}$), which needs to be re-supplied by convection from material in the envelope. The convective turnover time-scale is short compared to most β^+ decay time-scales in typical hydrogen burning channels. Nevertheless [Cannon \(1993b\)](#) showed that hydrogen burning could proceed by a channel known as the interrupted rapid proton capture (irp) process. This is a chain of rapid proton captures terminated by β^+ decays, when the decay time is shorter than the time-scale for the next proton capture. As stated, since the convective turnover time-scale in the burning region is so fast, that the proton-capture products are swept out of the burning region before the β^+ decay occurs. [Cannon \(1993b\)](#) and [Biehle \(1994\)](#) suggest that most or even all p-process elements in the Universe could be produced in TŻOs.

Observational opportunities for the detection of TŻOs may likewise exist in the supernovae of TŻOs. [Moriya \(2018\)](#) and [Moriya & Blinnikov \(2021\)](#) propose that a TŻO may explode, once envelope fuel is exhausted. At this point, the envelope should begin to collapse on to the neutron star, accreting in a disk at a super-Eddington rate. This occurs because, as the stellar material nearest to the neutron core continues to infall and contract, the temperature continues to rise, until the accretion becomes neutrino limited, leading to super-Eddington accretion onto the core. This super-Eddington accretion continues until the behaviour of the infalling material becomes dominated by centrifugal forces. If we assume an angular velocity from [Cannon \(1993b\)](#) of around $3 \times 10^{-9} \text{ s}^{-1}$, and further assume that TŻO envelope rotation is rigid, as a result of the very efficient convection in the envelope, then we may expect roughly Keplerian velocity at the neutron core, shortly after the onset of collapse. Efficient accretion now continues onto the neutron core from a thick accretion disk. The rapidly accreting neutron core may then collapse to a black hole, launching a spherically symmetrical outflow. It is suggested that, dependant on the exact time-scale on which post-collapse accretion continues to function effectively, that a wide range of energy release could be attained, anywhere from the order of the envelope binding energy of around 10^{47} erg or less, all the way up to the energy of a highly energetic Type II supernova, such as OGLE-2014-SN-073 ($12.4_{-5.9}^{+13.0} \times 10^{51} \text{ erg}$, [Terreran et al. \(2017\)](#)), or an accretion powered superluminous

explosion ([Dexter & Kasen, 2013](#)) such as the ultra-luminous type II-L supernova, 2008es (around 1.1×10^{51} erg), as described by [Gezari et al. \(2009\)](#) and [Miller et al. \(2009\)](#). A new statistical photometric analysis approach was proposed by [Inserra et al. \(2018\)](#) to identify (specifically hydrogen-poor) superluminous supernovae, without setting any underlying *ad hoc* magnitude threshold. Such an approach could be used (coupled with models of T $\ddot{\text{Z}}$ O explosions), to identify candidate (former) T $\ddot{\text{Z}}$ O. The detection of a candidate T $\ddot{\text{Z}}$ O, HV2112, in the SMC by [Levesque et al. \(2014\)](#), although itself far from an observational confirmation of a T $\ddot{\text{Z}}$ O highlights the need for further study of these objects, with a particular focus on the creation of nucleosynthetic observables. A nucleosynthetic observable is any sort of anomalous chemical abundance in a stellar object that is in principle observable, i.e. material with anomalous chemical abundances that are present in the photosphere of a star and are hence potentially observable by spectroscopy. In chapter 5 we produce modern structural models of T $\ddot{\text{Z}}$ O envelopes, to compare and contrast with earlier models and to consider the implications of these investigations on potentially observable quantities.

2.2 Canonical Structure Solutions of T $\ddot{\text{Z}}$ O

Here I shall briefly describe the two main *canonical* models of the structure and the nucleosynthesis of Thorne-Żytkow Objects — those as originally described by [Thorne & Żytkow \(1977\)](#) and those described in a series of follow up studies by [Cannon et al. \(1992\)](#) and [Cannon \(1993b\)](#). Computations of T $\ddot{\text{Z}}$ O structure have also been produced by [Bisnovatyi-Kogan & Lamzin \(1984\)](#); [Eich et al. \(1989\)](#); [Biehle \(1991\)](#); [Podsiadlowski et al. \(1995\)](#) and others. Reference to these too will be made where relevant.

2.2.1 Canonical models: Thorne & Żytkow 1977

The classical structure of T $\ddot{\text{Z}}$ O was constructed and described in detail by [Thorne & Żytkow \(1977\)](#). These models are defined by a number of physically distinct regions. Starting from the surface of the star, these are the photosphere, at optical depth $\tau = 2/3$, the static envelope, which is convective and reaches down to a point at which the inflow of material towards the core is significant, the inflowing envelope, which reaches down from that point until the knee, the knee which is the base of the convective envelope, the region of gravitational energy release or halo, which reaches down from the knee to a density of around $10\rho_k$, where ρ_k is the density at the knee, an insulating layer, which covers the region of the halo from where electron degeneracy becomes significant down to the neutron drip line, and finally an isothermal ($T \approx \text{const}$, see section 5.1.1) neutron-star core. Giant-style solutions (envelope

mass $\lesssim 10M_{\odot}$) differ from supergiant-style models ($M_{\text{env}} \gtrsim 10M_{\odot}$) only in the position of the hydrogen burning shell, which is interior to the knee in the giant solutions but overlaps with the convective envelope in the supergiant models.

The halo in TŻ's models is located just above the core, where the pressure scale-height, H_P is of order 1 m. By a radial distance of around 15 m above the core, the density falls rapidly from around 10^6 g cm^{-3} to around 1 g cm^{-3} . TŻ suggest that either the sudden generation of e^- and e^+ pairs, or the increase of the local luminosity to near the Eddington luminosity could lead to the necessary decrease in density, although they construct only models where this condition is achieved as a result of the latter mechanism. Ultimately, their models have a local luminosity that is super-Eddington at this point, so driving up the pressure scale-height. This luminosity is generated in the halo almost exclusively (in the giant models) from the release of gravitational potential energy from inflowing material, above this $\rho \approx 1 \text{ g cm}^{-3}$ point drives convection, marking the end of the halo and beginning of the knee. They argue, because the luminosity is so large here and that at larger radii the temperature continues to fall and opacity continues to rise, that the continuously falling critical luminosity leaves the entire stellar envelope super-Eddington and hence convective from this point outwards to the photosphere. The knee in these models is extremely sharp, with the isothermality of the halo terminating so abruptly as to lead to a near discontinuity in the slope of the $\rho(T)$ relation for their low-mass models. However TŻ note that considering more carefully the effects of convective overshoot at the knee would result in a relatively minor softening of the knee. The nuclear burning shells in these models have an extremely thin physical thickness, around 2 to 4 m for the hydrogen and helium burning shells and around 20 m for any metal burning shells. This extremely thin shell burning is an important assumption of the envelope integration routines they employed, and indeed did others such as [Eich et al. \(1989\)](#). The outer regions of these models are nearly indistinguishable from those of red (super)giants with degenerate (white dwarf-like) or non-degenerate cores. Indeed, it is shown that the total stellar luminosity and the temperature at the photosphere are nearly completely insensitive to the specific conditions at the knee and in the halo. We likewise find in section 5.2.1 that, despite very fundamental differences between the models we compute and those of TŻ, that indeed our envelope structures agree almost exactly. We also note that this series of models admits a mass gap between the giant and supergiant solutions where no envelope solution converges. TŻ explain this by the sharpness of the turning-on of pair production around $\log_{10}(T/\text{K}) \approx 8.7$, rapidly dropping the (gravitational redshift corrected, due to proximity to the highly compact neutron core, see section 5.1.1) critical luminosity, resulting in neither a giant nor a supergiant solution with the correct knee radius for a given total luminosity, or vice versa.

2.2.2 Canonical models: Cannon et al. 1992, 1993

The models of T $\ddot{\text{Z}}$ O produced by [Cannon et al. \(1992\)](#) and [Cannon \(1993b\)](#), and similar models by [Biehle \(1991, 1994\)](#) are in principle the same as those of T $\dot{\text{Z}}$ but with a few important differences. While the models of T $\dot{\text{Z}}$ use the Generate Outer Boundary (GOB) envelope integration program ([Paczyński, 1969, 1970a](#)) to produce a static envelope solution, these models are evolved with a Henyey code, in this case, a heavily modified variation of the STARS evolution code ([Eggleton, 1971; Eggleton et al., 1973](#)). The relativistic formulation of the standard stellar structure equations (section 5.1.1) is used and the core itself is modelled with the phenomenological GR equation of state, section 2.5a of [Cooperstein \(1988\)](#). This core region is connected to the envelope by a the neutronizing artifice as described in section 5.1.2 such that, at densities above around 10^6 g cm^{-3} , the effective mass of electrons is increased exponentially with the electron degeneracy ψ . This creates an [Oppenheimer & Volkoff \(1939\)](#)-like equation of state at high ψ that is connected to the core, a standard envelope equation of state ([Eggleton et al., 1973](#)) at lower ψ and a smooth but artificial region joining the two, the core-envelope artifice. [Cannon et al. \(1992\)](#) found it is necessary to modify the meshing function of the STARS code in order to ensure that the eigenvalue Q increases monotonically with mass. Models of T $\ddot{\text{Z}}$ O are then generated by neutronizing the hydrogen depleted core of a low-mass giant stellar model. A range of models are created by adding or removing mass at the photosphere and allowing the core to accrete material from the envelope with the artifice. [Cannon et al. \(1992\)](#) notes that, unlike T $\dot{\text{Z}}$, they are able to produce models across the entire plane of ranges of core masses and total masses, constrained only by the Tolman–Oppenheimer–Volkoff (TOV) limit on the maximum core mass and the requirement that the velocity of material inflowing on to the core be at every point lower than the local convective velocity, because otherwise only an advective flow could transport material downward quickly enough. Cannon et al. find that all their models have a deep convective envelope that reaches down to the core, with a knee at which there is a very steep gradient in gas pressure, where the local pressure scale-height is of the order of a few metres. Cannon’s plane of T $\ddot{\text{Z}}$ O models is split into three possibly overlapping regions, case (A) where a hydrogen burning shell exists entirely below the knee and there is no energy release above the knee at all, case (B) where some, but not necessarily all, hydrogen burning occurs above the knee in the convective envelope and where at no point in the star is the production of e^- and e^+ pairs important, and case (C) where hydrogen burning occurs exclusively in the convective envelope and the knee itself is hot and dense enough for pair production to dominate the opacity at that point. We note the similarity between case A models and T $\dot{\text{Z}}$ giant solutions and case C and T $\dot{\text{Z}}$ supergiant solutions. Case B models fill the region in which the mass gap exists in the model series of T $\dot{\text{Z}}$. Outside of case A

the luminosity is no longer fixed to the release of gravitational energy and so the linking of the burning regions and the envelope by convection leads to a large reservoir of fuel. In our series of models, despite very considerable differences in the structure of the models themselves, we find likewise that the linking of the convective envelope with the hydrogen burning region leads to a nearly inexhaustible supply of fuel and the curious result that neglecting mass loss which we would expect to be significant, higher-mass TŻO models have longer lifespans than the lower-mass. Importantly, all of TŻ's and Cannon's models appear as extreme M (red) supergiants (as do ours) and furthermore we note that such envelopes surrounding degenerate white dwarf cores undergo rapid mass loss, possibly on the order of $10^{-5} M_{\odot} \text{ yr}^{-1}$, so that entire envelope of the object is lost within a few 10^6 yr . In the Cannon et al.-style models, as predicted by the TŻ-style models, the lifespans are predicted to be anywhere from around 10^5 yr , if the lifespan were limited by available fuel, to a few 10^8 yrs , when the lifespan is limited by mass loss. In our models we find that the fuel-limited lifespan of the models is a function of the envelope mass but is around a few 10^6 yr . Hence, while we have not considered the effects of mass loss in section 5.2.1, we may expect there to be model envelope masses for which the exhaustion of envelope fuel sets the lifespan and a class for which the lifespan is indeed set by the mass loss, as Cannon et al. predicted.

2.3 Nuclear energy generation, nucleosynthesis and the irp process

[Cannon \(1993b\)](#) describes how supergiant-type solutions lead to an interrupted rapid proton capture (irp) process. In these, with envelope masses above about $14 M_{\odot}$, the proton-rich material in the region at the base of the convective envelope, where nuclear burning takes place, provides an ideal site for the rapid proton capture (rp) process. While "proton process" is often used to refer to any process that produces proton-rich nuclei (that cannot be created via the r-and s-processes) we use it to refer specifically to processes involving a proton capture. The rp process involves short-lived nuclei that, owing to the very high proton density in the stellar material, are able to capture one or more protons before β decay. In the rp process the chain of proton captures is limited not by the β decay rate but rather by the proton drip line itself. This allows production of more massive, more proton-rich and rarer nuclei. In figure 2.1 we show as an illustrative example the reaction flow for one of the main rp process sites in the universe, an accreting neutron star. The dominant reaction paths in the supergiant models of [Cannon \(1993b\)](#) depend on the balance between proton capture reactions, photodissociation and β decay. In the burning zone, proton capture occurs until

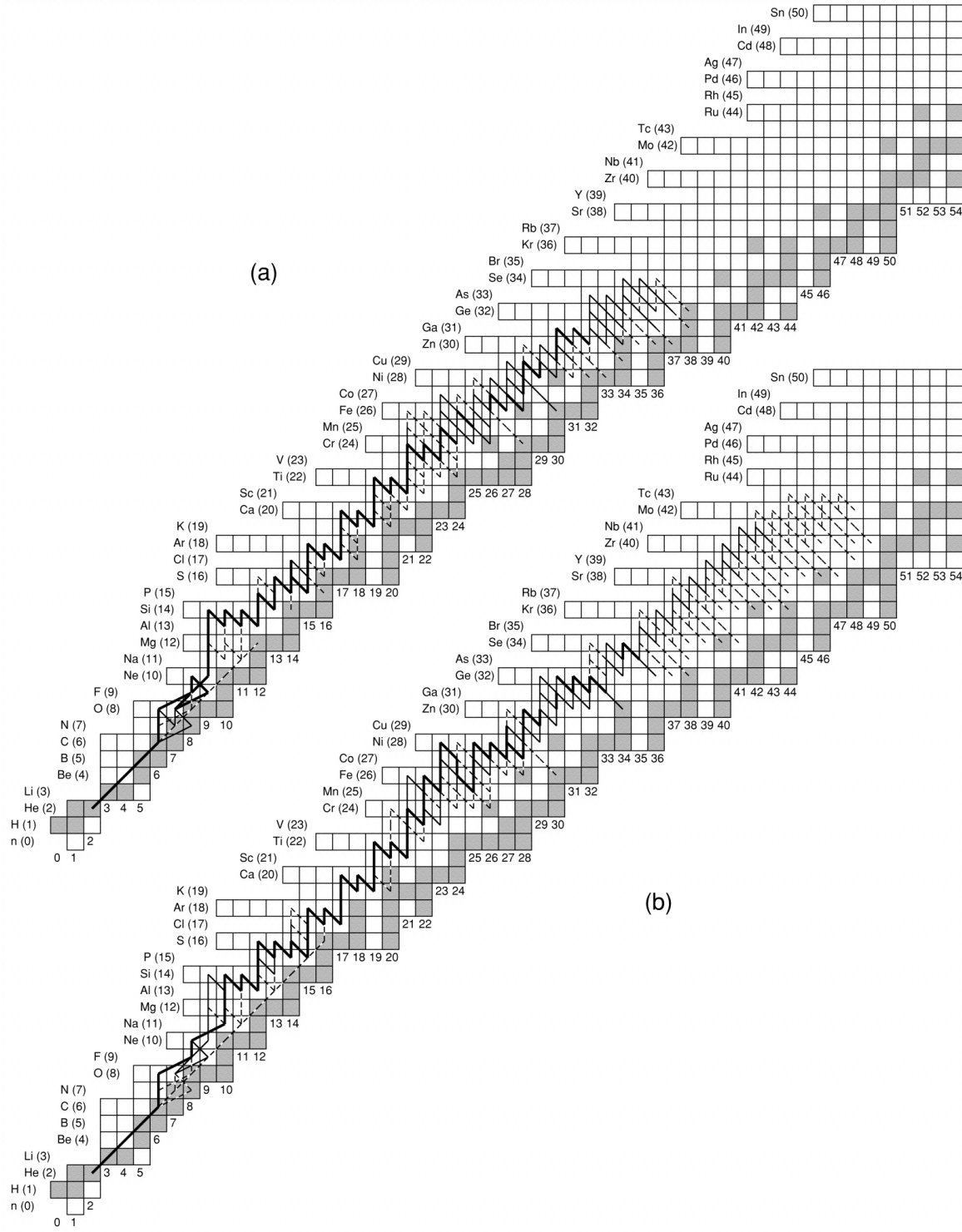


Figure 2.1 Reaction flow rate (normalized to 3α rate, thick line, more than 50% flow, thin line, 10% - 50% flow and dashed line 1% - 10% flow) for rapid proton burning during neutron-star accretion. Rates and integrated nucleosynthetic calculation are by Schatz et al. (1999). The calculation for case (a) is performed for Eddington limited accretion onto the neutron star, as we would expect for accretion onto the neutron cores of TŻOs. Case (b) is for $5m_{Edd}$, which may be an appropriate rate to consider during the neutrino dominated accretion that occurs after a TŻO has exhausted its irp seed elements, and begins to collapse.

the photodissociation reaction for the next step begins to dominate. If the decay time-scale for the species in question is short then the nucleus may decay and undergo further proton capture in the burning zone. However, at higher atomic masses, proton capture is interrupted before a species with a sufficiently short photodissociation time-scale is reached. This is the interrupted rapid proton capture process. In the region where the irp process dominates, the reaction chain proceeds as a series of vertical steps up the reaction network, the addition of protons, followed by the interruption, during which there is a slow decay back down towards the region of β stability. During the proton addition phase, the reaction proceeds largely as illustrated in figure 2.1, particularly as in case (a) in that figure, where the Eddington limited accretion rate onto the neutron star is also a suitable rate for the accretion of infalling material onto the neutron core of a TŻO. At higher and higher mass numbers the proton capture reactions become sufficiently slow that they may no longer be assumed to go to completion. For species that are near stable (long in comparison to the time-scale for the proton captures, given that there are no stable species here), close to the proton drip line, photodissociation is unlikely to be important and the time-scale of the interruptions is sufficiently long to allow for β decays. Hence, it is the slowing rate of the proton capture reactions themselves that sets the ultimate limit of the irp process. This point is strongly dependent on the temperature in the burning zone ([Biehle, 1994](#)).

2.4 Hydrodynamic Evolution of TŻOs

Although our focus will be on the secular, hydrostatic evolution of TŻOs', the hydrodynamical evolution of these objects cannot be ignored. Specifically, there are two phases of evolution where we cannot, or rather should not, treat the accretion of material on to the neutron core in a purely hydrostatic manner. The primarily proposed formation mechanism for a TŻO involves a phase of common envelope evolution (CEE) between a giant/supergiant star and a neutron star companion. While a wide range of CEE prescriptions exist, largely in population synthesis codes as a means of parameterising the effects of such evolution on a population (e.g. the commonplace α formalism by [Tutukov & Yungelson \(1979\)](#)), the inspiral of a neutron star into the envelope of a massive, evolved star and the subsequent merging of the NS and the stellar core are intrinsically hydrodynamical processes. Any attempt to reduce these processes to hydrostatic, one-dimensional prescriptions necessarily involves a great deal of simplification and abstraction. Importantly this is not merely a case of us ensuring realistic initial conditions for a hydrostatic model. Indeed, the nucleosynthesis that may occur during this initial inspiral may produce anomalous abundances of, for example calcium, that could act as a key spectral feature lifting the observational degeneracy between TŻOs

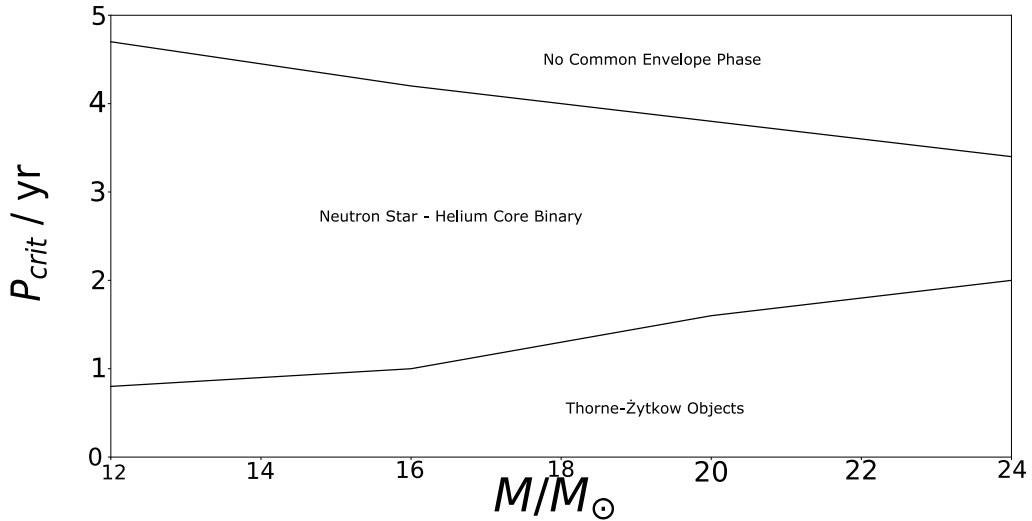


Figure 2.2 Critical binary orbit periods P_{crit} as a function of donor star mass M after [Terman et al. \(1995\)](#). For periods below the lower curve they expect the neutron star to merge with the core of the companion to form a TŻO. For periods above the upper curve the system fails to enter a period of CEE, while in the region delimited by the two curves a short period binary system consisting of the neutron star and the giant's core emerges.

and sAGBs ([Levesque et al., 2014](#); [Tout et al., 2014](#)). The second phase of TŻO evolution where a hydrodynamical approach is required is once they have exhausted their rp-process seed elements and/or have fallen below their minimum sustainable envelope mass via other processes (wind or episodic eruptive mass loss) and undergo a neutrino runaway, ultimately leading to their destruction. Here we shall briefly discuss these phases and the methodologies employed in order to study them.

2.4.1 Formation pathways for TŻOs

The most likely formation pathway of TŻOs is the merging of a neutron star and a giant star after a period of common envelope evolution (CEE) in an X-ray binary. The SPH simulations of merging X-ray binaries by [Terman et al. \(1995\)](#) suggest that a sizable proportion of all X-ray binaries end their lives by forming TŻOs with the fate of the system depending on the mass of the donor star and a critical period for the binary, as illustrated in figure 2.2. When the X-ray binary is a neutron star-helium core binary, up to 85% of the envelope mass is ejected during the period of CEE. Appropriately some work regarding the formation of TŻOs suggests that an unbinding of the envelope occurs, rendering the formation of a TŻO by this mechanism impossible. [Podsiadlowski et al. \(1995\)](#) refer to three likely pathways

for TŻO formation, one for low-mass and two for high-mass. [Ray et al. \(1987\)](#) describe a mechanism to form low-mass TŻOs by direct collision of a low-mass main-sequence star with a neutron star. The proposed high-mass formation mechanisms include the coalescence of a neutron star with a massive companion in an X-ray binary, as discussed. [Leonard et al. \(1994\)](#) also describe a scenario where the primary of a massive, tight binary explodes as a supernova and the asymmetric kick given to the formed neutron star happens to place the neutron star in a bound orbit with a pericentre distance sufficiently low that the neutron star becomes embedded in the secondary. As mentioned the preferred or classical formation mechanism maintains that TŻOs are the products of the evolution of massive X-ray binaries (MXBs). [Podsiadlowski et al. \(1995\)](#) note that, in these MXBs, when the massive component fills its Roche lobe the mass-transfer rate exceeds the Eddington rate of the neutron star by 3 to 5 orders of magnitude. Hence the excess unaccreted mass fills the neutron star's Roche lobe and the system enters a CEE phase. Gas drag then causes the neutron star to spiral in towards the centre of the system. If the orbital energy released is sufficient to eject the envelope the final product is a neutron star-helium core binary. Otherwise, a TŻO is formed. [Chevalier \(1993\)](#) argued that TŻOs may not be able to form at all because, during the spiral-in process of the CEE, accretion on to the neutron star may occur in a neutrino dominated rather than Eddington limited regime. That is in which the majority of the surplus orbital energy is lost to neutrinos. In this case, the system would likely collapse to a black hole. [Podsiadlowski et al. \(1995\)](#) note that this argument requires spherically symmetric accretion at a rate determined solely by the orbital motion of the neutron star. In addition Podsiadlowski refers to [Bhattacharya & van den Heuvel \(1991\)](#) for observational evidence of neutron stars having survived spiral-ins.

Recently, [Hirai & Podsiadlowski \(2022a\)](#) performed a series of 3D hydrodynamical simulations of collisions of neutron stars with their main-sequence binary companions, following the natal kick experienced by the NS. From the results of these simulations, they construct a semi-analytical prescription describing hydrodynamic drag inside the stars, specifically to deal with the deviation of their simulations from the standard Hoyle–Lyttleton model ([Hoyle & Lyttleton, 1939](#); [Hoyle & Lyttleton, 1941](#); [Bondi, 1952](#); [Mestel, 1954](#)). By applying the semi-analytical model to a variety of possible natal kicks, they find a range of possible outcomes, contingent on the direction and magnitude of the natal kick. In some scenarios (high impact velocities and impact parameters) the neutron star can plunge directly through the companion envelope without merging, while in a scenario with a lower impact parameter, they find that the NS may directly merge with the core of the companion so forming a TŻO. Hydrodynamical simulations of this nature will doubtlessly continue to prove important in better understanding the formation mechanism of these exotic objects. Furthermore, the

development of (semi-)analytical prescriptions of these mechanisms presents an opportunity to integrate this physics into binary population synthesis codes and improve the integration of T $\ddot{\text{Z}}$ O in such codes. This is potentially vital given the unusual nature of the nucleosynthesis that may occur in their interiors.

2.4.2 Final Fates of T $\ddot{\text{Z}}$ O

There are again distinct scenarios for the death of low- and high-mass T $\ddot{\text{Z}}$ O. Massive T $\ddot{\text{Z}}$ O end their lives in a neutrino runaway, when the steady state burning phase of the T $\ddot{\text{Z}}$ O is interrupted in one of two ways. In the first case the supply of elements needed to seed the rp-process is exhausted and it ceases to be efficient. In the second case the envelope mass falls below the minimum mass required for nuclear burning because of a strong stellar wind. This mass is expected to be around $14M_{\odot}$ but this limit is convection dependent as described by [Cannon \(1993b\)](#). [Podsiadlowski et al. \(1995\)](#) suggest that both of these cases occur after around 10^6 yr. After both of these a radiative zone is expected to form between the outer envelope and the burning region so removing the burning region's fuel supply. This causes the region above the core to heat until neutrino losses dominate and accretion on to the core ceases to be Eddington limited, leading to a neutrino runaway ([Bisnovatyi-Kogan & Lamzin, 1984](#)). The effects of this runaway depend strongly on the angular momentum of the envelope. This is of order the angular momentum of the progenitor X-ray binary, on the assumption that the envelope of the T $\ddot{\text{Z}}$ O undergoes uniform rotation. Given the deep convective envelope of a T $\ddot{\text{Z}}$ O, this is a well motivated assumption. Podsiadlowski suggests that T $\ddot{\text{Z}}$ O should be relatively slow rotators, by comparing the angular momentum in a typical MXB with the break-up velocity of the T $\ddot{\text{Z}}$ O. This means that the majority of the mass accreted by the neutron star is accreted at low specific angular momentum, leading to its spin down. In the runaway scenario all of the material that has less specific angular momentum than the maximum allowed for the neutron star falls on to the neutron star on a dynamical time-scale, and the neutron star is spun up.

The effect of the runaway on the envelope of a high-mass T $\ddot{\text{Z}}$ O depends on the interplay between the cooling and viscous time-scales. After the neutrino runaway the inner envelope is initially centrifugally supported. If the viscous time-scale of the envelope is shorter than the cooling time-scale then viscous energy transport supports the envelope by supplying it with energy released from the contraction of the inner envelope. The cooling time-scale is initially of the order of the Kelvin-Helmholtz time of the T $\ddot{\text{Z}}$ O (about 10 to 100 yr). For an envelope where convection is the dominant angular momentum transport mechanism the viscous time-scale is of order the convective turnover time-scale multiplied by the square of the number of pressure scale heights in the envelope ([Goldreich & Schubert, 1967](#); [Fricke,](#)

[1968](#)). For the bulk of the envelope material this is of order a few times the dynamical time-scale and so not much shorter than the Kelvin-Helmholtz time ([Krolik, 1984](#)). So initially the envelope is supported by the viscous transfer and dissipation of gravitational energy. The mass in the inner, centrifugally supported region of the disc increases and eventually the envelope may form a Keplerian disc with characteristic radius similar to the initial X-ray binary separation. The disc-like structure may then fragment or form bars owing to gravitational instabilities which, along with the possibility of the inner regions of the disc accreting on to the central neutron star, may lead to the formation of a number of interesting final states such as a pulsar or stellar-mass black hole surrounded by planets or low-mass stars formed from disc fragments. Podsiadlowski notes that these may be good candidates for soft X-ray transient progenitors.

Chapter 3

Highly Magnetized Compact Objects: B-WDs and B-NSS

Various accidents may intervene to save the star, but I want more protection than that. I think there should be a law of Nature to prevent a star from behaving in this absurd way.

Sir Arthur Eddington
On “relativistic degeneracy,”
Eddington (1935a)

In this chapter, I shall briefly introduce, describe and discuss the phenomenon of highly magnetized compact objects, astrophysical objects primarily supported by some form of degeneracy pressure and hosting a magnetic field, such that the magnetic pressure exerted is significant when compared with other pressure terms (degeneracy pressure, thermal pressure, radiation pressure *etc*).

3.1 Highly magnetized neutron stars

While we have investigated only the structure and evolution of highly magnetized white dwarfs in this dissertation, much of the theoretical background of this field is closely linked with the study of highly magnetized neutron stars. From the detection of signals from radio pulsars, and more saliently, from the spin down rates of these pulsars, a magnetic dipole model was proposed and then developed by [Pacini \(1967\)](#); [Gold \(1968\)](#) and [Ostriker & Gunn \(1969\)](#). Here, the energy for the radio emission from a rapidly rotating neutron star is sourced from its rotation. This model has, since its inception constrained the surface magnetic fields for pulsars from as low as 10^8 G up to around 10^{14} G for the most rapidly spinning down pulsars ([McLaughlin et al., 2003](#); [McLaughlin et al., 2009](#); [Cordes & Wasserman, 2016](#)). Other mechanisms such as the direct decay of magnetic fields may power other, more luminous classes of pulsars, such as the anomalous X-ray pulsars (AXPs) and the soft gamma-ray repeaters (SGRs), both of which routinely have surface fields (as computed by

the dipole method) in excess of 10^{15} G, but have X-ray luminosities (around 10^{35} erg s $^{-1}$) well in excess of their spin down luminosities. The SGRs are known for being transient sources that burst repeatedly on a timescale of seconds, while also undergoing superflaring on the 100s timescale, although not repeating. These SGRs also undergo quiescent X-ray pulses (Kouveliotou et al., 1998), with properties very similar to those of the AXPs. This implies that both of these classes of magnetar are likely the same variety of object, highly magnetized neutron stars powered by the active decay of their magnetic fields (Thompson & Duncan, 1993), in addition to their usual spin down luminosities.

3.2 Highly magnetized white dwarfs: background and introduction

Gupta et al. (2020) describes how observations of overluminous type Ia supernovae (Howell, 2006; Scalzo et al., 2010; Silverman et al., 2013) imply the existence of super-Chandrasekhar white dwarfs, white dwarfs with masses $M > 1.44M_{\odot}$. Das & Mukhopadhyay (2012) show that, with a sufficiently large local magnetic field, the equation of state (EoS) of electron degenerate matter is modified by Landau quantization. The new EoS allows for the existence of super-Chandrasekhar white dwarfs with masses up to $2.58M_{\odot}$. Gupta et al. (2020) investigate the luminosity of magnetised white dwarfs and the effect of the magnetic field on the mass–radius relationship. This they do by analytically solving the magnetostatic equilibrium, photon diffusion and mass conservation equations in a Newtonian framework. It has been shown that the effects of GR, particularly in the weak field regime, are negligible (Bandyopadhyay et al., 1997). Here we expand on this work and on the work of Bhattacharya et al. (2021), Mukhopadhyay et al. (2021), Bhattacharya et al. (2018), Chatterjee et al. (2017) and Drewes et al. (2021) by implementing the prescriptions they describe and those of Gupta et al. (2020) in the equation of state solving subroutines in the STARS stellar evolution code (Pols et al., 1995; Eggleton, 1971). STARS is a fully self-consistent non-Lagrangian stellar evolution code capable of modelling a great variety of stars and star-like objects. In section 6.1 we describe the implementation of these prescriptions in the STARS code and the models that we have computed.

In general, when considering the nature of such objects, initially from an analytical perspective, we should distinguish between limiting weak- and strong-field scenarios. We take the transition between these states to occur once ζ , the ratio of the (mass) averaged relativistic magnetic field density contribution $\tilde{\rho}_B$ to the average matter density, $\tilde{\rho}$ goes above around 0.01. Taking the most simple assumption of an $n = 3$ polytropic model for a white dwarf,

this limit roughly corresponds to central field densities of around 10^{14} G. [Subramanian & Mukhopadhyay \(2015\)](#) showed that this limit also corresponds to roughly the point where nonsphericity of the WD structure due to the presence of a large magnetic field may be expected. Here, the star adopts a prolate configuration, due to the anisotropic magnetic pressure induced by the toroidal field. These distortions were investigated by [Sinha et al. \(2013\)](#) for hypernuclear matter in neutron stars, computing the (total) energy density of the system directly from the energy-momentum tensor from the total Lagrangian density, which in a static magnetic field can be written as,

$$\mathcal{L} = \mathcal{L}_m + \mathcal{L}_f \quad (3.1)$$

with \mathcal{L}_m , the matter component of the Lagrangian is,

$$\mathcal{L}_m = \sum_B \bar{\Psi}_B (i\gamma_\mu D^\mu - m_B + g_{\sigma B} \sigma - g_{\omega B} \gamma_\mu \omega^\mu - g_{\rho B} \gamma_\mu \tau_B \cdot \rho^\mu) \Psi_B \quad (3.2)$$

$$+ \frac{1}{2} \partial_\mu \sigma \partial^\mu \sigma - \frac{1}{2} m_\sigma^2 \sigma^2 - U(\sigma) \quad (3.3)$$

$$- \frac{1}{4} \omega_{\mu\nu} \omega^{\mu\nu} + \frac{1}{2} m_\omega^2 \omega_\mu^\mu - \frac{1}{4} \rho_{\mu\nu} \cdot \rho^{\mu\nu} + \frac{1}{2} m_\rho^2 \rho_\mu \cdot \rho^\mu \quad (3.4)$$

$$+ \sum_{l=e,\mu} \bar{\Psi}_l (i\gamma_\mu D^\mu - m_l) \Psi_l, \quad (3.5)$$

where, as by [Boguta & Bodmer \(1977\)](#); [Glendenning \(1982\)](#); [Glendenning \(1987\)](#); [Sinha et al. \(2013\)](#), the index B maps to the baryons in the matter, the fields ψ_B , ψ_l , σ , ω and ρ are the baryon, lepton and σ -, ω -, ρ -mesons, with corresponding masses m_B , m_l , m_σ , m_ω , m_ρ respectively, with meson-baryon interaction coupling constants $g_{\sigma B}$, $g_{\omega B}$ and $g_{\rho B}$. $U(\sigma)$ is the scalar self interaction term as by [Glendenning \(1985\)](#) and

$$\omega_{\mu\nu} \equiv \partial_\nu \omega_\mu - \partial_\mu \omega_\nu, \quad (3.6)$$

$$\rho_{\mu\nu} \equiv \partial_\nu \rho_\mu - \partial_\mu \rho_\nu, \quad (3.7)$$

$$D^\mu \equiv \partial^\mu + ieQ A^\mu, \quad (3.8)$$

up to a choice of field vector potential gauge A^μ . The electromagnetic field Lagrangian density is

$$\mathcal{L}_f = -\frac{1}{16\pi} F_{\mu\nu} F^{\mu\nu}, \quad (3.9)$$

where F is the usual electromagnetic field tensor, as such, we compute the energy-momentum tensor as

$$T^{\mu\nu} = T_m^{\mu\nu} + T_f^{\mu\nu}. \quad (3.10)$$

Following the mean field approach by [Sinha et al. \(2013\)](#) and [Das & Mukhopadhyay \(2014\)](#), we find, in the rest frame of the fluid, with a radial magnetic field, the two components of the energy-stress tensor as,

$$T_m^{\mu\nu} = \begin{pmatrix} \epsilon_m & 0 & 0 & 0 \\ 0 & P_m - MB & 0 & 0 \\ 0 & 0 & P_m - MB & 0 \\ 0 & 0 & 0 & P_m \end{pmatrix}, \quad (3.11)$$

$$T_f^{\mu\nu} = \frac{B^2}{8\pi} \begin{pmatrix} 1 & 0 & 0 & 0 \\ 0 & 1 & 0 & 0 \\ 0 & 0 & 1 & 0 \\ 0 & 0 & 0 & -1 \end{pmatrix}, \quad (3.12)$$

where P_m is the matter pressure, B the magnetic field, such that $B^\mu B_\mu = -B^2$, and M the magnetization per unit volume. Therefore, the total energy density of the entire system is,

$$\epsilon = \epsilon_m + \frac{B^2}{8\pi}. \quad (3.13)$$

Therefore, the pressures perpendicular and parallel to the magnetic field are,

$$P_\perp = P_m - MB + \frac{B^2}{8\pi}, \quad (3.14)$$

and,

$$P_\parallel = P_m - \frac{B^2}{8\pi}, \quad (3.15)$$

leading to the anisotropic behaviour expected at very large magnetic field strengths.

3.3 Thermal neutrino generation processes

In contrast to non-degenerate stellar objects, in which the generation and emission of neutrinos from non-nuclear burning processes is negligible until the final stages of evolution before a supernova, the production of neutrinos from these processes, collectively referred to as thermal neutrino losses, are significant and may in fact dominate the evolution of degenerate

objects at certain times. Three major thermal neutrino processes occur. We shall consider here, pair annihilation, the photoneutrino process and plasmon decay. In neutron stars, or more specifically, in the cores of neutron stars, there is an addition series of fast neutrino emission processes. These can only occur deep in the inner cores of NSs, at well above the nuclear density. The most effective neutrino generation process in this case are direct Urca processes, in either conventional nuclear matter or in some form of exotic plasma. [Yakovlev & Pethick \(2004\)](#) provide examples of Urca-like processes in nuclear matter, as,



Whereas in unconfined QCD matter, such a reaction would proceed directly via quark interconversion, as,



Finally, in the inner core of a NS, the presence of other exotic phases of matter lead to the emission of neutrinos via Urca-like processes operating on quasiparticles. In a pion-condensed environment, the processes proceed via a nucleon quasiparticle, \tilde{N} , a neutron-proton superposition. In a kaon-condensed environment, two coherent baryonic quasiparticles exist ([Pethick, 1992](#)), a neutron-like particle, which is a coherent superposition state of neutrons and Σ^- particles, and a proton-like state, comprising a superposition of protons and mixed states of Σ^0 and Λ hyperons, through which the Urca-like process generates neutrinos. These processes do not occur outside of the inner core of NSs, and as such do not influence our models of the much less dense magnetized WDs either.

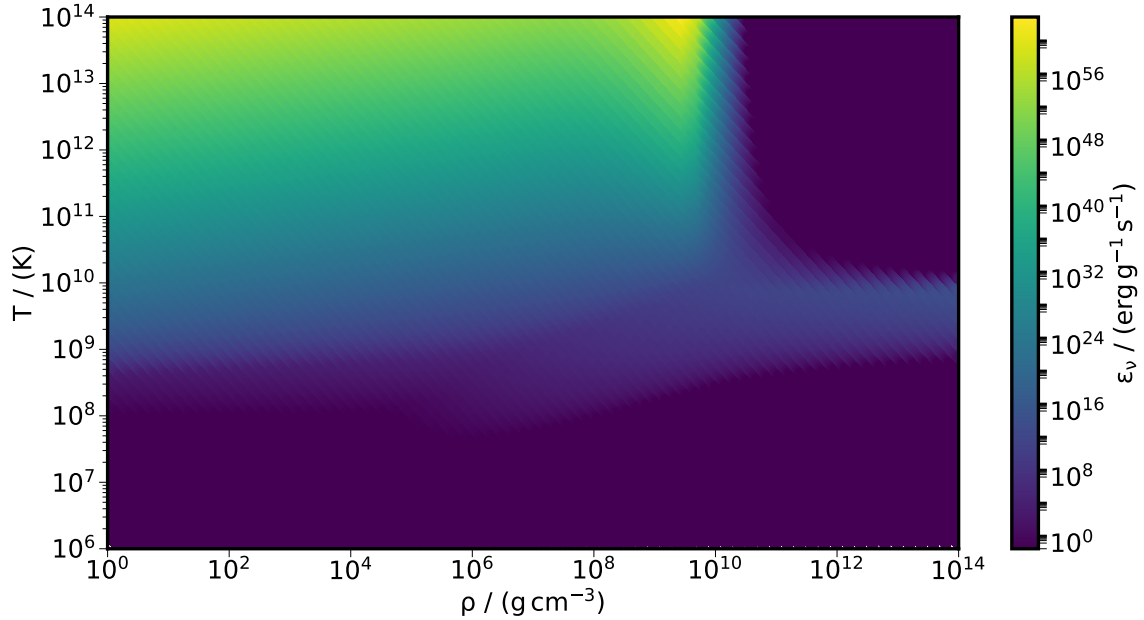


Figure 3.1 Plot of the specific energy loss rate by thermal production of neutrinos in our STARS implementation for B-WD cooling. Although we make use of our expanded opacity tables as described in section 4.2.2.2.1, at densities and temperature above $10^{14} \text{ g cm}^{-3}$ and 10^{12} K , respectively, our opacity becomes less and less physically attested or motivated. At densities below 1 g cm^{-3} and temperatures below 10^6 K , we assume the effective neutrino loss rate vanishes, for computational purposes but we note that, at the lower temperature boundaries, the computed loss rates begin to fall below our machine precision regardless. Hence, we are well justified in making such a cut here. We plot the neutrino generation rate as a function of both the temperature and density of the stellar material. We note the regions dominated by the three main mechanisms discussed in the text are pair annihilation at high temperatures and lower densities, plasmon decay at lower temperatures and higher densities, and the photoneutrino mechanism at lower temperatures and densities. We do not include the effects of (neutrino) Bremsstrahlung, because, according to Itoh et al. (1996b), this mechanism, which is regardless non-dominant in our models, is a function⁴ of the metalicity, which we in principle allow to vary from model to model.

3.3.1 Pair annihilation

Pair annihilation occurs mostly in massive stars as their cores enter a regime of density-temperature space where the production of electron-positron pairs becomes important. For non-degenerate material this is above temperatures of around 10^{12} K. [Fowler & Hoyle \(1964\)](#) computed a branching ratio of around 10^{-19} between the competing radiation annihilation process,

$$e^- + e^+ \rightarrow \gamma + \gamma, \quad (3.20)$$

and,

$$e^- + e^+ \rightarrow v_e + \bar{v}_e. \quad (3.21)$$

However when stellar material is degenerate, this process is strongly suppressed, as first noted by [Beaudet et al. \(1967\)](#). This is due to the filling of phase space in the degenerate object, as higher momentum electron states are occupied. This greatly shrinks the spectral range at which pair production itself can occur and so this mechanism is significant only in the case when there is sufficiently high temperature, non-degenerate stellar material in which the branching ratio into electron capture is negligible.

⁴Specifically, $\epsilon_v = \frac{1}{3} \frac{(Ze^2G)^2}{(2\pi)^8} \int \{ F^{\mu\nu} [2x_\mu x_\nu + g_{\mu\nu}(x \cdot x)] \}_{q_0=0} \frac{1}{E_1 E_2} f(E_1) [1 - f(E_2)] (E_1 - E_2) p_1^2 d^3 p_1 q^2 d^3 q d \cos\theta_q d^3 p_2$ where,

$$\begin{aligned} \{ F^{\mu\nu} [2x_\mu x_\nu + g_{\mu\nu}(x \cdot x)] \}_{q_0=0} = & 8 \left[\frac{1}{q^2 + q_s^2} \frac{1}{[(p_2 + q) \cdot (p_2 + q)] - m^2} \right]^2 \{ 4(p_1 \cdot p_2) z_2 [z_1 - 2E_2 (E_1 + E_2)] - 2z_2^2 (p_1 \cdot p_2) \right. \\ & + 2(p_1 \cdot p_2)^2 (q^2 - 4E_2^2) + 2z_2^2 [m^2 - 2E_1 E_2 + 2z_1] + (p_1 \cdot p_2) \left[4E_2^2 (3m^2 - q^2 + 4z_1) + q^2 \left(\frac{1}{2} q^2 - 4E_1 E_2 - 3m^2 - 2z_1 \right) \right] \\ & + z_2 [4E_2^2 (2z_1 + m^2) + 4E_1 E_2 (2m^2 - q^2 + 2z_1) + 2z_1 (q^2 - 2z_1 - 2m^2) + m^2 q^2] \\ & + E_2^2 [4(q^2 - 3m^2 - 2z_1) z_1 - 4m^4 + 2m^2 q^2] + q^2 E_1 E_2 (4m^2 - q^2 + 4z_1) + m^2 q^2 (z_1 + m^2) \} + \{ p_1 \leftrightarrow -p_2; E_1 \leftrightarrow -E_2 \} \\ & - \frac{8}{(q^2 + q_s^2)^2} \frac{1}{[(p_1 - q) \cdot (p_1 - q)] - m^2} \frac{1}{[(p_2 + q) \cdot (p_2 + q)] - m^2} \{ (p_1 \cdot p_2) z_2 [8E_1 (E_1 + 3E_2) + 2q^2 + 4z_1] \\ & + 4(p_1 \cdot p_2)^2 (4E_1 E_2 + q^2) + 2z_2^2 [4E_1 (E_1 + E_2) - m^2] + 4z_2 [E_1^2 (q^2 - 2z_1 - 2m^2) - 2E_2^2 z_1 + E_1 E_2 (2q^2 - 6z_1 - 4m^2)] \\ & + (p_1 \cdot p_2) [8E_1 E_2 (q^2 - 3m^2 - 3z_1) - 8E_2^2 z_1 + q^2 (q^2 - 2m^2 - 2z_1)] + 2m^2 E_1^2 q^2 \\ & + E_2^2 [4z_1 (2m^2 - q^2) + 2m^2 q^2 + 8z_1^2] + E_1 E_2 [2q^4 + 8z_1^2 - 8q^2 z_1 + 8m^2 (2z_1 - q^2 + m^2)] - 2m^2 (z_1^2 + m^2 q^2) \}, \end{aligned}$$

as by [Cazzola et al. \(1971\)](#)

3.3.2 The photoneutrino process

The photoneutrino process can be thought of as the neutrino equivalent of the Compton electron scattering process, processes for which the final effective reaction is,

$$e^\pm + \gamma \rightarrow e^\pm + \nu_e + \bar{\nu}_e, \quad (3.22)$$

which is familiar as the usual Compton process, with the outgoing scattered photon replaced with a neutrino-antineutrino pair. As in the Compton process, scattering of photons off of a positron into a neutrino-antineutrino processes is likewise possible, with the same cross section, although, of course, the specific rate in actual stellar material is vanishingly small by comparison. For low density and high temperature, but with non-relativistic electrons, the cross-section of this process scales linearly with electron density. Hence the rate of energy loss is proportional to temperature and independent of the density (Clayton, 1983). For degenerate material, as for pair annihilation, this process is suppressed by the increasing dearth of free states in the electron phase space. With fewer possible states for the outgoing electron (or positron) to scatter into, the reaction is suppressed.

3.3.3 The plasmon decay process

Finally, and most pertinently for our purposes, the plasmon decay process dominates the formation of thermal neutrinos at the high densities found in degenerate environments. These are conditions when the local plasma frequency of the stellar material is high so the energy of plasmons is comparable to the thermal energy. This is when

$$\hbar\omega_{\text{plasma}} \approx k_B T. \quad (3.23)$$

A plasmon is a quasiparticle, a quantization of the oscillation of free electron density in a plasma. Similarly to a phonon, the quasiparticle quantum of mechanical oscillation in a solid, the plasmon is most simply thought of as the analogous quantization in an ionized medium. In practical terms, (Kantor & Gusakov, 2007) a plasmon behaves analogously to a photon in a vacuum with an associated non-zero rest mass. While plasmons can exist in transverse modes, with polarization perpendicular to the wavevector, we can, as for a photon, also construct a *longitudinal* plasmon, by the quantization of Langmuir waves in the plasma. It then behaves analogously to a phonon in a solids.

Plasmons can then decay directly into (anti-)neutrinos, as,

$$\gamma_{m^*} \rightarrow \nu + \bar{\nu}, \quad (3.24)$$

where γ_{m^*} is a plasmon state behaving with effective mass m . The total neutrino generation rate from plasmon decay is the result of the decay of three separate components, although the third component of the rate, corresponding to the decay of the transverse (photon-like) plasmons, under the action of the axial term of the Hamiltonian, is insignificantly small in comparison to the other two terms ([Kohyama et al., 1994](#)). The other two terms correspond to the decay of the longitudinal (phonon-like) plasmons, Q_L , and of the decay of transverse plasmons under the action of the vector term of the Hamiltonian.

Chapter 4

Stellar Evolution Codes

“Miracles *do* not happen:” – ‘t is
plain sense,
If you italicize the present tense;
But in those days, as rare old
Chaucer tells,
All Britain was fulfilled of miracles.

Sir Gawain and the Green Knight

One-dimensional, Henyey-based hydrostatic stellar evolution codes are the fundamental backbones that have defined research in the field of theoretical stellar astrophysics for over half a century now ([Henyey et al., 1959](#)). When we consider the vast range of research projects that themselves use results informed by the output of stellar evolution codes as subgrid physics or that use such results to inform observational priorities the importance of these codes is enormous. These codes are the base upon which a range of research tools have been developed, including population synthesis calculators (Initially [Eggleton et al. \(1989\)](#) expanded to binary systems by [Tout et al. \(1997\)](#), with an analogous, independent binary code in use by [de Kool & Ritter \(1993\)](#)). Modern codes such as `binary_c` by [Izzard et al. \(2006\)](#) are based on the analytical evolution algorithms SSE and BSE by [Hurley et al. \(2002\)](#)) and large scale cosmological simulations ([Crain et al., 2015](#)).

In this chapter, I discuss very briefly the relevant equations of stellar structure and evolution, including consideration of convective energy transport and the diffusion of chemical species, atomic diffusion, gravitational settling, extended post-processing nuclear networks, mesh spacing algorithms and much more. The implementations of these equations and systems of equations are discussed in the context of the two one-dimensional stellar evolution codes used throughout this work, STARS and MESA. The workings and use of these codes are also described in some detail, to acquaint the reader with the standard workflows required to modify, use, and interpret the output.

4.1 Henyey Implicit Integration Approach

Direct, e.g. Runge-Kutta, integration is inefficient for solving stellar structure equation since, in brief, the equations governing the behaviours of matter and those of energy are coupled – failing to solve energy generation and radiative transfer equations in parallel with

those of mass continuity and hydrostatic equilibrium may result in problems. Since we apply boundary conditions at both the surface and the centre of the star, and given that the equations that we solve are very sensitive to those boundary conditions, we must apply a double shooting in order to generate robust and realistic solutions. The description presented here should be sufficient to allow the reader to easily understand the details and discussion in the next sections of this chapter. For more detailed and comprehensive information on this technique and its myriad applications, especially in the historical context, I would suggest [Heney et al. \(1959, 1964\)](#); [Larson & Demarque \(1964\)](#); [Kippenhahn et al. \(1967\)](#); [Nobili & Turolla \(1988\)](#) and [Martin et al. \(2018\)](#), in addition to any of a wide range of classic stellar evolution textbooks, for example [Kippenhahn et al. \(2013\)](#).

Simply speaking, we begin by rewriting the equations of mass continuity and hydrostatic equilibrium as:

$$\frac{d \ln r}{dm} = \frac{1}{4\pi \rho r^3}, \quad (4.1)$$

and,

$$\frac{d \ln P}{dm} = -\frac{Gm}{4\pi Pr^4}, \quad (4.2)$$

respectively. Following the lead of [Heney et al. \(1959\)](#), we define $x \equiv \ln r$, $y \equiv \ln P$ and $q \equiv \ln \rho$. To facilitate the closure of this system of equations, we introduce an equation of state, $P(\rho)$ ⁵, or rather, in this formalism, its inverse. These equations of state can be tabulated, and interpolated, as in MESA's differentiable Skye EoS ([Jermyn et al., 2021](#)), or an analytical approximation, as by [Eggleton et al. \(1973\)](#) and utilized in the STARS code⁶. In order to solve these differentially equations numerically, these equations are reformulated as finite difference equations,

$$\phi_i = G(8\pi)^{-1}(m_i^2 - m_{i-1}^2)e^{-\frac{1}{2}(y_i + y_{i-1}) - 2(x_i + x_{i-1})} + y_i - y_{i-1}, \quad (4.3)$$

$$\psi_i = -G(4\pi)^{-1}(m_i - m_{i-1})e^{-\frac{3}{2}(x_i + x_{i-1}) - \frac{1}{2}(q_i + q_{i-1})} + x_i - x_{i-1}. \quad (4.4)$$

We note that this is a simplified approach, in which the distribution of mass with respect to the calculation mesh cannot vary. This is not the case in a non-Lagrangian meshing code such as STARS. In addition, we must reformulate these difference equations at the inner and outer boundaries, where x and y both diverge, respectively. There are a number of potential

⁵Of course, any realistic equation of state will also be a function of temperature, metalicity, etc.

⁶The STARS equation of state does not actually make use of density nor pressure as an independent variable, but rather a code internal variable f which describes the degree of electron degeneracy in the stellar material at any particular code calculation point. Additionally independent are the temperatures and compositions at each of these points. This hugely simplifies solving the Fermi-Dirac integrals, allowing the ionization equations to be calculated without needing additional iterations, at the expense of physical transparency. We additionally provide a means to compute an approximation to the pressure ionization at this point.

solutions to these problems, discussed in detail in the literature stated earlier. In general, one makes an assumption of an ideal, incompressible fluid at the centre, a simple asymptotic expansion around the centre works for our purposes here. At the surface one might assume that the polytropic index is constant near the surface, or one could make use of the Eddington grey atmosphere boundary conditions ([Eddington, 1930](#)). For a maximally realistic model, we may fit instead to a full model atmosphere. With boundary conditions thusly selected, the expressions for ϕ and ψ are to be Taylor expanded as

$$\phi_i + a_i \Delta x_{i-1} + b_i \Delta y_{i-1} + c_i \Delta x_i + d_i \Delta y_i = 0, \quad (4.5)$$

$$\psi_i + a'_i \Delta x_{i-1} + b'_i \Delta y_{i-1} + c'_i \Delta x_i + d'_i \Delta y_i = 0, \quad (4.6)$$

where Δz_i is the change required in variable z_i to zero out the difference equations. Finally, the terms a, b, c, d map directly to the derivatives

$$a_i = \frac{\partial \phi_i}{\partial x_{i-1}}, b_i = \frac{\partial \phi_i}{\partial y_{i-1}}, c_i = \frac{\partial \phi_i}{\partial x_i}, d_i = \frac{\partial \phi_i}{\partial y_i}, \quad (4.7)$$

$$a'_i = \frac{\partial \psi_i}{\partial x_{i-1}}, b'_i = \frac{\partial \psi_i}{\partial y_{i-1}}, c'_i = \frac{\partial \psi_i}{\partial x_i}, d'_i = \frac{\partial \psi_i}{\partial y_i}. \quad (4.8)$$

Conveniently, these equations are linear in the Δ terms, so each Δx term can be written in terms of the corresponding Δy term, or vice versa, as

$$\Delta x_i = -\gamma_i - \alpha_i \Delta y_i, \quad (4.9)$$

$$\Delta x_{i-1} = -\gamma_{i-1} - \alpha_{i-1} \Delta y_{i-1}. \quad (4.10)$$

This allows the coefficients, γ_i and α_i , to be solved for in terms of these coefficients at the previous calculation points, γ_{i-1} and α_{i-1} , as

$$\gamma_i = \frac{(\phi_i - a_i \gamma_{i-1})(b'_i - a'_i \alpha_{i-1}) - (\psi_i - a'_i \gamma_{i-1})(b_i - a_i \alpha_{i-1})}{c_i(b'_i - a'_i \alpha_{i-1}) - c'_i(b_i - a_i \alpha_{i-1})}, \quad (4.11)$$

$$\alpha_i = \frac{d_i(b'_i - a'_i \alpha_{i-1}) - d'_i(b_i - a_i \alpha_{i-1})}{c_i(b'_i - a'_i \alpha_{i-1}) - c'_i(b_i - a_i \alpha_{i-1})}. \quad (4.12)$$

Finally, the Δy_{i-1} term can be solved for, as

$$\Delta y_{i-1} = -\frac{(\psi_i - a'_i \gamma_{i-1} + c'_i \Delta x_i + d'_i \Delta y_i)}{(b'_i - a'_i \alpha_{i-1})}. \quad (4.13)$$

Now, from an initial structural solution, such as a simple polytropic model ([Cowling, 1966b](#)), we can iterate repeatedly until an acceptable solution is converged upon. Each step of this

iteration is itself a Newton iteration for some N variables where N is the number of variables we intent to solve for at each mesh point, multiplied by the number of mesh points. Now we have N equations with which we construct a system of equations,

$$\vec{E}(\vec{V}) = 0, \quad (4.14)$$

where \vec{V} is a vector of magnitude N. We form a solution matrix \hat{H} , with matrix elements,

$$\hat{H}_{ij} = \frac{\partial E_i}{\partial V_j}. \quad (4.15)$$

We now update \vec{V} as

$$\vec{V}' = \vec{V} - \hat{H}^{-1} \vec{E}. \quad (4.16)$$

It is vital therefore, that we construct \hat{H} to be block diagonal in structure, so as to be easily invertable.

4.2 The Cambridge Stellar Evolution Code (STARS)

STARS has a number of novel features as well as additional modifications I have made in order to allow the simulation of exotic stellar objects. Here I shall briefly discuss the core matrix inversion algorithm that STARS uses, as well as the modifications to the equation of state (including tables of opacities and thermal neutrino generation rates) routines that have been made to this end. In figure 4.1, we present a simplified, schematic representation of the basic program structure and flow of the STARS code. In general, the program flow occurs as follows:

- Initialization; `main.f` calls `printa.f` in the initialization mode in order to load in an initial stellar model from a provided input file. The relevant tables for opacities, nuclear reaction rates and coefficients for spline interpolation in those opacity tables are loaded into memory. The non-initialization run of `printa.f` then occurs for the first time, setting up the solution matrices (`H`, `DH`, *etc.*) before returning control to `main.f`.
- Solver loop; `main.f` sets up the matrices for manipulation. The iterative loop then begins for the current timestep, the surface meshpoint is computed by calling `difrns.f` and then `divide.f`, followed by calls to `difrns.f`, `elimn8.f` and `divide.f` for the next-to-surface meshpoint. This is followed by similar calls for the other meshpoints, and finally corrected directly at the central meshpoint, via a final call to `divide.f`.

- `difrns.f` then acts as the main driver for setting up and solving the equations of stellar structure. This involves the structural (`equns1.f / funcs1.f`) and nucleosynthesis (`equns2.f / funcs2.f`) equation solvers. These subroutines make calls to other subroutines that deal with microphysics, such as `statef.f` for the equation of state computations and `nucrat.f` for nuclear reaction rates.

For the purposes of completeness, we briefly outline the function of several of the most important subroutines in question.

main.f is the main program control routines, and the entry point for code execution. It will call `printa.f` in order to load in an initial model, and will use it at each timestep to compute the best next timestep, and to produce relevant output. During each timestep, `main.f` calls to `solver.f` in order to solve the equations of stellar structure at each timestep for each meshpoint.

printa.f handles the vast majority of all input/output functions. It is call by `main.f` at the start of program execution in order to load in an initial model. At each timestep, `printa.f` is called in a different mode in order to store variables for emergency restart, to call `printb.f` for output and to compute the best next timestep.

printb.f is called by `printa.f` in order to handle output, producing files detailing the stellar models produced at each timestep. The calculations needed to produce these outputs, such as computing the binding energy of the envelope, are performed here too.

printc.f is a debugging output routine, that produces a file containing details of the progress of the solution packages.

solver.f is the entrance to the general solution system for solving simultaneous difference equations of first and second order, with relevant boundary condition. Strictly speaking, `solver.f` and its relevant co-routines form a generic solution package, that while optimized for solving the stellar structure equations, is not actually restricted to solving these, making it easy to modify these routines in order to solve for new equations, for the purposes of adding new physics *etc.* `solver.f` solves the system of equations that are set up in the first instance by `equns1.f` and `equns2.f`.

difrns.f produces the difference equations needed to evolve a model of a star. In each case, the derivatives of these equations are solved for numerically, by directly varying each independent variable, one at a time, in the order defined by the user in the ID block of the data input file. This relaxes a particular structure solution at the current timestep.

elimn8.f performs a series of matrix multiplication needed to perform successive GJ elimination.

divide.f is the custom matrix inverter, as described in detail in section 4.2.1.

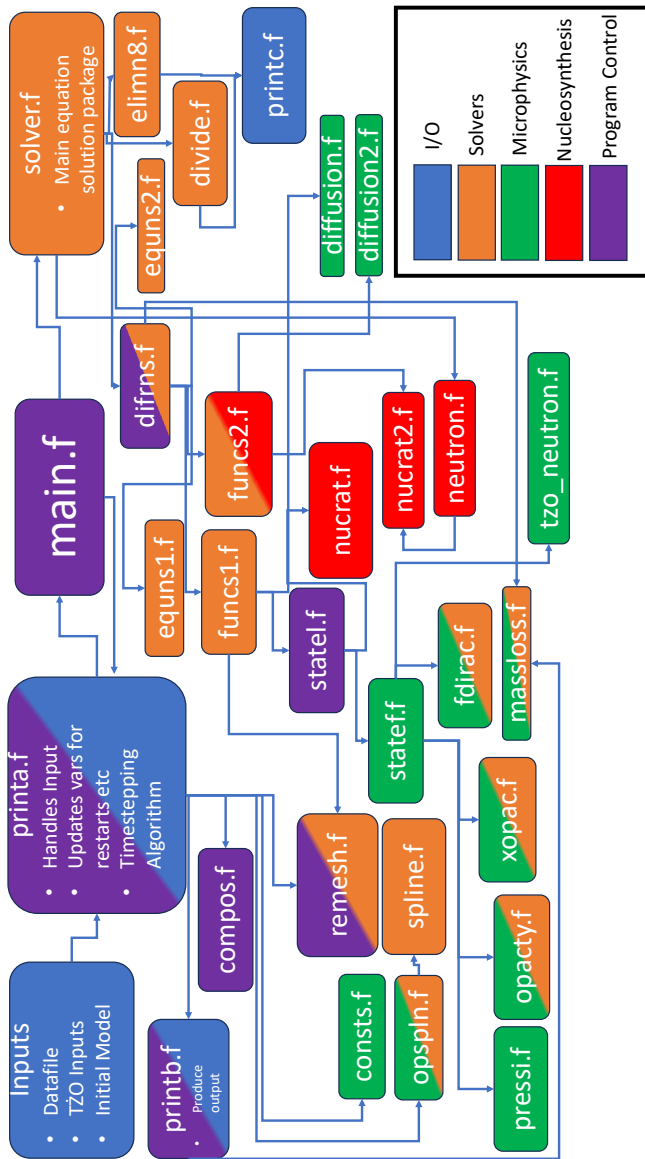


Figure 4.1 Illustrative schematic diagram of the basic structure and program flow of the STARS stellar evolution code. Rectangular shapes indicate a program subroutine, while headed unidirectional arrows indicate an instance of a subroutine making a call to a second subroutine. We note that not all program iterations will make all the indicated program calls (e.g. statef.f will only make a call to statef.f if the thermodynamic properties at a calculation point need to be updated during the current timestep.) and some subroutines will call the same second subroutine multiple times per iteration, for example, funcs1.f will be called two separate times when computing a timestep in full binary mode. The colour-coding of each shape indicates the nature of its main function(s), during normal, nominal program execution.

func1.f computes the equations of stellar structure, as well as the mesh spacing function, of each independent variable at each meshpoint as required to set up the difference equation. **func2.f** extends **func1.f** for the purposes of nucleosynthesis. The derivatives of these 42 second order equations are directly analytically computed here.

equns1.f initializes the boundary conditions and then populates the difference equations, using calls to **func1.f** to populate the relevant values for gravitational acceleration, pressure *etc.*

equns2.f populates the equations as needed for the nucleosynthesis computations, taking input from **func2.f** and then performing direct analytical integration to solve for these in place.

nucrat.f/nucrat2.f evaluate the nuclear reaction rates via interpolation in the relevant tables as relates to the structural and minor element nucleosynthesis species, respectively.

statef.f is called by **func1.f** and will call **statef.f** if an update to the equation of state is needed, avoiding slowdown.

statef.f is the primary microphysics routine, that computes the equation of state, based on [Eggleton et al. \(1973\)](#). Calls are made to **pressi.f** to compute pressure ionization, **opacty.f/xopac.f** for opacity calculations, and **tzo_neutron.f** for the neutron opacity and chemical potential computations as needed for solving models of TZO's.

fdirac.f evaluates the Fermi-Dirac integrals, solving for a matrix D which contains ρ , P and Q in its first row, the logarithmic derivatives of these with respect to temperature in the second row and those same derivatives with respect to f , the independent variable associated with degeneracy (see section 4.2.2) in the final row. Second and third derivatives of density with respect to temperature and f are also computed here, as they are needed in **pressi.f**. **pressi.f** provides a series of non-ideal adjustments to the equation of state, that is, including the contribution of a free energy term $\Delta(F) = -kTN_eG(X_I, T_I)$ where $X_I = n_e m_u$ and $T_I = 1eV/(kT)$. Corrections are then produced for pressure ionization and for Coulomb interaction.

opspln.f uses **spline.f** and a table of pre-computed spline coefficients to create a bicubic spline.

opacty.f and xopac.f then (depending on the user's selection of opacity settings) make use of the bicubic spline as computed by **opspln.f** to produce a fit in temperature and density to produce an opacity at the current meshpoint and timestep. If selected in the data input, this opacity can include opacities due to molecules at low temperatures, as well as Potekhin-like opacities for material harbouring extremely large magnetic fields.

tzo_neutron.f computes opacities for material that is completely neutronized, or that has begun to partially neutronize via a core-envelope artifice (see section 5.1.2.. as well as as

computing alternate neutrino generation rates that are a better fit to a neutron-rich environment ([Yakovlev et al., 2005](#)), as well as effective masses/chemical potentials for neutrons and protons in a neutron-rich environment.

4.2.1 Custom matrix inversion algorithm

Here I describe briefly how the custom matrix inversion algorithm crafted by Peter Eggleton, originally conceived of in 1969, works. In practice, this section describes how the two subroutines, `divide` and `el1mn8` manipulate a matrix of derivatives of each of the structural equations in order to improve the accuracy of the inversion. The brief description I include here for completeness is derived primarily from a brief write up by Eggleton in the documentation supplied with the TWIN/EV evolution code. One may find this in a repository maintained by Rob Izzard ⁷. While the description here has been simplified as was Peter Eggleton's original description, but extending this framework for a fully-fledged and detailed stellar model is trivial.

The core element of this inversion technique begins with a matrix of derivatives, A , where each term of the matrix is given as:

$$A_{ij} = \frac{\partial eqn_i}{\partial var_j}, \quad (4.17)$$

where eqn is a difference equation, of the form described in section 4.1, or an equation setting a boundary condition to the model, var represents a code variable such as mass coordinate m or luminosity L . Here, as in the document maintained by Glebbeek (2020, private communication), where a brief but somewhat more technical summary is hosted, we describe a trivial configuration of this framework to produce an illustrative stellar model. We note here that this is a toy model, it does not describe a realistic model of a star, but rather serves as a demonstrative example of how such a stellar model is computed, while being simple enough to allow each pertinent step to be illustrated in full. We consider six internal structure variables, f , the code internal degeneracy parameter, representing the level of electron degeneracy at any given calculation point, T , the temperature m the mass coordinate, X , the hydrogen mass fraction, r , the radius, and L , the luminosity. The electron degeneracy f is related to the typical ([Dingle, 1957](#)) Fermi-Dirac electron degeneracy parameter ψ by

$$\psi = \ln \frac{\sqrt{I+f} - I}{\sqrt{I+f} + I} + 2\sqrt{I+f}. \quad (4.18)$$

⁷<https://gitlab.surrey.ac.uk/ri0005/TWIN>

In our toy model, we consider only three mesh points to perform the calculation over, the surface, the internal structure and the centre. The model is structured around a single eigenvalue C , which describes the spacing algorithm of the calculation mesh, as are all models computed with the STARS code. The eigenvalue C describes how the mass coordinate varies as a function of the calculation point k , such that:

$$C = m' = \frac{dm}{dk}. \quad (4.19)$$

Our structural computation solves for three surface boundary conditions:

$$P(f) = g(r), \quad (4.20)$$

$$L = r^2 T^4, \quad (4.21)$$

$$\dot{m} = f(T), \quad (4.22)$$

where these equations fix the surface pressure, the blackbody luminosity and the mass-loss rate at the surface of the star, respectively. While this is intended to be as generic an example model as possible, one could for example select $g(r)$ in the first boundary condition to be zero, setting the surface pressure to zero, and set $f(T)$ to be zero to suppress mass-loss. Naturally, a realistic mass-loss rate will depend on the composition *etc* in addition to the surface temperature. We note that constants such as the factor of $4\pi\sigma$ in the blackbody luminosity are incorporated into the variable in question, for simplicity. Here, and later on, lower case Latin characters are used to refer to some function of the relevant variable. These are to be physically motivated, for example, the derivative of the luminosity (with respect to the mesh point) depends on the temperature not in some trivial way, but rather via the nuclear reaction network, the composition *etc*. We stress again that this is just a simplified model to illustrate the workings of the solution package itself.

One first order surface boundary condition equation is considered:

$$h(f)X' = 0. \quad (4.23)$$

Next, our matrix contains the derivatives for five first order difference equation:

$$r' = \frac{C}{d(f)}, \quad (4.24)$$

$$L' = Ce(T), \quad (4.25)$$

$$P' = Cg(r), \quad (4.26)$$

$$T' = CL, \quad (4.27)$$

$$m' = C. \quad (4.28)$$

Then, the matrix contains a single second order difference equation:

$$X'' = R(T). \quad (4.29)$$

Then, we add the first 5 first order difference equations again, followed by a first order centre boundary condition, $h(f)X' = 0$.

Finally, three zeroth order central boundary condition equations are added:

$$r = 0, \quad (4.30)$$

$$L = 0, \quad (4.31)$$

$$m = 0. \quad (4.32)$$

This forms the block diagonal matrix shown in table 4.1, which is organised so that the most significant terms lie on the main diagonal. Calls to the `difrns` subroutine by the solver set up successive rows in the matrix. Inside of `difrns`, calls are made to first `elimn8` and then `divide` in order to perform step-wise Gauss-Jordan elimination. This first call to `divide` reduces the leading 3^2 block to the corresponding identity, as in table 4.2. A series of row-leading sub-matrix multiplications, row-initialization with `difrns`, dividing through to reduce the leading diagonal elements to unity via `divide` and GJ eliminations via `elimn8`, we eventually produce the matrix presented in table 4.8 in which that corrections to each one of our code internal variables can be computed at the central meshpoint via back-substitution. After this point, finding the corrections at each of the other meshpoint requires only a further series of back-substitutions. This series of matrix manipulations as described form a solver package that outperforms most standard solution packages, at least, in the case of the specific matrix structure that is commonly encountered when solving for stellar structures. When tackling a real stellar evolution problem, we of course make use of more equations for more independent variables, consider for example, that the STARS code is capable of evolution a binary system in parallel, requiring equations for orbital and spin angular momentum, as

well as typically having more than one independent composition variable⁸, and in addition, generally wish to make use of more than three calculation points to ensure sufficient spatial resolution — this requires a larger such matrix, and the time complexity of the solver package algorithm is found to go as the cube of the rank of the matrix under consideration. This efficient solver package allows the STARS code, running on 30 year old hardware (say, a Type 7008 PowerStation with 33MHz POWER1 CPU architecture) to evolve a $15M_{\odot}$ ZAMS stellar model to the onset of core carbon ignition in the same time that MESA takes to evolve an equivalent stellar model on modern desktop hardware (say, at 3.2GHz clock speed, on a Skylake architecture core) (Eggleton & Lattanzio 2022, private communication).

4.2.2 The STARS Equation of State

STARS makes use of a semi-analytical equation of state, first described by [Eggleton et al. \(1973\)](#) and updated many times since, most notably by [Pols et al. \(1995\)](#), who added molecular hydrogen dissociation, Coulomb interactions and pressure ionization. Here we briefly describe the underlying unmodified EOS, while in section 4.2.2.2 we detail the modifications made we have made to the EOS, as well as to other facets of the code in order to model Thorne-Żytkow Objects.

The EOS itself is based on the principle of Helmholtz free energy minimization, a technique employed for thermodynamic calculations in systems of nonideal gasses since the seminal work by [Grabske et al. \(1969\)](#). The free energy equation is then cast in the form,

$$F(V, T, N_e, N_i) = -\frac{1}{3}aT^4V \quad (4.33)$$

$$+ kT \sum_i N_i \left(\ln \frac{N_i h^3}{\omega_i V (2\pi m_i kT)^{3/2}} - 1 + \frac{\chi_i}{kT} \right) \quad (4.34)$$

$$+ F_e(N_e, V, T) \quad (4.35)$$

$$+ \Delta F_e(N_e, V, T), \quad (4.36)$$

where V is the usual specific volume ($1/\rho$), N_i is the number of particles of species i per unit mass, and N_e is the analogous term for electrons. The expression on the first line is the standard radiation pressure. The second line is the contribution from atoms and molecules. The third line includes the electron contributions to the free energy when treating electrons as particles strictly obeying Fermi-Dirac statistics, and the final line includes all the non-ideal behaviour; here these are the Coulomb interactions and the pressure ionization. Regarding

⁸The non-nucleosynthesis mode has, in fact, 7, with the mass fractions of ^{14}N , ^{20}Ne , ^{12}C , ^1H , ^4He , ^3He and ^{16}O all solved for separately within the included (small) nuclear reaction network. The mass fraction of ^{24}Mg is found via connection of the initial metalicity with the independent composition variables.

EQNS – VARS	f	T	m	X	r	L	f	T	m	X	r	L	C
$P(f) = g(r)$	★				•								
$L = r^2 T^4$		★			•	•							
$\dot{m} = f(T)$		•	★										
$h(f)X' = 0$	•		★				•	★					
$r' = C/d(f)$	•			★			•		★				
$L' = Ce(T)$		•		★			•			★			
$P' = Cg(r)$	★			•	★		•			★			
$T' = CL$	★			•	★					•			
$m' = C$		★			★						•	•	•
$X'' = R(T)$	•	★			•	★			•	★			★
$r' = C/d(f)$				★			•		★		•		
$L' = Ce(T)$				★			•			★			
$P' = Cg(r)$				★			•			★			
$T' = CL$				★			•			★			
$m' = C$				★			•			★			
$h(f)X' = 0$				•	★				★				
$r = 0$									★				
$L = 0$									★				
$m = 0$										★			

Table 4.1 Initial derivative matrix for our example case stellar model from section 4.2.1. The variables and equations are ordered as described there. The ★ symbol indicates the presence of a significant term, while the • symbol indicates a minor term, one that might be comparable to the significant terms, but are not *required* to be. All other regions not filled contain no terms at all. All the leading diagonals with the exception of the final, bottom-right term contain significant terms.

EQNS - VARS	f	T	m	X	r	L	f	T	m	X	r	L	C
$P(f) = g(r)$	1	•	•	•	•	•							
$L = r^2 T^4$	1	•	•	•	•	•							
$\dot{m} = f(T)$		1	•	•	•	•							
$h(f)X' = 0$	•	★			•	★							
$r' = C/d(f)$	•	★	★	★	•	★	★	★	•	•	•	•	•
$L' = Ce(T)$		•			•								
$P' = Cg(r)$	★	★	•	★	★	•							
$T' = CL$			•	•	★	★							
$m' = C$		★	★	★	★	★							
$X'' = R(T)$	•	★			•	★			•	★			
$r' = C/d(f)$					★	★	★	★	•	★	★	•	•
$L' = Ce(T)$					★	★	★	★	•			•	•
$P' = Cg(r)$					★	★	★	★	•		•	•	•
$T' = CL$													★
$m' = C$													
$h(f)X' = 0$		•	★		★		★						
$r = 0$									★		★		
$L = 0$													
$m = 0$										★			

Table 4.2 As in table 4.1, here, the first call to the divide subroutine reduces the first 3×3 block to unity by (left) multiplying the initial 3 rows with the inverse of that leading 3×3 block.

EQNS – VARS	f	T	m	X	r	L	f	T	m	X	r	L	C
$P(f) = g(r)$	1			•	•	•							
$L = r^2 T^4$		1		•	•	•							
$\dot{m} = f(T)$			1	•	•	•							
$h(f)X' = 0$				★	•	•				★			
$r' = C/d(f)$				•	★	•				★			
$L' = Ce(T)$				•	•	•				•	★		
$P' = Cg(r)$				•	•	•				★	•		
$T' = CL$				•	•	•				★	•		
$m' = C$				•	•	•				★	•	•	•
$X'' = R(T)$		•		★			•	•	★				
$r' = C/d(f)$					★	★	•			★			
$L' = Ce(T)$					★	★	★	•		★			
$P' = Cg(r)$					★	★	★	•		•	•	•	•
$T' = CL$					★	★	★	•		•	•	•	•
$m' = C$					•	★	★	★		★	★	★	★
$h(f)X' = 0$										★	★	★	★
$r = 0$											★	★	★
$L = 0$											★	★	★
$m = 0$												★	★

Table 4.3 As in table 4.2, here a second call to `difrns` to populate the next 6 rows, and then another call to `elimn8` to eliminate (almost) all terms below the leading 3×3 identity matrix.

EQNS - VARS	f	T	m	X	r	L	f	T	m	X	r	L	C
$P(f) = g(r)$	1		•	•	•								
$L = r^2 T^4$	1	•	•	•	•								
$\dot{m} = f(T)$	1	1	•	•	•								
$h(f)X' = 0$	1					•	•						
$r' = C/d(f)$						•	•	•	•	•	•	•	
$L' = Ce(T)$		1				•	•	•	•	•	•	•	
$P' = Cg(r)$						•	•	•	•	•	•	•	
$T' = CL$			1			•	•	•	•	•	•	•	
$m' = C$						1	1	1	1	1	1	1	
$X'' = R(T)$	•	★			•	★			•	★			
$r' = C/d(f)$							★	★	•	•	★	★	
$L' = Ce(T)$							★	★	•	•	★	★	
$P' = Cg(r)$							★	★	★	•	•	•	
$T' = CL$							★	★	★	★	•	•	★
$m' = C$									★	★	★	★	★
$h(f)X' = 0$						•	★		★		★		
$r = 0$										★		★	
$L = 0$											★		
$m = 0$												★	

Table 4.4 As table 4.3, here, we divide those 6 new rows by the terms of the entire leading 6×6 sub-matrix.

EQNS - VARS	f	T	m	X	r	L	f	T	m	X	r	L	C
$P(f) = g(r)$	1			•	•	•							
$L = r^2 T^4$		1		•	•	•							
$\dot{m} = f(T)$			1	•	•	•							
$h(f)X' = 0$				1									
$r' = C/d(f)$					1								
$L' = Ce(T)$						1							
$P' = Cg(r)$							1						
$T' = CL$								1					
$m' = C$									1				
$X'' = R(T)$									★	•	•	•	•
$r' = C/d(f)$									•	★	•	★	•
$L' = Ce(T)$									•	•	★	•	•
$P' = Cg(r)$									•	•	•	•	•
$T' = CL$									•	•	•	•	•
$m' = C$									•	•	•	•	•
$h(f)X' = 0$									•	★	★	★	★
$r = 0$										★	★	★	★
$L = 0$										★	★	★	★
$m = 0$											★	★	★

Table 4.5 As table 4.4, here we populate as before the next 6 rows, with another call to `difrn`. One more call to `elimn8` removes all terms below the leading identity diagonal.

EQNS - VARS	f	T	m	X	r	L	f	T	m	X	r	L	C
$P(f) = g(r)$	1		•	•	•								
$L = r^2 T^4$		1	•	•	•	•							
$\dot{m} = f(T)$			1	•	•	•							
$h(f)X' = 0$				1			•	•	•	•	•	•	★
$r' = C/d(f)$					1		•	•	•	•	•	•	
$L' = Ce(T)$						1	•	•	•	•	•	•	
$P' = Cg(r)$							1	•	•	•	•	•	
$T' = CL$								1	•	•	•	•	
$m' = C$									1	•	•	•	
$X'' = R(T)$									1				
$r' = C/d(f)$										1			
$L' = Ce(T)$											1		
$P' = Cg(r)$												1	
$T' = CL$												1	
$m' = C$													★
$h(f)X' = 0$							•	★	★	★	★	★	
$r = 0$													
$L = 0$													
$m = 0$													

Table 4.6 as in table 4.5, here another call to divide reduces the entire leading 6×6 matrix to unity.

EQNS – VARS	f	T	m	X	r	L	f	T	m	X	r	L	C
$P(f) = g(r)$	1		•	•	•								
$L = r^2 T^4$		1	•	•	•	•							
$\dot{m} = f(T)$			1	•	•	•							
$h(f)X' = 0$				1				•	•	•			
$r' = C/d(f)$					1			•	•	•			
$L' = Ce(T)$						1		•	•	•			
$P' = Cg(r)$							1	•	•	•			
$T' = CL$								1	•	•			
$m' = C$									1	•			
$X'' = R(T)$									1	•	•	•	•
$r' = C/d(f)$										1	•	•	•
$L' = Ce(T)$											1	•	•
$P' = Cg(r)$											1	•	•
$T' = CL$											1	•	•
$m' = C$												1	•
$h(f)X' = 0$												★	•
$r = 0$												•	•
$L = 0$												•	★
$m = 0$												•	•
												•	★

Table 4.7 As table 4.6, here the final 4 rows are set via a call to `difrns`. Then, as before, a call to `e1imm8`, removing again the terms below the unit-reduced diagonal. It can be seen that the series of multiplications and Gaussian elimination must place a term with a significant magnitude in the very bottom right corner of the matrix. As [Egginton \(1971\)](#) notes in his own supplement to that work, the penultimate `e1imm8` call will in fact place the product of two significant terms in this place, one element of this multiplication comes from $m' = C$ term, specifically from the eigenvalue term, C . The second element of comes from the central mass boundary condition, $m = 0$. The 4×4 sub-matrix at the lower right of the overly matrix *should* at this point be relatively computationally inexpensive to invert.

EQNS – VARS	f	T	m	X	r	L	f	T	m	X	r	L	f	T	m	X	r	L	C
$P(f) = g(r)$	1		•	•	•														
$L = r^2 T^4$		1	•	•	•	•													
$\dot{m} = f(T)$			1	•	•	•													
$h(f)X' = 0$				1					•	•	•								
$r' = C/d(f)$					1				•	•	•								
$L' = Ce(T)$						1			•	•	•								
$P' = Cg(r)$							1		•	•	•								
$T' = CL$								1	•	•	•								
$m' = C$									1	•	•								★
$X'' = R(T)$									1						•	•	•	•	•
$r' = C/d(f)$										1					•	•	•	•	•
$L' = Ce(T)$											1				•	•	•	•	•
$P' = Cg(r)$												1			•	•	•	•	•
$T' = CL$													1		•	•	•	•	•
$m' = C$														1	•	•	•	•	•
$h(f)X' = 0$															1				
$r = 0$																1			
$L = 0$																	1		
$m = 0$																		1	

Table 4.8 As table 4.7, here we observe the effects of the previously described matrix inversion. From here, a set of back-substitutions can be performed to obtain the needed corrections in the code internal variables, dL , dr , etc, at the central meshpoint, and then the second to centre (our only intermediate meshpoint, in this simple example), and finally at the surface meshpoint.)

the atomic/molecular contributions, included are the contributions of all cations of hydrogen and helium, as well as neutral and molecular hydrogen, and neutral helium. In terms of heavier species, included are C, N, O, Ne, Mg, Si and Fe, which are treated as being fully ionized. We note too that partition functions, ω_i are in principle non-trivial functions of temperature *etc*. However, for simplicity, these are computed just as the statistical weights of the ground states of each species, except for molecular hydrogen, for each [Pols et al. \(1995\)](#) adopted the partition function for pressure equilibrium by [Vardya \(1960\)](#), modified by a truncation factor, $\zeta(T)$, to prevent an ultraviolet divergence ([Webbink, 1975](#)). In the third term, F_e , which is defined as,

$$F_e = N_e \psi kT - VP_e, \quad (4.37)$$

where N_e is the electron number density per unit mass, and P_e is the electron pressure integral and ψ is computed as,

$$\psi = \ln f + 2 \left(\sqrt{I+f} - \ln \left(I + \sqrt{I+f} \right) \right), \quad (4.38)$$

again as by [Eggleton et al. \(1973\)](#). The final line contains non-ideal corrections for Coulomb interactions and pressure ionization. For Coulomb interactions, the (strong) plasma interaction parameter, typically given as,

$$\Gamma_i = \frac{z_i^2 e^2}{r_i kT}, \quad (4.39)$$

where r_i is the ion-sphere radius, is approximated as ([Pols et al., 1995](#)),

$$\gamma = \left(\frac{4\pi}{3} \right)^{1/3} \frac{n_e^{1/3} e^2}{kT} \left(\frac{N_{e0}}{N_0} \right)^{2/3} \left(\frac{\sum_j \left(X_j Z_j^2 / m_j \right)}{N_{e0}} + \theta_e \right), \quad (4.40)$$

giving a final expression for the Coulomb interaction term,

$$\Delta F_{\text{Coulomb}} = -N_e kT \frac{N_0}{N_{e0}} g(\gamma). \quad (4.41)$$

4.2.2.1 The core-envelope interaction artifice

Here we explain and demonstrate the mechanism used to connect the envelope structure, computed with a standard equation of state to the neutron degenerate core of a Thorne-Żytkow Object (TŻO) making use of a range of modifications I made to the STARS code. For a discussion of the physical nature and background of these objects, please see chapter 2. The proposed structure of a TŻO as detailed in that chapter has led to the development of this

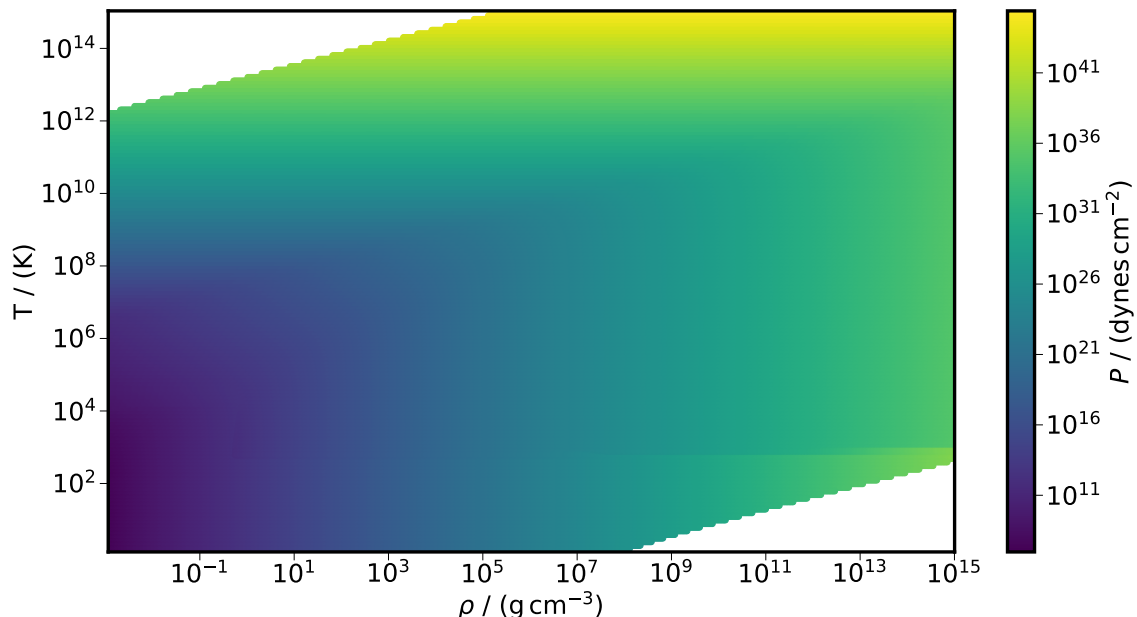


Figure 4.2 The unmodified equation of state in the STARS code, originally by [Eggleton et al. \(1973\)](#). While the independent variables used by the EOS are f , which is related to the electron degeneracy parameters, as in equation 4.38, we present the total pressure as a function of the density and the temperature instead — for ease of comparison with, e.g. Skye ([Jermyn et al., 2021](#)), FreeEOS ([Irwin, 2012](#)) etc. The values of f chosen to produce this illustrative model correspond to maximum values of ψ of around 10^6 , which are obtainable for any realistic stellar model. In addition, the extremely high density – low temperature region of the ρ – T space would in reality be dominated by physics well beyond what is considered here. What is to be noted, as illustrated in figure 4.6, is the same selection of values of f , that is, the same densities and temperatures, produce much larger maximum values of ψ , due to the neutronizing artifice present in those calculations.

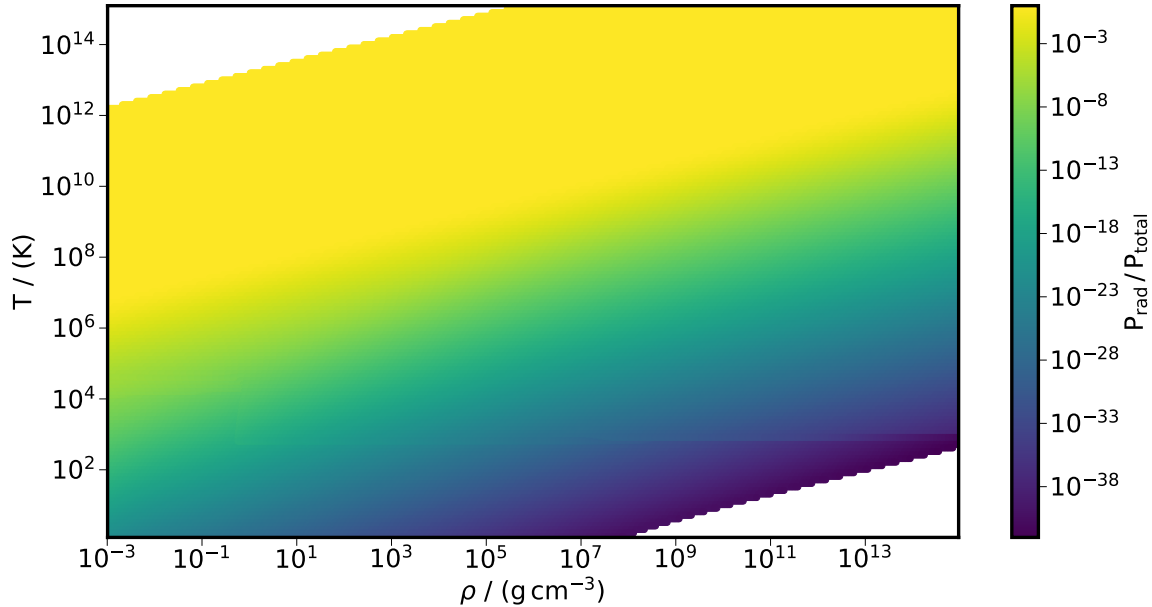


Figure 4.3 As in Figure 4.2, here we present the ratio of the radiation pressure to the total pressure for the standard STARS equation of state. As discussed in section 4.2.2, the equation of state solver allows for the effects of pressure ionization to be included, which dominates in a hydrogen rich environment at high densities and lower temperatures, that is, where radiation pressure is less important.

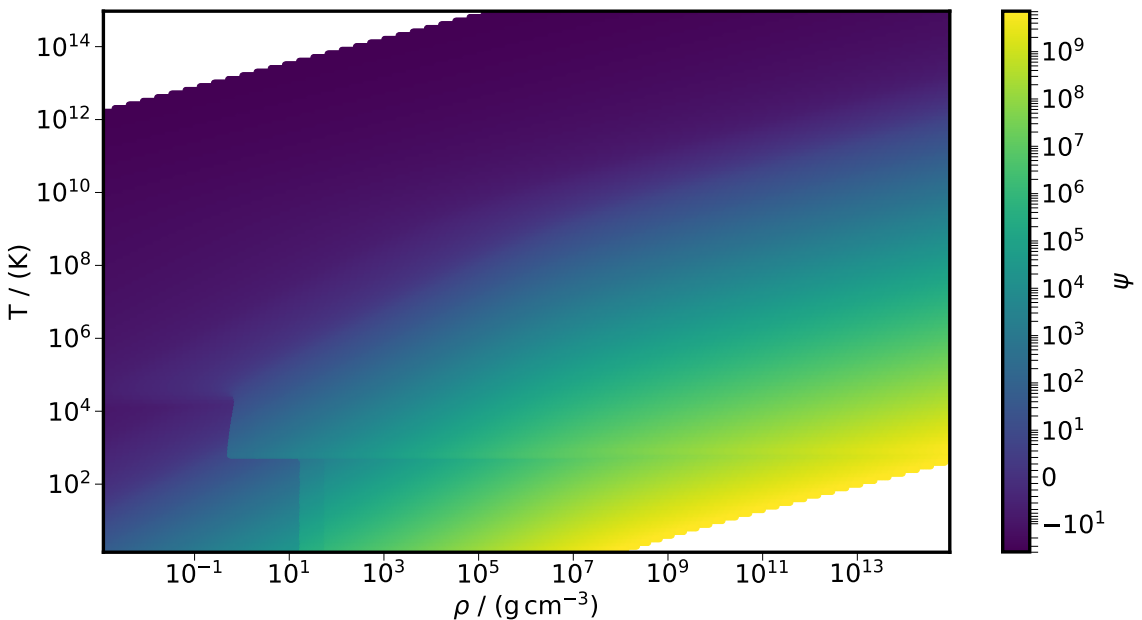


Figure 4.4 As in Figure 4.2, here we show the the value of the electron degeneracy parameter, ψ as a function of temperature and density for the unmodified STARS equation of state. While we present ψ as a function of ρ and T , as before, for ease of comparison, it is in fact density that is computed as a function of ψ .

tool, the core-envelope interaction artifice. In the seminal works by Thorne & Żytkow (1975) and Thorne & Żytkow (1977) the Generate Outer Boundary (GOB) program (Paczyński, 1969) was used to compute the models of TŻOs by dividing the model into an outer region where the envelope is static, a middle region where the envelope is inflowing and an inner region, the neutron core. Thorne & Żytkow (1975) state clearly that these computational regions do *not* map onto the three qualitatively and physically distinct regions as discussed in section 2.2.1. Thorne & Żytkow (1975) and Thorne & Żytkow (1977) asserted that the thermal conductivity of their stellar plasma at the high densities at the neutron core could only support a negligibly small amount of heat transport out of or in to the core. They note that this computation relies on a standard conductivity, that is, one following Canuto (1970) and Flowers & Itoh (1976, 1979), which does not necessarily reflect the transport properties of an electron gas that is not just degenerate, but also could be expected to be highly magnetized as well. Therefore, they impose a series of inner boundary conditions, setting the inner radius boundary condition to the radius of the core, as informed by canonical neutron star models, setting likewise the inner mass boundary condition to the neutron star mass. The central luminosity is set to zero, a choice informed by the assertion that the material here supports only minimal heat transport, while the temperature is solved for during iterations of the GOB program. It is crucial here to note that they set this boundary condition at a fixed density, $\rho = 3 \times 10^8 \text{ g cm}^{-3}$. This has a very profound influence on the nature of the models that they compute, forcing a very high density at the boundary of the neutron core. We note, as they did, that inflowing material reaching the upper boundary of the neutron core at such high densities and temperatures (between 10^8 K and 10^9 K in their models) can energetically access the electron capture mechanism (Bahcall, 1964), allowing for the conversion of stellar plasma to neutron-rich neutron star material. The models of TŻ were all static models and as such this process was not explored. Cannon et al. (1992) produced evolutionary models of TŻOs and as such required some mechanism to deal with this possibility. Furthermore, as in low ($M_{\text{env}} < 7M_{\text{core}}$) mass TŻOs, the static models by TŻ predict that the release of gravitational potential energy from material falling onto the neutron core should dominate the energy generation. Nine stellar structure equations were used, in order to allow the models to be consistent with the relativistic formalism for stellar structure as described Thorne (1977)⁹. These are the five first order equations for mass, radius, luminosity, pressure and temperature, a second order equation for hydrogen abundance (Cannon et al. (1992) considered models with only hydrogen and helium) and eigenvalue equation for the mesh spacing constant, as we describe in section 4.2.1. Two additional equations are then used, one for the gravitational potential energy and one for the gravitational mass, which is now distinct from the rest

⁹We describe the means by which our models make contact with these same equations in appendix A.1

mass. [Ball et al. \(2012\)](#) reformulated these relativistic corrections in such a way as to remove the need for additional structure equations to be solved, at the cost of accuracy of the corrections. [Cannon et al. \(1992\)](#); [Cannon \(1993b\)](#) elect to model the core as a part of the stellar model. They do not compute *ab initio* the neutron core, but rather take the general relativistic neutron matter equation of state by [Cooperstein \(1988\)](#). Hence, they make use of a device, the core-envelope interaction artifice which they place at densities above $\rho > 10^6 \text{ g cm}^{-3}$. In order to simulate the mechanism by which the degenerate stellar plasma becomes neutronized, the [Eggleton et al. \(1973\)](#) equation of state is modified so that the mass, or rather, the effective mass of electrons increases as the electrons become more degenerate, until that mass reaches the mass of the neutron, simulating a neutron matter-like equation of state as follows

$$m'_e = \begin{cases} m_e, & \text{if } \psi < 0 \\ e^\psi m_e, & \text{if } 1 < e^\psi < k \\ km_e, & \text{if } e^\psi > k \end{cases} \quad (4.42)$$

For $\psi < 0$ or $k = 1$ this produces a purely electron equation of state, while for sufficiently large ψ and $k = m_n/m_e$ produces the equation of state for a degenerate neutron gas from [Oppenheimer & Volkoff \(1939\)](#). This is then connected directly to the core equation of state. We describe this specific implementation further in section 5.1.2.

4.2.2.2 Modifications made to the STARS code for the purposes of modelling TŻOs and B-WDs

We describe here the series of modifications that were made to the STARS code in order model TŻOs. These modifications were then used as a basis for a similar series of modifications made to the MESA stellar evolution code, with the noteworthy exception of the core-envelope interaction artifice, as we motivated the use of a different set of central boundary conditions, as explained in section 5.1.2 by concerns regarding the validity of the assumption of neutronization of infalling stellar material, given the considerably lower temperatures and densities at the halo of our models presented there in comparison to the models of TŻ, Cannon et al. and others. The following sections (4.2.2.2.1 - 4.2.2.2.5) describe the majority of the actual software development on the STARS code performed during the course of the work presented in this dissertation. Adding the additional physics needed to model TŻOs and B-WDs generally revolved around the modification of the equation of state subroutines in order to model the neutron core of the TŻOs and the magnetic field, magnetic pressure support and magnetic mass-energy density contribution for B-WDs. Section 4.2.2.2.5 describes a series of modifications we made in order to aid in converging challenging models. The

presence of extremely large densities and temperatures near the cores of T $\ddot{\text{O}}$ s, as well as the extremely large magnetic fields in B-WDs cause considerable difficulties in converging models. Generally, this is due to large changes in the structure matrix relative to the underlying computational mesh occurring in short periods of time. For example, when we try to form a T $\ddot{\text{O}}$ model by directly collapsing a electron degenerate carbon core in an AGB model into a neutron-star core (a technique of “stellar engineering” that we have dubbed “slow-motion supernova”), the core shrinks in terms of radius from a white dwarf-like value (around 1 R_\oplus) to a neutron star-like value (around 10km) within a very short period of time, approaching the dynamical timescale. This forces the computational mesh to move at a tremendous “speed”, to catch up, causing severe numerical diffusion of chemical species, which can drag helium into the extremely hot core, where it burns explosively, causing the code to crash. If the mesh spacing function is altered to make the mesh move slower, then errors accumulate extremely rapidly in all structural variables, as the mesh cannot keep up with the collapse of the core fast enough to resolve it spatially. Using too small a timestep causes numerical errors to build up in an oscillatory fashion, while too large a timestep fails to resolve the core collapse temporally. A large portion of the code development time and effort we expended was on designing and implementing the convergence aids that we describe in that section.

4.2.2.2.1 Opacity

The standard opacity tables used in the STARS code need to be augmented with a set of opacity tables that cover a larger range of temperatures and densities. A set of opacity tables suitable for this temperature and density range was obtained from R. Church (Private Communication) and implemented into the current version of STARS. This table format was, with modification, compatible only with a linear or cubic spline interpolation scheme in the absence of C/O dependent opacities. While the current version of STARS is to some degree hard-coded to operate on the standard OPAL ([Iglesias & Rogers, 1996b](#)) tables it was straightforward to modify the opacity subroutines, opacty.f and opspln.f, along with the I/O subroutines to accommodate the new tables. As seen in figure 4.5 the modified opacity tables cover a much larger region in temperature density space than the original table or the C/O adjusted table of [Eldridge & Tout \(2004\)](#), extending up to 10^{12} K in temperature and 10^{18} gcm^{-3} in density. These extended ranges reflect the more extreme conditions expected in models of T $\ddot{\text{O}}$ s, particularly in the neutron core and in the burning regions, owing to the irp-process (section 2.3).

The standard opacity tables are however, mostly sufficient for the purposes of simulating B-WDs. We did however, modify the opacity routine in order to implement the relatively straightforward opacity prescription by [Potekhin & Yakovlev \(2001\)](#); [Ventura & Potekhin](#)

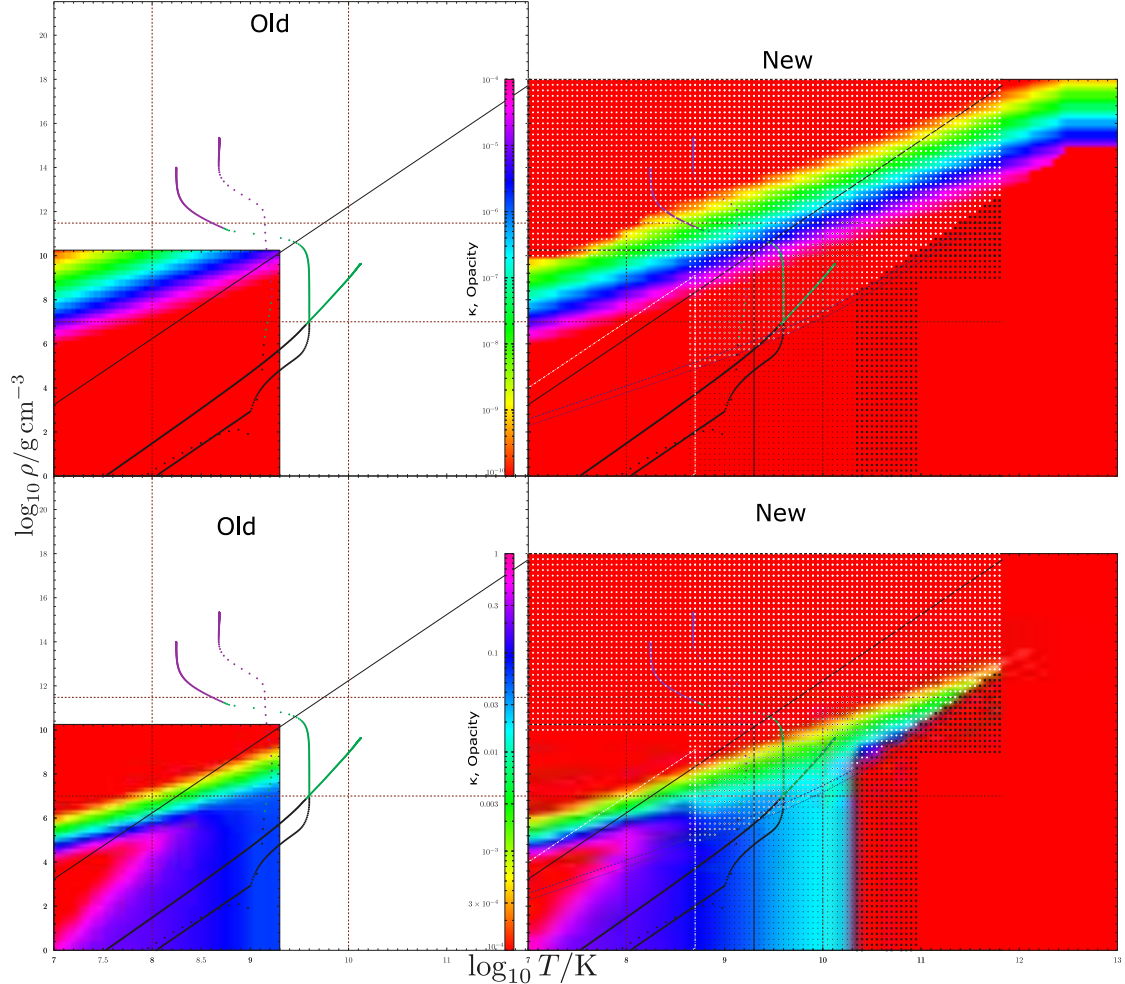


Figure 4.5 Visualisation of modified opacity table used, based on work by R. Church. The graphs on the left hand side of the figure depict the old opacity table used in STARS ([Iglesias & Rogers, 1996b](#)). The graphs on the right hand side depict the new, expanded opacity tables, dubbed V4, used in the TZO modification. The images at the top and bottom of the figure depict the tables in linear and log scale in opacity respectively. The basis of table is log temperature and log density. This differs from the tables of [Eldridge & Tout \(2004\)](#) where $\log(\mathcal{R} = \rho/T_6^3)$ replaces $\log(\rho)$. The opacity is indicated by colour with the individual crosses and dots on the right side of the figure representing the individual data points in the table. The coloured curves through the images indicate sample cubic splines through the table, demonstrating smooth interpolation through the table, as required.

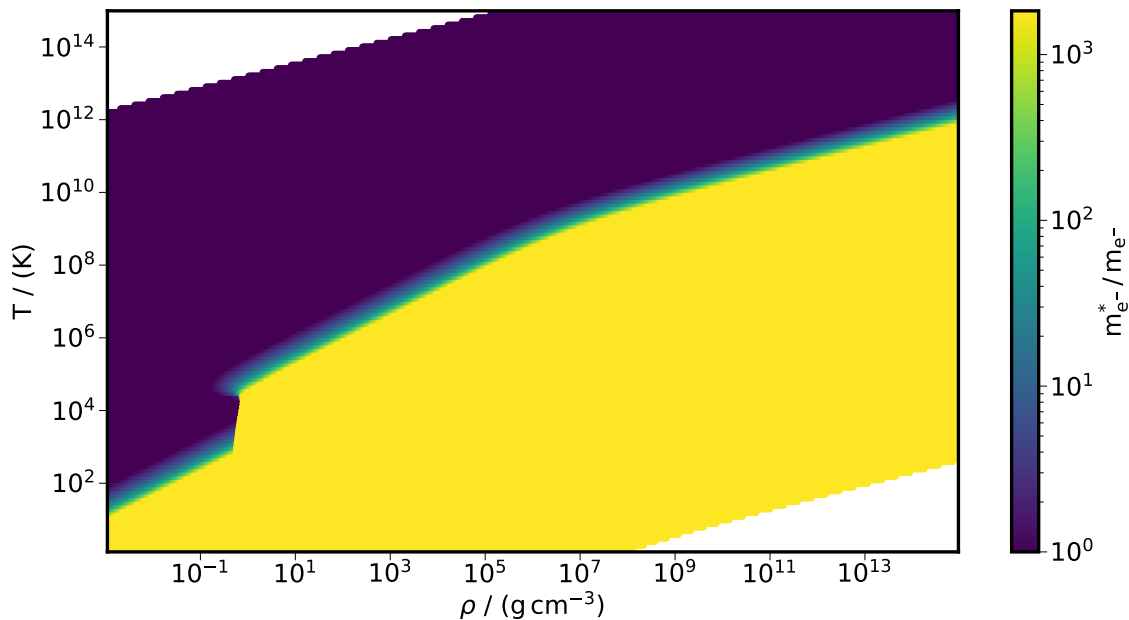


Figure 4.6 The modified STARS EOS is presented, demonstrating the neutronizing artifice, as by Cannon et al. (1992); Cannon (1993b) and Podsiadlowski et al. (1995). Here we show the effective mass of the electron, as per the artifice, again, as a function of ρ and T , where, as before, the density is itself a function of the underlying degeneracy parameter. Much larger densities are obtained for the same values of f as used in figure 4.2 — this is owing to the increased density of a “neutronized” Eggleton et al. (1973)-like electron equation of state. Additionally included are the effects of thermal neutrino production as by Yakovlev & Levenfish (1995) and Itoh et al. (1996b).

(2001) for environments where the magnetic pressure is large in comparison to the thermal pressure. We add this opacity, which is computed as a simple function of the local density of the stellar material, temperature and magnetic field density, in reciprocal with the tabulated opacities in order to provide a smooth and accurate set of opacity values throughout our series of B-WD models.

4.2.2.2 Modified Electron Mass

The fundamental idea behind Cannon’s approach to produce models of TŻOs involves modification of the electron mass used in the equation of state calculation. STARS does not utilize tabulated equations of state but instead computes these analytically for each model mesh point. This has the advantage of allowing the first and second derivatives of the thermodynamic quantities to be easily computed. Two different schemes for altering the electron mass were implemented. The most simple scheme, based on that of Cannon

et al. (1992) and Thorne & Żytkow (1977) sets the mass of the electron in the equation of state routine in accordance with equation 4.42. This scheme simply sets the electron mass equal to the neutron mass above some degeneracy parameter threshold, with an exponential drop down to the normal electron mass below this point. This causes a problem because, when the core of a model becomes sufficiently degenerate to cross this threshold for the first time, the mass of the electrons in the innermost few mesh points of a model are immediately converted to neutrons. This sudden change prevents successful convergence of these models. An improved scheme was implemented with an additional parameter, the time-derivative of the logarithm of the desired final electron mass. This desired mass replaces the neutron mass as the mass to which electrons are brought up as the degeneracy threshold is reached and is slowly increased over time. The rate is set by this time derivative parameter. Because this is a time derivative and not a time-step number derivative the increase in the desired final electron mass grows more slowly when the time-step is short. This further helps to achieve a converged model. This method prevents the sudden change in the mass of the electron found in the first scheme. While no converged models with the first scheme were produced at all, the second scheme allowed the mass of the electrons in the core of a massive AGB star to be increased to around $20 m_e$ which, while certainly an improvement, is still considerably short of the neutron mass.

4.2.2.3 Neutron Opacity

Simply increasing the mass of the electron in the equation of state is insufficient. In order to capture fully the effects of a very neutron-rich or pure neutron region other effects must be accounted for. An increasing neutron number density is simulated by increasing the effective density in the equation of state. For these regions of increased neutron number density the issue of opacity must also be addressed. For regions where the electron mass is unchanged, the opacity is computed as normal. In regions where the electron mass is increased, a weighting factor representing how neutron-like the material is is introduced. A separate opacity routine, `tzo_neutron.f` is called in order to compute the neutron opacity. This routine initially computes the critical density as in equation 2.5.12 of Shapiro & Teukolsky (1983). If the neutron adjusted density is below the critical density, there are effectively no neutrons present as far as the opacity is concerned. The proton and neutron number densities are then iteratively solved for with equation 2.5.17 of Shapiro & Teukolsky (1983). The proton, neutron and electron chemical potentials/effective masses are then computed with their equations 2.5.16 and 2.5.7. This also allows the electron collision frequencies (summed over the colliding species) to be computed. Electron conductivity, when scattering off of

protons is expected to dominate, makes use of equation 77 of [Gnedin & Yakovlev \(1995\)](#). Neutrino loss rates are computed as by [Yakovlev & Levenfish \(1995\)](#).

4.2.2.2.4 Magnetic Fields

The STARS evolution code has no inbuilt support for magnetic fields, hence we implemented a radial field model into the code as described by [Bhattacharya et al. \(2021\)](#). Within the equation of state subroutines, we computed a radial magnetic field density, as a function of the local density¹⁰. This gives a magnetic field density at every computation point throughout the star, that is computed simultaneously with the rest of the thermodynamic variables, as the equation of state routines are called from the solver. At each point, the magnetic field density is used to compute a local (radial) magnetic pressure term and a magnetic mass-energy density term. The density of the stellar material is augmented by the amount of mass-energy density that the magnetic field contributes, and then the pressure, as computed by the STARS standard equation of state, including thermal and degeneracy pressure is summed with the computed magnetic pressure support to give the new total pressure at the calculation point, which is then passed back to the solver. The opacity value returned from the standard opacity routine is when modified to include the Potekhin opacity (section 4.2.2.1). A B-WD model will almost always fail to converge if the magnetic field is suddenly turned on, that is, set to a (large) non-zero value from zero in a single timestep. Therefore, we also developed a ramping-up function, that, once the user has turned on the magnetic field, will exponentially increase the magnetic field density throughout the star until the magnetic field reaches the desired profile and values. The function is tuned to grow the field rapidly enough that no significant evolution (cooling) of the white dwarf occurs during the ramp up, which would harm the utility of the models by introducing an undesirable, physically unmotivated period of evolution at early times. At the same time, the field is not ramped-up so rapidly as to cause significant errors to accumulate in the solution, or so that the model would fail to converge entirely. Unfortunately, no algorithm was found that worked sufficiently well in all or most of the models we produced, and as such the coefficients of this exponential (as a function of time) ramp-up were computed heuristically for the range of WD masses and field profile parameters that were investigated throughout chapter 6, by use of brute-force trial-and-error.

4.2.2.2.5 Convergence Aids

In general it is very difficult to produce a converged model with the modifications described here. So various modifications were made in order to converge models more easily rather

¹⁰The exact physical implementation, including a saturation radius prescription we devised are described in chapter 6, along with the results that we obtained.

than for strictly physical reasons.

The first of these is the ability to switch between the [Cannon \(1993c\)](#)/[Thorne & Źytkow \(1977\)](#) method of altering electron mass and the smoother version based on the work from R. Church (Private Communication). In addition we implemented a setting which strips the He out of a selected number of model meshpoints, from the centre out. This is to prevent numerical diffusion of helium into the core because we expect all the inward moving helium to be burned off in the helium burning shell ([Meynet et al., 2004](#)). There are then three more binary settings. The first, when activated, stops higher burning. That is burning of elements other than hydrogen in non-degenerate regions of the model. This prevents scenarios where, for example, a helium burning shell migrates outward in the envelope. The second stops all burning in neutron rich regions, regions where the effective electron mass has been increased. This prevents explosive burning in the neutronizing core itself. The final binary setting eliminates all normal nuclei from the composition of the core. What mass boundary constitutes the core can be computed automatically or can be manually set. The compositions of neon, oxygen, carbon, helium and hydrogen are set to zero inside the core. This better simulates a pure neutron core, by leaving only modified mass electrons as the interacting species in the core. There is then a number of real number settings that can be used as convergence aids. The first of these are the target modified electron mass and the rate of change of the logarithm of this mass. This value sets the target mass to which sufficiently degenerate electrons should be increased. It is usually set to the neutron mass. The rate of change is utilized by the Church-type scheme for slowly ramping up the mass of fully degenerate electrons in order to ensure the smooth development of a neutronized core. Next, the maximum allowed time-step in years may be set, allowing a constant time-step if needed. Then one can set a factor by which the hydrogen burning rate in non-degenerate regions may be reduced in order to reduce problems caused by overly rapid hydrogen shell burning or an over-abundance of helium in the inter-shell region. The next term allows a constant artificial energy generation term to be introduced. This scales with the effective electron mass. It serves to prop-up the massive, degenerate core, preventing it from collapsing, because models in which the core is beginning to collapse no longer converge. Next is the ability to set a cap on the maximum neutrino energy loss, as well as setting the rate at which this changes, and a maximum cap for this change.

Then one can set the degeneracy threshold. This is the degeneracy parameter above which the electron mass begins to increase. It essentially sets the boundary of the neutron core. It can also be set to increase or decrease with time, as well as to have maximum and minimum limits. Fine-tuning these parameters is normally the most significant setting to determine the outcome of an attempted model. The most successful scenarios were found to be those

where the threshold degeneracy was slowly brought down to meet the increasing degeneracy in the core of a massive AGB model.

In addition, the rate of convective diffusive mixing (RCD) can be tuned and set to change over time. RCD is a code parameter that sets the diffusion coefficient for convective mixing. This coefficient is computed as $RCD \times \frac{2(\nabla - \nabla_{ad})}{t_{nuc}}$. Typically RCD is set to around 10^6 but reducing RCD or even setting it to zero can assist in convergence by reducing or shutting off diffusive mixing. The mesh fluidity, the rate of change of this fluidity, and the minimum allowed fluidity can also be manipulated. Referring back to section 1.2, the STARS code makes use of a moving, non-Lagrangian mesh, the spacing of which is defined by the mesh spacing function. The mesh fluidity then sets the effective fluidity of the motion of the mesh points themselves. Very low mesh fluidity effectively locks the mesh points in mass. This prevents the mesh points from moving too rapidly so that species are not moved around, especially towards the core, owing to the effects of numerical diffusion. On the other hand locking the mesh of the entire star is likely to cause problems because the mesh is unable to move to the regions of the model where more spatial resolution is required. This may lead to lost detail or lack of convergence. Next, the convective mixing parameter can be set along with its rate of change and maximum. This allows the MLT mixing length to be tuned in order to prevent convergence problems brought about by over efficient or under efficient convective mixing. The MLT mixing length is the characteristic length over which a fluid element in a convective system conserves its properties before mixing with the surrounding fluid (Gough, 1977).

Then there is a set of tools for selection and manipulation of the coefficients of the mesh spacing function. Maxima and rates of change for selected coefficients can also be selected. The mesh spacing function (MSF) utilized by STARS can be written as

$$Q = \log \left(\frac{1}{c_6} \left(\frac{m}{M^*} \right)^{\frac{2}{3}} + 1 \right) - c_3 \log \left(\frac{r^2}{c_8} + 1 \right) + c_7 \log \left(\frac{T}{T + c_0} \right) \quad (4.43)$$

$$+ c_4 \log p + c_5 \log \left(\frac{p + c_9}{p + c_{-1}} \right) + c_2 \log \left(\frac{p + c_{10}}{p + c_{-1}} \right),$$

where c_x is the x^{th} mesh spacing coefficient, $c_0 = 20\,000\text{K}$ and $c_{-1} = 10^{10c_1}$. The STARS code places the mesh points at evenly spaced intervals of Q which, when initialized with the standard MSF coefficients, ensures that processes that move rapidly in, for example, mass or radius coordinates, move slowly in mesh coordinates by increasing the number of mesh points in important areas such as burning shells. By tuning the MSF coefficients and allowing them to change in time the burning shells and the edge of the neutron core can be given a

higher spatial resolution at the expense of the outer envelope. This makes a smaller number of mesh points sufficient to spatially resolve the TZO processes we seek to investigate. Finally the ability to alter the rate at which the various hydrogen, helium and carbon burning processes occur was added. This allows burning to be shut off when needed, in order to shut off a particular problem burning shell, for example, or to slow a certain burning rate in order to ensure that a particular burning process occurs less explosively, so limiting rapid changes in various thermodynamic variables that can prevent convergence.

4.3 Modules for Experiments in Stellar Astrophysics (MESA)

MESA ([Paxton et al., 2010, 2013, 2015](#); [Paxton et al., 2018b](#); [Paxton et al., 2019](#)) is a widely used, modular, and open-source stellar evolution code. MESA is an excellent complimentary tool to the STARS code. While the STARS code is fully non-Lagrangian with a user-definable mesh spacing function, MESA uses a Lagrangian mesh description, where computation points may be merged or split in terms of the mass they enclose, but never moved (in the code's fully hydrostatic mode). The STARS code makes use of a semi-analytical equation of state ([Eggleton et al., 1973](#)), where thermodynamic quantities and their derivatives and analytically computed at each timestep with input from tabulated opacities, thermal neutrino loss rates, nuclear reaction rates *etc.*, while MESA uses a blend of the OPAL ([Rogers & Nayfonov, 2002a](#)), SCVH ([Saumon et al., 1995a](#)), FreeEOS ([Irwin, 2004](#)), HELM ([Timmes & Swesty, 2000a](#)) and PC ([Potekhin & Chabrier, 2010](#)) EsOS, with opacities primarily from OPAL ([Iglesias & Rogers, 1993, 1996c](#)), with low-temperature data from [Ferguson et al. \(2005a\)](#) and the high-temperature, Compton-scattering dominated regime by [Buchler & Yueh \(1976\)](#) and electron conduction opacities from [Cassisi et al. \(2007\)](#). In the regions of Thorne-Żytkow Objects that are of particularly salient interest to us, that is, at and below the base of the convective envelope, we make use of the more recent Skye equation of state ([Jermyn et al., 2021](#)). Skye is blended with the other MESA equations of state, but in these regions comprises either the vast majority, or the entirety of the blend. While of course not as easily customised as an analytical equation of state is in STARS, Skye is a differentiable equation of state, that equips MESA with a set of automatic differentiation machinery. As in [Jermyn et al. \(2021\)](#), Skye includes the effects of positrons, relativity, electron degeneracy, Coulomb interactions, nonlinear mixing effects, and quantum corrections. This covers a wide range of relevant effects for the study of exotic compact objects and TZOs that we are required to account for by hand in STARS, while also allowing relative ease of modification for, e.g., including the effects of Eddington limited accretion of envelope material onto a neutron degenerate core in a TZO, by writing the [Cannon \(1993b\)](#) accretion luminosity prescription in terms of the free

energy delta, and allowing the auto differentiation routine to compute the first and second order derivatives.

MESA’s nuclear reaction rates are from JINA REACLIB ([Cyburt et al., 2010](#)) plus additional tabulated weak reaction rates ([Fuller et al. 1985](#); [Oda et al. 1994](#); [Langanke & Martínez-Pinedo 2000](#)) and screening is included by the prescription of [Chugunov et al. \(2007\)](#). As in the STARS code, thermal neutrino loss rates are from [Itoh et al. \(1996a\)](#). We provide, for completeness, a discussion of the relevant nuclear reaction networks, and in particular, the ([Heger et al., 2002](#))-style adaptive nuclear network that we made use of, in appendix B.2. The modular nature of MESA makes it well suited to our purposes here, and while direct modification of the various routines handling the equation of state, opacity, *etc.* are not quite as simple to perform directly as in STARS, given the much larger codebase, the user definable *hooks* into the MESA source code have been incorporated by its developers for the purposes of making this sort of modification more accessible to the end user. As we discuss in more detail in sections 5.1.1, 5.1.2 and 5.2.1, writing the modifications we need in the form of these hooks is usually sufficient for most situations in which a change to the code is needed, and while these are strictly speaking more complex (in the sense that they represent an overwriting of some pre-selected section of the original source) and less powerful (in the sense that the underlying source code itself cannot as easily be directly modified) than simply altering the source code directly, there are some very significant benefits to the hook approach. The MESA code must be installed from a source package, in the first instance, making use of a software development kit (SDK), supplied separately. Individual model runs are then compiled from this installation, that is, the hooks that are used to modify the source code are complied into a runtime binary directly on top of the underlying source. This usually takes on the order of 10s and hence is negligible compared to the usual runtime of the models we discuss in chapter 5, which is typically on the order of 5 hrs, running on a 4th generation i7 processor. In comparison, modifying the MESA source directly and reinstalling the entire codebase takes around 1 hr on the same hardware. As we discuss in more detail in chapter 5, we use such hooks to add boundary conditions to replicate the interaction between a giant envelope and a central neutron star, including the effects of accretion of infalling envelope material on to the neutron core. In addition, we include the effects of GR, as discussed in section 5.1.1.

4.3.1 Overview of code developed for MESA

The code development that was undertaken to adapt MESA for modelling TŻOs consisted of designing and writing the aforementioned hooks. The hooks themselves consist of a large amount of boilerplate code within which one redefines the relevant functions that

the hook in question is overwriting. I developed three main hooks for simulating T $\ddot{\text{Z}}$ O's in MESA, the exact physics which was implemented into each one being described in detail throughout the beginning of chapter 5. The first such hook was written in order to compute the accretion of material onto the central neutron-star core. A Eddington-limited accretion scheme (section 5.2) based on a similar prescription originally devised by [Cannon \(1993b\)](#). We determine if a particular calculation point corresponds to the base of the convective envelope (or is at least the closest such point) based on the local value of the convective velocity. The opacity at this point is used to determine the accretion rate on to the core. We also allow the user to select a custom, fixed accretion rate. As stated earlier in this section, the accretion luminosity was also computed by directly altering the free energy, and importing and using the auto-differentiation framework by [Jermyn et al. \(2023\)](#) to recompute all the needed thermodynamic derivatives self-consistently. In the second hook, we implemented the GR corrections we discuss in section 5.1.1. This involved first using the included pressure overwriting hook to alter the equation of hydrostatic equilibrium to the Tolman-Oppenheimer-Volkoff (TOV) equation. The other equations of stellar structure that needed to be altered as per the GR approximating prescription by [Ball et al. \(2012\)](#) were then implemented into a custom hook based on the inbuilt pressure equation hook.

The final hook that we constructed dealt with all of the new input and output needed for building the T $\ddot{\text{Z}}$ O models. This involved a range of custom input settings for the accretion rate, the accretion luminosity efficiency, the core radius and density and (custom, if needed) nuclear reaction networks.

Chapter 5

A new equilibrium model for supergiant-like Thorne-Żytkow Objects

Главное, делайте всё с
увлечением, это страшно
украшает жизнь

Vitally – do everything with
passion, this greatly enriches life.

Lev Landau (attrib.)

Driven by the need to investigate the envelope structure of TŻOs with modern, detailed models, we use the MESA stellar evolution code. [Paxton et al. \(2010\)](#) describes the initial code release, the microphysics, opacities, thermonuclear and weak reactions, nuclear reaction networks, mixing length theory and convective overshooting implementation, atmospheric boundary conditions, diffusion and gravitational settling, the structure and composition equations and how the solutions of these are converged. Machinery such as the time-step selection, meshing functions and adjustment, mass-loss and accretion prescriptions, sensitivity to resolution in space and time and a description of support for multi-threading is included. [Paxton et al. \(2013\)](#) describe updates to enable the code to model giant planets and perform astroseismological computations with the attached ADIPLS adiabatic pulsation code. They describe a numerical recasting of the Ledoux criterion, which impacts the way thermohaline mixing and semi-convection are computed. Diffusion of angular momentum as well as chemical abundances enable calculations of rotating-star models. A new treatment of radiation-dominated envelopes to allow the uninterrupted evolution of massive stars to core collapse is also explained. The coupled structure and composition equations are recast in a way that allows efficient computation on multi-core processors. The equation of state, opacity, nuclear reaction rates and atmospheric boundary conditions modules are also updated. Importantly for the consistent computation of the envelopes of our higher mass models, a new method to deal with superadiabaticity, MLT++ is included. MLT++ was developed in order to deal with superadiabaticity in the envelope of massive stars causing prohibitively small timesteps during evolution. It reduces the superadiabaticity

in some radiation dominated convective zones. At each model, MESA computes β_{\min} and λ_{\max} , the minimum gas pressure to total pressure ratio and maximum radiative luminosity to Eddington luminosity respectively. When β_{\min} is small and λ_{\max} is large the superadiabaticity $\delta_V \equiv \nabla_T - \nabla_{ad}$ is reduced by a factor of $\alpha_V f_V$, where f_V is user-definable and α_V is, at each timestep, a linear combination of itself at the previous timestep and $\widetilde{\alpha}_V(\lambda_{\max}, \beta_{\min})$, the running time averaged value of α_V at the largest λ_{\max} and smallest β_{\min} at each point. [Paxton et al. \(2015\)](#) further update the code to improve the modelling of the suppression of differential rotation in binary stars under the influence of tides, including also the effects of mass transfer. Greatly expanded, fully coupled nuclear reaction networks allow for the modelling of supernova progenitors. The GYRE non-adiabatic pulsation code and its coupling to the MESA code is described. [Paxton et al. \(2018a\)](#) largely make ease of use improvements, as well as a new more consistent approach to locating convective boundaries, together with more fleshed-out physics, including improved treatments of element diffusion, latent heat release, and blending of equations of state to allow for the more detailed modelling of white dwarfs. [Paxton et al. \(2019\)](#) update the code to include RSP, a tool that models non-linear stellar pulsations. Numerical energy conservation capabilities, including during mass changes are also improved. We use revision 15140 in this work to produce a number of such models. The MESA EOS is a blend of the OPAL ([Rogers & Nayfonov, 2002a](#)), SCVH ([Saumon et al., 1995a](#)), FreeEOS ([Irwin, 2004](#)), HELM ([Timmes & Sweaty, 2000a](#)) and PC ([Potekhin & Chabrier, 2010](#)) EsOS. Radiative opacities are primarily from OPAL ([Iglesias & Rogers, 1993; Rogers & Nayfonov, 2002a](#)), with low-temperature data from [Ferguson et al. \(2005a\)](#) and the high-temperature, Compton-scattering dominated regime by [Buchler & Yueh \(1976\)](#). Electron conduction opacities are from [Cassisi et al. \(2007\)](#). Nuclear reaction rates are from JINA REACLIB ([Cyburt et al., 2010](#)) plus additional tabulated weak reaction rates ([Fuller et al. 1985; Oda et al. 1994; Langanke & Martínez-Pinedo 2000](#)). Electron screening is included by the prescription of [Chugunov et al. \(2007\)](#). Thermal neutrino loss rates are from [Itoh et al. \(1996a\)](#).

5.1 Construction of Model Grid

Initially, we construct a small grid of static core models, models of Thorne-Żytkow Objects wherein the rate of accretion onto the neutron-star core is set to zero. In these models, we use the core relax subroutine in MESA, in combination with the ability to create and relax a pre-main-sequence (PMS) model, to create an object with an inert core. The core density is set in order to roughly represent the mean density of an astrophysical neutron star. As an example, the models discussed in section 5.2.1 have mean core densities of $10^{15} \text{ g cm}^{-3}$.

The radius of the core is then set from the initial core mass and core density. In the models discussed in section 5.2.1 we maintain a constant core radius, even as mass is accreted from the envelope on to the core, so mimicking an extremely stiff NS EOS.

Once the model envelope has been relaxed on to the core, we begin simulating the evolution of the envelope, using a range of nuclear reaction networks and prescriptions for the effects of General Relativity.

5.1.1 General Relativistic Corrections

As [Thorne & Zytkow \(1977\)](#), and others since, have done, we consider in a limited way the effects of GR on the model, in particular in relation to a correction that is applied to the gravitational potential. We correct the equation for hydrostatic equilibrium by implementing the Tolman-Oppenheimer-Volkoff (TOV) equation. We do this simply by replacing the hydrostatic balance equation

$$\frac{dP}{dr} = -\frac{Gm}{r^2}\rho \quad (5.1)$$

with

$$\frac{dP}{dr} = -\frac{Gm}{r^2}\rho \left(1 + \frac{P}{\rho c^2}\right) \left(1 + \frac{4\pi r^3 P}{mc^2}\right) \left(1 - \frac{2Gm}{rc^2}\right)^{-1}. \quad (5.2)$$

Naturally, this reduces to the Newtonian hydrostatic balance in the limiting case when envelope material is far from the neutron core. As discussed in section 5.2.1.3, the effect of this general relativistic correction, as well as similar corrections to the enthalpy and radiative gradient equations, is minimal with regards at least to the key structural component of the models. That is, the position of the base of the convective envelope as a function of core mass, envelope mass and time does not vary. This agrees with the work of [Cannon et al. \(1992\)](#) and [Cannon \(1993b\)](#), who showed that their Newtonian analysis of massive TŻO models reproduced what was found by [Thorne & Zytkow \(1977\)](#) and [Podsiadlowski et al. \(1995\)](#), where a set of such corrections were included. In fact TŻ's treatment of the gravitational and baryonic mass as separate variables, with additional structure equations solved to relate them, ensures that such effects could not have been neglected accidentally. Where necessary, we consider a more complete set of GR corrections to the models. These corrections are based on a reformulation of the standard equations of stellar structure (see [Eddington \(1920\)](#), [Schwarzschild \(1958\)](#), [Kippenhahn et al. \(2012\)](#), [Maeder & Meynet \(2012\)](#) and many others) by [Thorne \(1977\)](#). [Thorne \(1977\)](#) defines five auxiliary functions, the Redshift Correction Factor \mathcal{R} , the Volume Correction Factor \mathcal{V} , the gravitational acceleration correction Factor \mathcal{G} , the Energy Correction Factor \mathcal{E} and the Enthalpy Correction factor \mathcal{H}

by

$$\mathcal{R} \equiv \exp(\phi/c^2), \quad (5.3)$$

$$\mathcal{V} \equiv (1 - 2GM_{\text{tr}}/c^2r)^{-\frac{1}{2}}, \quad (5.4)$$

$$\mathcal{G} \equiv \frac{M_{\text{tr}} + 4\pi r^3 P/c^2}{M_r}, \quad (5.5)$$

$$\mathcal{E} \equiv 1 + (\Pi - B)/c^2 = \rho_t/\rho, \quad (5.6)$$

and

$$\mathcal{H} \equiv 1 + (\Pi - B + P/\rho)/c^2, \quad (5.7)$$

where ϕ is the gravitational potential, M_{tr} is the total mass¹¹ inside the radius r , M_r is the rest mass interior to the radius r and B is the binding energy of nuclei, relative to the proton rest mass m_p per unit rest mass, such that

$$B \equiv \left(1 - \sum_i \frac{m_i X_i}{m_p A_i}\right) c^2, \quad (5.8)$$

where m_i is the mass of species i , in the ground state, m_p is the mass of the proton, A_i is the number of baryons in the species i and c is the speed of light. Furthermore, Π is the relativistic specific internal energy, the total mass-energy of a sample of stellar material per unit rest mass of that sample less the nuclear binding energy of the sample

$$\Pi \equiv \frac{U_{m,\text{tot}}}{M_r} - B - c^2. \quad (5.9)$$

Finally, ρ_t is the mass density of non-gravitational mass-energy,

$$\rho_t \equiv \rho (1 - B/c^2 + \Pi/c^2). \quad (5.10)$$

We note that these relativistic correction factors are dimensionless, and reduce to unity in the Newtonian limit, as required. This allows the Schwarzschild metric to be written in terms of the correction factors as

$$ds^2 = -\mathcal{R}^2 c^2 dt^2 + \mathcal{V}^2 dr^2 + r^2 (d\theta^2 + \sin^2 \theta d\varphi^2), \quad (5.11)$$

¹¹This is the total mass in the General Relativistic context, which includes the rest mass and equivalent energy-mass from the nuclear binding energy, gravitational potential energy and contributions from the total internal energy of the stellar material.

where t is the time coordinate chosen so that $\partial/\partial t$ at constant r is the time-translation Killing vector and t the proper time at infinity. These relativistic corrections allow the standard equations of stellar structure to be rewritten in Lagrangian form (Thorne, 1977)

$$\frac{\partial r}{\partial M_r} = (4\pi r^2 \rho \mathcal{V})^{-1}, \quad (5.12)$$

$$\frac{\partial M_{tr}}{\partial M_r} = \frac{\mathcal{E}}{\mathcal{V}}, \frac{\partial \phi}{\partial M_r} = \frac{GM_r}{4\pi r^4 \rho} \mathcal{G} \mathcal{V}, \quad (5.13)$$

$$\frac{1}{\mathcal{R}^2} \frac{\partial (L_r \mathcal{R}^2)}{\partial M_r} = \varepsilon_{\text{nuc}} - \frac{1}{\mathcal{R}} \frac{\partial \Pi}{\partial t} + \frac{P}{\rho^2} \frac{1}{\mathcal{R}} \frac{\partial \rho}{\partial t}, \quad (5.14)$$

and

$$\frac{\partial P}{\partial M_r} = -\frac{GM_r}{4\pi r^4} \mathcal{G} \mathcal{H} \mathcal{V}, \quad (5.15)$$

where ε_{nuc} is the energy generation per unit rest mass, accounting for neutrino losses. Equation (5.15) is completely equivalent to the TOV equation for hydrostatic equilibrium (equation 5.2).

The equations of energy transport by radiative and convective processes can be translated into a GR framework in much the same way but we have not considered them here because of the difficulty in practically implementing them. This is because an extra difference equation, equation (5.13) must be implemented to close the system. In a code, such as MESA, that has been optimised to solve its specific set of differential equations, this is a non-trivial engineering issue. Instead, we use the approach of Ball et al. (2012), to simplify the correction factors by setting $M_{tr} = (\mathcal{E}/\mathcal{V})M_r$ and $\phi = 1/2c^2 \ln|1 - 2Gm/c^2r|$. These assumptions remove the need for the extra differential equation (5.13) and allow the correction factors to be reformulated and implemented as

$$\mathcal{R} = \sqrt{1 - \frac{2Gm}{c^2 r}} = \mathcal{V}^{-1}, \quad (5.16)$$

$$\mathcal{G} = 1 + \frac{4\pi r^3 P}{mc^2}, \quad (5.17)$$

$$\mathcal{E} = 1 + \frac{\Pi - B}{c^2}, \quad (5.18)$$

and

$$\mathcal{H} = \mathcal{E} + \frac{P}{\rho c^2}. \quad (5.19)$$

This results in a less exact set of corrections but Ball et al. (2012) showed that this and also the inclusion of post-Newtonian effects in general, were unimportant in their study of quasi-stars. We likewise show (in section 5.2.1.3) that these effects are negligible in the

majority of our scenarios and sufficiently small in others that this formulation of the GR corrections is perfectly sufficient for our purposes.

5.1.2 The Core-Envelope Interface Artifice

We first discuss the concept and later the past and current implementation of an artifice, originally described by TŻ, but discussed in more detail by Cannon et al. (1992), that smoothly connects the (unmodelled or modelled) neutron core of a TŻOs with the envelope. As implemented by Cannon et al. (1992), the artifice serves to connect a neutron core equation of state, in this particular case 2.5a of Cooperstein (1988), to the envelope equation of state (Eggleton et al., 1973). The device alters the envelope equation of state by increasing the effective mass of the electron to m'_e which varies with the electron degeneracy parameter ψ , itself a function of the electron chemical potential, η that the Skye (Jermyn et al., 2021) equation of state provides so that for $\psi < 0$ or $k = 1$ this produces a purely electron equation of state, while for sufficiently large ψ and $k = m_n/m_e$ it produces the equation of state for a degenerate neutron gas of Oppenheimer & Volkoff (1939). This is then connected directly to the core equation of state.

Cannon states that, because this is in the region where $\rho > 10^6 \text{ g cm}^{-3}$, inverse β decay is actually active in this region and so provides a physical motivation for the artifice. However inverse β decay



is unlikely to be particularly significant at these temperatures and densities (see Oralbaev et al. 2016 and Vogel & Beacom 1999 for details). So we do not agree that this is a good physical motivation for this device. Alternatively if we consider instead that the neutronizing process that the artifice represents is electron capture,



the process that produces neutrons in the formation of a proto-neutron star during core collapse (Langanke & Martínez-Pinedo, 2014), then an issue arises because the density (and temperature) in the region in which the artifice is applied is insufficiently large for this process to contribute significantly to the neutron number density (Fu et al., 2008; Ravlić et al., 2020; Langanke et al., 2021).

However Cannon mentions that, even if this region is to be considered completely artificial, given that it is very narrow (in both mass and radius), as well as the fact that, other than gravitationally, the neutron core should be essentially decoupled from the envelope (TŻ), that

this is a reasonable simplification. While we consider this likely to be the case for a static model, the models of Cannon et al. (1992) and Cannon (1993b), in which the neutron core is allowed to grow over time by this artifice, are potentially problematic because they comment that the core can grow up to the TOV mass limit, and that nuclear ash metamorphoses into neutrons via the artifice and compresses down on to the core, causing radial contraction of the core because the Cooperstein (1988) equation of state requires that this material does actually transmute into neutrons at some point.

While, given the previous justifications, and good correspondence between individual evolutionary timesteps in the models by Cannon and the static envelope models of TŻ (with the exception of models that were produced in or evolved through the TŻO mass-gap), it is reasonable that, even if unphysical, the nature of the artifice is unlikely to affect a given model in a problematic manner. The fact that, during an evolutionary sequence, the neutron core itself grows in terms of mass requires some mechanism to convert electron degenerate material into neutron degenerate material. This requires electron capture to occur in a region where it is energetically inaccessible. Hence, in order to explore this possible issue, as well as to better understand the effects of the artifice on the qualitative structure of the models themselves, we, in section 5.2.1 initially construct a series of fiducial models where the presence of a neutron star core is emulated by means of central boundary conditions alone, with no artifice employed, accepting the likely occurrence of a steep discontinuity in the effective equation of state as we transition across the core-envelope interface.

5.2 Fiducial Relaxed Core Models

In MESA terminology, we produce a small, demonstrative grid of models with a `relax_core` approach. We use an initial inlist with the `create_pre_main_sequence_model` setting, to create a PMS model of the desired mass and metallicity. All of our models have a metallicity of 0.02.

The `relax_core` routine has been used to create inert rocky cores in the study of giant planets (Paxton et al., 2013) and to create inert neutron stars with fixed temperatures at the surface for the modelling of X-ray bursts in their atmospheres (Potekhin, 2014; Paxton et al., 2010, 2013). We select a core mass, to which the central boundary condition of the model is relaxed, a core average density, which is used to determine a core radius to which the central radius boundary condition is relaxed, and a core mass-averaged energy generation rate, which sets a core luminosity, to which the central luminosity boundary condition is relaxed. While studies of neutron star atmospheres typically make use of a fixed temperature at the surface of the neutron star, we do not wish to impose such a condition and furthermore,

based on the results of [Thorne & Żytkow \(1977\)](#), [Cannon et al. \(1992\)](#) and others, we would expect the neutron core to be isothermal regardless. We assume, as TŻ and others assumed, no neutrino runaway, and hence no temperature inversion in the core. Therefore, we allow the envelope relaxation to determine consistently the temperature at the core-envelope interface. Because the core is expected to be isothermal with the core-envelope interface, we choose $L_c = 0$ to be our central luminosity boundary condition. While we expect negligible heat transport in to and out of the core, we allow material to contract on to the core, releasing energy purely through the release of gravitational potential energy, using the prescription for the energy released from the contraction of stellar material. In the following models, we choose an initial core mass of $1 M_\odot$ and an initial core mean density of $10^{15} \text{ g cm}^{-3}$, and so a core radius of 7.8 km. For our purposes, this is an acceptable model of a neutron star that is not informed by any particular neutron star equation of state. If desired, it is trivial to use the mass-radius relationship for any neutron star EOS under consideration. Also, for these models, when we consider inflow and accretion of envelope material on to the neutron core, we do not adjust the radius of the core, so making the assumption of an infinitely stiff equation of state for our neutron core.

Once our model of an unprocessed envelope surrounding an inert neutron core has converged it is allowed to evolve for approximately 100 converged timesteps to ensure that thermal equilibrium has been established. During this process, we utilize a *hook*, an additional user-written set of routines that supplement or override the default MESA routines, into the `cgrav` routine to include our GR corrections. For this set of models, we include only the correction to the equation of hydrostatic equilibrium, as discussed in section 5.1.1, by replacing the standard hydrostatic balance equation ([Paxton et al., 2010](#)) with the TOV form from equation (5.2). We then switch on chemical evolution, by the `basic.net` nuclear reaction network. This is automatically switched over to `co_burn.net` upon the onset of carbon burning (if present) and finally to `approx21.net` if more advanced burning stages become important. An additional *hook* is used to manage accretion on to the neutron core. We take the luminosity balance argument presented by [Cannon et al. \(1992\)](#) to compute a required accretion rate, in order to generate the expected luminosity owing to the release of gravitational potential energy¹² at the knee. The luminosity at the knee is assumed to be

¹²The release of specific gravitational potential energy due to contraction or expansion is implemented into the MESA code as ([Paxton et al., 2010](#))

$$\varepsilon_{\text{grav}} = -T \frac{ds}{dt} = -TC_P \left[(1 - \nabla_{\text{ad}}\chi_T) \frac{d\ln T}{d\ln t} - \nabla_{\text{ad}}\chi_P \frac{d\ln \rho}{dt} \right].$$

We show in appendix (A.1) that the [Thorne \(1977\)](#) formulation of the non-neutrino related terms in the luminosity equation reduce to this form in the Newtonian limit.

according to equation (10) of [Cannon et al. 1992](#)):

$$L_{\text{knee}} = L_r^{\text{crit}} \equiv 4\pi c G M_r \kappa^{-1}. \quad (5.22)$$

[Cannon et al. \(1992\)](#) state that in their models the luminosity at the knee is dominated by the accretion luminosity L_{grav} (equation 11 of [Cannon et al. 1992](#)) so that

$$L_{\text{grav}} = \frac{GM_c \dot{M}}{R_c}. \quad (5.23)$$

Because we are not modelling the core as an intrinsic part of the star, but enforce boundary conditions at the surface of the neutron star, we use this prescription to compute \dot{M} . We do not set a fixed accretion luminosity at the knee, checking as part of convergence testing that the luminosity at the knee does in fact agree with equation 5.22 using the MESA prescription for thermal energy release from contracting stellar material to connect the two. Additionally we do not fix the location of the knee in either radius or mass. Instead, we use a *hook* into the MESA routines, a routine that used the Cannon luminosity balance approach, to compute \dot{M} at each timestep and alter the mass central boundary condition to the previous timestep M_c plus the $\dot{M}dt$, where dt is the new model timestep. We have assumed an infinitely stiff neutron star equation of state so we do not alter the central radius boundary condition. Gravitational potential energy release is computed as the $\varepsilon_{\text{grav}}$ term in the MESA implementation ([Paxton et al. 2010](#) equation 12) as the envelope reestablishes thermal equilibrium during the subsequent solver iterations.

We then allow MESA to continue to evolve the model until the timestep control suggests an overly small timestep or until the model fails to find a converged solution after 200 model restarts¹³. Any model with more than five restarts required to continue was re-run, to ensure that no numerical effects were being introduced.

5.2.1 Fiducial Relaxed Core Model Results

A small grid of example models was produced with this prescription. In all models the initial mass of the neutron core was $1 M_\odot$, and the total mass of the models was varied from $5 M_\odot$ to $50 M_\odot$. Given our relatively simple prescription for accretion onto the core, it is not surprising that it was, in general, not possible to construct such models with total star masses below around $4.8 M_\odot$. In the models of TŻ, [Biehle \(1994\)](#), [Cannon et al. \(1992\)](#)

¹³We find, however, that no model is reliably able to recover from more than around 5 restarts, or once dt falls below around 10^{-4} yr.

Table 5.1 Position of the knee above the core in radius, mass contained interior to the knee, and density and temperature at the knee for the final hydrostatically consistent model timestep as a function of the initial model total mass M_{tot} .

$M_{\text{tot}} / M_{\odot}$	$M_k - M_c / 10^{-7} M_{\odot}$	$R_k - R_c / 10^7 \text{ cm}$	$\rho_k / 10^2 \text{ g cm}^{-3}$	$T_k / 10^8 \text{ K}$
5	2.1873	5.4106	0.9739	3.8864
6	2.9812	7.1502	1.3779	3.9487
7	4.1972	6.8396	1.6073	4.1485
8	3.7546	7.6909	1.6332	4.0415
9	5.0967	6.8836	1.7721	4.2428
10	6.5802	7.2025	1.9471	4.2992
11	7.0708	8.8260	1.8360	4.0231
12	7.9714	8.9050	1.7447	3.9636
13	8.6691	7.1905	2.3136	4.4904
14	7.9995	6.2516	3.9273	5.1375
15	10.1331	9.1161	1.9262	4.0390
16	10.2394	10.3422	1.9356	3.9147
17	9.4335	6.3930	5.5483	5.3699
19	10.8250	5.1843	3.2593	5.3086
20	11.3388	4.3359	6.0105	6.4525
25	16.0811	9.7558	2.5034	4.2358
30	19.7545	10.0979	2.4114	4.1618
35	21.8984	10.6767	2.6635	4.2037
40	24.8789	12.1505	2.5332	4.0160
50	30.5749	13.9121	2.4821	3.8588

and Cannon (1993b), the dominant luminosity contribution to the luminosity of low total mass TŻO models is from gravitational potential energy released at the halo from material accreting on to the neutron core. We do not expect models where accretion is the main energy source to be necessarily consistent because our treatment of that process is simplified.

5.2.1.1 Surface Properties

Our models show similar surface properties to those of TŻ. That is, $\log_{10} R/R_{\odot}$ of around 3 and $\log_{10} T_{\text{eff}}/\text{K}$ of around 3.5. Indeed, with the exception of their surface abundances, our models should, to an observer, look externally analogous to those of TŻ owing to similar radii,

¹⁴The Humphreys-Davidson (HD) limit occurs at a constant luminosity in this region of the HR diagram, and is hence presented as such. At higher T_{eff} , the HD limit kinks upward to higher luminosities, as the more complete ionization of, primarily, iron, renders more of the transitions associated with inducing such envelope instabilities inactive.

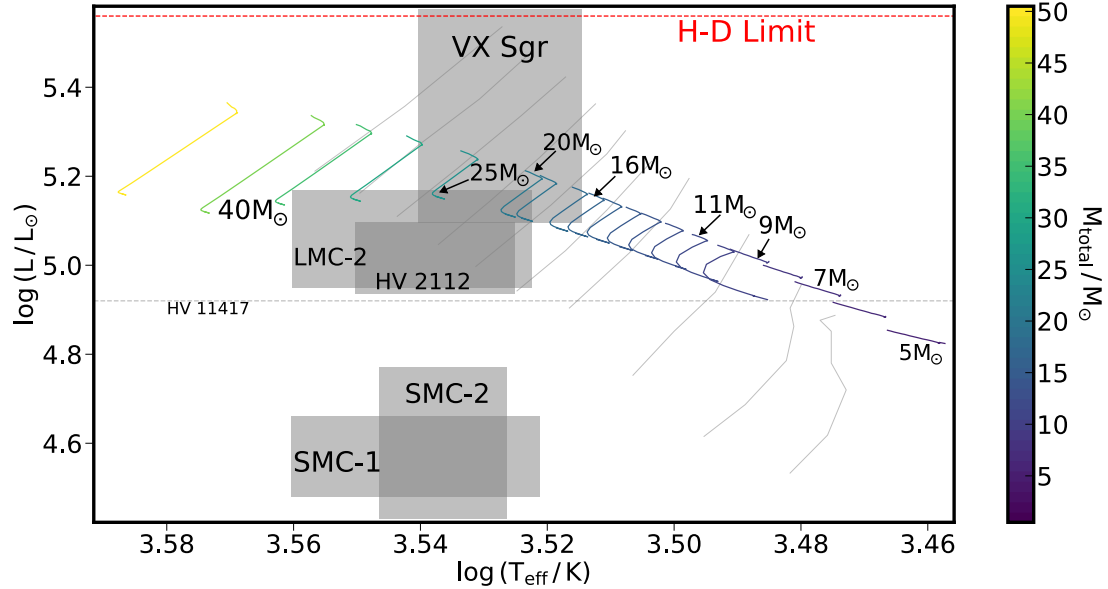


Figure 5.1 Hertzsprung-Russell (HR) diagrams for each of our fiducial models, as a function of their total masses. Each model is as described in Table 5.1, and all begin with a $1 M_{\odot}$ neutron core. In all cases, we find the models evolving to lower effective temperatures and higher luminosities. We show in grey the evolutionary tracks of the TŻO models produced by Cannon et al. (1992). In our models, as in those by Cannon et al., models evolve in time always toward higher luminosities. Unlike Cannon, our models begin with a sharp movement toward higher effective temperatures as the envelope relaxes to thermal equilibrium. We then observe evolution along tracks near exactly parallel to the Cannon et al. (1992) models, to higher luminosities and lower effective temperatures. Finally, our models, unlike those of Cannon et al., hook sharply to the left, to higher effective temperatures and luminosities, as they deplete their nuclear fuel. We show also the constraint on luminosity for TŻO candidate HV 11417 as computed by Beasor et al. (2018), as the horizontal dashed grey line, as well as the Humphreys-Davidson (HD) Limit (Humphreys & Davidson, 1979) as the horizontal¹⁴dashed red line. Additionally presented are observational constraints on a number of TŻO, (s)AGB and other highly variable stars. Showed for illustrative purposes are constraints for VX Sagitarii (Tabernero et al., 2021), a representative sample of SMC and LMC highly variable stars from O’Grady et al. (2020); O’Grady et al. (2023), and constraints on the most promising TŻO candidate to date, HV 2112 (Levesque et al., 2014; Tout et al., 2014; O’Grady et al., 2023).

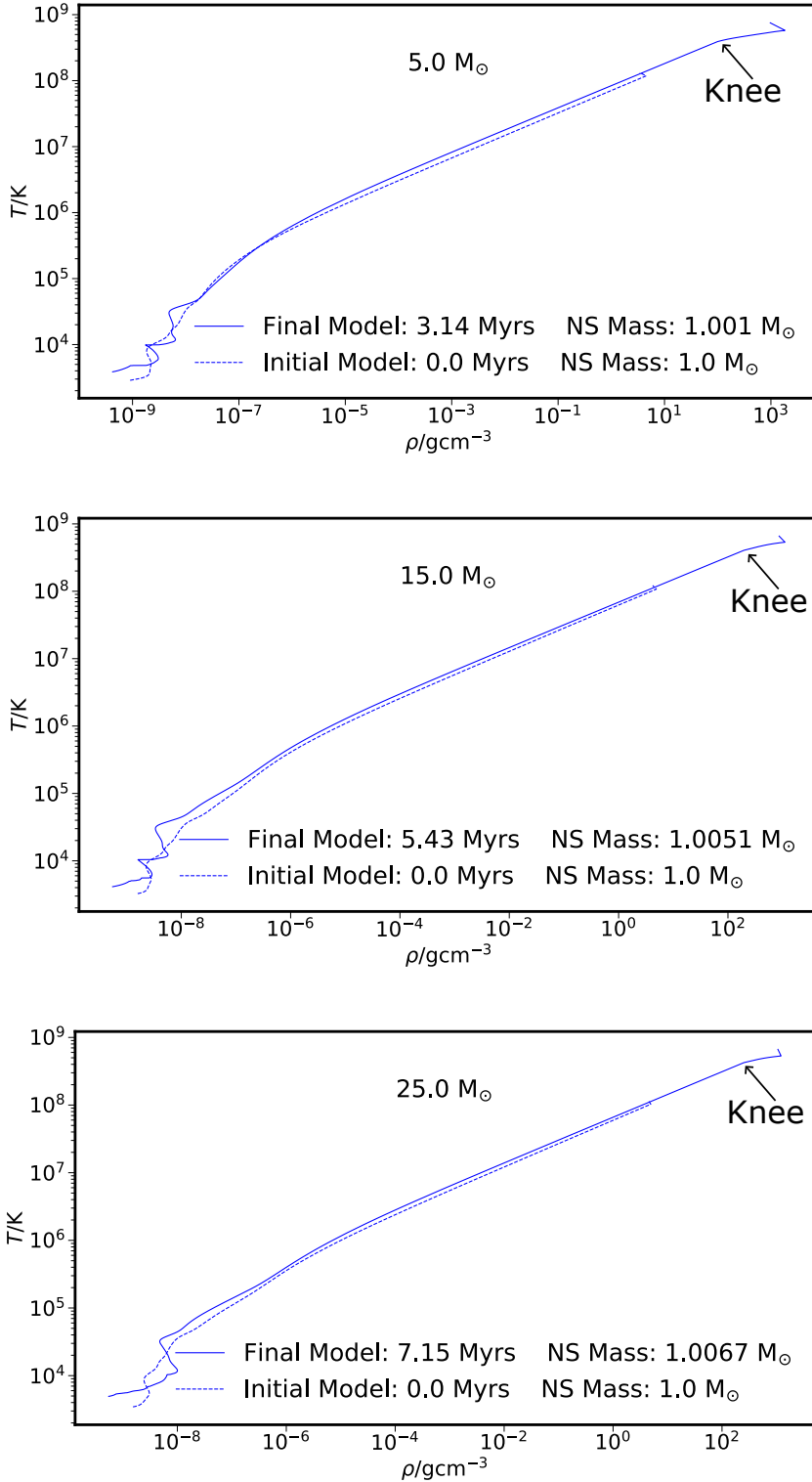


Figure 5.2 Temperature T as a function of density ρ for a selection of fiducial models. With effective accretion rates around $\dot{M} \approx 10^{-10} M_{\odot} \text{ yr}^{-1}$, the neutron core does not grow substantially over the lifetime of these models. While these $\rho - T$ profiles differ dramatically from those of TŻ, we note the presence of inflection points, corresponding to the base of the convective envelope — the knee. In all our models the knee and the isothermal region interior to the knee are at much lower densities and temperatures than in the models of TŻ.

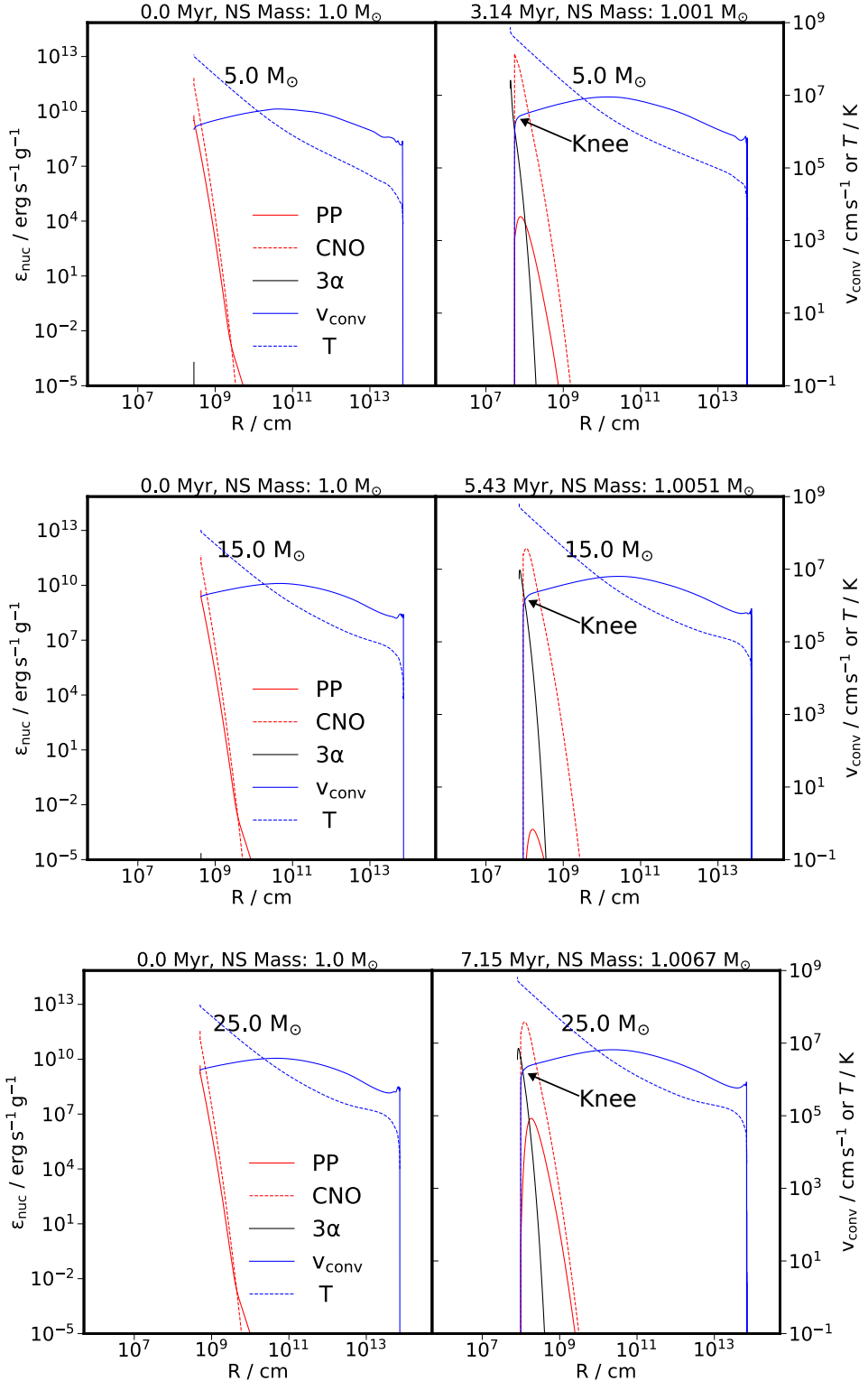


Figure 5.3 Temperature and convective structure of the fiducial models. The convective (turbulent) velocity is used as a measure of the stability of a region of the model to convection. We show also the energy generation rates of the PP chains, the (cool) CNO burning and the 3α process. We observe the formation of a knee, or base of the convective envelope, as the models evolve and the formation of distinct, but close together, both in radius and mass, hydrogen and helium burning shells. The hydrogen burning shell coincides with the base of the convective envelope, while the peak of helium burning occurs just interior to the knee.

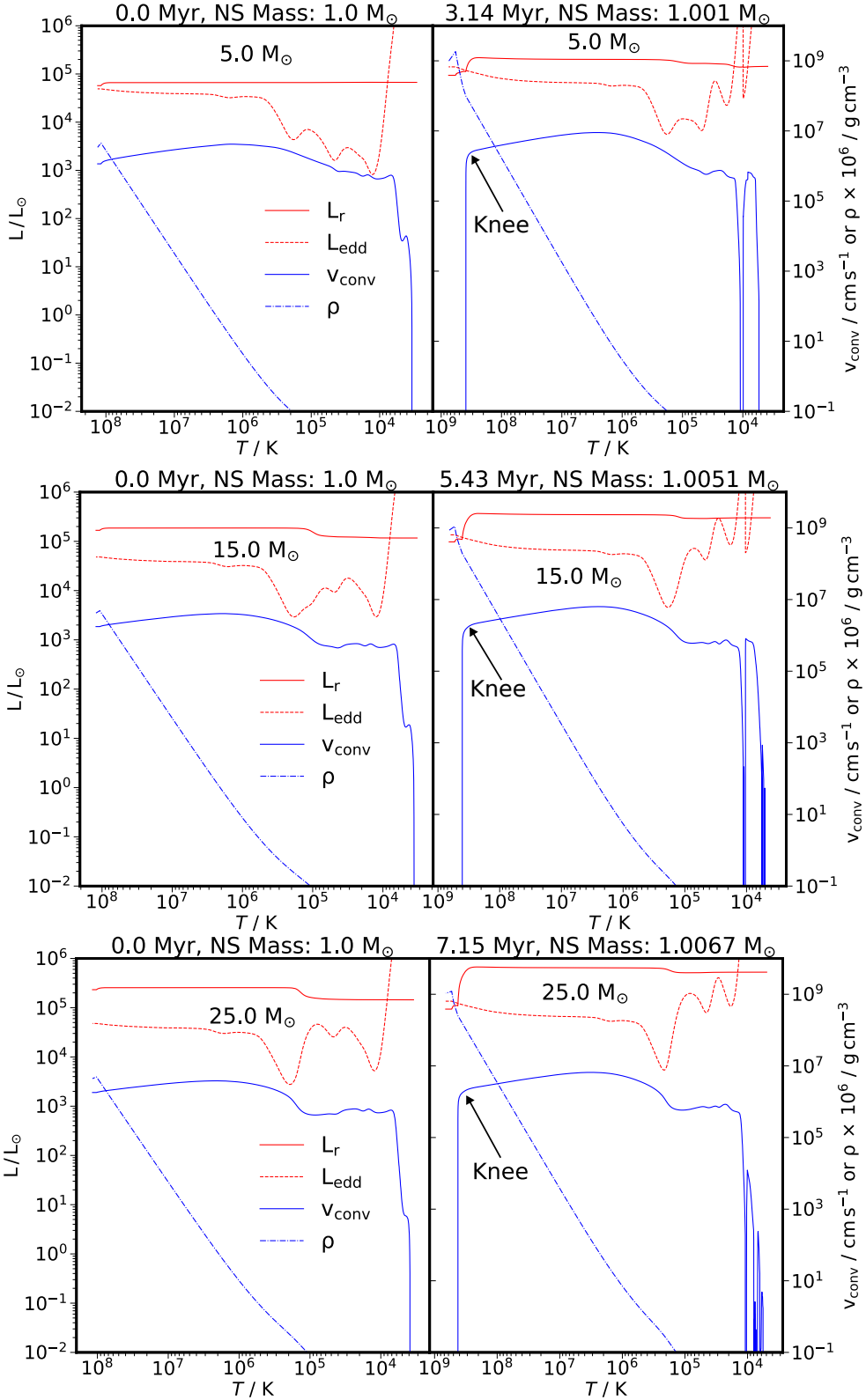


Figure 5.4 A comparison of the luminosity with the critical Eddington luminosity. As in Fig. 5.3, we plot the convective velocity and, here, the density of the stellar material as a function of the temperature. At the low-temperature end of our plots, we observe the expected ionisation features of our extended envelopes. As we shall see in Fig. 5.6, despite the profound differences in the structures between our models and theirs, we reach the critical luminosity at the knee, as did Cannon et al. (1992).

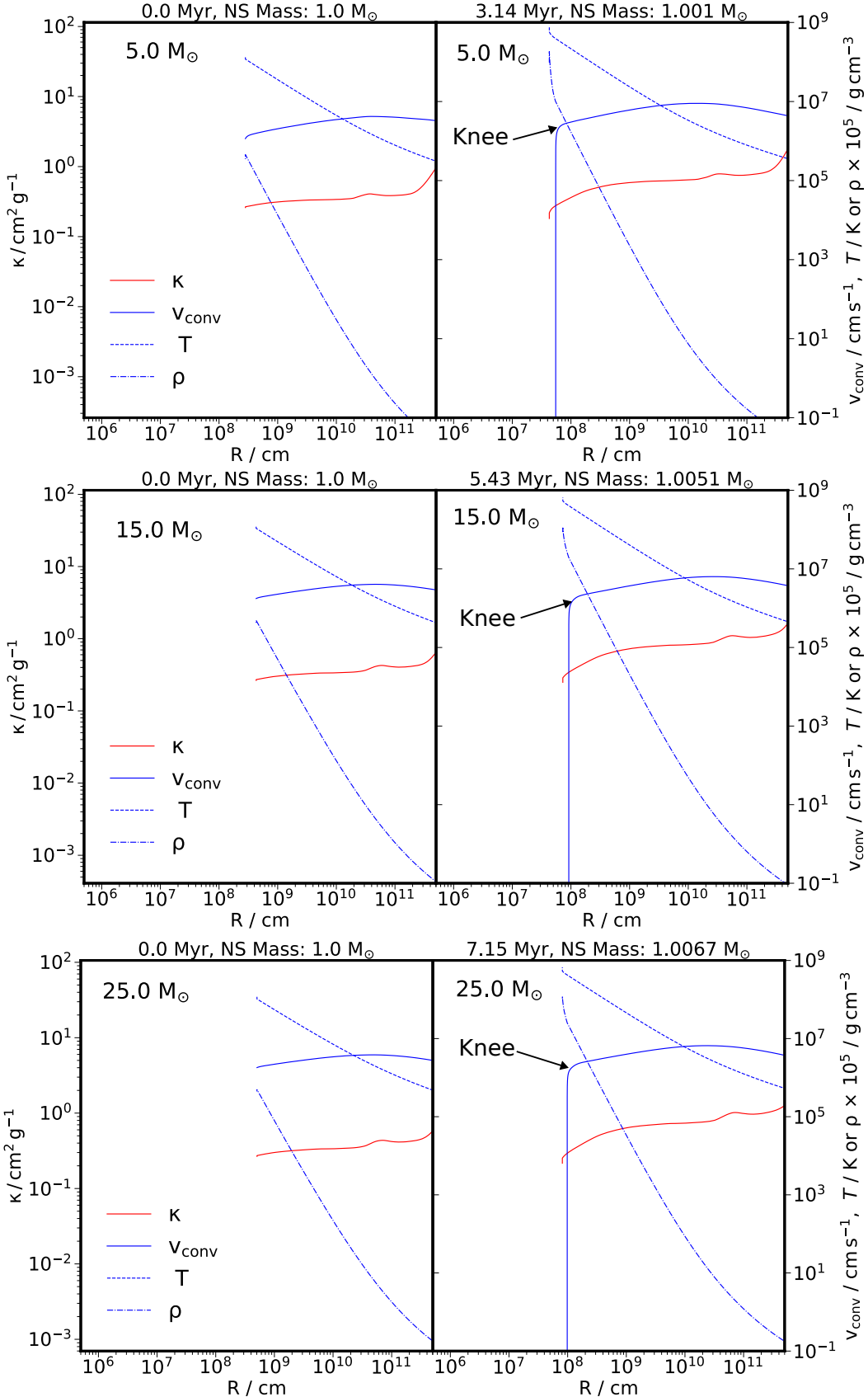


Figure 5.5 The opacity of stellar material as a function of the stellar radius. As before, the convective velocity, temperature and density are shown. We see that the opacity falls steeply below the knee. This differs from TŻ's models, where the temperature interior to the knee (in high-mass models) is sufficiently high to allow the effective creation of $e^- - e^+$ pairs, resulting in a dramatic increase in the opacity (Hu et al. 2019 & Lightman et al. 1987).

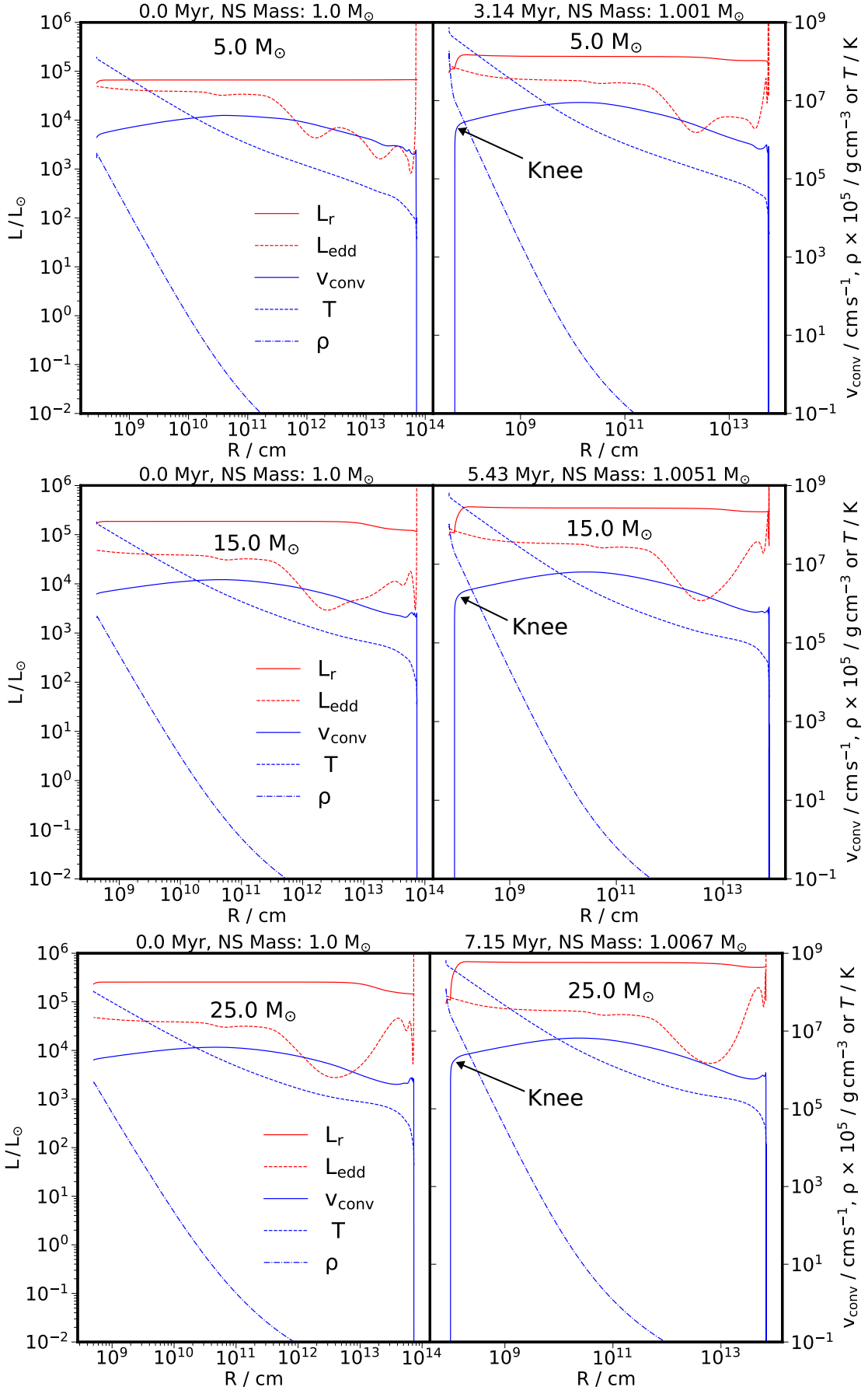


Figure 5.6 Luminosity compared with critical luminosity as a function of radius for our fiducial models, as per Fig. 5.4.

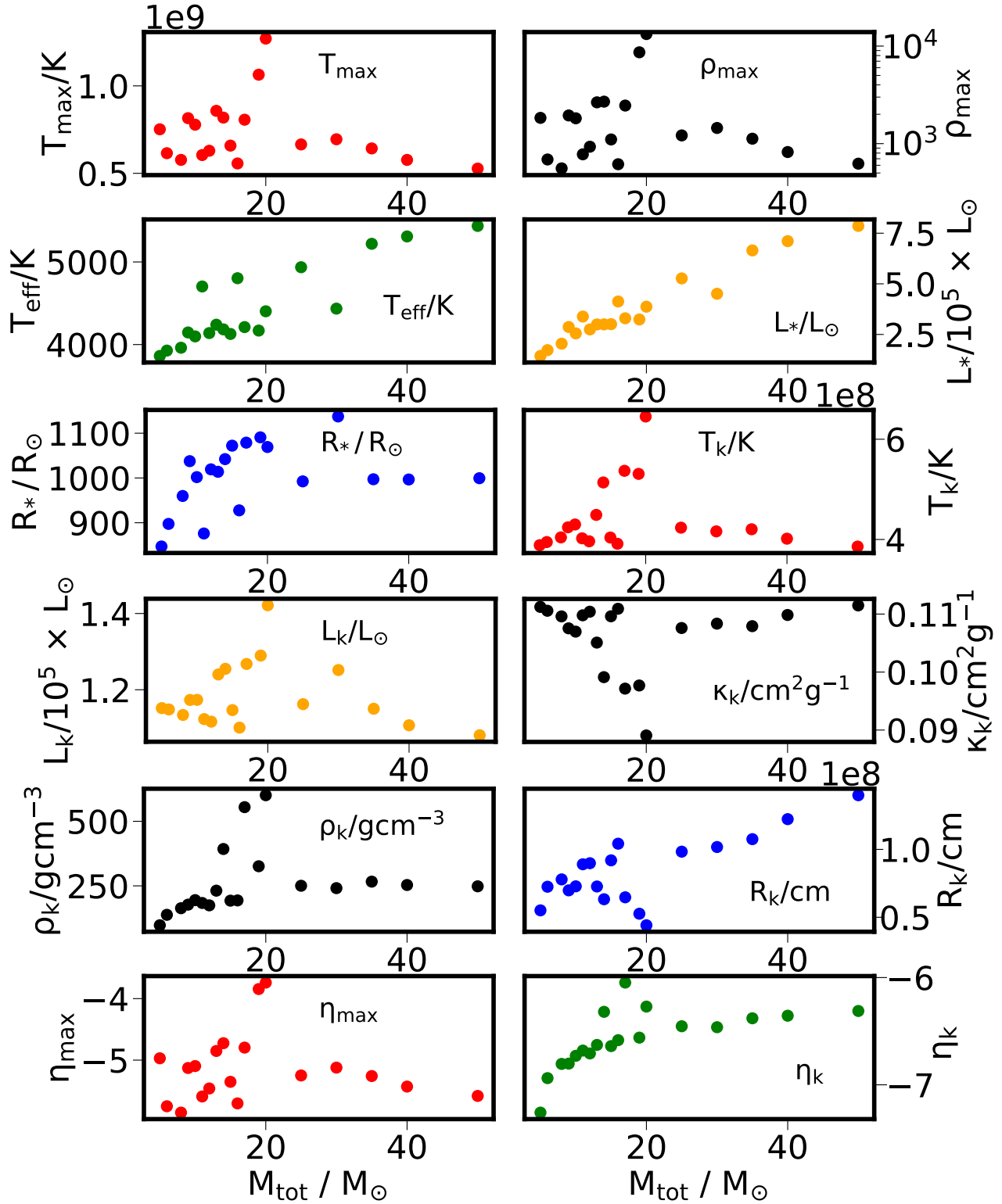


Figure 5.7 (Continued on the following page.)

Figure 5.7 Summary of a sample of our fiducial models with accretion as described by [Cannon et al. \(1992\)](#). Each plot shows the variation of the labelled physical property as a function of the total mass of the model in question. The top row of the plot shows the maximum temperatures and densities reached in the models (in all cases in the radiative halo that lies below the base of the convective envelope) and the photosphere radius. The second row shows the effective temperature, the photospheric luminosity and temperature at the knee, the base of the convective envelope. The third row shows the density at the knee, as well as the radial distance from the centre of the neutron core to the knee and the luminosity at the knee. The final row shows the electron degeneracy parameter η defined as to be the ratio of the electron chemical potential to $k_B T$ at the point in the model (deep in the halo at the point just exterior to the density inversion at the helium burning shell) where it reaches a maximum and at the knee. We also plot the opacity, κ , at the knee. We note the very small range of opacities realised at the point at which convection ceases becomes, in general, more opaque as total stellar mass increases but this curve is almost entirely flat so the opacity is, for all intents and purposes, constant.

luminosities, effective temperatures *etc*. Figure 5.1 shows a series of evolutionary tracks of our models, on an HR diagram. As stated, we include a series of similar evolutionary tracks for models as computed by [Cannon et al. \(1992\)](#), depicted here as the light grey tracks. Additionally, we include a series of constraints from observational studies of TŻO and (s)AGB candidates, as well as a dashed horizontal line showing the HD limit, above which we should not expect to see objects with RSG-like envelopes ([Higgins & Vink, 2020](#)). With the exception of sharp, blueward hooks at the start and end of our evolutionary tracks, we observe that the majority of our models follow tracks that are parallel to those of [Cannon et al. \(1992\)](#), always evolving to larger luminosities. Our models undergo their initial blueward hooks on the KH timescale, as their envelopes relax, and the core begins to accrete. At the end of the TŻO sequence, the second blueward hook occurs once the nuclear fuel begins to deplete in the convective envelope. This is not unlike the blueward movement observed in yellow supergiants (YSGs)/post-red supergiants (RSGs) ([Gordon & Humphreys, 2019](#)). Otherwise, at higher and higher total masses, our models resemble more and more closely the corresponding Cannon et al. model of the same total mass. The differences here in maximum luminosity of the models can be most readily attributed to the differences in α_{mlt} . [Cannon \(1993b\)](#) found differences between the evolutionary tracks of their supergiant TŻO models and those of TŻ, and attributed them to the fact that TŻ used $\alpha_{\text{mlt}} = 1$, while they used $\alpha_{\text{mlt}} = 1.5$. As has been widely investigated, as by, [Joyce & Tayar \(2023\)](#), for example, their use of a smaller value of α_{mlt} leads to less luminous models for a given total mass. The calibration of a value for α_{mlt} , as is done for a standard solar model, for example, is not trivial for models of TŻOs. Indeed, calibrated values for α_{mlt} are likely non-universal

amongst ordinary stellar populations (Pinheiro & Fernandes, 2013), and as such we would not expect a solar calibrated value for α_{mlt} to be suitable for all, or even for any model for a TŻO population. To this end, Cannon (1993b) derived a luminosity relationship for a range of TŻO masses, from around $4 M_\odot$ to around $60 M_\odot$ as,

$$L \propto \alpha_{\text{mlt}}^2 m_c^{1/2} m_{\text{total}}^{2/3}, \quad (5.24)$$

where m_c is the core mass, and m_{total} is the total mass of the star. In addition, our fiducial models are constructed with an initial core mass of $1 M_\odot$, while Cannon et al. (1992); Cannon (1993b) generally computed models with initial core masses of $1.4 M_\odot$, further explaining the differences between our series of models. Given that our models internally resemble the supergiant-like TŻO solution from Cannon et al. (1992) it is expected that the evolution tracks should more closely resemble those of Cannon et al. towards higher total mass. Hence, at the lower end of masses, where Cannon et al. (1992) found structures corresponding to the giant-like structures described by TŻ, and we instead find supergiant-like solutions all the way down to minimum masses (for a $1 M_\odot$ core) of around $4.8 M_\odot$, our evolutionary tracks diverge most significantly. Having included constraints on some candidate TŻOs in figure 5.1, we can see that our sequence of models is inconsistent with some SMC (s)AGB candidates such as SMC-1 and SMC-2 (O’Grady et al., 2020), but potentially consistent with a particularly luminous LMC (s)AGB/TŻO candidate, LMC-2. Making use of different values of α_{mlt} allows some of these model tracks to be consistent with constraints on HV 2112, a promising TŻO candidate (Levesque et al., 2014; Tout et al., 2014; O’Grady et al., 2023). A wide number of models are additionally consistent with constraints on the highly variable VX Sgr (Tabernero et al., 2021). As required for the stability of their RSG-like envelope configurations, all of our model tracks remain below the HD limit.

5.2.1.2 Internal Structure Properties

We note that there are very significant differences between our models and those of TŻ, Cannon, Biehle, Barkov et al. (2001) and even similar models of extended envelopes on other compact objects such as strange stars, such as those modelled by Hajyan et al. (1998). In Fig. 5.3, we show the temperature, density, energy generation and convective structure with radius in our models. It is in the internal structure of the models that we encounter considerable differences. The base of the convective envelope, the knee, is at a much greater radius, with significantly more mass ($\log_{10} M/M_\odot \approx -7$ in contrast to -10 or less in the TŻ models) interior to the knee. The temperature and density, and consequently the electron degeneracy and plasma interaction parameter (see Jermyn et al. 2021 for details of the Skye equation

of state)¹⁵, are all considerably smaller than in those models. Our envelope is successfully supported by considerably larger and less intensely burning hydrogen and helium shells, though the qualitative structure of hydrogen burning above and helium burning at and below the base of the convective envelope is reminiscent of the models of TŻ. Unlike those of Cannon and TŻ, our models generate much less luminosity in the release of gravitational potential energy from matter inflowing on to the core. We do find this energy is released in a considerably larger (in terms of mass and radius) region than the halo found in the models of TŻ and our halo equivalent region is not isothermal but rather increases in temperature significantly as we approach the core. In particular, once helium burning is established, exclusively below the base of convective envelope in our models, a density inversion is set up as we approach the core, as shown in figure 5.2. Naturally, this raises a possible concern with regards to dynamical stability. TŻ investigated the possibility of dynamical instabilities in the envelope as well as thermal instabilities in the radiative burning shells below the knee. [Kippenhahn & Thomas \(1983\)](#) described the existence of a vibrational instability in a radiative burning shell, which, given the properties of our halo region, could be here applicable. This leads to a mild oscillation that results in small scale movement of the knee with time, because its location is determined primarily by the conditions in the halo. The stability of, specifically, a thin helium burning source in a high-mass star is discussed by [Dennis \(1971\)](#) and [Yoon et al. \(2004\)](#). We consider a simple sanity check on the stability of our helium burning region using equations (11) and (12) by [Dennis \(1971\)](#)

$$\Delta r/r < f(\beta)|Q|^{-1}, \quad (5.25)$$

where

$$f(\beta) = \frac{\beta(32/3 - 8\beta - \beta^2)}{32/3 - 16\beta + 6\beta^2}, \quad (5.26)$$

where $\beta = P_{\text{gas}}/P$ and Q is defined as by [Schwarzschild & Härm \(1965\)](#)

$$Q = \left(\left(\frac{\delta r}{r} \right)_2 \Big/ \left(\frac{\delta P}{P} \right)_2 - \left(\frac{\delta r}{r} \right)_1 \Big/ \left(\frac{\delta P}{P} \right)_1 \right)^{-1} \quad (5.27)$$

and $Q = -6$ is suggested as reasonable, for the radial thickness limit for an unstable burning shell. Taking our $15M_\odot$ fiducial model as an example, we find $\Delta r/r \lesssim 0.1838$, making the

¹⁵ Skye, while blended ([Paxton et al. 2010](#)) with OPAL ([Rogers & Nayfonov, 2002b](#)), SCVH ([Saumon et al., 1995b](#)), FreeEOS ([Irwin, 2012](#)) and HELM ([Timmes & Swesty, 2000b](#)) by default in MESA, composes the entire equation of state blend in the region near the base of the convective envelope, and is only blended with other equations of state further out in the envelope, where the Skye assumption of complete ionisation begins to break down.

most conservative assumption that the largest β in the helium burning region characterises the entire region. Our helium burning region is orders of magnitude thinner than this criterion. So ameliorating somewhat our concerns about this feature. This (otherwise) stable helium burning region, with a mild, small amplitude oscillation is as described for helium burning regions by [Stothers & Wen Chin \(1973\)](#).

The density inversion seen in figures 5.2, 5.3, 5.4 and 5.5 also presents a possible issue regarding the physical nature of the accretion on to the core, in particular with regard to the assumption of isothermal behaviour between the core and the core envelope interface. In the work of Cannon, material accreting on to the core is neutronized by means of an artifice that transmutes a non-hydrogen abundance (helium in models of [Cannon et al. 1992](#) and carbon in those of [Cannon 1993b](#)) at high electron chemical potential into neutrons by increasing the effective electron mass logarithmically with the effective electron degeneracy parameter, as originally envisioned by TŻ. This tool smoothly but artificially connects the envelope with the core. Hence the material that inflows on to the core is neutronized and its density is artificially increased to match a neutron gas-like equation of state ([Oppenheimer & Volkoff, 1939](#)). In these models, we do not employ such an artifice, implicitly making the assumption that effective neutronization of stellar material only occurs after material has already been accreted by the neutron star, as did [Yakovlev et al. \(2005\)](#). Given that the equation of state for the degenerate electron gas is not stiff, this is not itself a fully consistent assumption, as it would require no interaction between the core and the envelope, disallowing any accretion. To check the validity of our assumption then, we make use of the hydrodynamic features of the MESA code. These allow the computation of an acceleration term in the hydrostatic balance equation by assigning a cell-centre velocity to each computational cell. Running a selection of our models with this feature enabled results in cell centre velocities at the knee of no larger than around $10^{-2} \text{ cm s}^{-1}$, suggesting that accretion is indeed slow enough to use this assumption, as well as validating the use of a purely hydrostatic approach to compute models of TŻOs.

5.2.1.3 Effects of GR corrections

We have recomputed our grid of fiducial models with our general relativistic hydrostatic equilibrium correction as described in section 5.1.1 inactivated, and another grid in which the GR corrections to enthalpy are included alongside the TOV equilibrium correction. We find there is essentially no difference between any two equivalent models between these grids, with a maximum GR TOV correction of around 1.006. This is as expected, given the relatively low densities and pressures in these models. This is in good agreement with, for

example, the results of [Biehle \(1991\)](#) and [Eich et al. \(1989\)](#), where their considerably denser and centrally condensed models are likewise not significantly affected by the inclusion or exclusion of these corrections.

5.2.1.4 Fiducial model results in the UV plane

We now make use of the $U - V$ plane to investigate the structure and thermodynamic consistency of our envelope solutions. The $U - V$ plane is a tool used to investigate the structure of stellar models that could be reasonably approximated by (at least) two distinct regions, most usually for studying stars with a convective core, and a radiative envelope or with an isothermal core and a radiative envelope ([Schwarzschild, 1958](#); [Hayashi et al., 1962](#)). This *characteristic plane of stellar evolution* is defined by the homology invariants U and V

$$U \equiv 4\pi r^3 \frac{\rho}{M_r} = \frac{\partial \ln M_r}{\partial \ln r}, \quad (5.28)$$

$$V \equiv GM_r \frac{\rho}{rP} = \frac{-\partial \ln P}{\partial \ln r}, \quad (5.29)$$

where M_r is the mass enclosed within a sphere of radius r . Given these definitions, we naturally select boundary conditions at the centre and surface of an arbitrary stellar model as,

$$U = 3, V = 0, \quad (5.30)$$

and

$$U = 0, V \rightarrow \infty \quad (5.31)$$

respectively. A sample of our fiducial models (with Cannon et al. accretion rates) is shown on the $U - V$ plane in Fig. 5.8. Discounting the deviation from standard polytropic behaviour near the surface, we observe both solutions with and without loops. A standard analysis of the problem of giganterythrotropism (GET), the tendency for stars to evolve from main-sequence dwarfs to centrally condensed giants with extended envelopes ([Eggleton & Cannon, 1991](#)), notes that solutions for dwarf-like stellar configurations and those of giant-like stellar configurations show none, and one loop in the characteristic ($U - V$) plane of stellar evolution respectively([Sugimoto & Nomoto, 1980](#); [Yahil & van den Horn, 1985](#); [Sugimoto & Fujimoto, 2000](#); [Stancliffe et al., 2009](#)). Fig. 4 of [Sugimoto & Fujimoto \(2000\)](#) provides a good reference example for the differing topologies of a dwarf-like (a HB star) and a giant-like (a RG star) solution. Therefore, strictly speaking about the models presented, only the 7 and $9M_\odot$ initial total mass models admit giant-like solutions. This sort of analysis is of

course inhibited because the structure at and around the knee in these models is not a simple composition of polytropes and, as noted by [Sugimoto & Fujimoto \(2000\)](#), an envelope inflated to a large radius need not admit a giant-like topology in the characteristic plane, provided the $U - V$ curve of such a solution approaches $D \equiv 2U + V - 4 = 0$. This condition is satisfied here, as shown in the bottom panel of Fig. 5.8, corresponding to the divergence in D^{-1} that occurs at the knee in all models. In a formal polytropic derivation (cf. [Fujimoto 1982](#)) full divergence is required here, naturally. Because our computed models are not idealised polytopes D^{-1} peaks at around a few times 10^3 instead.

5.2.2 Fiducial Relaxed Core Models: Sensitivity to central radius boundary condition

Because we have produced a series of models which differ substantially from those of TZ, it is prudent to investigate the sensitivity of our model structures to the central boundary conditions we use to emulate the presence of a neutron core. In particular, we vary the radius boundary condition, which serves as an effective hard boundary. Because the mass central boundary condition influences only ϕ and, given that our initial assumption of isothermal behaviour at the interface enforces an $L_c = 0$ luminosity BC, we elect to vary R_c , across a wide range, the vast majority of which does not represent realistic neutron star equations of state. We note that, at the higher end, we may enter the infall cavity parameter space for Bondi-Hoyle quasi-stars, as described by [Ball et al. \(2012\)](#).

As discussed, the lack of an artifice to connect the envelope to the core, we are constrained to have a hard boundary condition. A strong dependence of the qualitative structure of the models on the boundary conditions would then pose a considerable problem, because we could then construct an arbitrary burning and convective structure at the base of the envelope. Hence, we select a range of radius boundary conditions $R \in \{0.01, 0.1, 1, 10, 50, 100, 500, 1000\}$ km kilometers. In fig. 5.10, we show the convective, luminosity and burning structure of each of these models, as in fig. 5.6. Outside of the models with $R_c = 500$ km and 1000 km, some of our most unphysical models, in terms of compliance with published neutron star equations of state, varying the radius boundary condition serves only to move the location of the base of the convective envelope, and consequently the location of the peak energy generation from hydrogen and helium burning, the point where the local luminosity crosses the critical luminosity and the point at which the opacity falls off are moved outwards (inwards) in the same manner.

In table 5.2 we show radial distance between the knee and the core and the mass interior to the knee in each of these considered models as a function of the radius boundary condition

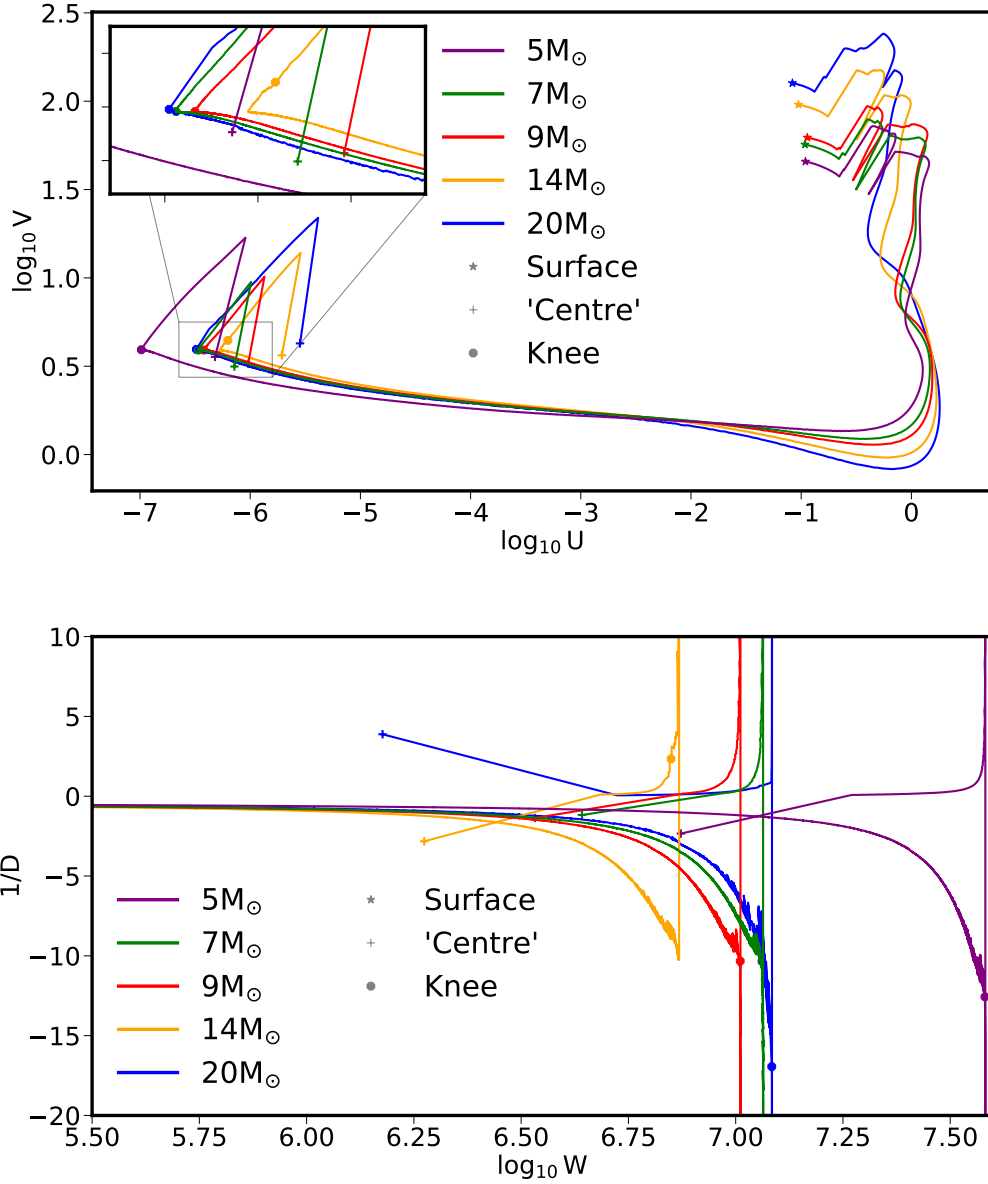


Figure 5.8 *Top*: A sample of relaxed core fiducial model structures on the characteristic $(U - V)$ plane (Schwarzschild, 1958; Kippenhahn et al., 2012). Each model has a Cannon et al. accretion rate and an initial core mass of $1 M_\odot$. The $U - V$ homology invariants are defined as $U \equiv \frac{d \ln m}{d \ln r}$ and $V \equiv -\frac{d \ln P}{d \ln r}$. The position of the photosphere (*), knee (octagon) and ‘centre’ (+) – the centre most computation cells are labelled with the corresponding symbols. The strong deviation from loaded polytropic behaviour near the surface is a result of the shallow envelope ionization zones, as expected for extended, cool envelopes (Lopes & Gough, 2001; Everson et al., 2020). The inset shows in greater detail the region around the knee where several models closely overlap.

Bottom: The sample of fiducial models plotted on the characteristic differential $(W - D)$ plane of stellar structure (Sugimoto & Fujimoto, 2000). The $W - D$ variables are computed as the derivatives of the $U - V$ homology invariants, such that $W \equiv V/U$ and $D \equiv (2U + V - 4)$.

Table 5.2 Position of the knee above the core in radius and mass contained interior to the knee for the final hydrostatically consistent model timestep as a function of the radius boundary condition R_c .

R_c /km	$M_k - M_c$ $/10^{-7} M_\odot$	$R_k - R_c$ $/10^7 \text{cm}$
1×10^{-2}	9.1865	8.2587
1×10^{-1}	8.0273	5.5059
1×10^0	8.9667	9.3613
1×10^1	9.1062	8.5482
5×10^1	8.9428	9.5705
1×10^2	9.1553	7.5749
5×10^2	49.1838	0.5663
1×10^3	900.3960	2.3626

employed. As discussed in section 5.2.1, our $R_c = 10\text{km}$ model, a physically motivated BC, shows extremely marked difference to previously computed models of TŻOs. However, importantly for consistency, the models presented are largely insensitive to the radius boundary condition within a surprisingly large range from the canonical 10km model.

Fig. 5.12 (a) demonstrates that, with the exception of the extremely large core radius models, which as shown in figs 5.10 and 5.9, have a $\rho - T$ burning and convective structure much more akin to that of a red (super)giant, the maximum temperature and density, both of which occur at some point interior to the base of the convective envelope, are largely unaffected by our choice of R_c and hence our selection of a neutron star equation of state¹⁶. This is inconsistent with the model structure found by TŻ but is a simple consequence of our structure. The region interior to the knee in our fiducial models is at low densities ($\rho < 10\text{ g cm}^{-3}$) and at high temperatures ($T > 10^8\text{ K}$), acting much like an ideal *mantle-like* region in a red-giant structure (see [Miller Bertolami 2022](#) for a comprehensive discussion). This serves to effectively decouple (barring gravity) the knee from the core itself. Again, we see an analogue to the decoupled nature of the core as in TŻ’s models, but with a much more extended (in the Eulerian and Lagrangian sense) configuration of knee, halo and burning shells.

In the model with the largest radius boundary condition, we note an (approximately) isothermal region interior to the core (see fig. 5.9), with densities peaking at the central boundary at around 10^6 g cm^{-3} . The knee also occurs interior to the knee in all of the other models. Investigating this model in further detail in fig.5.11 we note, as mentioned, that

¹⁶Indeed, insensitive even to the selection of a highly unphysical such equation of state.

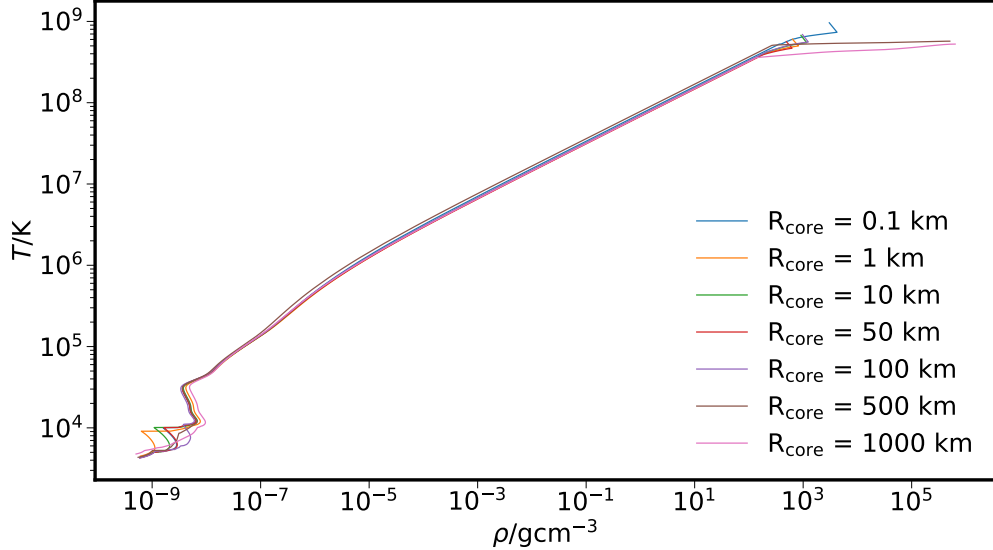


Figure 5.9 A density–temperature structure plot for a selection of our models used to investigate the effects of a varying central radius boundary condition. All models have an initial core mass of $1 M_{\odot}$, $L_c = 0$ and a total mass of $17 M_{\odot}$. Models with core radii of 0.1, 1, 10, 50, 100, 500 and 1000 km are presented here.

the knee occurs at a smaller radius and at higher density than in the other models and that no hydrogen burning occurs interior to the base of the convective envelope, while helium burning energy generation peaks strongly just interior to the base of the convective envelope, where it proceeds under degenerate and near isothermal conditions. This, and the effect of a more massive core, and hence a steeper gravitational gradient ($\frac{dg}{dm}$), at later times owing to our accretion rate prescription is responsible for the differences between this model and our other fiducial models. Although this extended central radial boundary condition is similar, specifically, to that used for the modelling of quasi-stars as by Ball et al. (2012), the much lower total stellar mass and low accretion rate results in a structure that is different from this and the models of Begelman et al. (2008) and Schleicher et al. (2013).

5.2.3 Fiducial Relaxed Core Models with extended hydrogen burning network

Before progressing to further studies based on our fiducial models or attempting to construct a TŻ-like neutronizing artifice, it behooves us to investigate these current fiducial relaxed core models with a different set of nuclear reactions under consideration. We make use of the `h_burn.net` nuclear reaction network (Paxton et al., 2015), which includes the pp chains,

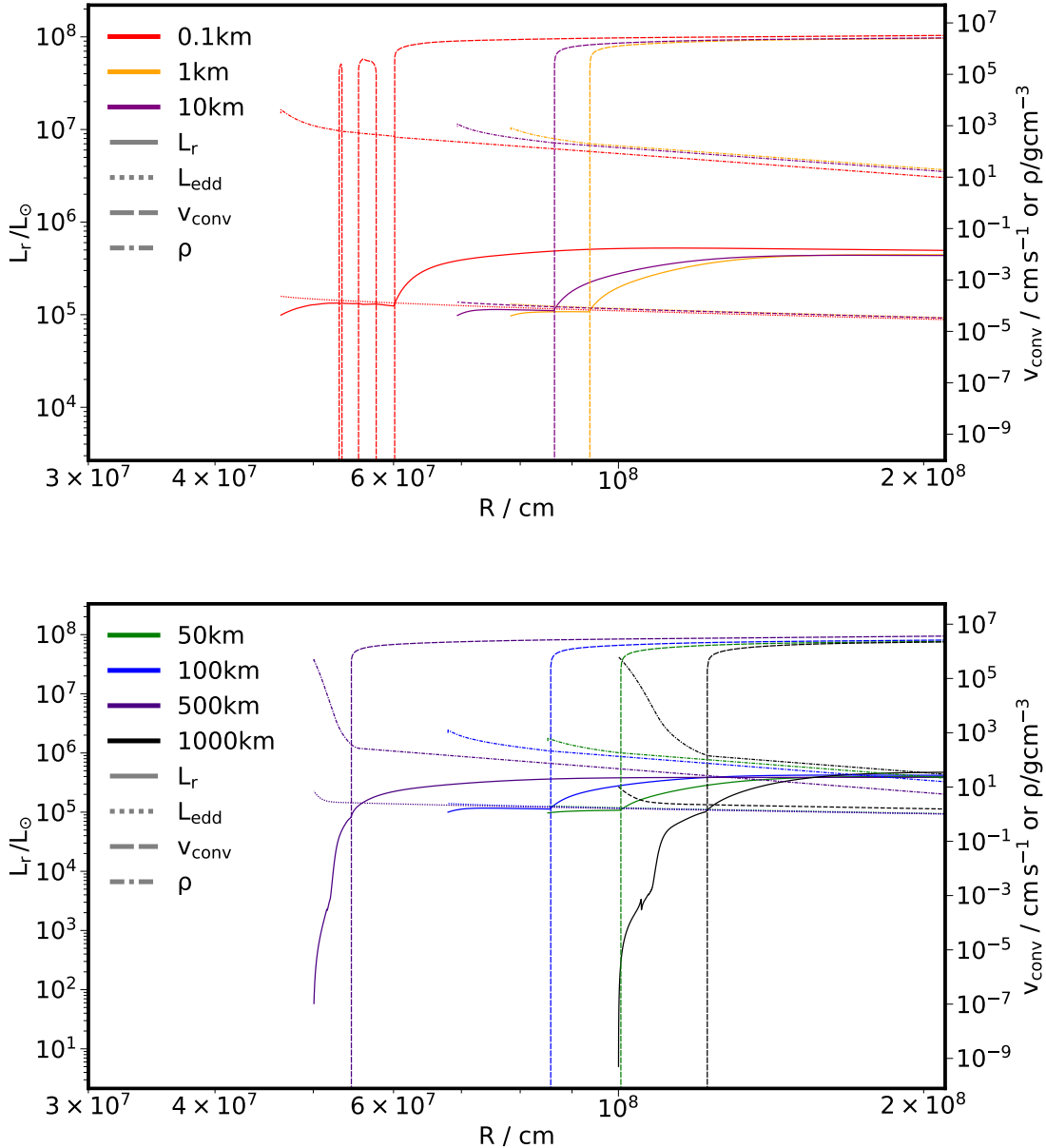


Figure 5.10 The luminosity, density and convective structure as a function of radius for the radius boundary condition investigation models. These are constructed as in fig. 5.6. We note that for the models with R_c close to that of the physically motivated boundary condition, although moving the location of the knee in radius, have near identical convective, luminosity and density structures to the $R_c = 10$ km model.

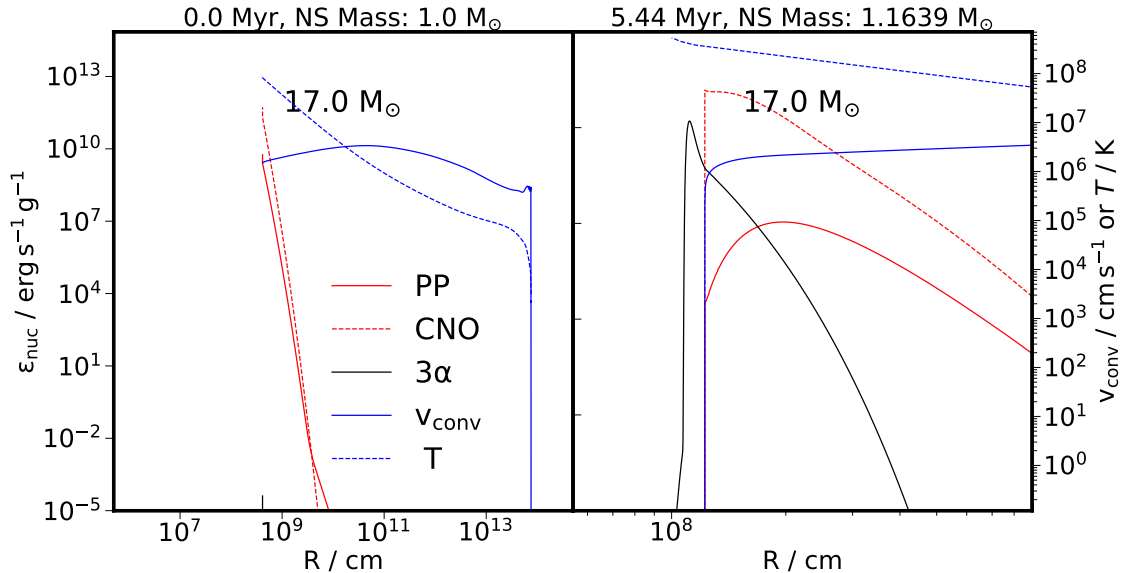


Figure 5.11 Plot as fig. 5.3 for the $R_c = 1000$ km boundary condition test model. We note the presence of the sharp knee at a radius interior to that of all of our other fiducial models. All hydrogen burning occurs exclusively in the convective region, peaking at the knee itself and stopping entirely interior to this point. While 3α burning occurs within the convection envelope, the peak of helium burning occurs under degenerate conditions at much higher densities, explaining the considerable structural differences, notably the isothermal nature of the region interior to the knee, between this and the other models. We note that the accretion rate in this model is large, peaking above $5 \times 10^{-8} M_\odot \text{yr}^{-1}$, as a result of the prescription of Cannon et al. (1992) that we have used. This produces a more massive core at later times, resulting in a larger gravitational potential and, consequently, a steeper pressure and density gradient, contributing further to the divergence between the structure of this and the other models.

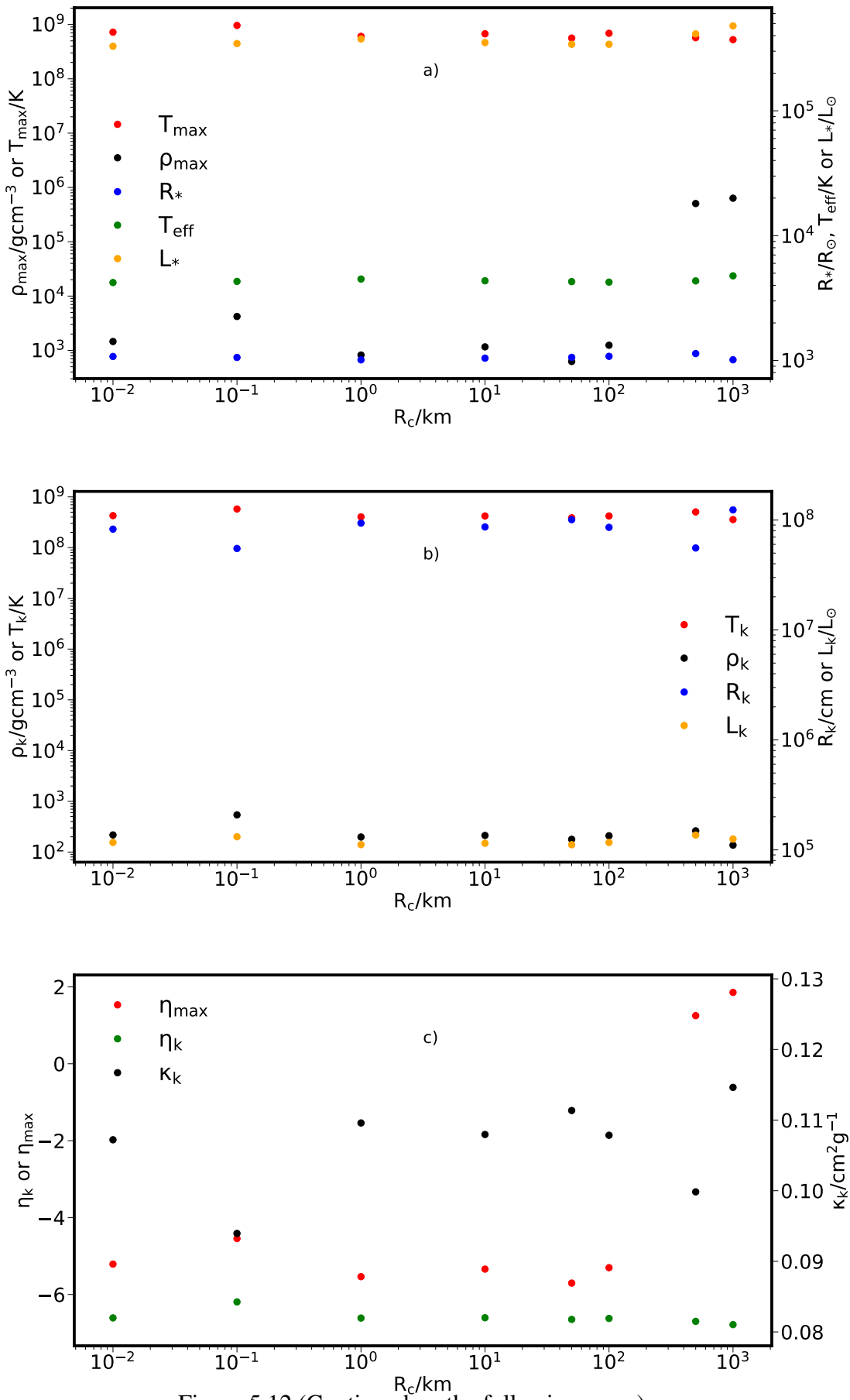


Figure 5.12 (Continued on the following page.)

Figure 5.12 Plots, a), b) and c) from top to bottom, demonstrating the effect of varying radius boundary conditions on our fiducial models. Each of these models is initialized with a total mass of $17 M_{\odot}$ and initial $M_c = 1 M_{\odot}$. We use the prescription by Cannon et al. (1992) as discussed in section 5.2.1. Radius boundary conditions are then set at 0.01, 0.1, 1, 10, 50, 100, 500 and 1000 km.

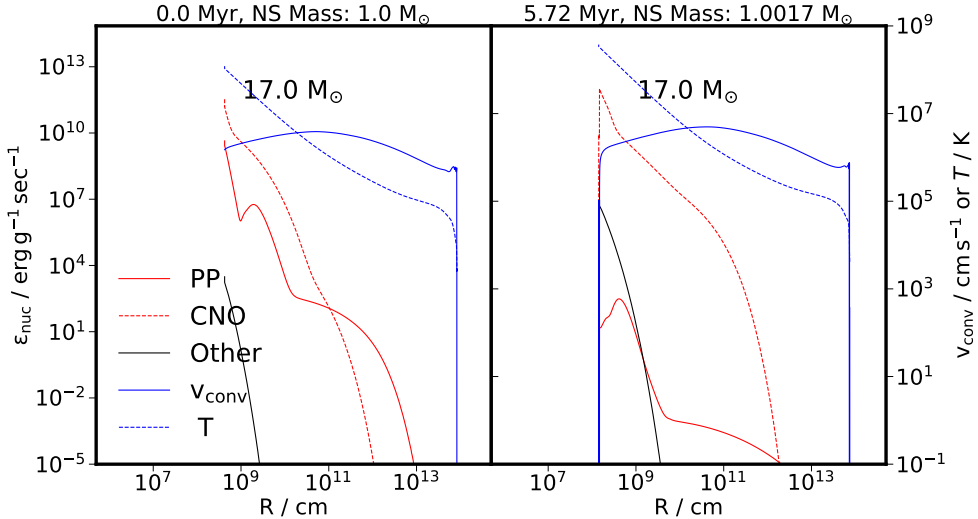
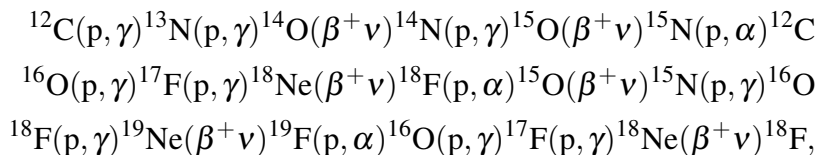


Figure 5.13 Plot as fig.5.3, with all non-PP chain and cold CNO cycle hydrogen burning shown combined, in solid black, for a $17 M_{\odot}$ model with an initial $M_c = 1 M_{\odot}$. We use, as before, the accretion rate of Cannon et al. (1992). Using the `h_burn.net` nuclear reaction network, we prevent the ignition of helium burning below the knee as in our other fiducial models. We note that, even with the complete suppression of all nuclear energy generation below the knee, as per the Cannon et al. case A models (see section 2.2.2 for details), that the qualitative structure of our models remains largely unchanged, with hydrogen burning occurring exclusively in the convective envelope.

cool and hot (β limited) CNO cycles as well as the Ne–Na and Mg–Al hydrogen burning cycles (Clayton, 1983; Goerres et al., 1989; Izzard et al., 2007). For a complete discussion of these processes see Wiescher et al. (2010). In short summary, this network includes the hot CN, NO (which short-circuits across the third cold CNO cycle) and ^{18}F -seeded chain of reactions as:



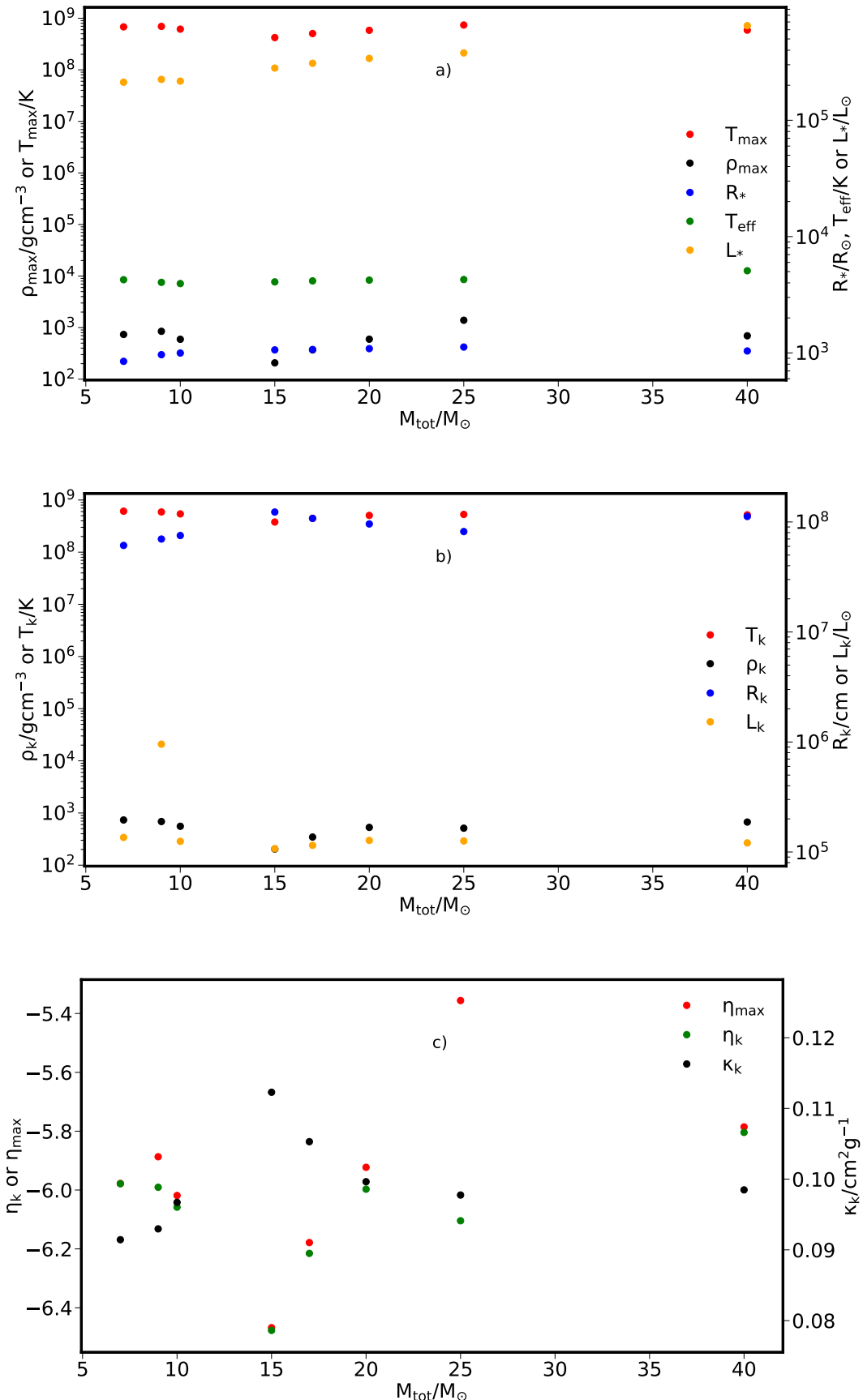


Figure 5.14 Plots, a), b) and c) from top to bottom, summarizing a sample of the grid of models computed with a modified h_burn.net nuclear reaction network.

respectively. We then modify this reaction network to remove all helium burning reactions. This allows us to investigate, in an energetically consistent sense, the extended region of hydrogen burning space that may be accessed in our models. Removing helium burning in these models follows the approach of Cannon et al. (1992) who assumed helium rich material is accreted on to the neutron core and is converted to neutrons via their core-envelope interface artifice.

5.2.4 Fiducial Relaxed Core Models with varying accretion rate

Having considered the effect of the central radius boundary condition on the structure of our fiducial models in section 5.2.2, we now consider the effect of the the accretion rate itself on the structure of the models. Given that varying the radius of the core, which would alter the accretion rates computed under the Cannon et al. accretion prescription did not alter the qualitative structure of our models, other than for the most extremely unphysical scenarios considered, we should investigate how sensitive the qualitative model structure is to the accretion rate itself. We consider a model with a total mass of $17 M_{\odot}$ and an initial M_c and R_c of $1 M_{\odot}$ and 10km respectively. We then evolve a selection of models with accretion rates fixed at $10^{-12}, 10^{-9}, 10^{-8}, 10^{-7}, 10^{-6}$ and $0 M_{\odot}\text{yr}^{-1}$. We also compute a model with the Cannon et al. accretion prescription and a model with 100 times the Cannon et al. rate. While this prescription causes a small variation of the accretion rate with time, the time-averaged accretion rate is close to $10^{-10} M_{\odot}\text{yr}^{-1}$ in the former case and $10^{-8} M_{\odot}\text{yr}^{-1}$ in the latter.

In fig. 5.15 (a), we present the effect of the core accretion rate on the surface observables, R_* , T_{eff} and L_* when the envelope has attained hydrostatic equilibrium. We also show the temperature and density at the point where each of them attain their maxima. We note that the envelope is somewhat inflated for the static model and more considerably inflated at very high accretion rates of $10^{-6} M_{\odot}\text{yr}^{-1}$. This is not unexpected given the additional gravitational potential energy being deposited at the base of the convective envelope. The other surface observables are not as sensitive to the accretion rate with the effective temperature largely unaffected, again with the exception of the inflated $\dot{M} = 10^{-6} M_{\odot}\text{yr}^{-1}$ model, which, as expected, is cooler. The total luminosity is therefore largest for the model ($\dot{M} = 10^{-7} M_{\odot}\text{yr}^{-1}$) with the largest T_{eff} . The maximum temperature and density in all models occur at radii interior to the base of the convective envelope as for our fiducial models. We note the inflated envelope of the $\dot{M} = 10^{-6} M_{\odot}\text{yr}^{-1}$ model has a correspondingly low maximum density. The maximum temperature is lower in the the model with the 100 times Cannon et al. accretion rate than in the model with a fixed accretion rate around the time averaged 100 times Cannon accretion rate. Upon inspection of the model we find this is due to a larger accretion rate at

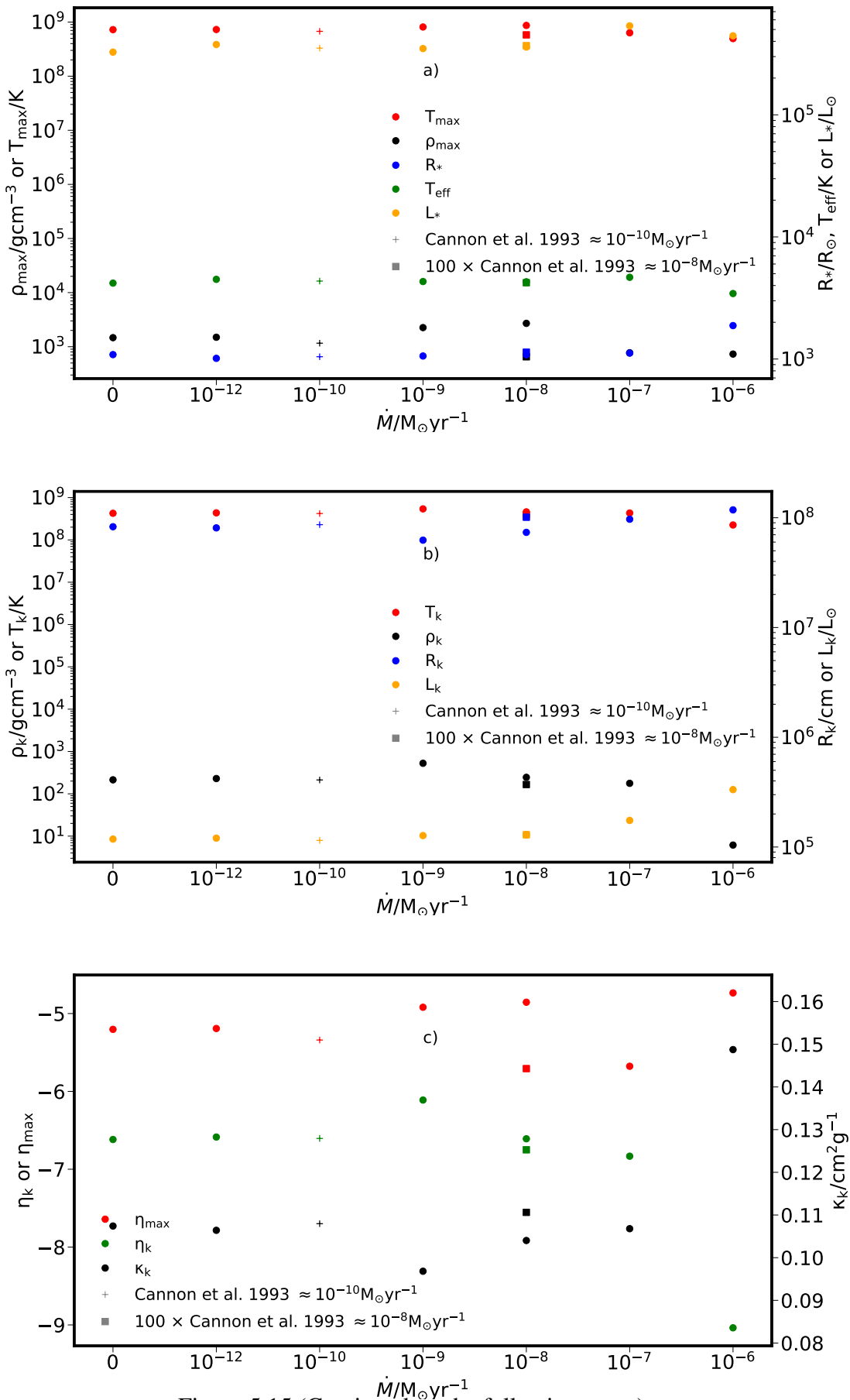


Figure 5.15 (Continued on the following page.)

Figure 5.15 Plots, a), b) and c) from top to bottom, demonstrating the effect of varying core accretion rates on our fiducial models. Each of these models is initialized with a total mass of $17M_{\odot}$, $M_c = 1M_{\odot}$ and $R_c = 10\text{ km}$. We then fix an accretion rate on to the core, with selected rates of $10^{-12}, 10^{-9}, 10^{-8}, 10^{-7}, 10^{-6}$ and $0 M_{\odot}\text{yr}^{-1}$. We also consider a model with the accretion rate prescription of Cannon et al. (1992) as discussed in section 5.2.1 and a model with a rate 100 times the Cannon et al. rate. While these two prescriptions vary the accretion rate with time, the rates they generate are at all times approximately equal to a few times 10^{-10} and $10^{-8} M_{\odot}\text{yr}^{-1}$ respectively.

this point owing to the lower density around the knee leading to a higher luminosity from gravitational potential energy and hence requiring less nuclear burning luminosity to support the envelope.

In fig. 5.15 (b), we present the sensitivity of the location and thermodynamic properties of the knee to the accretion rate. As TZ , we define the knee to coincide with the base of the convective envelope. Here R_k is the radius at this point. As before the $\dot{M} = 10^{-6} M_{\odot}\text{yr}^{-1}$ model, with its inflated envelope, has a correspondingly lower knee density and temperature and higher knee radius and luminosity. The knee is in effect being pushed outwards by the larger gravitational energy release below the knee. At lower accretion rates the knee moves inwards as the accretion rate increases because, at very low accretion rates, considerable energetic support is provided by intense ($\varepsilon_{3\alpha} \gg 10^{11} \text{ erg g}^{-1} \text{ s}^{-1}$) helium burning below the knee, driving it outwards. As the accretion rate increases, more luminosity is supplied by $\varepsilon_{\text{grav}}$, the luminosity per unit mass liberated from the release of gravitational potential energy, reducing the helium burning luminosity and allowing the knee to move closer to the core. The knee gets closest to the core at $\dot{M} = 10^{-9} M_{\odot}\text{yr}^{-1}$. After this point, the $\varepsilon_{\text{grav}}$ luminosity is sufficient to begin to drive the convective envelope outwards, correspondingly reducing the density and temperature at the knee. As in fig. 5.15 (a), the 100 times Cannon rate model, a somewhat higher accretion rate than the fixed $\dot{M} = 10^{-8} M_{\odot}\text{yr}^{-1}$ rate model has the knee occur at a higher radius and correspondingly lower density.

In fig. 5.15 (c) we present the opacity at the knee and the maximum and knee electron chemical potentials η as functions of the accretion rate. The behaviour of these variables can be well understood in terms of the results presented in the previous two plots. The maximum η occurs in all models at a point interior to the knee, close to the core. So increases gradually up to around the Eddington rate as the knee moves inwards to higher and higher densities. Then, as the accretion rate increases beyond this point η_{max} falls sharply as more $\varepsilon_{\text{grav}}$ luminosity is liberated below the knee. For the highest accretion rate model, η_{max} increases sharply again. This is due to the greatly increased mass below the knee in this model, see table 5.3. If we consider the degeneracy parameter at the knee itself in this model, we find

Table 5.3 Position of the knee above the core in radius, and mass contained interior to the knee for the final hydrostatically consistent model timestep as a function of the core accretion rate.

\dot{M} $/M_{\odot}\text{yr}^{-1}$	$M_k - M_c$ $/10^{-7}M_{\odot}$	$R_k - R_c$ $/10^7\text{cm}$
Cannon et al. (1992)	9.1062	8.5482
Cannon et al. (1992) $\times 100$	8.8569	10.0133
0	9.0461	7.9872
10^{-12}	9.2170	8.1794
10^{-9}	7.7367	6.1492
10^{-8}	9.2090	7.2585
10^{-7}	8.5325	9.5940
10^{-6}	5.7903	11.6953

that it is in fact considerably reduced instead, fitting well with our understanding of this being a more inflated model, where a large $\varepsilon_{\text{grav}}$ luminosity has driven the knee out to larger radii, lower densities and correspondingly higher κ , as seen here. Otherwise, all the models behave as expected here with the most compact and dense knee being correspondingly the most degenerate and least opaque.

In table 5.3 the mass and radius interior to the knee is given as a function of the accretion rate. Because the mass that the core has grown to by the breakdown of hydrostatic equilibrium is dependent on the accretion rate at the highest accretion rates, the knee is at the largest total radii and mass but is in fact not significantly further from the core itself in terms of mass and is further from the core in terms of radius only by a small amount. The mass interior to the knee at this point (around $5 \times 10^{-7}M_{\odot}$) is around an order of magnitude larger than that of the lower total mass models of TŻ ($2.7 \times 10^{-8}M_{\odot}$), although this is still considerably larger than in the the highest mass TŻ models ($3.5 \times 10^{-10}M_{\odot}$). The knee in all cases sits around 10^4 to 10^5 times further from the core than in the TŻ models, where the knee is situated from about 5000 to 10,000 cm above the core. These are similar to the radii found by Cannon et al. (1992) and Cannon (1993b). This again illustrates the discrepancy between our models, where no artificial device is used to link the core and envelope equations of state, to those models where such an artifice is employed.

5.2.4.1 Static accretion rate models in the UV plane

Analysing a selection of models of varying total mass with a zero core-accretion rate on the characteristic plane of stellar evolution, as before in figure 5.8 for our fiducial models with Cannon et al. accretion rates and as discussed in section 5.2.1.4, we find that, qualitatively

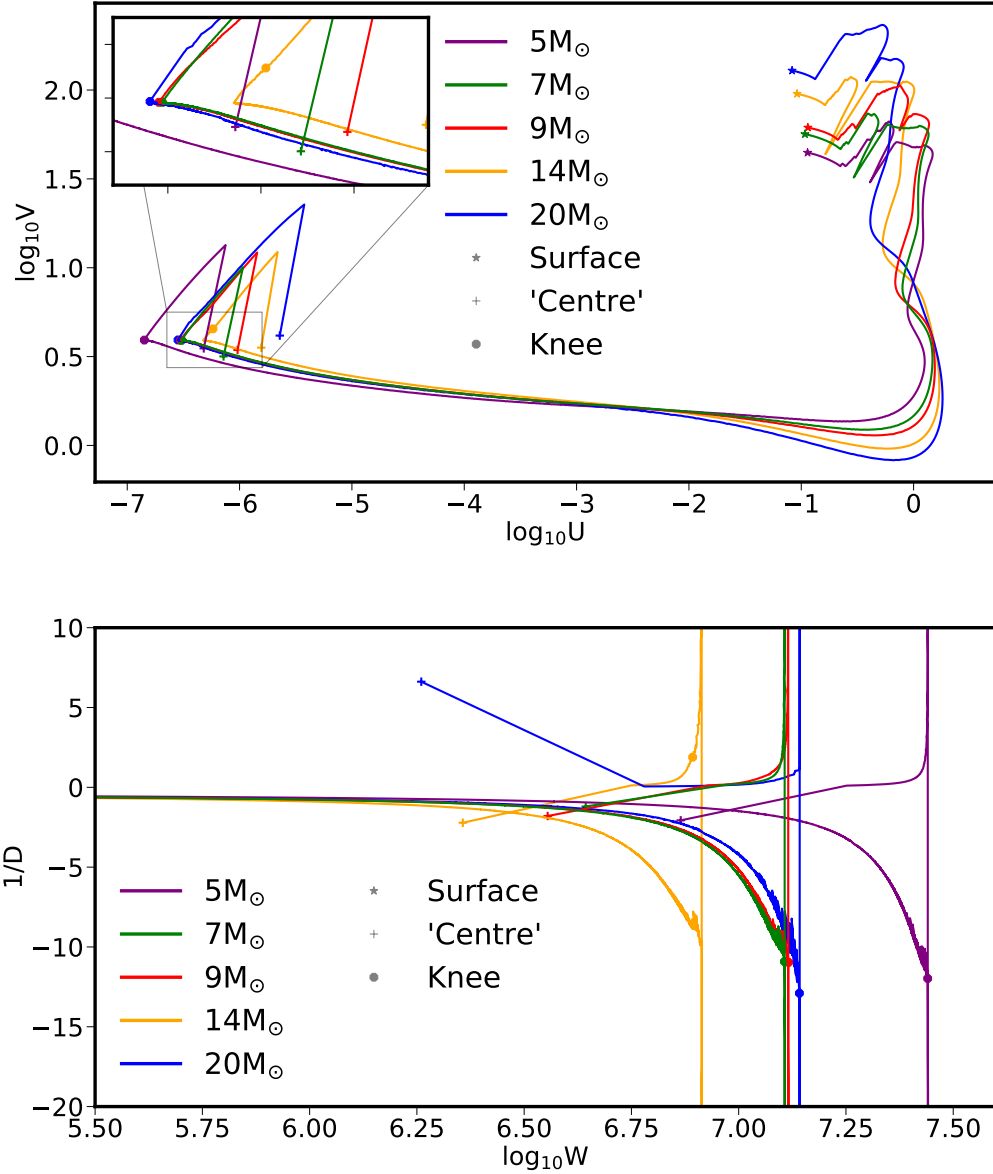


Figure 5.16 *Top*: A sample of relaxed core fiducial model structures on the characteristic $(U - V)$ plane as in and with homology invariants as defined in fig 5.8. Each model has a static core, that is a zero core accretion rate, and an initial core mass of $1 M_\odot$. The position of the photosphere (*), knee (octagon) and ‘centre’ (+) are labelled as before. *Bottom*: The sample of fiducial models plotted on the characteristic differential $(W - D)$ plane of stellar structure, again as in fig 5.8.

speaking, the structure of our models is not strongly dependant on the core accretion rate. Indeed, the behaviour of models across a large range of initial total masses depends on the mass with little difference otherwise between models with a Cannon et al. accretion rate, with average accretion rate around $10^{-10} M_{\odot} \text{yr}^{-1}$ or with a completely static boundary, with zero accretion rate. This indicates that characteristic plane topology of our envelope solutions is invariant under varying accretion rates and lends further credence to the idea that this new series of envelope solutions that we have computed is valid. By this, we mean that the structure solutions we found are not overly sensitive to our initial conditions, and rather that these structures constitute a general solution to the question of TŻO evolution. We find this even allowing for a great deal of uncertainty in exactly how the interface of the infalling halo with the surface of the neutron star is to be constructed and what physical processes must be considered or may be ignored in this region. Furthermore, the topological isomorphisms between the homologous curves for models with static and accreting cores indicate that these envelope solutions may in fact describe a wider range of compact-object–diffuse-envelope interactions than we consider here or that have been given due consideration in the literature.

5.3 TŻO Structure Investigations with STARS

For the purposes of comparison and completeness, we used the STARS code, with the modifications as described in section 4.2.2.1 to create models of TŻOs. The difficulties in creating such models, particularly with a fully self-consistent model that does not rely on a fixed core equation of state, or a purely analytical stellar material equation of state, including opacities, is well known and has been documented by Cannon (1993a). We briefly outline the attempts to produce models in this manner as follows. Using the STARS code and the modifications as described we attempted to produce self-consistent structure models of TŻOs. The basic workflow for this consisted of producing a zero-age main-sequence (ZAMS) model of a star. We computed ZAMS models for a wide range of stellar masses, from $1 M_{\odot}$ up to $120 M_{\odot}$. These models were then evolved up to an advance stage. For the lower-mass models this was usually the AGB stage, after the onset of shell helium burning, while for the higher-mass models we produced models both before and after the onset of core carbon burning. The consumption of species in nuclear burning was then halted, so that nuclear burning would continue to provide thermal support, without using up the burning species. We then used the various TŻO code modifications in order to attempt to produce a TŻO model. There was a great degree of variance in the success of these attempts, with the majority of these being unable to converge with any increase in the electron mass. For higher mass (more than about $13 M_{\odot}$) models, there was a considerable difference between the earlier

models with much lower and the later models with much higher central degeneracy. The less degenerate models initially converged once electron mass began to increase, but would fail to converge once electron mass exceeded around $2m_e$, although this could be increased or decreased somewhat by tweaking the exact way in which the degeneracy threshold is altered to cross the current central degeneracy. The more degenerate models typically fail to converge as soon as the electron mass is altered. More success was found with the lower-mass models of around 7 to 9 M_\odot . With careful tweaking of the appropriate parameters the electron mass at the centre of these models could be increased to around $30m_e$. While this is still significantly short of the required $1836m_e$ to produce neutrons.

Despite the difficulties, the fact that models could be made to converge with any increase of electron mass suggests that this approach should be capable of producing models with the appropriate electron mass to simulate a TŻO. Extensive continued modifications of the convergence aid parameters , in particular those relating to the effective rate of increase of the exponent in the neutronizing artifice allowed progress to be made. We evolved a conventional star up to the development of a helium depleted core. Then a TŻO model is produced by gradually increasing degenerate electron mass in the core. To achieve this, we scale exponentially the effective electron degeneracy parameter in the equation of state solver routines, keeping track of appropriate chemical potentials. Increase of this effective electron mass produces a fully self-consistently computed core with characteristics between that of a WD (with effective electron mass equal to the electron mass) and a NS (with effective electron mass equal to the neutron mass). The final capping of this procedure will be at the neutron mass (around 1836 electron masses). To properly incorporate neutron properties, we use chemical potentials from [Shapiro & Teukolsky \(1983\)](#). We also use updated electron conductivities for proton scattering ([Gnedin & Yakovlev, 1995](#)) and expanded thermal neutrino loss rates by [Yakovlev & Levenfish \(1995\)](#). In Figure 5.17 we show the 4 computed fiducial $5M_\odot$ models with minor element nucleosynthetic post-processing from the ZAMS to the end of the AGB. We consider these models to be fiducial in the sense that they form a representative sample to investigate the behaviour of this family of solutions. We discuss further the details of this nuclear network in Appendix B.1. We dub the models with hybrid rather than white dwarf cores to be hybrid-AGBs, for a convenient shorthand.

5.3.1 Structural Results

Our computed fiducial models behave structurally as AGB stars, with the exception of the model with 10x effective electron mass. As the core effective electron mass increases, the maximal degeneracy pressure support also increases, allowing the core to grow to masses in excess of that of the standard (1x electron mass) AGB model. As the effective electron mass

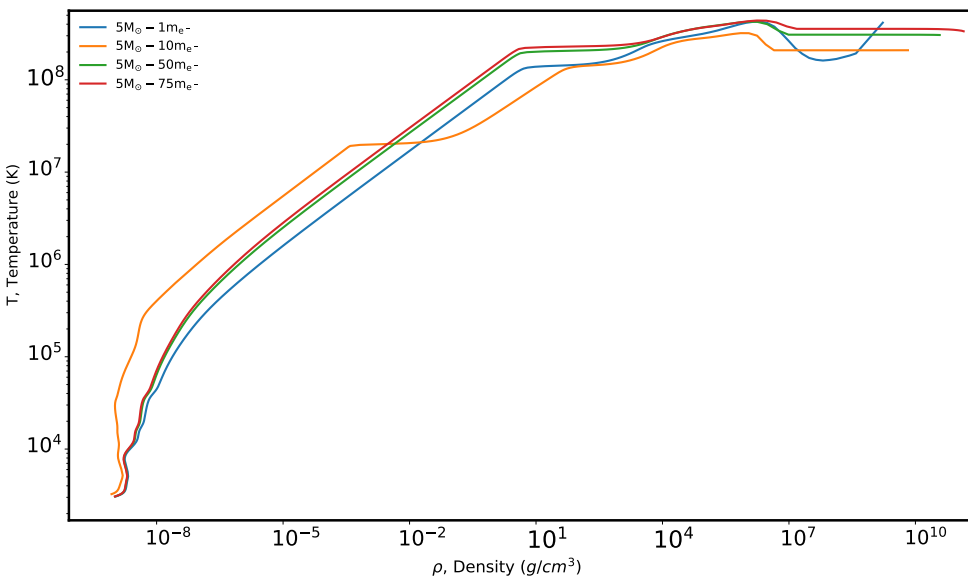


Figure 5.17 Density - temperature structure for the four fiducial $5 M_{\odot}$ AGB models computed. We note the temperature inversion due to the beginning of core carbon burning for the WD core model. Isothermal hybrid WD/NS cores at 10x and 50x electron mass, and a temperature inversion due to neutrino losses at 75x electron mass. We note that, since the neutronizing is only partially completed at this stage, in comparison to a full TZO model, the core is considerably hotter, and is still being actively heated, allowing for the effective operation of thermal neutrino generating processes, leading to neutrino losses that set up the temperature inversion as seen.

increases, we observe a larger and more compact core, with a sharper transition from core to envelope, leading to a smaller region in which nuclear burning occurs towards the end of the AGB/hybrid-AGB. We note that the larger core at 10x electron mass is a temporary artificial result, and that there is no expectation that the neutron core of a TŻO should be able to grow to such a large mass. Figure 5.18 shows the HR diagrams for four of our computed $5 M_{\odot}$ models, each with a different maximum effective electron mass in their cores. The very close overlap between the tracks in the plot for all of the models further suggests, as discussed by [Thorne & Żytkow \(1977\)](#); [Cannon et al. \(1992\)](#); [Cannon \(1993b\)](#); [Levesque et al. \(2014\)](#); [Tout et al. \(2014\)](#) and [O'Grady et al. \(2023\)](#), that sAGBs, TŻOs and transitory objects with hybrid-like cores all have very similar outward appearances. This is also in agreement with our envelope models as computed using MESA, which have near identical surface properties. In Figure 5.20, we present four plots, each detailing the internal structure of each of the four aforementioned $5 M_{\odot}$ stellar models. The top panel of Figure 5.20 shows the density profiles of each of the stellar models as a function of radius. The standard AGB model, that is, where the maximum effective electron mass is simply the normal electron mass, has a oxygen-neon-rich core, supported by electron degeneracy, and with the properties of a white dwarf with equivalent mass. As the maximum effective electron mass is increased the transition from convective envelope to radiative halo to neutron(-like) core becomes more and more sharp. The second panel of Figure 5.20 show an equivalent plot, this time for the temperature as a function of the radius. In the AGB model, the temperature rises sharply above around $10^{8.5}$ K as we move inwards through the hydrogen burning shell, the helium shell and the carbon shell in rapid succession, in terms of radius, falling off after this point and then starting to rise once again as we move into the contracting electron degenerate core. As we increase the maximum effective electron mass, the neutron-like core becomes isothermal¹⁷ a result of the superconductive nature of the neutronizing material, as expected. The increasingly large and increasingly sharp spikes in the temperature, as a function of the maximum effective electron mass map to the increasing narrow (in radius) region of the halo in which the gravitational potential energy of stellar material accreting on to the neutronizing core is liberated. The third panel of Figure 5.20 shows the thermal energy generation rate, that is, the energy generated by the contraction, or consumed by the expansion of stellar material, as a function of radius. The stochastic spikes of the AGB model are a result of the increasingly unstable thermal pulsations that an AGB star undergoes at the end of the TP-AGB ([Iben & Renzini, 1983](#)). As we have run all of these models until a breakdown in

¹⁷In the model with the highest maximum effective electron mass, the core actually begins to cool as we move to higher and higher densities, as the efficiency of thermal neutrino generation processes begins to increase. This may lead to the kind of destructive neutrino runaway theorized by, for example, [Bisnovatyi-Kogan & Lamzin \(1984\)](#).

hydrostatic equilibrium occurs, this is the last such thermal pulsation that our code is able to compute, additional, terminal, pulsations being too violent and inherently hydrodynamical in nature to be followed. The final panel of Figure 5.20 shows rate of nuclear burning in the models as a function of radius. For the AGB model, we see the standard, more complicated structure of a terminal AGB star. Starting at the largest radius and moving inwards, we see the relatively thick (although very thin in absolute terms, as per [Paczyński \(1969, 1970b\)](#)) and intensely burning hydrogen shell, below which the burning rate falls in the intershell region. Below this point, the burning rate increases as helium burns more intensely at higher and higher temperatures. Interior to this the rate again falls in the intershell, before rising again in the carbon burning shell. As we are considering a model at the terminal stages of the TP-AGB, below this point we begin to see the O-Ne core ignite, although we will be unable to follow this deflagration further, due to its hydrodynamical nature. The burning structure of the hybrid-AGBs is entirely different. Only hydrogen burns at an appreciable rate, as most of the objects' luminosity comes instead from the release of gravitational potential energy from material accreting on to the core. Which much less mass is involved in burning, and it occurs in a much more narrow region, the burning itself is much more intense, and overlaps almost completely with the base of the convective envelope, as predicted by [Thorne & Żytkow \(1975\); Thorne & Żytkow \(1977\)](#).

One of the main difficulties in producing a model of a TŻO that computes the neutron core as a self-consistent component of the entire stellar model is dealing with the assumption of isothermal core material. While the object is being evolved, the core is heated by energy released from accretion until it is sufficiently hot and dense to generate a large thermal neutrino luminosity, at which point it goes into neutrino runaway, making further computation challenging. As discussed in section 5.1.2, the models computed by [Cannon et al. \(1992\)](#) and others made use of the [Cooperstein \(1988\)](#) neutron star equation of state, forcing a static and isothermal core. This once again raising the same initial concern regarding the core-envelope interaction artifice that we have contended with, namely that a specific set of conditions in density and temperature are being forced to occur at some point in the model, rather than arising naturally from self-consistent simulation. Here, as in [Thorne & Żytkow \(1975\); Thorne & Żytkow \(1977\)](#), where a density of approximately 10^8 g cm^{-3} was enforced at the boundary condition corresponding to the edge of the base of the halo, there is a greatly increased density at the base of the halo, that arises as a result of computational techniques rather than being strictly physically motivated. As this halo region is both small in radius, and contains little mass, a greatly increased density even at just the very base of the halo, right above the neutron core, has an out-sized effect on the entire core-halo-knee structure of the TŻO model.

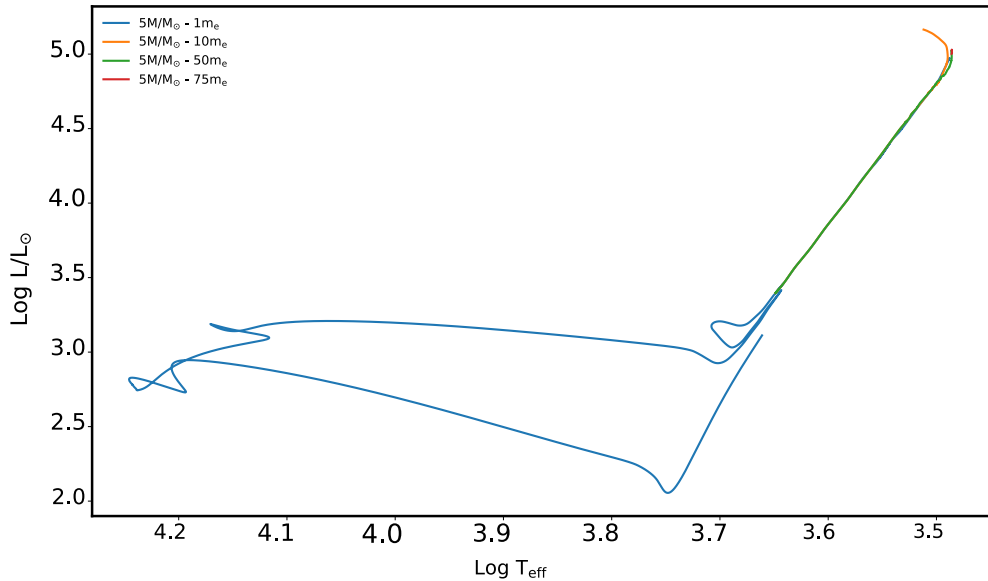


Figure 5.18 HRDs for the four fiducial $5 M_{\odot}$ models. We note here and in the following figures relating to the internal structure of the models that the 10x electron mass hybrid-AGB model was able to grow to a core mass of around $3.5 M_{\odot}$ by the end of the AGB. The very close overlap of all of the models with one another suggests, as already discussed, that TŻOs, hybrid-AGBs (if we suppose for the sake of argument that one could exist in this state in nature) and sAGB stars of similar total masses all have near identical observable surface characteristics in terms of luminosity, radius, effective temperature *etc*, with anomalous surface chemical abundances being the only available discriminant between these classes of objects.

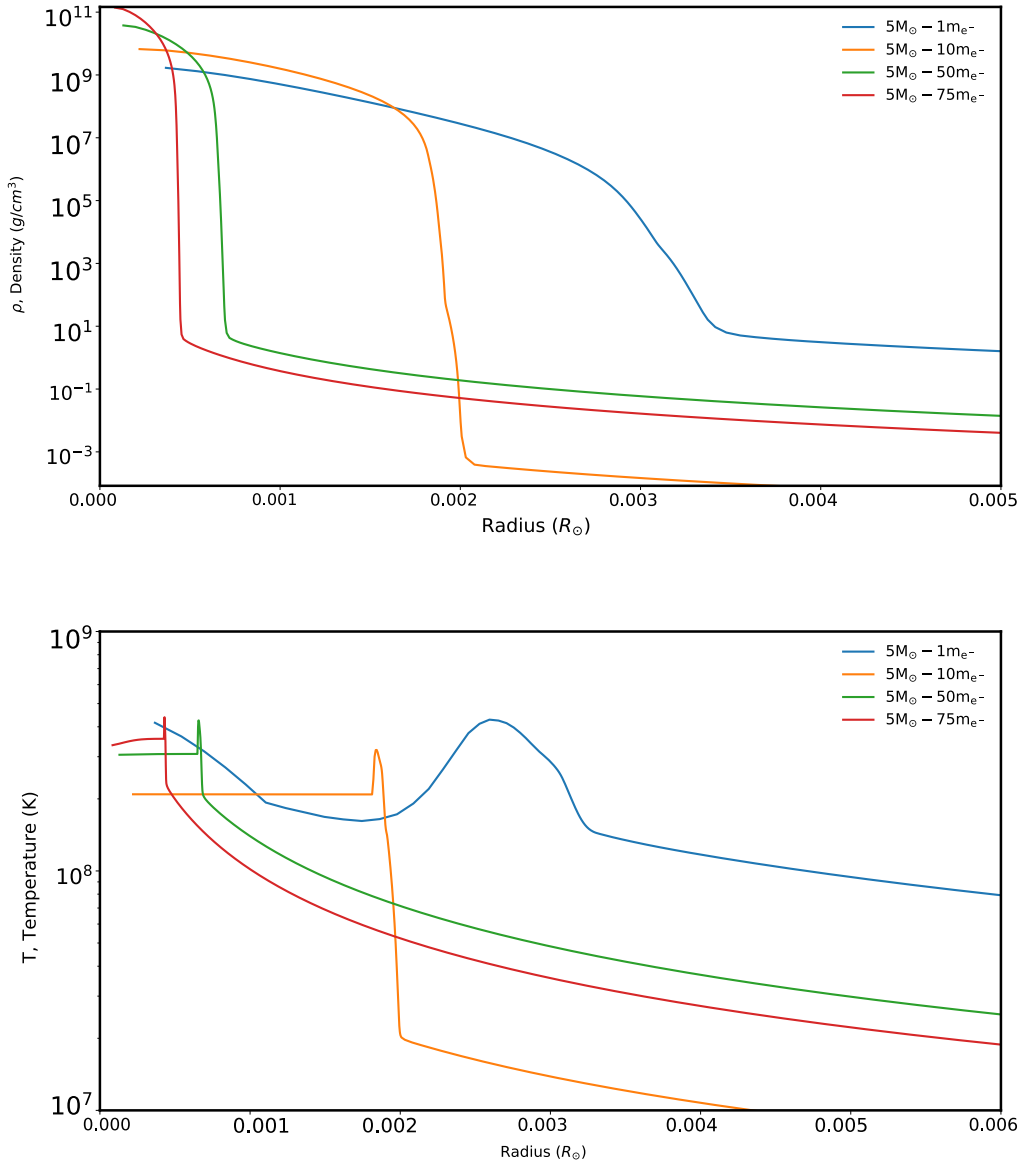


Figure 5.19 Structures for the four fiducial $5M_\odot$ models, showing density in the top panel and temperature in the bottom panel, as a function of radius for our terminal AGB/hybrid-AGB timestep.

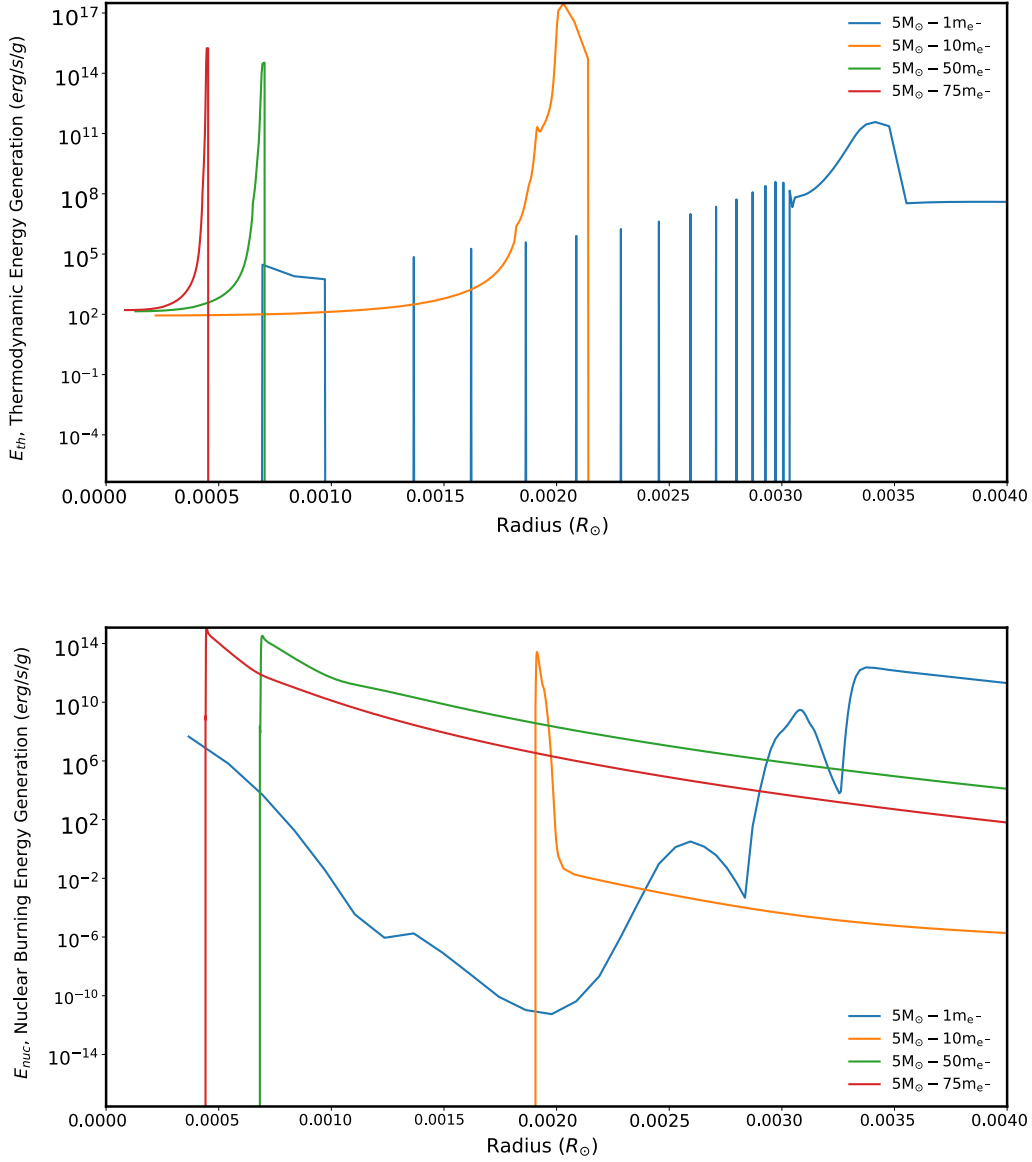


Figure 5.20 Structures for the four fiducial $5M_\odot$ models, showing the rate of thermal energy release in the top panel, and the rate of nuclear energy generation, in the bottom panel, as a function of radius for our terminal AGB/hybrid-AGB timestep. Note the very considerably enlarged core of the 10x electron mass model, which falls in a region of enhanced support against collapse, where there is sufficient degeneracy pressure support from partial neutronization to considerably increase maximum core mass without the corresponding increase in matter density at higher effective electron masses. We do not expect this configuration to be physically attainable in nature, but it does provide a useful illustrative case study for hybrid stars, greatly exaggerating the structural and, as we present in Figures 5.21 and 5.22, nucleosynthetic properties of these objects.

5.3.2 Nucleosynthesis Results

Our models already show considerable variation in internal chemical composition. Convection here reaches the burning layers; thus ‘dredge up’ leads to potentially observable differences in surface chemical abundances by the end of the (hybrid-)AGB. These computations were performed by making use of the extended post-processing nucleosynthesis network in the STARS code. We describe in greater detail that network in Appendix B.1. In short, once the structural variables (including the structural chemical species) have been solved for, the abundances of minor chemical species are computed. This allows us to compute, for example, s- and r-process nucleosynthesis, but, notable, as the network is post-processed, it is not thermodynamically consistent, the energy that should be liberated (or consumed) from each of the minor element reactions is not taken into account. This is not a significant issue for reactions that only contribute negligibly to the energy budget of the star, such as the AGB s-process reactions. However, even for low mass T $\ddot{\text{O}}$ s, at least those models as constructed by T $\ddot{\text{Z}}$, [Cannon et al. \(1992\)](#), etc, at least a few percent of the total energy budget are expected to be contributed by irp process burning (see section 2.3 for further discussion.). While our extended network is capable of following the proton addition reactions and decays of the irp process, we cannot follow the reactions energetically, posing a fundamental limitation on our structure calculations. In order to investigate the internal chemical evolution of the models that we computed in section 5.3.1 we present, in Figure 5.21 the internal chemical structure of two models. We select a range of species relevant to the s-, r- and irp-processes and show their relative abundances as a function of radius for the terminal time-step of each model run. In Figure 5.22 we show the final surface abundances in each model for every chemical species included in our nucleosynthesis network. As previously mentioned, the model with a maximum effective electron mass of ten times the electron mass acts as an exaggerated hybrid-AGB, which a considerably oversized degenerate core. We follow, in Figure 5.21, the abundances of four species as a function of radius, ^{13}C , ^{22}Ne , ^3He and (g), gallinos, which we discuss in more detail in Appendix B.1. For our purposes here, gallinos act as an artificial sink of neutrons. If there is a neutron capture reaction onto a species that is both energetically available to us and where the parent and/or daughter species is beyond the range of the network. Simply ignoring the reaction would result in an unphysically large abundance of neutrons, so a sink particle is needed to remove the excess neutrons. A convenient side effect of this approach is that the abundance of this species, (g), serves to follow the combined abundances of all the s-process species beyond the scope of the reaction network. As discussed in Chapter 2 T $\ddot{\text{O}}$ s and sAGB stars are very challenging to differentiate observationally. As the differences in chemical abundances at the surface of these objects is likely to be the only realistic observational

approach to lift this degeneracy, we show the final surface chemical abundances by species for each of the four illustrative models. While the internal chemical structures of each model is different, altering surface abundances requires one or more episodes of Third Dredge Up (TDU) in order to move the products of the s-, r-, or irp process to the line generation regions, where they can produce spectroscopically observable effects. The structure of AGBs, hybrid-AGBs and full TŻOs leads to unstable double shell burning, as such, we expect to observe, and, in the case of the hybrid-AGB models computed, do observe, the TDU¹⁸. During the TDU, the instability in the double shell burning structure of the star results in the convective envelope moving rapidly inwards, and penetrating into the chemically-enriched radiative layers below, dredging the products of helium burning and s-process reactions into the envelope, and up to the surface of the star. An equivalent TDU-like phase occurs in our hybrid-AGB models, moving material from the hydrogen depleted regions below the base of the convective envelope (the knee, in the parlance of TŻ) up to the surface, where it would be in principle spectroscopically observable (Levesque et al., 2014; Tout et al., 2014; O’Grady et al., 2023). The current final chemical profiles suggest that exploring further interrupted rapid proton processes (irp) and the heavier element s-processes may be fruitful. Our current approach of using increased effective electron mass in the equation of state calculations for core as a transitional state toward fully self-consistent nucleosynthetic modelling of low-mass TŻOs shows some promise. We produce altered internal chemical structures and hence anomalous surface abundances at the end of the AGB/hybrid-AGB.

5.4 Discussion

We have produced a grid of models representing a novel series of envelope solutions for Thorne-Żytkow Objects. Here we discuss the wide breadth of differences between our models and the models of Thorne & Żytkow (1977), Eich et al. (1989), Biehle (1991), Cannon et al. (1992), Biehle (1994) and Podsiadlowski et al. (1995). Models of TŻOs in the past have been either static constructions or have employed some form of core-envelope interaction interface, in which we have identified some possible limitations (section 5.1.2). We therefore attempt to summarise the limitations and simplifying assumptions in our own models as well as the differences in model construction, considered microphysics and general computational approach that may help to elucidate the reasons for these differences.

¹⁸In order to compute a TDU in STARS, an additional mixing term, as well as a suit of meshing controls are required to produce the extra mixing required (Mowlavi, 1999). We make use of these controls to compute these models, following Stancliffe (2005).

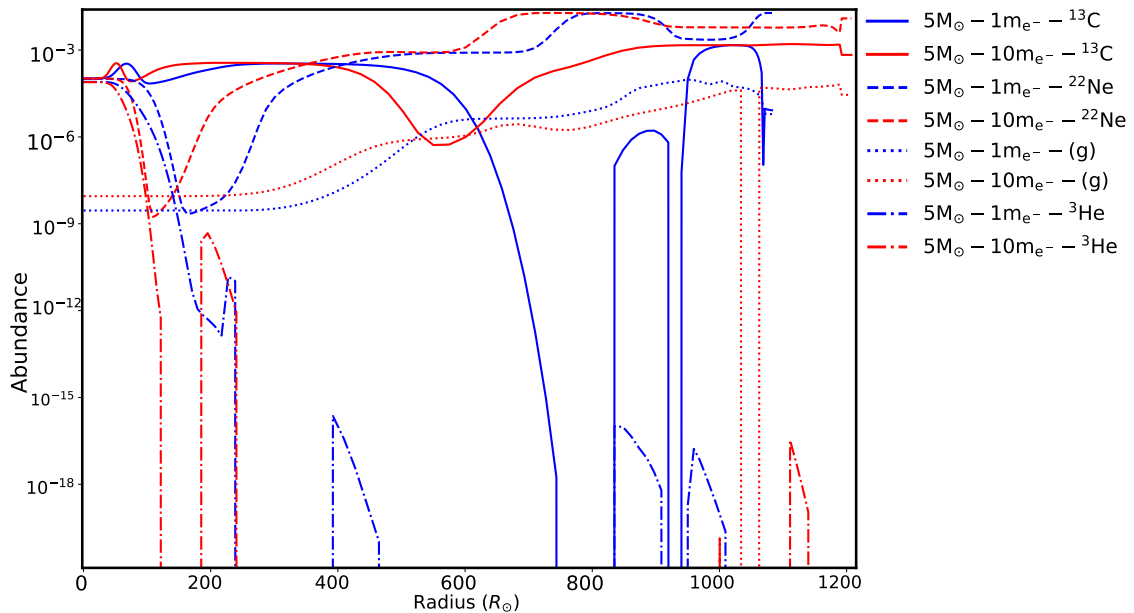


Figure 5.21 Here we show the internal chemical composition of our AGB (1x electron mass) and current final hybrid-AGB (10x electron mass) models as a function of radius. We show abundances of AGB/sAGB, irp, and s-process relevant species, along with gallinos (g), a proxy species in the nucleosynthesis network onto which free neutrons capture, hence, standing in for heavier s-process elements not explicitly computed in the network. (See Appendix B.1 for further details.)

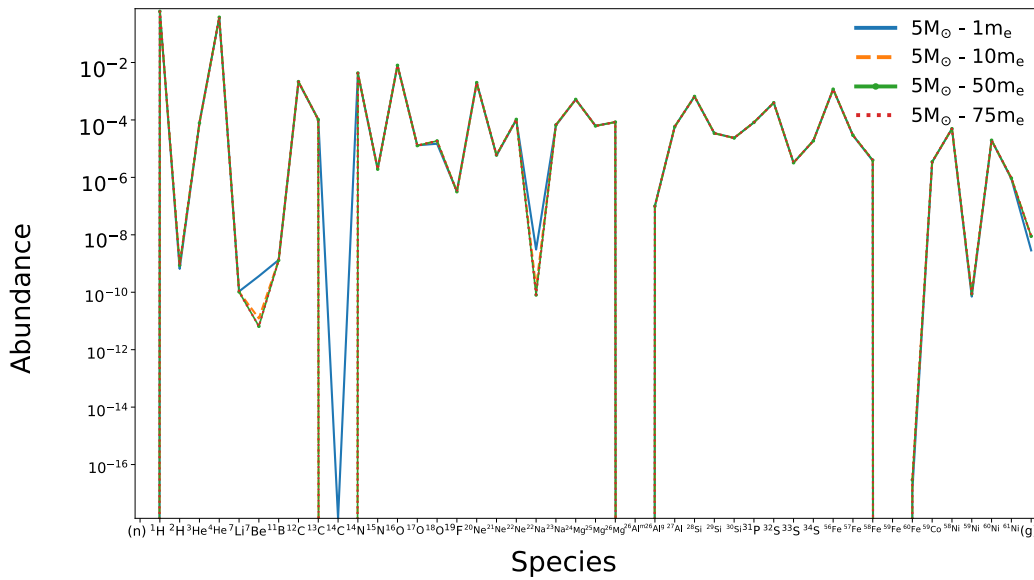


Figure 5.22 Plot of the final model surface abundances for each of the fiducial models, for each species included in our nucleosynthesis network. We note generally negligible differences in surface abundances between models, a notable exception of enrichment of (g), indicating the production and dredging of additional s-process elements to the surface with increasing effective electron mass, and depletion of surface beryllium with increasing effective electron mass. Additionally, there is a minor depletion of surface lithium, in contrast with the notable enrichment of surface lithium in high mass supergiant TŻOs in [Biehle \(1994\)](#).

5.4.1 Comparison with models of TŻ and Cannon et al

The sample of fiducial models that we presented in section 5.2.1, even those with non-Cannon et al. accretion rates outwardly resemble very closely those of TŻ and others. These are M supergiant surfaces with extended, diffuse envelopes and low surface temperatures. Like those of TŻ, our models are considerably reddened and lie close to the Hayashi track. The internal structures of models around the knee resemble an extended version of those of TŻ and Cannon et al. (1992), with correspondingly lower densities. In comparison between our fiducial model with an initial total mass of $12M_\odot$ and the equivalent model by TŻ, our model has about $8 \times 10^{-7}M_\odot$ between the knee and the core, while TŻ find only $3.6 \times 10^{-10}M_\odot$ in this region. Likewise, our knee is located about 9×10^7 cm above the core, while TŻ's knee sits just 5×10^3 cm above the core. The density of stellar material at the knee in our model is around 1.745×10^2 g cm $^{-3}$, notably larger than the around 0.5×10^2 g cm $^{-3}$ in the TŻ model. Finally, our model knee temperature is around 4×10^8 K while TŻ's model is more than twice as hot at the knee, with temperature around 9.5×10^8 K. If we compare instead our $5M_\odot$ initial total mass model to the $5M_\odot$ model of TŻ, we find closer agreement in terms of mass below the knee, with $2.7 \times 10^{-8}M_\odot$ of material between the knee and the core in the TŻ model and around 10 times more in our model around $2.2 \times 10^{-7}M_\odot$. The giant solution TŻ model has a radial distance of around 10^4 cm between the core and the knee while, in our $5M_\odot$ model, the knee is located around 5×10^7 cm from the core, 5000 times further out from the core. The density at the knee in our model is around 5×10^2 g cm $^{-3}$, considerably larger than the 5×10^{-2} g cm $^{-3}$ in the TŻ model. The temperature at the knee in our model is actually larger than in the TŻ model, around 3.89×10^8 K in comparison to around 1.78×10^8 K in their model.

In general, the models of Cannon et al. (1992) adhere to the TŻ structure, a consequence of the computational methodology they employ. This line of comparison between our models and those of TŻ, Cannon et al. etc. indicate that the series of envelope models we have computed do not admit separate giant-like and supergiant-like solutions as per TŻ but rather smoothly vary across the total mass parameter space considered. We essentially find a greatly expanded supergiant-like knee-halo structure in all of our models, in which luminosity is supplied overwhelmingly by the burning of hydrogen at and above the base of the convective envelope and by the burning of helium under radiative and non-degenerate conditions in a mantle-like halo region below the knee. At lower total stellar masses, where the TŻ models are supported mainly by the release of gravitational potential energy of inflowing material, our models instead generate a higher temperature at the knee leading to an increase in the nuclear energy generation rate, supporting the envelope as needed. While the the hot CNO cycle and other high-temperature hydrogen burning processes can operate in our models, the

breakout into non-equilibrium hydrogen burning or rapid proton capture chains is unlikely to be particularly significant. This represents a significant departure from conclusions drawn by, for example, [Biehle \(1994\)](#) who identified the abundance signatures of such reactions to be one of the more potentially observable indicators of that TŻO structure solutions occurring in nature. An occasional critique of the standard models of TŻOs (sections 2.2.1 and 2.2.2) is whether the assumptions of mixing length theory ([Böhm-Vitense, 1958](#)) are valid in the regime considered ([Bisnovatyi-Kogan & Lamzin, 1984](#); [Barkov et al., 2001](#)). While [Biehle \(1991\)](#); [Cannon \(1993b\)](#) and [Biehle \(1994\)](#) accounted for the fact that particularly vigorous convection at the base of the convective envelope in high-mass models and relatively rapid inflow of material through the burning shells below the knee in low-mass models could pass fuel through a burning region on a timescale short compared to the β -decay timescale by considering a chain of interrupted proton capture processes, the irp process ([Wallace & Woosley, 1981](#); [Bildsten, 1997](#)), the validity of the MLT approximation is harder to investigate. While, for example, some alternate formulation ([Arnett et al., 2015](#)) for 1D convection, or insight from targeted hydrodynamic simulations ([Arnett et al., 2018c](#)) could assist in such an investigation, in our models the ratio of the convective velocity near the base of the convective envelope to the physical dimensions of that region and the underlying halo are sufficiently small so as to allow MLT to be used with fewer concerns about its validity.

5.4.2 Explaining the internal structure differences between the canonical models and our own

The internal structures of our models and the canonical models are *qualitatively* similar; this results in very similar behaviour in the HR diagram, for example. However, the models differ *quantitatively* in terms of the location of the knee and of the characteristics of stellar material at and below the knee. Here we try to understand the reasons for these differences. Figures 5.23, 5.24 and 5.25 show the neutrino luminosity and its partial derivatives of the neutrino luminosity wrt density and temperature, for a range of plasma densities and temperatures relevant to the study of TŻOs, across three relevant compositions. Figure 5.23 is at a roughly solar-like composition, corresponding to the environment in, for example, the convective envelope of a TŻO. Figure 5.24 is at a pure helium composition, corresponding to the region below the hydrogen burning region at the knee of the models assuming a very efficient conversion of hydrogen to helium at the knee. Figure 5.25 is a pure carbon-12 composition, which we find below the helium burning region in our models' halos. Since [Cannon et al. \(1992\)](#) included only hydrogen burning reactions in their nuclear network, and as such, we may expect the pure helium composition to be the most suitable point of comparison here.

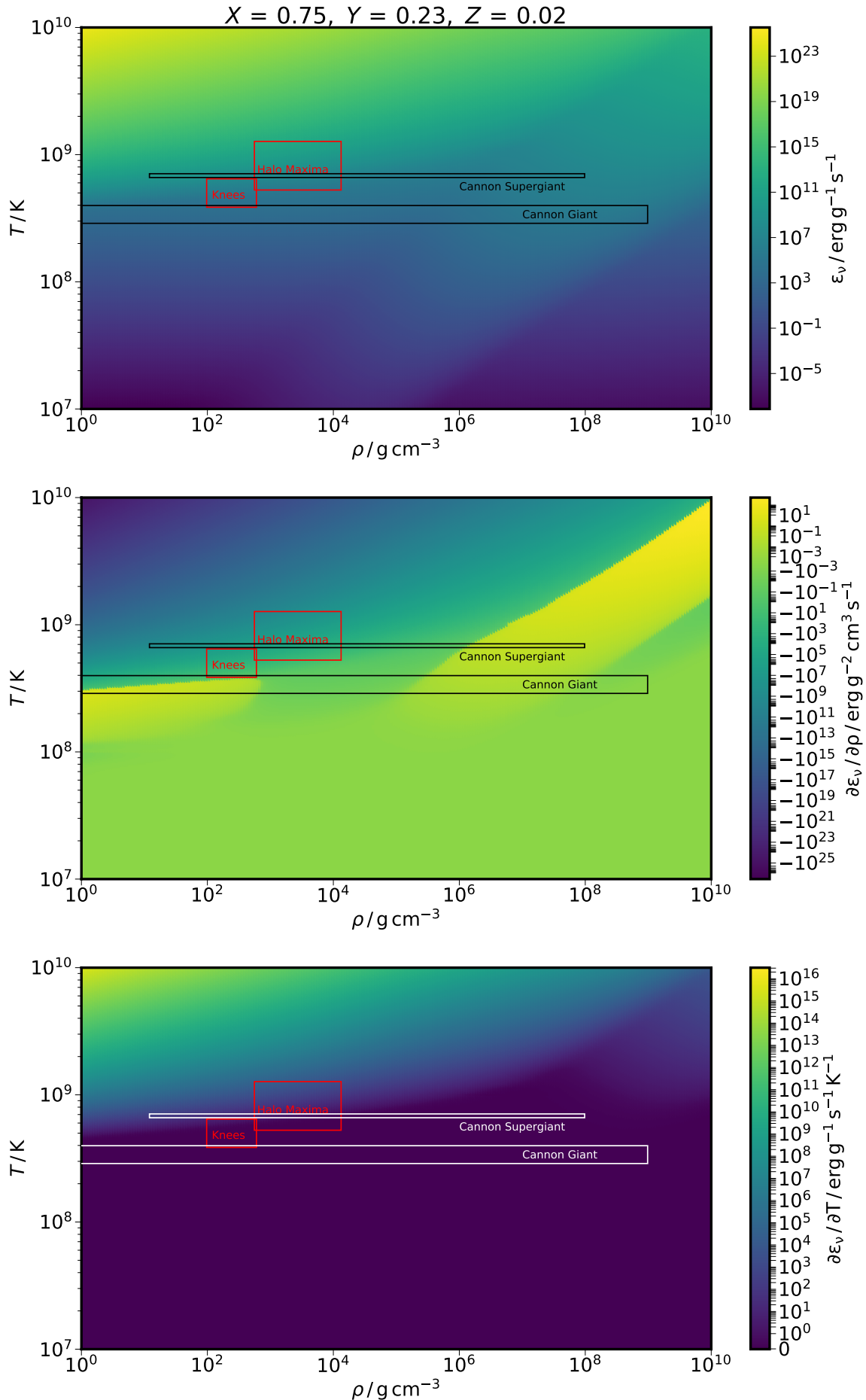


Figure 5.23 (Continued on the following page.)

Figure 5.23

Top panel: Plot of specific neutrino luminosity as a function of plasma density and temperature.

Middle panel: Plot of the partial derivative of specific neutrino luminosity with respect to density at constant temperature as a function of density and temperature.

Bottom panel: Plot of the partial derivative of specific neutrino luminosity with respect to temperature at constant density as a function of density and temperature

In all cases, neutrino generation rates are computed assuming $Z = 0.02$, *i.e.* a solar-like plasma composition, corresponding to composition conditions above the knee, where minimal nuclear processing has occurred. Neutrino luminosity is computed as a sum of contributions from neutrino pair production, plasmon decay, photoneutrino generation, neutrino Bremsstrahlung and neutrino generation from recombination. On all plots, the red outline marked *Knees* indicates the region in ρ - T space where the knees of our fiducial TŻO models occur, over the range of masses considered in figure 5.7. The red outline marked instead, *Halo Maxima* indicates the region of parameter space within which are located the most extreme (highest T and ρ) points in each of those aforementioned models' radiative halos. For comparison, the black (white, in the bottom panel for the purposes of better contrast) outlines marked *Cannon Giant* and *Cannon Supergiant* indicate the entire region of parameter space in which the halos of the [Cannon et al. \(1992\)](#) giant (case A) and supergiant (case C), respectively, may occupy. We define the knee of a [Cannon et al. \(1992\)](#) model as the point where $v_{\text{conv}} = 0$ and end of the halo / start of the core as the point where $\log_{10} \kappa < -4$, *i.e.* where superconductivity begins to set in. Note that the Cannon Giant region extends down in density to around $10^{-1.2} \text{ g cm}^{-3}$

The actual values and behaviours of the neutrino luminosity and its derivatives do not change nearly as dramatically with composition as they do with temperature or density ([Itoh et al., 1996b](#)). Therefore, the following discussion is independent of the assumed compositions. If we, like [Cannon et al. \(1992\)](#), TŻ *etc.* assume that the neutron core is thermally isolated from the rest of the stellar structure, then the core, which may well be considerably heated during the CEE event that forms a TŻO, will efficiently cool via neutrinos generated in the upper regions of the neutron core by means of plasmon decay, and further down by the direct Urca process and other, Urca-like processes occurring in dense material, as discussed in chapter 3. These neutrino losses are not considered here, and in any case, occur at much greater densities than anything found in the halos of any TŻO models. [Cannon et al. \(1992\)](#); [Cannon \(1993b\)](#) did not have access to modern tables of thermal neutrino generation rates, most notably those by [Itoh et al. \(1996b\)](#), and as such, we invoke the differences in neutrino generation rates used as one of the main reasons for the observed quantitative differences between our models, and the canonical TŻO models. In all of the previously computed canonical models, neutrinos created in nuclear reactions, both in structural and nucleosynthetic calculations are taken into

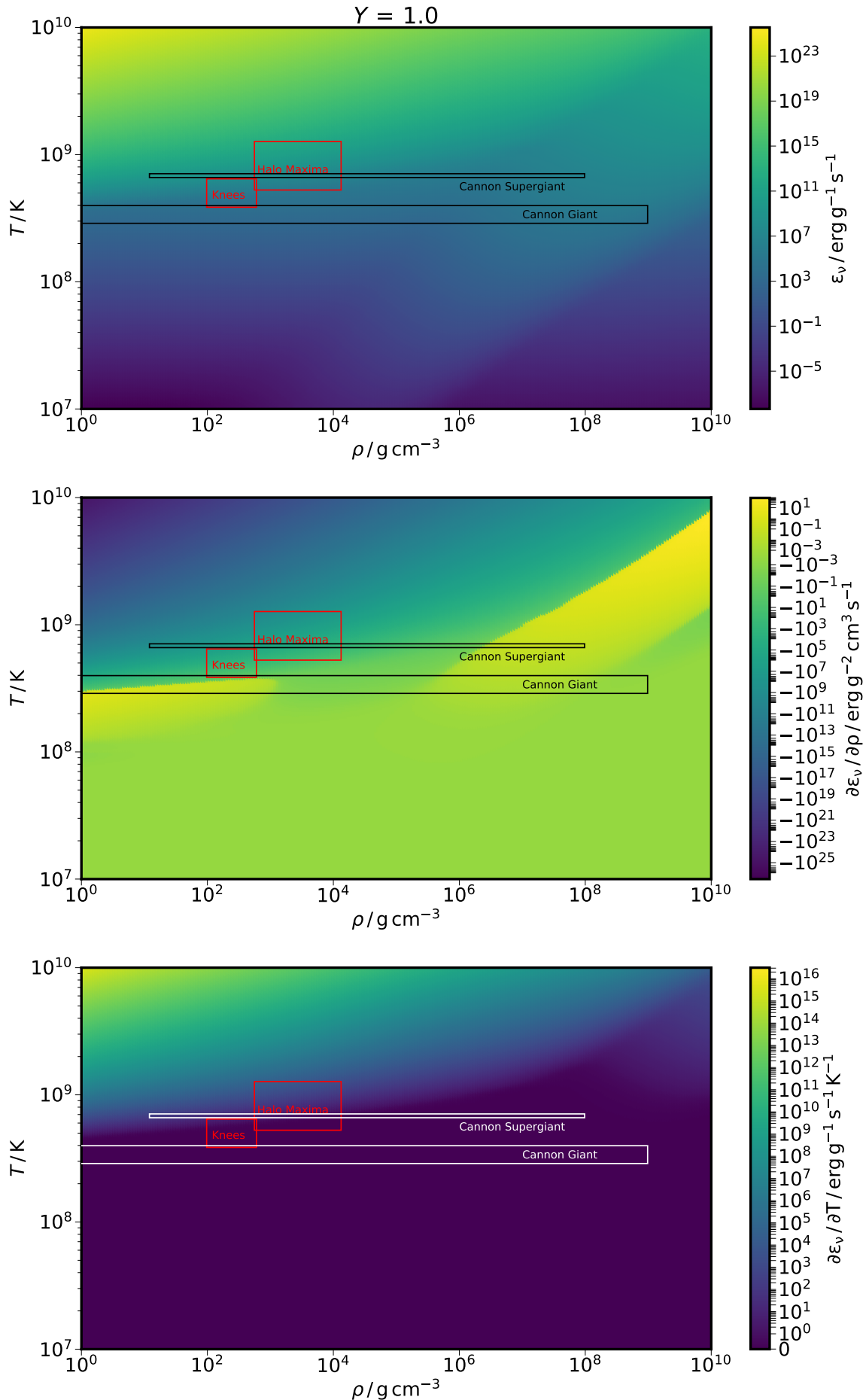


Figure 5.24 As in figure 5.23, but for a pure ionized helium composition.

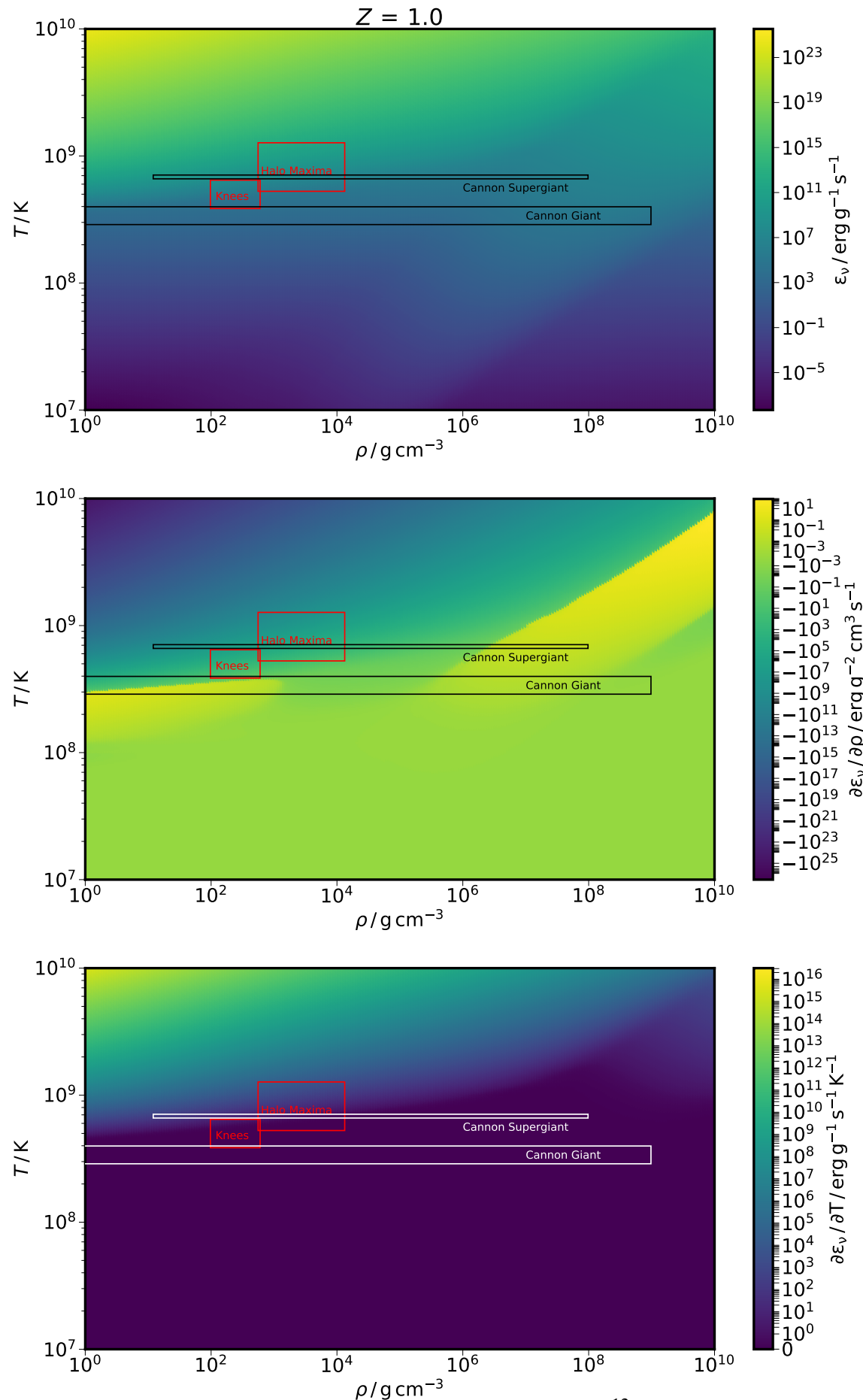


Figure 5.25 As in figure 5.23, but for a pure ionized ^{12}C composition.

account. We are referring here exclusively to thermal neutrinos, generated by (neutrino) pair production, plasmon decay, photoneutrino production, neutrino Bremsstrahlung and neutrinos generated through recombination. Plasmon decay is less salient here, given the extremely high densities needed for this mechanism to dominate. Earlier work by TŻ, Eich et al. (1989); Cannon et al. (1992) and Cannon (1993b) used older neutrino rates (e.g. Beaudet et al. 1967) which were extrapolated to deal with higher densities and temperatures. Compared to Itoh et al. (1996b), Beaudet et al. (1967) tend to have generally underestimated loss rates overall, and specifically to have underestimated plasmon decay rates at lower temperatures as well as having seriously underestimated the photoneutrino rate at temperatures above around $10^9 K$. Looking at figure 5.24 for the pure helium case, our knees occur in a region where neutrino losses are moderate, between $\varepsilon_\nu = 10^5 \text{ erg g}^{-1}\text{s}^{-1}$ and $10^8 \text{ erg g}^{-1}\text{s}^{-1}$, with our hottest halos reaching up towards rates above $\varepsilon_\nu = 10^{12} \text{ erg g}^{-1}\text{s}^{-1}$. By contrast, the Cannon Giant model halos occur at considerably cooler temperatures, but span a much larger range of densities, with knees occurring below $\rho = 0.1 \text{ g cm}^{-3}$ and the most dense regions of the halos at around $\rho = 10^9 \text{ g cm}^{-3}$. Considering the the second panel of figure 5.24, where we show the value of the partial derivative of the neutrino loss rate with respect to density at constant temperature as a function of density and temperature, $(\partial \varepsilon_\nu / \partial \rho)_T$, we see that throughout the majority of the parameter space, increasing the density of the plasma reduces the neutrino loss rate, as the phase space into which neutrinos can be produced, via pair production or photoneutrino generation, become increasingly more occupied. At much higher densities, beyond the range of this plot, this derivative would become very positive, as the plasmon decay mechanism becomes more and more effective, while the photoneutrino contribution grows rapidly up to around $\rho = 10^9 \text{ g cm}^{-3}$, at around helium burning temperatures, at which point it falls off rapidly (Itoh et al., 1996b). However, at temperatures below our knee temperatures, and at around and below those knee densities, there is a region where the neutrino loss rate increases sharply with density instead, as this is part of a small region where recombination production of neutrinos is effective ($e_{cont}^- \rightarrow e_{bound}^- + v_e + \bar{v}_e$). If the Beaudet et al. (1967) rates do indeed significantly underpredict the neutrino loss rates here, we could expect the outermost halo regions of Cannon giant models near to the knee to lose more energy through neutrino losses, leading to a contraction and increase in density at this point. This would likely raise the density and temperature to the point where they both more closely resemble our halos, and allow helium to burn more intensely¹⁹. We suspect that this would both reduce the density deep in the model halos and increase the density at the knee in these models, along with an overall increase in the halo temperature. Given the increase in the nuclear

¹⁹Given that these giant models do not include burning beyond the CNO cycle, this could not have been simulated, regardless of the neutrino loss rates.

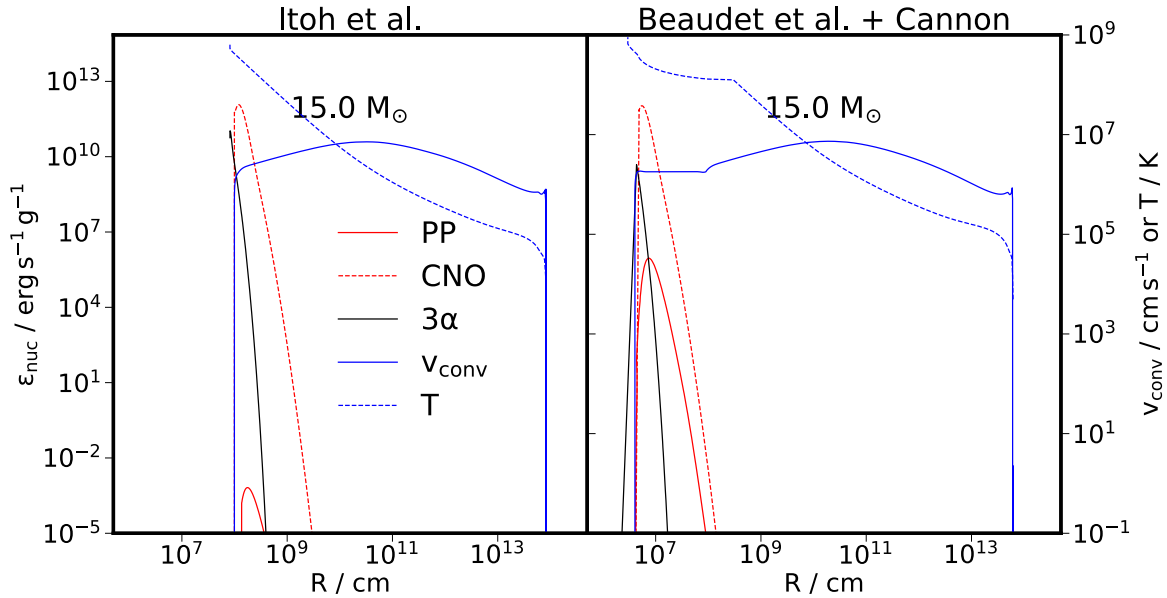


Figure 5.26 Plot as in figure 5.3, showing the structure at and around the knee of our $15 M_{\odot}$ fiducial model (on the left), and of an equivalent model, computed using the neutrino loss rates by [Beaudet et al. \(1967\)](#). We note that the base of the convective envelope has moved in considerably with the older neutrino rates, as expected, which helps to explain the majority of the quantitative structural differences between our models and those by Cannon et al. Given the relatively extreme distribution of mesh points needed to compute this model, we must caution that the convergence here is very poor in contrast to our fiducial models, and so all conclusions derived herein must be made with appropriate consideration.

burning rate that this would create, this would reduce the ratio of gravitational potential energy release to nuclear energy release, perhaps creating models more akin to supergiants, as opposed to giants.

In order to investigate this hypothesis, we re-implemented the [Beaudet et al. \(1967\)](#) neutrino loss rates into MESA, by making use of the *other_neu* hook. As before, we are required to extrapolate these rates in order to cover the same range of the parameter space as covered by the [Itoh et al. \(1996b\)](#) rates. In figure 5.26, we show the structure at and around the knee for our $15 M_{\odot}$ fiducial model and an equivalent $15 M_{\odot}$ model with [Beaudet et al. \(1967\)](#) neutrino loss rates. As had been suspected, making use of the older tables of neutrino loss rates produced a TŻO supergiant structure that was much more akin to those of Cannon et al., with the knee moving inwards to below 100 km above the neutron core. While this is still considerably further out than in the canonical models, it does suggest that the majority of the quantitative differences between our models can be attributed to the differences in neutrino loss rate tables used, specifically with regards to the behaviour of $\partial \epsilon_v / \partial \rho$ in the region of $\rho - T$ space corresponding to the outer part of the halo. Of course, these models do

not exactly reproduce the models of Cannon et al., suggesting that additional differences in microphysics prescriptions are having a non-negligible effect. The most significant difference here is likely to be related to the opacity tables used. As detailed in section 4.3, opacities that we use are primarily from OPAL (Iglesias & Rogers, 1996a,c), while Cannon et al. (1992); Cannon (1993b) used tables by Hubbard & Lampe (1969b), for conductive opacity in dense material, *i.e.* in the neutron core, and by Cox & Stewart (1970) for the remainder of the stellar material. As the OPAL and Cox & Stewart (1970) opacity tables do differ significantly from one another²⁰, this is likely responsible for the majority of the remaining differences between the models.

5.4.3 Limitations and caveats

Given that our models, as described in section 5.2.1 and discussed in section 5.4.1, differ considerably from existing envelope solutions for TŻOs, we must consider any likely or possible limitations of our models or caveats on their validity. Astrophysical TŻOs are likely to form via neutron star inspiral in a CEE event (see Chevalier 2012; MacLeod 2021; Marchant et al. 2021 and section 2.1), the exact pre-CEE envelope structure and composition of the (super)giant component could in principle take a wide variety of forms. For example, a TŻO could form from a HB, RGB/RSG, AGB/sAGB or even a post-AGB neutron star companion. Given this, we tested implementing the central neutron star emulation boundary conditions into a range of stellar structures, including a ZAMS, TAMS, a star at the beginning of core helium burning, a star on the TP-AGB and a range of pre-main sequence models. In all cases (although generally requiring a large number of timesteps, with a considerable number 10+ of solver iterations per timestep) after approximately a thermal timescale the models regenerate the envelope structure for the equivalent stellar mass in the grid of our fiducial models. Given the depth to which convection reaches in our models, chemical abundance structures in, for example, a TP-AGB star are disrupted and the envelope rapidly becomes chemically homogeneous, with the exact abundances in the envelope being the only trace retained of the previous stellar structure. Therefore our envelope solution should be a valid structure for any TŻO formed through the canonical formation mechanism.

While, as we mentioned in section 5.4.1, the use of a mixing-length formalism for convection in our models is less likely to be problematic than in the standard TŻO models, the structure of our models may well be sensitive to inclusion or exclusion of overshooting. TŻ mention this as a possible point of concern in their original work, suggesting that it should soften

²⁰Differences in the evolution of, *e.g.* RR Lyrae stars, when using OPAL opacities as opposed to Cox & Stewart (1970) were demonstrated by Yi et al. (1993) as early as the year of the initial preliminary OPAL data release.

the knee. We consider this to be a likely outcome here as well, with the added caveat that, because the base of our convective envelope behaves neither as a good analogue of a core convective zone nor as a shell burning driven convective zone (as [Collins et al. 2018](#)), there is not necessarily a sensible suggestion for an overshooting parametrization to use, or indeed if additional overshooting processes such as convective settling ([Andrássy & Spruit, 2013](#)) should be considered.

Finally, we must acknowledge that, by failing to model comprehensively the neutron core itself, we are forced to make assumptions of isothermality at the core envelope interface and, in particular, our models cannot account for the possibility of heat transfer from the neutron star outward into the envelope, or indeed, for the possibility that burning in the halo could itself heat the neutron star. As we discuss in section 5.1.2, the interaction of the envelope with the neutron core itself can be modelled by the use of a core-envelope artifice. However this is also an artificial tool and, as such, without a direct hydrodynamical simulation of the entire halo-knee region and the core itself, this will remain a notable limitation of all models of TŻOs. Such a simulation is realistically outside the range of computational feasibility for the time being and, in any case, would be limited by our understanding of the neutron star equation of state itself.

Finally, we expect the mass loss for such an envelope solution to be large, of order $10^{-5} M_{\odot} \text{yr}^{-1}$ ([Kudritzki & Reimers, 1978](#)), and as such to deplete the envelope on a timescale similar to the nuclear burning lifespan of these models. We have not considered fully the effects of mass loss so this is an additional limitation to our models.

5.5 Conclusions

We have constructed a grid of fiducial models describing a series of envelope solutions for Thorne-Żytkow Objects ([Thorne & Żytkow, 1977](#)) with the 1D open-source and modular stellar evolution code MESA. In section 5.2.1 we described the structure of our models, finding that, as discussed in section 5.4.1, they have very marked differences to the models of TŻOs as constructed by TŻ, Cannon et al., Biehle and others. In broad qualitative terms, our models do agree structurally with the canonical supergiant-like TŻO envelope solutions, with a sharp knee, the point at the base of the convective envelope. As in those supergiant solutions, we too find that the envelope is supported primarily by the burning of nuclear fuel above the knee, in the convective envelope, with hydrogen burning turning off sharply at the knee. Furthermore, our models (with the exception of the [Cannon et al. \(1992\)](#)-like models described in section 5.2.3, where an expanded hydrogen burning network is employed, and helium burning suppressed) have considerable helium burning in a radiative halo region

located below the knee. On the other hand, our models are much more expanded with relation to the knee-halo region than the canonical models with the knee located considerably further from the core, both in terms of radial distance and mass interior to the knee. In terms of evolution, once helium burning below the knee is established, our models evolve on a nuclear timescale until fuel exhaustion. Because the hydrogen burning shell is connected by convection to the rest of the envelope the nuclear burning lifespan for our models increases with the total envelope mass. In all cases, the lifespan is of the order of Myrs and, as such, the effects of the high mass-loss rates expected for such extended envelope structures ([Kudritzki & Reimers, 1978](#)) are likely to be significant and may in fact set the lifespan of envelopes. Given our novel models and in particular the differences between them and the canonical series of TŻO models, we have carefully considered the validity and consistency of the solutions. We do not propose these envelope solutions as replacements to the existing models because, given the differences in some key assumptions we make, in particular regarding the presence of a core-envelope interface artifice (see section 5.1.2), means that too much is dependent upon poorly determined physical processes. Instead, these are an alternate set of thermodynamically and energetically consistent envelope solutions that fulfil all the standard criteria expected, such as a characteristic plane topology consistent with valid envelope solutions, as discussed in section 5.2.1.4. We investigated the sensitivity of our models to varying central radial boundary conditions and accretion rate across a wide range of parameter space, as well as investigated and confirmed the ability of these models to remain structurally viable when employing alternate nuclear reaction networks, even when making an assumption, as did [Cannon et al. \(1992\)](#), that hydrogen burning ash accumulates on the core itself rather than being burnt in the halo. Finally, we constructed envelope solutions by setting neutron star emulating core boundary conditions in a variety of initial stellar structures, such as ZAMS, TAMS and core helium burning stars in order to cover the range of possible companions in a TŻO forming CEE event. In all cases, we find that our envelope solutions are very robust and are regenerated in all cases, even when deviating considerably from a standard physically motivated formulation of the problem, as for the highly super-Eddington accretion rates considered in section 5.2.4 or central radius boundary conditions inconsistent with published neutron star equations of state, as in section 5.2.2.

And then Eckart wrote back a letter
— "I am returning Mr.
C[handrasekhar]'s paper

...

I am sorry that I was in error in
criticizing his equation, but it seems
to me a rather remarkable thing that
this equation is true. I should not
have expected it at the first glance."

Interview of S. Chandrasekhar by
Spencer Weart on 1977 May 17,
Niels Bohr Library & Archives

Chapter 6

Highly Magnetised White Dwarfs

Following on from our discussion of highly magnetized white dwarfs in Chapter 3, we now present, analyse and discuss a range of numerical models of such objects, referring to a highly magnetized white dwarf, with central magnetic field densities in excess of 10^6 G as B-WDs. To further motivate what was outlined in that Chapter, we observe overly luminous SNe Ia in nature. Whether or not the progenitors (in the single degenerate channel) of these events are in fact super-Chandrasekhar mass CO white dwarfs is still contentious, [Chornock et al. \(2013\)](#) for example, observed such an event with Pan-STARRS1 and suggested it be categorized as such an overly luminous type Ia. Given that the event occurred at around $z = 1.388$, [Quimby et al. \(2013\)](#) contended that the transient had been lensed and hence magnified by some intervening galaxy, or, perhaps, by a quiescent massive black hole. If we do take it that such a SN does in fact originate from the deflagration of a CO white dwarf then we could suggest that such a progenitor WD must be super massive, that is, significantly in excess of the Chandrasekhar mass. Considering the effects of very large internal magnetic fields in such white dwarfs provides possible solutions for a number of these questions. Firstly, the presence of a large magnetic field, and hence, the additional pressure support this provides is shown here to increase the maximum stable mass for the structure of a white dwarf. Secondly, if we consider the decay of such a field owing to Ohmic decay and Hall Drift, for example, we obtain a possible trigger for the detonation of these objects. As the field decays and the maximum mass that can be supported by the magnetic pressure will fall below the current mass of the B-WD. If the latter exceeds the Chandrasekhar mass, a SN will follow. Given that B-WDs may provide both a method of producing and exploding overly massive white dwarfs, to serve as progenitors of overly luminous type Ia supernovae, we construct and investigate models of such B-WDs. In section 6.4.2 we present our results,

in particular cooling curves in multiple variables, including internal structural variables to compare the effects that the field structure parameters have on the cooling of the B-WDs. In section 6.4.2 we show detailed cooling curves for a $1.6 M_{\odot}$ model, with a wide range of magnetic field structure parameters. We also select one of these particular models as a fiducial highly magnetized super-Chandrasekhar mass white dwarf and analyze the evolution of its internal structure in detail as it cools. In section 6.3 we discuss, implement and make use of a modified plateau magnetic field prescription with a saturation radius in addition to a saturation density in order to produce models of super-Chandrasekhar mass B-WDs that, unlike the earlier models, solve a potential inconsistency with relation to the presence of physically unreasonable current sheaths. In section 6.5 we summarize our main results, comparing and contrasting them with analytical work, ([Chatterjee et al., 2017](#); [Drewes et al., 2021](#); [Bhattacharya et al., 2021](#)) as well as considering avenues for future work, such as implementing a prescription for magnetic field dependent neutrino emission.

As stated in the Acknowledgements of this dissertation, the content in this chapter is based in part on my contributions to [Bhattacharya et al. \(2021\)](#). All of the content, including text, figures, tables, and data used to produce them in section 5, and the paragraph in section 6 beginning “We have also explored a set of stellar evolution models...” in that paper are entirely my own work. The portion of section 6.1 in this chapter of this dissertation prior to the introduction of the concept of the saturation radius are based on my work in that paper. All of section 6.2 in this chapter is likewise based on my contributions to [Bhattacharya et al. \(2021\)](#). The portion of section 6.1 relating to the concept and implementation of the saturation radius, and the results presented in sections 6.3 and 6.4 and all the material from this point onward in this chapter are unrelated to [Bhattacharya et al. \(2021\)](#), and are also my own work, conducted independently.

6.1 Implementation

We produced a set of numerical stellar evolution models using a modified version of the STARS stellar evolution code ([Eggleton, 1971](#)). The EoS solving subroutine STATEF.F was modified to include the prescriptions of [Gupta et al. \(2020\)](#); [Bhattacharya et al. \(2021\)](#); [Mukhopadhyay et al. \(2021\)](#). This involved computing the magnetic field strength at each calculation shell in the model and then computing the magnetic contribution to pressure and density. In addition, at large field strengths ($B / 10^{12} \text{ G} \geq T / 10^6 \text{ K}$), the opacity is expected to be dominated by the magnetic field dependent Potekhin’s opacity rather than the usual Kramers’ opacity. Hence, alongside our usual tabulated opacity calculations, which include both OPAL opacities for the envelope ([Iglesias & Rogers, 1996b](#)) and electron conduction

([Itoh et al., 1983](#)), we compute the Potekhin opacity as prescribed by [Potekhin & Yakovlev \(2001\)](#); [Ventura & Potekhin \(2001\)](#).

$$\kappa_B \approx 5.5 \times 10^{31} \rho / \text{g cm}^{-3} (T / \text{K})^{-3/2} (B / \text{G})^{-2} \text{cm}^2 \text{g}^{-1}, \quad (6.1)$$

where κ_B is the Potekhin opacity, ρ is the density (unmodified by the local magnetic field), T is the temperature and B is the local magnetic field strength.

The overall opacity is then computed by summing the usual, tabulated opacity and the Potekhin opacity in inverse, $\left(\frac{1}{\kappa_{\text{tot}}} = \frac{1}{\kappa_{\text{TAB}}} + \frac{1}{\kappa_B} \right)$.

In order to compute the magnetic field strength itself we use the prescription of [Gupta et al. \(2020\)](#). This itself has been used extensively for magnetised neutron stars and white dwarfs ([Das & Mukhopadhyay, 2014](#); [Bandyopadhyay et al., 1997](#); [Bhattacharya et al., 2021](#); [Mukhopadhyay et al., 2021](#)). We modify this prescription in order to implement a saturation radius, in addition to the usual saturation density, in order to resolve the current sheath density problem as discussed below. It is given by

$$B \left(\frac{\rho}{\rho_0} \right) = \begin{cases} B_S + B_0 \left[1 - \exp \left(-\eta \left(\frac{\rho}{\rho_0} \right)^\gamma \right) \right] & r \leq R_c \\ B_S + B_0 \left[1 - \exp \left(-\eta \left(\frac{\rho_c}{\rho_0} \right)^\gamma \right) \right] & r > R_c \end{cases}, \quad (6.2)$$

where ρ_0 is a measure of saturation density, that is, the minimum density in the model at which the field reaches and maintains its largest strength and ρ_c is the density at the radius R_c . Interior to the radius R_c the field strength is set to the value that would be derived from the density at the cutoff radius, rather than from the, larger, densities interior to that radius. The surface magnetic field strength is B_S , B_0 is a scaling factor that determines the magnetic field at or above the saturation density ($B \rightarrow B_0$ as $\rho \gg \rho_0$) and η and γ parameterize the decay of the field from the centre to the surface of the model. [Gupta et al. \(2020\)](#) choose $\rho_0 = 10^9 \text{ g cm}^{-3}$, $\eta = 0.8$ and $\gamma = 0.9$. So, these are our defaults in the implementation of this prescription in the STARS code. They can easily be modified to fit to any parameterization desired.

However, as described by [Chatterjee et al. \(2017\)](#), a potential issue arises in this implementation, namely that the radial field gradient is positive throughout the model, resulting in a positive field gradient at the very centre of the WD. This would demand an exceedingly strong current sheet forming at very small spatial extent. This is not easily generated from any fossil field mechanism often invoked to explain WD magnetic fields in general ([Braithwaite & Spruit, 2004](#); [Wickramasinghe & Ferrario, 2005](#)). In order to address this issue, the form of the field profile as defined piecewise in equation 6.2 is used, that is, to hold zero gradient

interior to some selected radius, which we designate the cutoff radius, R_c . This produces a field profile where only a gradient-free magnetic field penetrates all the way to the very centre of the B-WD, and hence, where a more spatially extended and weaker current sheet is sufficient to generate the field densities investigated. In addition, in none of our models does the plateau field exceed 10^{15} G and hence we remain consistent with the findings of Chatterjee et al. (2017), Das & Mukhopadhyay (2014) and Otoniel et al. (2019). In section 6.4 we investigate a range of cutoff radii and in section 6.4.2 specifically the range of cutoff radii for which the magnetic field configuration in question can still support the super-Chandrasekhar mass of the B-WD model in particular. The routine STATEF.F takes the current density at a given mesh point in the model and computes the magnetic field strength as in equation 6.2. The magnetic contribution to density is then computed as $\rho_B = B^2 / 8\pi c^2$ and that to the pressure as $P_B = B^2 / 8\pi$. The magnetic pressure and density contributions are added to the current model mesh point pressure and density, before the subroutine continues to compute the remaining thermodynamic quantities as normal. The usual opacity computations are then completed, before the Potekhin opacity is computed as in equation 6.1 and added in inverse to the standard opacity. This allows the opacity to be computed in a self-consistent way rather than switching from an approximate Kramers' opacity, or Itoh et al. (1983) style electron conduction opacity, to the Potekhin opacity at some distinct point in magnetic field strength and temperature.

Finally, as we expect cooling owing to the emission of neutrinos to contribute very significantly to the overall cooling process, at least early on during the cooling for all the considered models, when the temperatures and densities throughout the model are sufficiently large for neutrino losses to dominate over surface photon emission, we include neutrino production in our code implementation. We utilize neutrino losses tabulated by Itoh et al. (1996b). These are interpolated to produce neutrino loss rates as a function of temperature and density. These tabulated rates include a wide range of neutrino production processes, including, at high temperatures, plasmon decay, pair annihilation and photoneutrino production and at lower temperatures, recombination and Bremsstrahlung. Figure 6.8 shows the importance of properly considering the contributions to cooling from neutrino losses. However, there is scope to improve this implementation further, in particular by implementing additional magnetic field dependant neutrino loss effects, such as synchrotron emission. The possibility of implementing this additional physics has been suggested by Drewes et al. (2021) and is discussed further in section 6.5.

6.2 Simulation Results

We use the STARS evolution code with the modifications described in section 6.1 to create a grid of B-WD models with a range of masses and field parameters. We use our grid of models to investigate qualitatively the B-WD mass–radius relationship at different fields, with the objective of numerically validating the analytical models by [Mukhopadhyay et al. \(2021\)](#). In table 6.1, we list the central density and radius for each of our fixed mass numerical models and for each set of field configurations. In all cases, the models are allowed to cool until the luminosity has reached $L = 10^{-4} L_\odot$. Furthermore, the stellar composition is held fixed. Unlike in analytical models, we do not consider separate core and envelope regions but instead allow for the cooling to occur naturally in the numerical models with no explicit prescription. It is not trivial to produce numerically stable B-WD models with arbitrary field configurations with STARS, so we limit the range of field configurations.

In table 6.1, we present a number of trends in ρ_c and R for a range of mass and magnetic field. As expected, the B-WD radius decreases with M . For models of the same mass, R increases very slightly as a function of the magnetic field, until field parameter $B_0 = 10^{14}$ G is reached, at which point R increases significantly, consistent with the analytical expectation from Section 3 of [Mukhopadhyay et al. \(2021\)](#). Here the central density ρ_c is not the density in the core but rather the density attained at the central calculation point in our model. This is equivalent to their core and envelope analytical approach. As expected, ρ_c increases rapidly with an increase in M . However, ρ_c drops marginally once the threshold field $B_0 \approx 10^{14}$ G is reached. This results from a corresponding reduction in R . The computed value of ρ_c for a given R clearly indicates that the central density does in fact increase as the field increases, with a sharp rise in the density as the critical B_0 is reached. This is in line with our earlier expectation that ρ_c must increase to compensate for the increased magnetic pressure as the field increases.

In Figure 6.1, we validate the mass–radius relations described by the analytical models we computed in [Mukhopadhyay et al. \(2021\)](#). As before, the effect of increasing B on the mass–radius relation is analogous to increasing L . This corresponds to an equivalent star earlier on its WD cooling curve. Rather than specifying a WD radius and then inferring its mass, it is more reasonable to base our numerical grid on fixed masses and then compute R . It should be noted that the numerical models here are not computed for a fixed luminosity but at the time when the models have cooled to the point where the code no longer converges. This is owing to the limitations of the EoS utilised in the STARS code at low temperatures and high densities. The radii of these models at low temperatures are almost entirely independent of luminosity. This is expected as the thermal pressure support in all of these models is negligible compared to degeneracy pressure support as well as the magnetic pressure support.

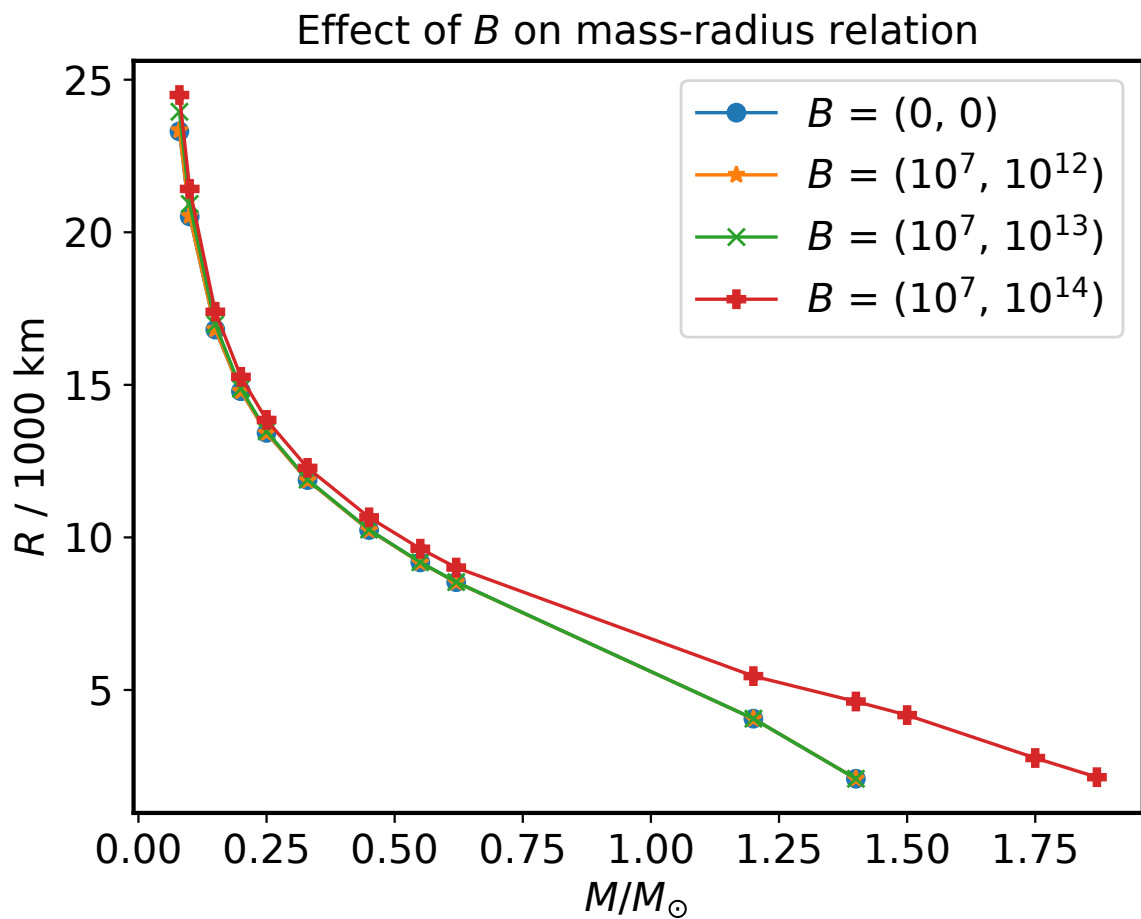


Figure 6.1 The effect of magnetic field on the mass–radius relation of highly magnetized WDs for $B = (0, 0)$ (blue circles), $B = (10^7, 10^{12})$ G (orange stars), $B = (10^7, 10^{13})$ G (green crosses) and $B = (10^7, 10^{14})$ G (red pluses). We do not compute these numerical models at a fixed luminosity, but rather at the stage where they have already cooled down to the point such that the code fails to converge further.

Table 6.1 The maximum attainable B-WD mass is computed for the STARS models as a function of magnetic field parameters (B_s, B_0). The central density and B-WD radius are listed for the corresponding cases.

$(B_s, B_0)/\text{G}$	$\rho_c/10^6 \text{ g cm}^{-3}$	$R/1000 \text{ km}$	Max Mass/ M_\odot
(0, 0)	2210	2.1177	1.4397
$(10^7, 10^{11})$	2257	2.1196	1.4358
$(10^7, 10^{12})$	2280	2.1227	1.4358
$(10^7, 10^{13})$	2295	2.1240	1.4373
$(10^7, 10^{14})$	2260	2.1412	1.8703

The three curves representing $B_0 = 0$, $B_0 = 10^{12} \text{ G}$ and $B_0 = 10^{13} \text{ G}$ almost completely overlap throughout. This is due to the fact that the magnetic pressure contribution only becomes comparable to the degeneracy pressure contribution for the highest field strength.

We obtain results that are in good agreement with the analytical formalism by [Mukhopadhyay et al. \(2021\)](#) and the magnitude of B_0 dictates the shape of the mass–radius curve. For stronger fields, specifically with a larger B_0 , the mass–radius relation deviates from the zero/low-field relation, with the deviation increasing at larger masses. In particular, for $B = (10^7, 10^{14}) \text{ G}$, we obtain super-Chandrasekhar WDs with limiting mass $\sim 1.9 M_\odot$. As anticipated, the radii inferred from our numerical models are not exactly equal to those computed analytically. The EoS for our numerical models is computed with the standard solver in STARS and this essentially differs from the purely analytical estimates. We also include the effects of neutrino losses in our numerical models. The neutrino cooling effect may cause non-negligible energy losses from the cores of very hot and/or dense WD stars. Based on the prescription given by [Itoh et al. \(1983\)](#), we model the neutrino losses that become significant once $T \geq 10^7 \text{ K}$ and $\rho \geq 10^{10} \text{ g cm}^{-3}$ in the stellar matter. While no $L = 10^{-4} L_\odot$ model is hot enough for these losses to occur, as listed in table 6.2, many of these models would have had sufficiently hot cores at other point on their cooling curves for neutrino losses to occur.

Next, we investigate the results presented in Section 3.3 of [Mukhopadhyay et al. \(2021\)](#), which suggest the possibility of obtaining super-Chandrasekhar WDs provided that the central magnetic field and B_0 are sufficiently large. Using our modified STARS code, we compute the highest stable mass model for a range of field configurations. Our results are summarised in table 6.2 and are consistent with the Chandrasekhar mass limit being retained for $B_0 \lesssim 10^{13} \text{ G}$, while allowing for the existence of super-Chandrasekhar B-WD models for larger B_0 . We consider a surface field $B_s = 10^7 \text{ G}$ for the WD models with $B_0 = 10^{14} \text{ G}$. Regardless, the limiting mass obtained for $(B_s, B_0) = (10^7, 10^{14}) \text{ G}$ with STARS is in perfect

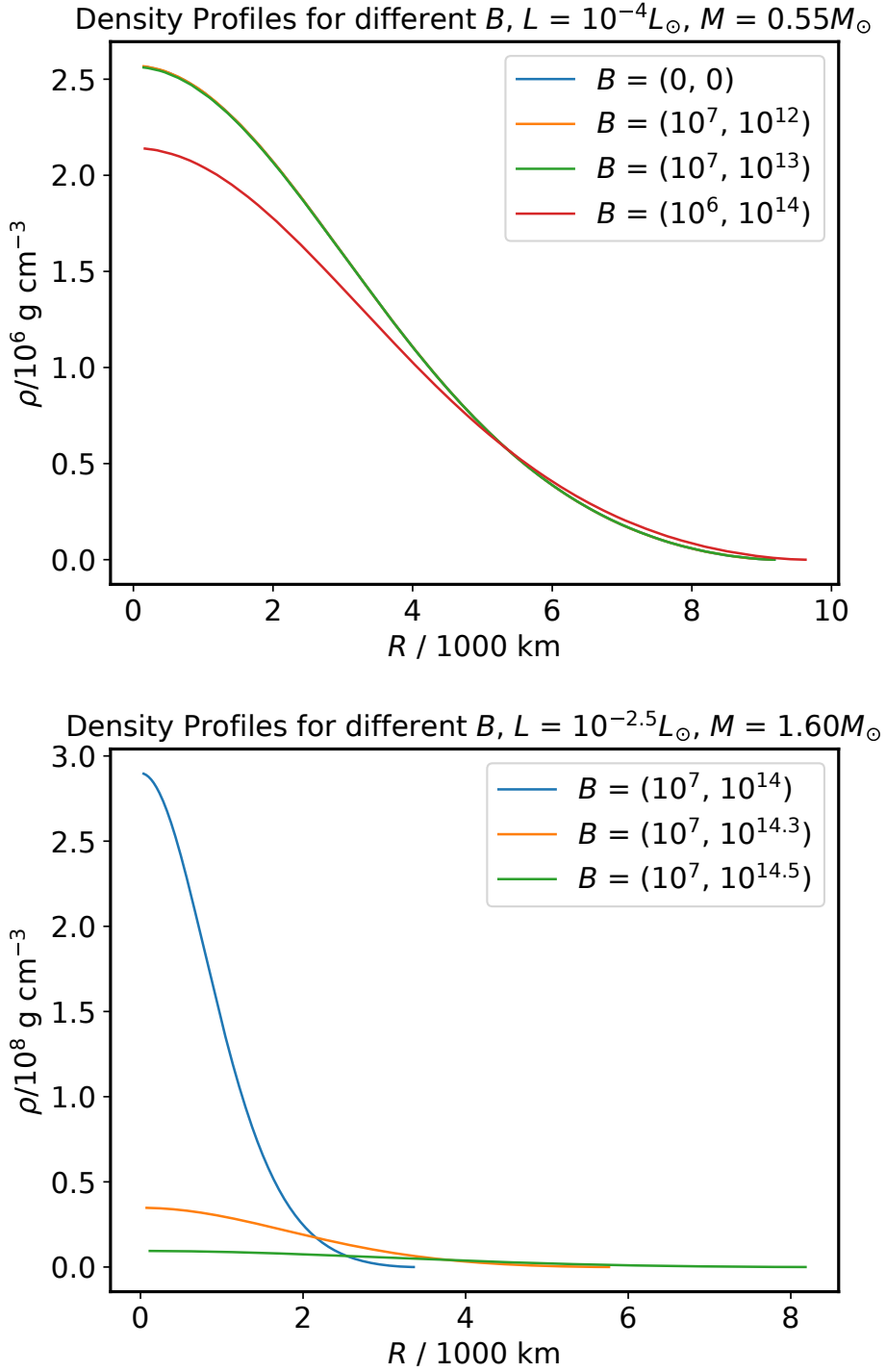


Figure 6.2 **Left panel:** The variation of density as a function of radius is shown for B-WDs with varying magnetic fields $B = (0, 0)$ G (blue), $B = (10^7, 10^{12})$ G (orange), $B = (10^7, 10^{13})$ G (green) and $B = (10^6, 10^{14})$ G (red). Each model has a mass $M = 0.55M_\odot$ and has been allowed to cool to a luminosity of $L = 10^{-4}L_\odot$. This model is essentially equivalent to those computed analytically in Figure 4. **Right panel:** The variation of density as a function of radius is shown as in the left panel, but for a super-Chandrasekhar model mass of $M = 1.6M_\odot$ with varying magnetic fields $B = (10^7, 10^{14})$ G (blue), $B = (10^7, 10^{14.3})$ G (orange) and $B = (10^7, 10^{14.5})$ G (green). Each model has been allowed to cool to a luminosity of $L = 10^{-2.5}L_\odot$. This larger luminosity was required as a result of the simulation's EoS encountering difficulties at lower temperatures.

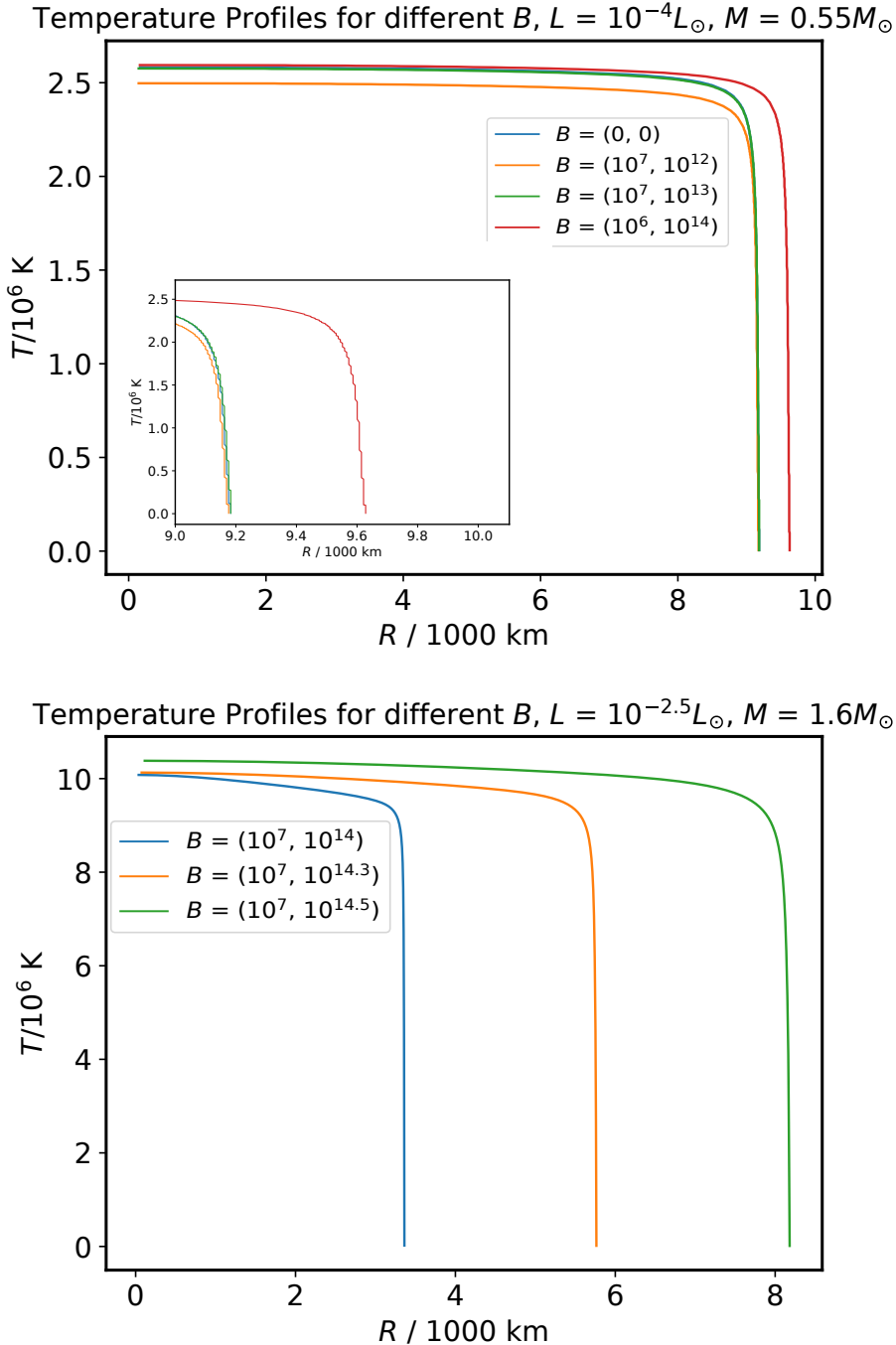


Figure 6.3 Top panel: The variation of temperature as a function of radius is shown for B-WDs with varying magnetic fields $B = (0,0)$ G (blue), $B = (10^7, 10^{12})$ G (orange), $B = (10^7, 10^{13})$ G (green) and $B = (10^6, 10^{14})$ G (red). These models are essentially equivalent to the analytical models presented in Figure 4. The mass is fixed at $M = 0.55 M_{\odot}$ for each model, so the radius varies as a function of the magnetic field. For each field configuration, the model has been allowed to cool until it reaches $L = 10^{-4} L_{\odot}$. **Bottom panel:** The variation of temperature as a function of radius is shown as in the left panel, but for a super-Chandrasekhar model mass of $M = 1.6 M_{\odot}$ with varying magnetic fields $B = (10^7, 10^{14})$ G (blue), $B = (10^7, 10^{14.3})$ G (orange) and $B = (10^7, 10^{14.5})$ G (green). Each model has been allowed to cool to a luminosity of $L = 10^{-2.5} L_{\odot}$.

agreement with $M \approx 1.865 M_{\odot}$ for $(B_s, B_0) \approx (10^{7-9}, 10^{14})$ G from Mukhopadhyay et al. (2021). This supports our earlier finding that B_s has no appreciable effect on the mass–radius relation. Figure 6.2 shows the numerical validation of the same trend for two mass models, i.e., for $M = 0.55 M_{\odot}$ and $M = 1.6 M_{\odot}$, with varying field configurations. At first sight, the numerical results appear to be inconsistent with earlier analytical prediction that ρ_c should increase to compensate for increased P_B as field increases. However, it should be noted that the analytical computations are performed with a fixed radius, whereas our equivalent numerical models are generated assuming a fixed mass. For the super-Chandrasekhar white dwarf models in the right panel of Figure 6.2 with $M = 1.6 M_{\odot}$, we cannot investigate the lower field cases as in the left panel of that figure as there are no solutions for lower values of B_0 , hence we elect to investigate field configurations with higher values of B_0 instead, in an attempt to elucidate a trend in density profiles for these models. We find that for $M = 1.6 M_{\odot}$ and $L = 10^{-2.5} L_{\odot}$ the radius and density profiles of the model are very strongly dependant on the value of B_0 . As B_0 increases from 10^{14} G to $10^{14.3}$ G to $10^{14.5}$ G, the radius of the model expands from ≈ 3500 km to ≈ 6000 km to ≈ 8000 km, while the central density falls considerably from $\approx 3 \times 10^8$ g cm $^{-3}$ to $\approx 2 \times 10^7$ g cm $^{-3}$ over the range of values considered for B_0 . This is good confirmation that for these models, the total pressure is dominated by the degeneracy pressure and magnetic pressure, with thermal support being negligible, as expected, and that the density structure and radii of the models are largely functions of the value of B_0 alone. Hence, a model’s radius is a function of its magnetic field parameters as well as its mass at a fixed luminosity. Therefore, the $M = 0.55 M_{\odot}$ model with a larger central field has a larger radius and hence a lower mean density. If we compare the central density of the model, rather than just the relative order, our numerical results are indeed consistent with the analytical results for $R = 10000$ km WDs, with central density $\rho_c \approx 2.2 \times 10^6$ g cm $^{-3}$ obtained for $B = (10^7, 10^{14})$ G.

We show the variation of the temperature as a function of the radius in Figure 6.3. The analytical models have suggested that the core temperature is primarily determined by the luminosity and is largely unchanged with variation in magnetic field. In good agreement with this prediction, we find here that the core temperatures of models with masses $M = 0.55 M_{\odot}$ and $M = 1.6 M_{\odot}$ are in fact largely unchanged with varying magnetic field. The small difference in central temperatures with magnetic field between these numerical models is a result of the difference in radius and hence in the mean density across the models. In the super-Chandrasekhar case however, the radii, central temperatures and central densities of the models are very highly dependant on the field configuration. This is, in part, a consequence of the pressure support no longer being dominated by degeneracy pressure, but rather both magnetic and degeneracy pressures. Hence, we observe that in the super-Chandrasekhar case

the density and temperature profiles, as well as the radii of the models are highly dependant on the field structure. Our numerical models further demonstrate that the radial temperature gradient dT/dr within the surface layers of each model falls as the magnetic field increases.

6.2.1 Summary of simulation results

We have produced a novel set of modifications to the STARS code based on our magnetic field prescription in order to compute a grid of numerical models of highly magnetised WDs. We have determined, as we had analytically, that the effect of the surface field B_s is not significant, while the central magnetic field and hence B_0 can significantly affect the B-WD mass–radius relation. This is confirmed because the mass $M \approx 1.87 M_\odot$ computed analytically for $(B_s, B_0) = (10^9, 10^{14})$ G, is in very close agreement with the mass $M \approx 1.89 M_\odot$ inferred from our numerical models for $(B_s, B_0) = (10^7, 10^{14})$ G, despite the two orders of magnitude difference in the surface magnetic fields between the two cases. By table 6.2, we have demonstrated that stable numerical models of highly magnetised super-Chandrasekhar WDs can be created provided that the central magnetic field is sufficiently large.

6.3 The Magnetic Field Plateau — magnetised white dwarf models with a field saturation radius

In the aforementioned models and as raised initially by Chatterjee et al. (2017), there exists a potential issue with the magnetic field prescription as described. As we explain (see section 6.1), by requiring a non-zero field density gradient at zero radius in the model, we have introduced a requirement for the presence of a divergent current sheet at arbitrarily small radii. While we have generated interesting results with this assumption, here we shall introduce the concept of a field saturation radius into our models, in order to drop this requirement for the presence of a current sheet that could not be well explained with any existing fossil field models. As we shall demonstrate, the key results regarding the existence, structure and cooling of super-Chandrasekar mass highly magnetised white dwarfs remain valid.

6.4 Models & Results

To produce models of strongly magnetised and super-Chandrasekhar white dwarfs the STARS code is used to produce a model of a zero-age main-sequence $3M_\odot$ star with $Z = 0.02$.

Because the mass is set directly before the initial luminosity is set and the composition of the resulting white dwarf is also set directly, the mass and metallicity of this initial model are not important. The star is then evolved up to the asymptotic giant branch (AGB) until the carbon–oxygen core has grown to about $0.6 M_{\odot}$. At this point the chemical evolution of the star is halted and an artificial mass-loss mechanism is enabled in order to strip the outer envelope of the model until a CO white dwarf with a thin atmosphere is formed. The magnetic field computation can then be enabled and the model in question can be relaxed and then allowed to proceed along its cooling track. In order to investigate a greater section of the cooling curves, we inject a uniform, constant artificial energy source into each model in order to drive the luminosity up to about $10^4 L_{\odot}$, well in excess of the predicted formation luminosity of the highest mass white dwarfs. This ensures that we explore almost the entire parameter space for these models that the STARS code modifications we have made can simulate. Setting a particularly large magnetic field (either in terms of a large B_S , a large B_0 or both) typically requires the field parameters to be increased in stages to allow the model to relax. Mass can then be directly added or removed from this model in order to produce a model of any desired mass.

6.4.1 Overview of Models with Plateau Central Magnetic Fields

We produced a series of models of high mass, highly magnetized WDs. Fig. 6.4 shows the density as a function of radius for a range of models of mass $1.2 M_{\odot}$ and $1.6 M_{\odot}$, different B_0 and different cutoff radii interior to which the field plateaus, as described in section 6.1. We find that neither B_0 nor the mass have a considerably greater effect on the density profile than the location of the cutoff radius. This may suggest that a significant range of r_c may in fact produce very similar cooling curves. As such, this provides us a free parameter of sorts that can be tuned to produce a model that, for example, correlates well with observations of over luminous Type-Ia supernovae, without requiring an unphysically strong current sheet in problematic regions of the model.

While we observe that the effect of B_0 on the density profile of the models dominates, in the left panel of Figure 6.4 we can see a higher central density at the end of cooling for the green model with the larger saturation radius in comparison to the red model with the reduced saturation radius. The larger plateau region results in a lower plateau field, over a larger region and, as such, less overall magnetic pressure support in this region and hence a higher central density. However a rather significant difference in the size of the plateau region results in only about a 5 per cent difference in central density, in comparison to the much larger reduction in density owing to the magnetic pressure support compared to the zero-field model.

Also demonstrated is the effect of the field configuration on the mass–radius relation, as noted by [Mukhopadhyay et al. \(2021\)](#) and [Bhattacharya et al. \(2021\)](#). That is, that the larger magnetic field density allows for smaller overall density throughout the model, including the very small contribution to the total density from the magnetic field mass–energy density term ([Bhattacharya et al., 2021](#)). This results in a larger radius and less compact WD at higher mass. It should be stated that this is a result of the need for a higher field strength to support white dwarfs of this mass however as a consequence, for fields much greater than 10^{14} G it is expected that increasing field density could result in a more, rather than less, compact WD ([Otoniel et al., 2019](#)). Based on suggestions by [Chatterjee et al. \(2017\)](#) we do not consider models with such strong fields so as to expect this effect nor do we require such large fields to produce and cool super-Chandrasekhar mass B-WDs.

In Figure 6.5 we show the structure of the magnetic field considered for the same selections of models as in Figure 6.4 as well as the effect of this field structure on the mass–radius profile of the models. As before, we look in detail at the $1.2 M_{\odot}$ models in order to better elucidate and illustrate the effects of the magnetic field structure. All the models shown are towards the end of their cooling phases, just before the point at which limitations in our equation of state, to deal with pressure ionization, lead to a failure to converge the model further. The top left panel of Figure 6.5 shows the effect of the implementation of the plateau magnetic field structure as described in section 6.1. The field becomes constant (gradient free) interior to the radius r_c , at B computed at that particular radius. As shown, this means that, for the same B_0 and for the same total mass, the magnetic field strength at which the plateau field is held is lower for a larger cutoff radius. The top right panel of Figure 6.5 shows the magnetic pressure contribution, as defined in section 6.1, as a function of radius. Considering only the $1.2 M_{\odot}$ models here makes the detail described for the previous panel more readily apparent. In the bottom left panel, we demonstrate that, at this point in the cooling phase for these models, the contribution of the relativistic mass–energy of the magnetic field to the total density of the model, towards the centre of the model at least, is actually large in absolute terms (compared to the central density of an equivalent mass ZAMS star), is actually negligible in comparison to the about 10^8 g cm^{-3} total central density of the models. The final plot in this figure illustrates the mass–radius profile for the considered models, showing more clearly both the effect of B_0 and the lesser, but here clearly evident, effect of the cutoff radius.

6.4.2 Super-Chandrasekhar Mass B-WD Model Results

Here we discuss in detail the cooling curves and evolution of internal structure during cooling of $1.6 M_{\odot}$ super-Chandrasekhar mass B-WDs. In Figure 6.6 we plot full cooling curves for

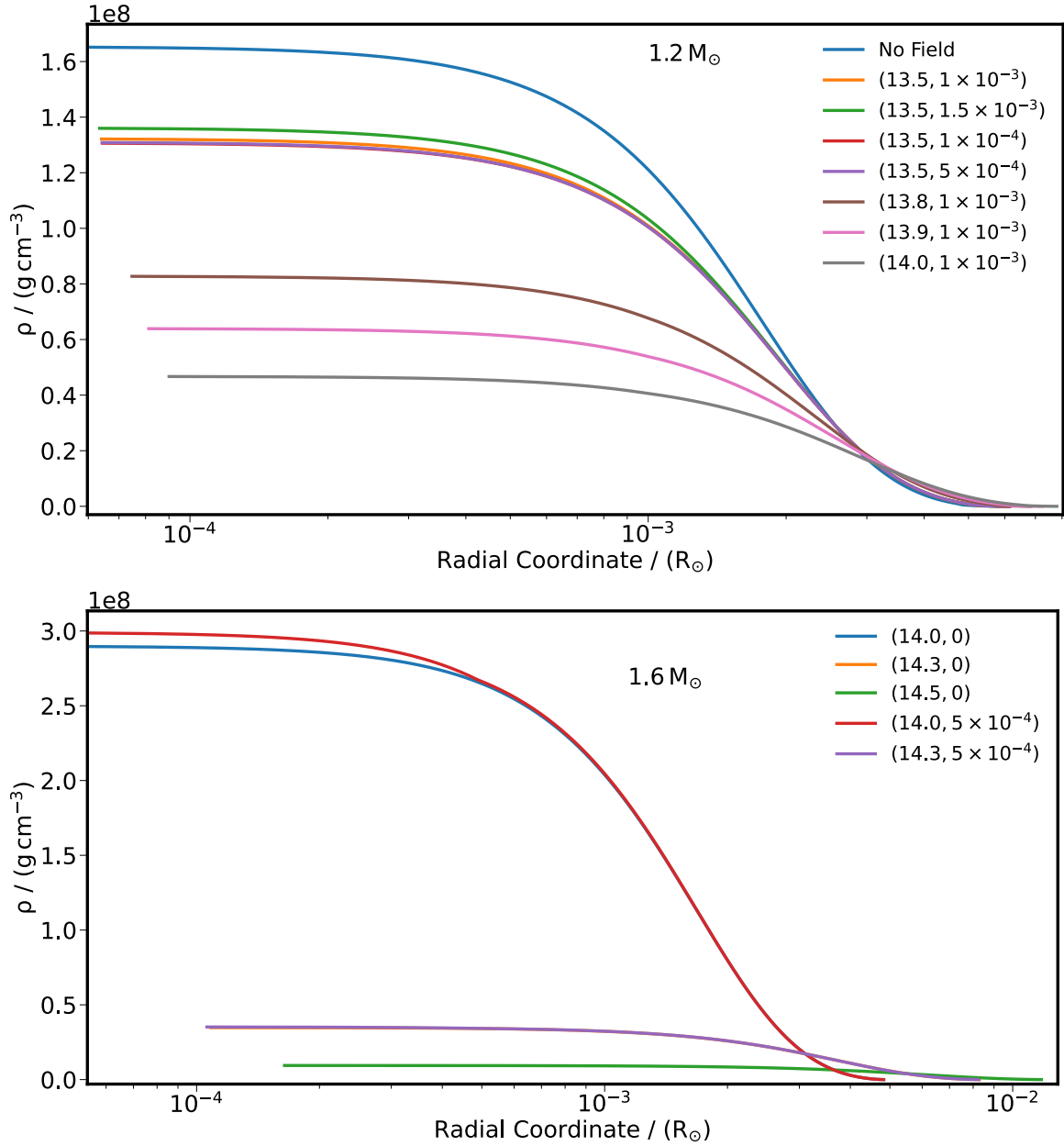


Figure 6.4 The variation of density as a function of radial coordinate, r , in the model is shown for magnetised white dwarfs with varying field strengths and cutoffs as labelled, with cutoff radii in R_\odot . The first number in parenthesis is $\log_{10}(B_0 / \text{G})$ as in [Mukhopadhyay et al. \(2021\)](#) and [Bhattacharya et al. \(2018\)](#). The surface field, B_s , is set to zero because, as shown by [Bhattacharya et al. \(2021\)](#) the magnitude of the surface field has negligible structural effects. (Continued on following page.)

Figure 6.4 Top panel (cont.): The second number in parenthesis is r_c / R_\odot , the radius of the field cutoff, interior to which the model magnetic field density is held constant. The models presented in this panel are those with masses of $1.2M_\odot$ and with a hydrogen rich atmosphere of approximately 10 per cent of the model mass. Each model's cooling curve is computed until the simulation can proceed no further, giving models that are of similar luminosities (for the same mass) but different ages. We find that the cooling timescale is shorter for a particular mass with a stronger magnetic field. We expect, as described by [Drewes et al. \(2021\)](#) for other compact objects, that this effect is due to the lower thermal pressure support required throughout the object in order to support a model of particular mass as the magnetic pressure grows larger.

Bottom panel: The variation of density, ρ as a function of radial coordinate, r is show as in the top panel, for models of super-Chandrasekhar mass, with a mass of $1.6M_\odot$ and a uniform CO composition throughout. We note that at super-Chandrasekhar mass the variation in field strength results in a very large change in central density.

all of our $1.6 M_\odot$ models, showing the evolution of the total luminosity, effective temperature, central temperature and central density with time. In the first three panels, the effect of altering the cutoff radius is imperceptible at this scale and so we consider this cooling only in the context of B_0 . Regarding luminosity, we observe three distinct phases of cooling. First, a very rapid initial phase, where the model luminosities are ordered, from largest to smallest in reverse order of B_0 . This corresponds to the luminosity suppression, at both very early and very late stages of cooling described by [Bhattacharya et al. \(2021\)](#) and [Mukhopadhyay et al. \(2021\)](#). During this early phase neutrino losses are the dominant cooling mechanism, as seen in Fig. 6.8, and where the dominant neutrino production mechanisms are plasmon decay and photoneutrino emission ([Drewes et al., 2021](#)). Between around 10^2 and 10^4 yr we enter the second phase of cooling, where the ordering of luminosities is inverted, with the highest field models having the highest temperatures. At the end of this phase there is another inversion and mild heating as the neutrino losses become negligible and the magnetic field density towards the centre of the models increases and the density of the core increases to compensate. The internal changes that result in this behaviour are apparent (for the fiducial model considered) in Figure 6.9. After this point we have stable, slow cooling owing to purely surface photon emission. In the highest field models, this is delayed by the additional magnetic pressure support towards the centre of the model, resulting in a longer (in time) cooling curve that reaches a smaller luminosity.

Similarly this three-stage cooling behaviour is observed, as expected, in the evolution of the effective temperature of the model. We note here that the small increases or bumps in both the luminosity and effective temperature of the (green line) highest field models at early times are due mainly to the stepped raising of B_0 up to the required level over the first few timesteps

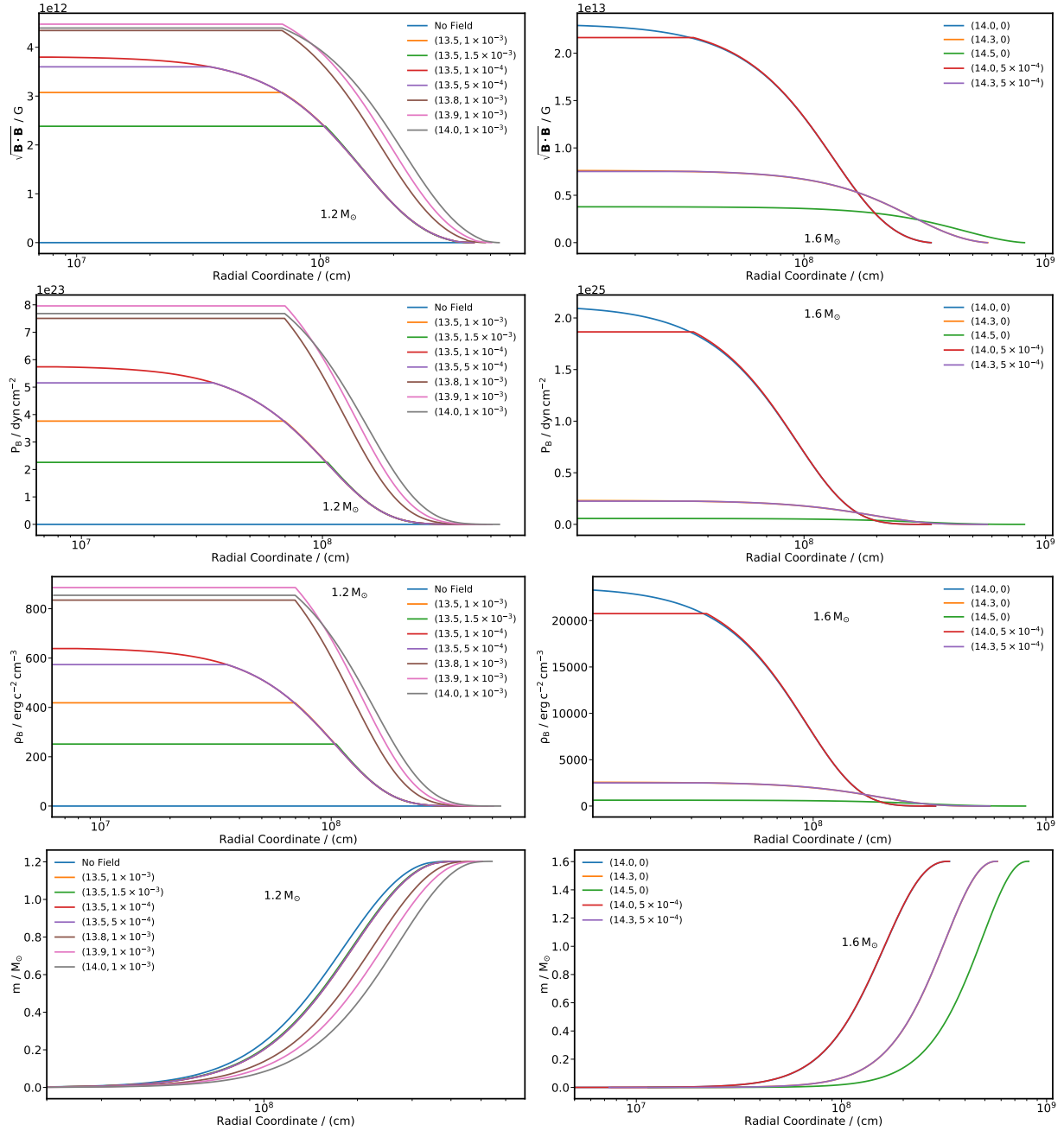


Figure 6.5 Top two panels: The variation of the model magnetic field density, $|\bar{B}|$, as a function of radius, r , is shown for the same $1.2M_{\odot}$ and $1.6M_{\odot}$ white dwarfs considered in Figure 6.4. Each one of these models is run until the point where the simulation cannot progress further owing to limitations of the equation of state. We note the presence and location of the various plateaux in the field profile, as well as the field density reached. The central field density does not exceed 10^{14} G in any of the considered models, so remaining consistent with the limits to such fields of Chatterjee et al. (2017).

Second two panels: The variation of the magnetic pressure contribution, P_B , as a function of r is shown with the super-Chandrasekhar mass results presented in section 6.4.2. We note that the brown curve, representing the model with $B_0 = 10^{13.9} \text{ G}$ with cutoff $0.001 R_{\odot}$ lies, at small radii, above the grey line representing the $B_0 = 10^{14} \text{ G}$ with cutoff $0.001 R_{\odot}$. This is due to the lower central density of the model with the larger B_0 , because there is more magnetic pressure support in this model at larger radii, as seen in the plot. This, somewhat counter-intuitively results in a weaker plateau field density.

Figure 6.5 Third two panels: As in the second two panels, but now showing the contribution of the relativistic magnetic field energy mass contribution, ρ_B . Given that central densities of highly evolved WDs of this mass are, as in Figure 6.4, of the order 10^8 to 10^9 g cm^{-3} , these contributions are, as expected, negligible. ([Bhattacharya et al., 2018](#))

Bottom two panels: The mass – radius profiles for these models are shown. We note the previously documented effect of the field strength on this relationship ([Mukhopadhyay et al., 2021](#)) as well as the notable, but considerably less pronounced, effect of the location of the outer edge of the field density plateau. While this implies a relatively free choice of this location as a free parameter in models, it suggests that constraining this parameter with observations may be challenging.

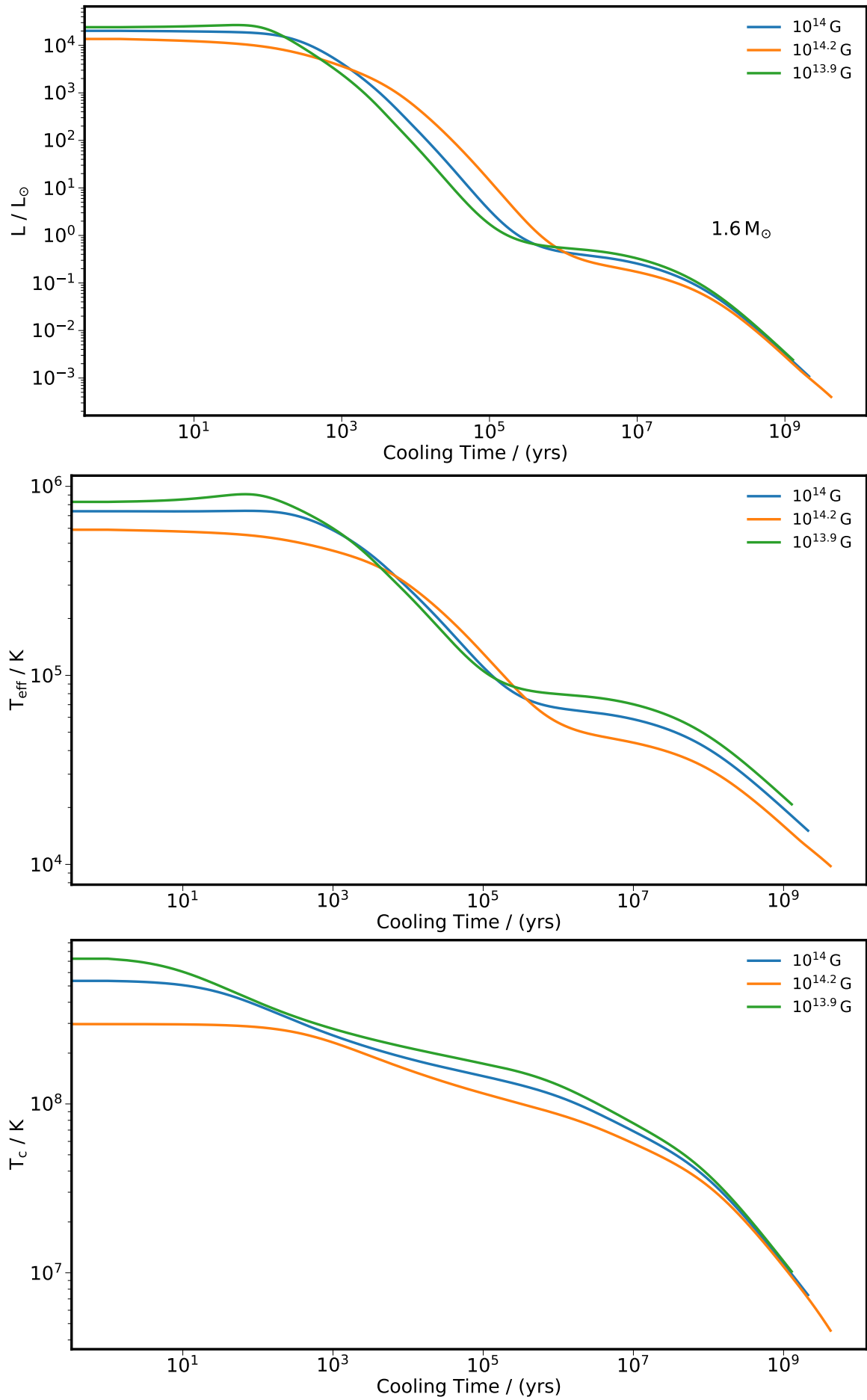
of the simulations as described in section 6.1 rather than any physical processes. Here we observe the effective temperatures of the models converge towards one another during neutrino dominated cooling and then move back apart after the inversion of temperature ordering and the onset of surface photon emission dominated cooling, when differences in the radii of the models have more significant effects on the luminosity and hence the cooling of the models. During the neutrino dominated phases of cooling the cooling rate is much more sensitive to the more similar (between models of differing magnetic field and cutoff parameters) internal temperatures and densities in the model, as observed in both figures 6.8 and 6.9. The evolution of the central temperature for these models is also as expected. In this case, once the cooling is dominated by surface photon emission towards the late part of the cooling curve the central temperatures of the different models converge to the same cooling track. However here there is no inversion of the central temperature throughout the cooling. This is because, as shown in figures 6.8 and 6.9, the majority of neutrino emission from the models during the neutrino dominated portion of the cooling is not from the centre of the model but actually from the higher temperature regions at greater radii. The temperature in this region, in the fiducial model, is larger during the earlier stages of cooling as a result of heating by the contraction of the outer regions of the B-WD as described in section 6.4.3. This high temperature region dominates the production of neutrinos during the earlier stages of cooling. This in turn dominates the cooling in general during the early stages of cooling. In the final panel of figure 6.6 we demonstrate the effects of B_0 and r_c on the evolution of central density as a function of radial coordinate and time. Here we can observe, as before, the effect of different cutoff radii on the central density of the model. Again, as before, having a large cutoff radius leads to a lower plateau magnetic field strength and thence a higher central density needed to support the B-WD. Once the interior of the B-WD has cooled off significantly this effect becomes more pronounced.

As mentioned earlier, there are phases in the cooling curves of our models of highly magne-

tised B-WDs where the cooling by neutrino losses is significant or even dominant compared to cooling by surface photon emission. As stated in section 6.1, we use neutrino loss tables of Itoh et al. (1996b). These take into account a wide range of neutrino production mechanisms, as a function of temperature and density. In figure 6.8 we present a series of plots, each showing the rate of neutrino energy loss, as a function of radial coordinate for all of the $1.6M_{\odot}$ models computed. In the early stages of cooling, in the top left panel, temperatures in the region of the B-WDs heated by rapid early contraction are sufficiently high for an extremely large neutrino production rate in this region. In addition, neutrino losses throughout the high-temperature core of the model are still very large in comparison to the later stages of cooling. In the lower B_0 models, the differences between models with different cutoff radii are more clearly differentiated, because, these are hotter and denser at this point in the cooling evolution and so the neutrino generation rate is much more sensitive to the higher temperatures in the hottest regions of these models when the field gradient is non-zero at lower and lower radii. Once the models have cooled sufficiently, to around $1L_{\odot}$, where the neutrino losses begin to diminish significantly, there is an oscillatory nature in radius for the loss rate because of small differences in the temperature profiles being interpolated in the tables of Itoh et al. (1996b), where the higher temperature neutrino production mechanisms are no longer dominant. Once the models have cooled further, only the very inefficient and slow neutrino production mechanisms, almost exclusively Bremsstrahlung, operate. By the end of the cooling curve, when the models have reached luminosities below $10^{-2}L_{\odot}$ the rate of neutrino production is almost completely absent and, as previously stated, the B-WDs continue to cool exclusively through surface photon emission.

6.4.3 Super-Chandrasekhar Mass Fiducial Model Results

In the interest of better understanding the effects of the implementation of our magnetic field prescription on the structure and cooling of super-Chandrasekhar mass B-WDs we now look in detail at the evolution of the internal structure of one particular fiducial model, a $1.6M_{\odot}$ B-WD with $B_0 = 10^{14}\text{G}$ and $r_C = 0.0007R_{\odot}$ or about 500km. As in section 6.4.2 we inject a radius independent, constant artificial energy generation term to increase the luminosity to about 10^4L_{\odot} then remove this and allow the models to cool until we are no longer able to converge on solutions owing to limitations of our equation of state. We then plot a series of Kippenhahn-like diagrams, plotting the evolution of luminosity, magnetic field strength, density, temperature, opacity and neutrino-loss rates as a function of both time and radial coordinate (Figure 6.9). Given our colour scheme, the edge of each coloured bar at the largest radial coordinate represents the effective surface of the B-WD envelope. The extent of the



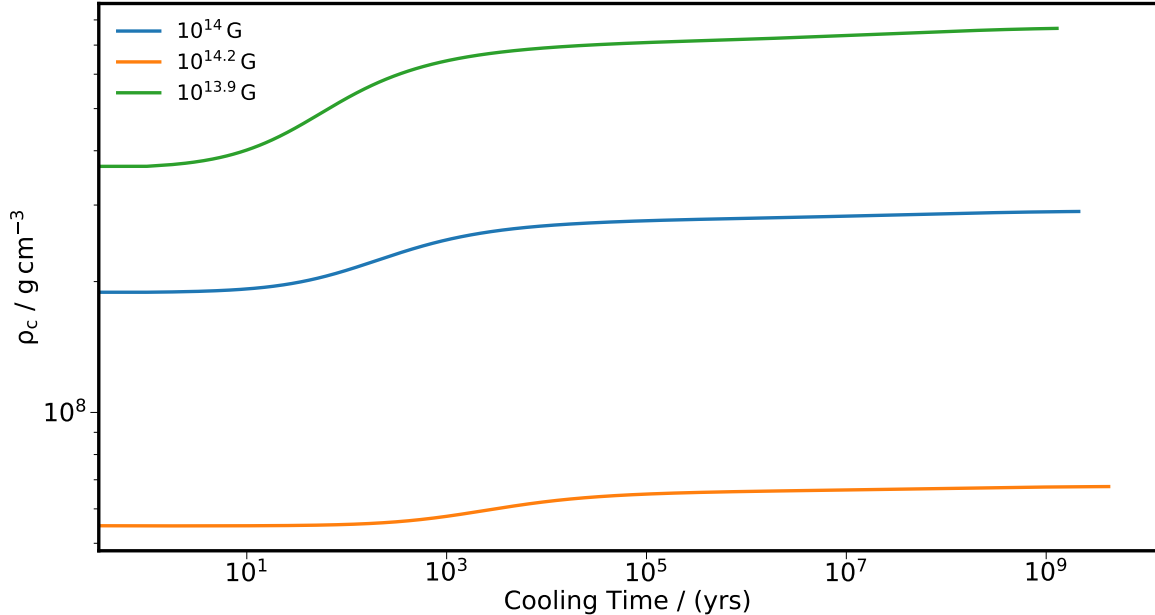


Figure 6.6 First panel: The cooling curves for the total luminosities of a series of $1.6 M_\odot$ super-Chandrasekhar mass B-WDs, with luminosity L . Each model began cooling from about $10^4 L_\odot$, achieved by uniformly injecting energy into the model, then removing this energy source and allowing the model to cool. At the higher temperatures and densities reached during the earlier portions of the curve, neutrino losses lead to a considerably more rapid cooling than radiative cooling. As shown in this plot, and the plots in the top right and bottom left panels, the cooling curves of the models in question are substantially affected by the magnitude of the magnetic field throughout the model, while the exact position of the field cutoff plateau has a much less significant effect. This cannot be easily seen at this scale.

Second panel: The evolution of the effective temperature, T_{eff} of the models is shown. As expected, the initial and final temperatures of the higher field models are lower than those of the models with lower strength fields. However there is a region between about 10^3 yr and 10^6 yr where there is an inversion in the ordering of the effective temperatures.

Third panel: The evolution of the central temperature, T_c of each model with time, t , is shown. The central temperatures and densities during the early phases of cooling are sufficiently large for efficient neutrino cooling.

Fourth panel: The evolution of the central density, ρ_c , of each model with time, t , is shown. Comparing with the plot in the bottom left panel, we can clearly see the ordering of the models as a function of the field parameters.

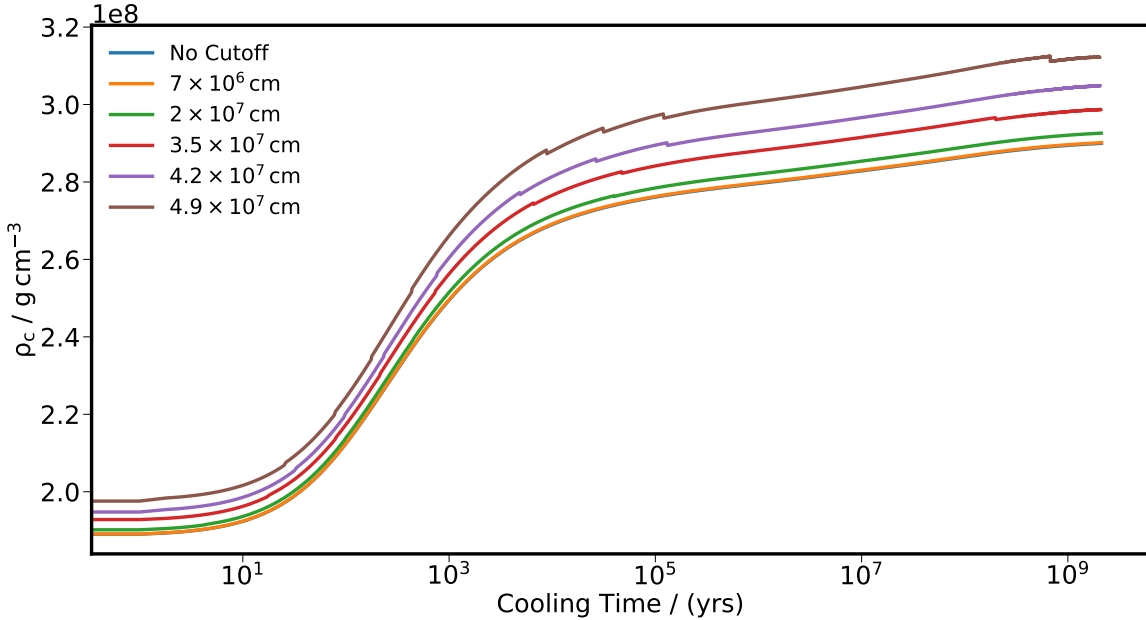


Figure 6.7 Plot of the time evolution of the central density during cooling for a 1.6M_\odot B-WD, with a saturation field density of $B_0 = 10^{14}\text{G}$, for a range of different cutoff radii, as in the fourth panel of figure 6.6. All of these models overlap very closely when the surface parameters as in panels one to three in figure 6.6 are concerned.

B-WD envelope at each timestep is most easily seen in our plots for temperature, opacity and neutrino-loss rate.

The seven panels that comprise figure 6.9 provide a fiducial example of the evolution of the model in question. We plot the time evolution of this model starting at $t_{\text{cool}} = 10^3\text{yr}$, chosen to avoid the small number of initial timesteps where the model is out of thermal equilibrium while the magnetic field distribution rearranges itself in order to reduce the (specific) entropy of the initial model on a timescale short in comparison to the thermal timescale. At early times, from around 10^3 yr to $10^{4.5}\text{ yr}$, the rapid contraction of the inflated over-luminous white dwarf generates a very significant amount of energy, peaking at above $10^6\text{ erg g}^{-1}\text{s}^{-1}$. As seen in the middle left panel of figure 6.9, this drives the temperature in a shallow region of the white dwarf just interior to the envelope towards approximately 10^9 K , allowing a number of thermal neutrino generation processes to operate with a significant energy loss. At these temperatures and densities, plasmon decay (Kantor & Gusakov, 2007) and photoneutrino production dominate (Braaten & Segel, 1993; Itoh et al., 1996b; Kantor & Gusakov, 2007). While, as seen, neutrino production continues until temperatures fall below those at which less efficient neutrino production processes, such as neutrino Bremsstrahlung, which dominates at lower temperatures (Odrzywołek, 2007; Drewes et al., 2021), (after around 10^8 yr) the effects of neutrino losses cease to be significant for the structural evolution

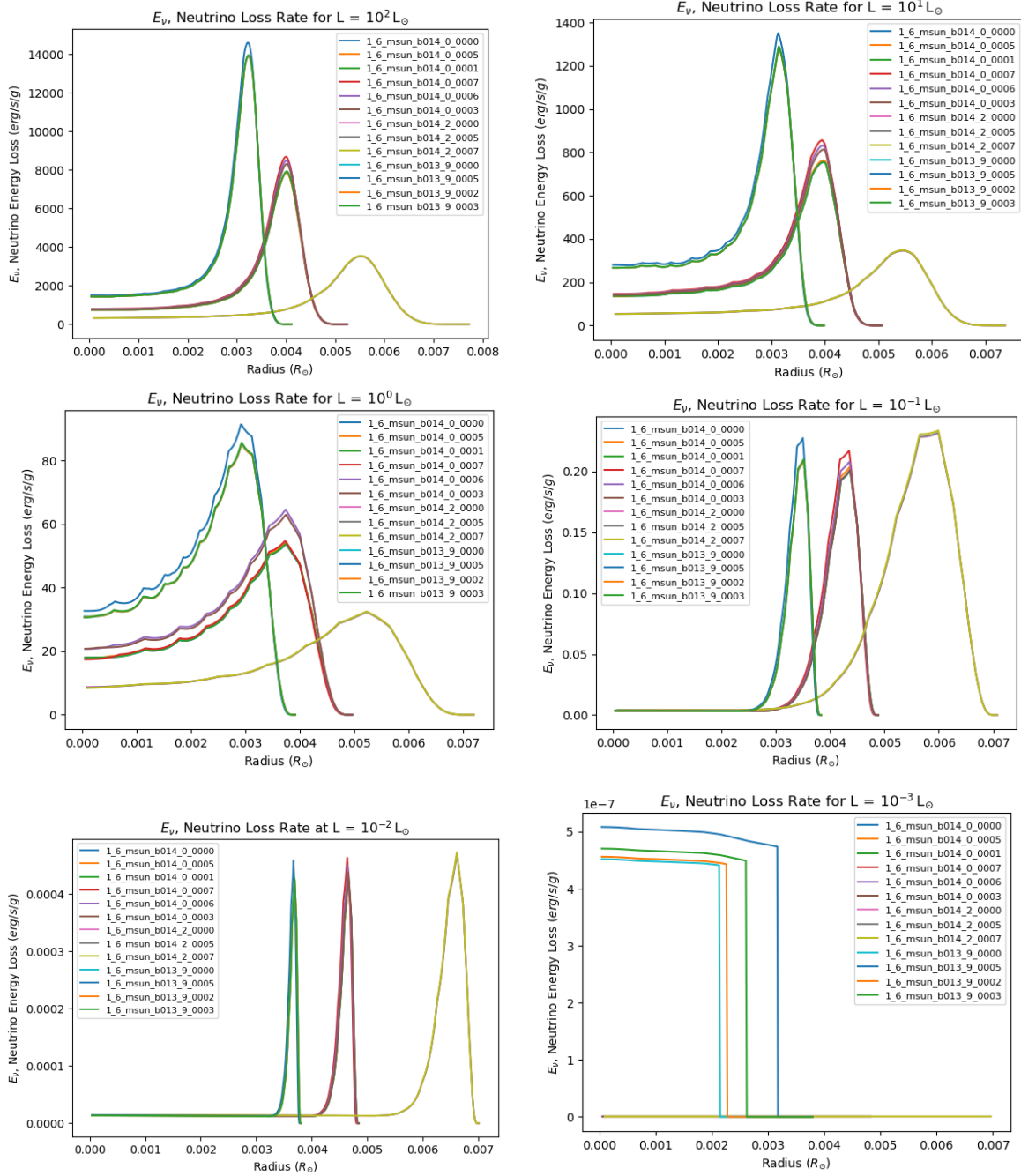


Figure 6.8 The neutrino loss rate E_ν as a function of radial coordinate in each of the models described in figure 6.6, at different points in the cooling curve (luminosities). We implement the neutrino-loss rates of Itoh et al. (1996b). Early in the cooling curve neutrino losses are extremely significant and drive a great deal of the rapid cooling observed in this section of the cooling curve. Because the higher magnetic field strength models are less condensed, with lower densities and temperatures throughout, they produce fewer neutrinos by processes dependent on these variables, such as plasmon decay, photoneutrino production and, at lower temperatures, Bremsstrahlung and recombination (see, Drewes et al. (2021)). Once the temperatures throughout the B-WD have fallen below about 10^8 K, the energy losses in neutrinos fall dramatically and cooling is dominated by surface photon emission (Shapiro & Teukolsky, 1983).

of the model after a few 10^5 yr. While specific energy losses by thermal neutrino generation of around $10^3 \text{ erg g}^{-1} \text{ s}^{-1}$ would be significant for the evolution of a lower mass white dwarf at the classical non-magnetic Chandrasekhar limit, here they are of order of the energy being released into this region of the object from continued contraction.

6.5 Summary & Conclusions

Here we have expanded upon the ideas presented by [Das & Mukhopadhyay \(2012, 2014\)](#); [Chatterjee et al. \(2017\)](#); [Bhattacharya et al. \(2018\)](#) and others in order to investigate the nature of supermassive, highly magnetized white dwarfs. The core motivation to investigate white dwarf structures that may exist above the Chandrasekhar mass is to provide a mechanism to explain overly luminous type Ia SNe ([Gupta et al., 2020](#)). Given a reasonable analytical prescription as by [Mukhopadhyay et al. \(2021\)](#), which is based on widely used prescriptions for the structure of magnetic fields in neutron stars ([Ootes et al., 2016](#); [Chamel et al., 2016](#); [Konar, 2017](#); [Raithel et al., 2019](#)), we produced a series of numerical models using STARS. These models validate the analytical prescriptions as described and provide a set of structure models that allow for the existence of overly massive WDs. It is important to note that these models do not provide an explanation for the *origin* of such objects. That is, we do not presuppose a mechanism for the generation of such large magnetic fields in WDs. A wide range of mechanisms for the generation of extremely large magnetic fields in compact objects has been proposed involving dynamo processes ([Ginzburg et al., 2022](#)), but perhaps most promisingly, via a fossil field inherited from the progenitor star ([Hu & Lou, 2010](#); [Keszthelyi et al., 2022](#)). An issue was identified in this approach, namely that the requirement for a non-zero magnetic field gradient to exist at all points throughout the star. Because, as first discussed by [Eggleton \(1971\)](#), the code variables m and r , or rather, the terms $\frac{d \ln P}{dm}$ and $\frac{d \ln r}{dm}$ are singular as $m \rightarrow 0$, we use $m^{2/3}$, r^2 , respectively, instead of m and $\ln r$ near $m = 0$. As such, the difference equations are solved for exactly at $m = 0$ where the boundary conditions are applied. Hence here we solve

$$\frac{d \log P}{d(m^{2/3})} = -3 \frac{G}{8\pi} \left(\frac{m^{2/3}}{r^2} \right)^2 P^{-1}, \quad (6.3)$$

for the pressure expression, and,

$$\frac{d(r^2)}{d(m^{2/3})} = \frac{3}{4\pi} \left(\frac{m^{2/3}}{r^2} \right)^{1/2} \rho^{-1}, \quad (6.4)$$

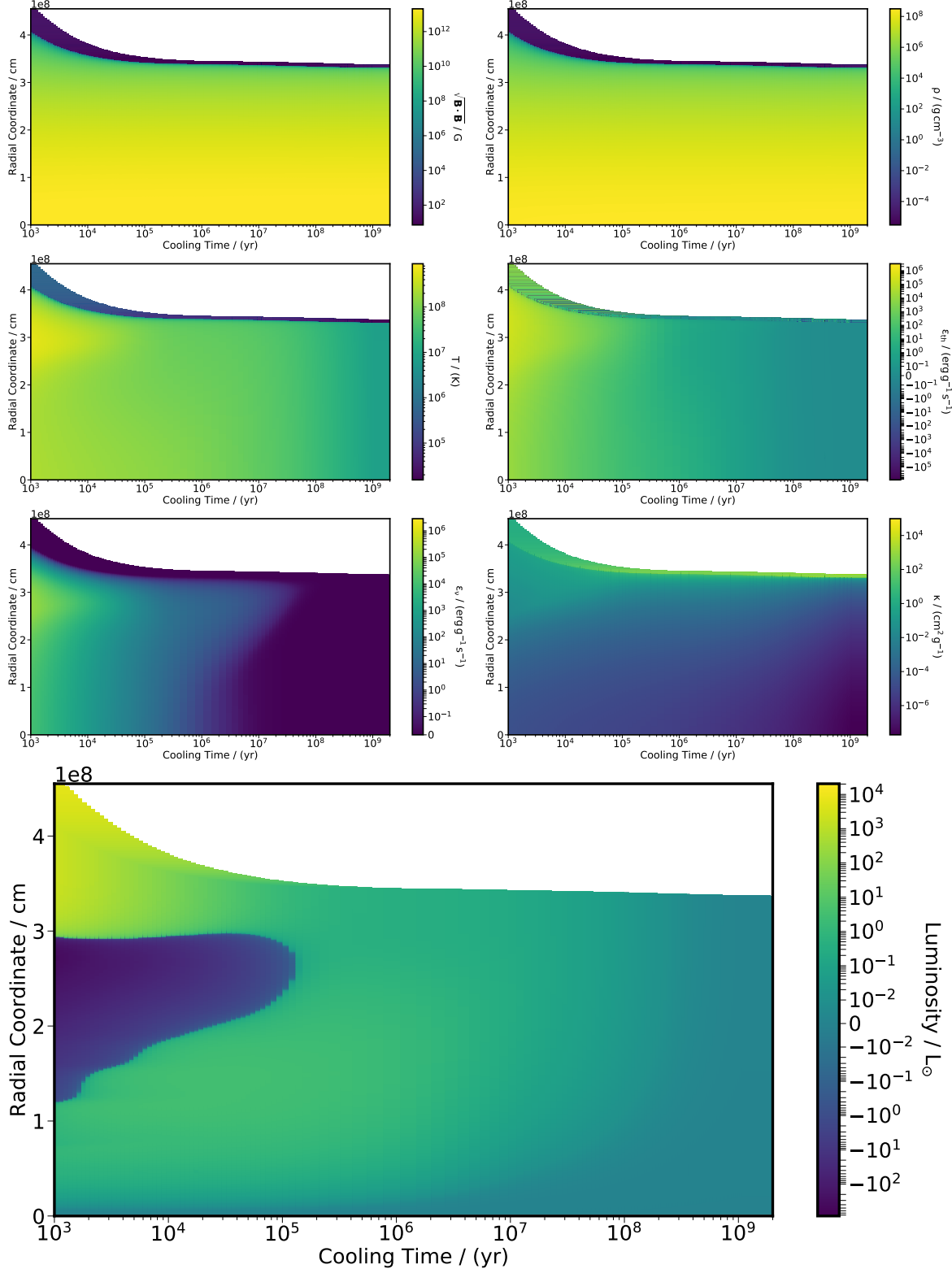


Figure 6.9 The internal evolution of various variables for a specific fiducial super-Chandrasekhar mass model, specifically one with mass = $1.6 M_{\odot}$, $B_0 = 10^{14}$ G, and with a magnetic field cutoff radius of $0.0007 R_{\odot}$. All plots track some internal variable as a function of the radial coordinate and the age of the model. (Caption continued on the following page.)

Figure 6.9 **Top left panel:** The evolution of the magnetic field strength throughout the model as a function of radial coordinate and time, as before. With the exception of the region where the cutoff is applied, the field is a smooth function of the density. Hence, as the model cools and its central regions contract further, the magnetic field increases to compensate, holding the model up at low luminosities. Naturally, this would not be the case if the field were decaying on the cooling timescale by, for example, Ohmic dissipation ([Bhattacharya et al., 2021](#); [Heyl & Kulkarni, 1998a](#)) or Ohmic dissipation enhanced by Hall drift ([Heyl & Kulkarni, 1998a](#); [Cumming, 2002](#)) or ambipolar diffusion.

Top right panel: The evolution of the density ρ as a function of radial coordinate and time.

Middle left panel: The evolution of the temperature throughout the model again as a function of radial coordinate r and time t . During the earlier stages of cooling we observe that the temperature is sufficiently high for effective neutrino cooling. In fact, during these stages, the cooling of the entire B-WD is dominated by neutrino losses. Only in the later stages of cooling when Bremsstrahlung is the dominant neutrino production mechanism is the neutrino loss rate sufficiently small for surface photon emission to overtake as the dominant cooling mechanism.

Middle right panel: The thermodynamic energy release (loss) owing to contraction (expansion) of the B-WD as a function of radial coordinate r and time t for the $1.6M_{\odot}$ fiducial model. We see that, once the rapid initial contraction of the model has concluded following the removal of the artificial energy source discussed in section 6.1 at the start of the cooling curve, the energy generation owing to thermodynamic contraction is small and constant as expected. The very rapid early contraction of the model heats the region between around 0.005 and $0.006 R_{\odot}$ very strongly further leading to the very strong neutrino production seen in this region.

Bottom left panel: The evolution of the neutrino-loss rate as a function of radial coordinate r and time t . Neutrino losses as implemented in the code are according to [Itoh et al. \(1996b\)](#) and include a wide range of neutrino production processes. As described in the caption for the Middle right panel, the neutrino loss rate, at least when processes such as photoneutrino production and plasmon decay are dominant is a strong function of temperature and density and the rapid cooling by neutrino losses can be easily seen when this plot is compared to the plot of temperature evolution.

Bottom right panel: The evolution of the opacity as a function of radial coordinate and time. In large regions of the model, the field is strong in opacity terms, that is to say, $B/10^{12} G \geq T/10^6 K$ (the point at which, roughly, the magnetic energy density is comparable to the thermal energy density), such that the opacity is dominated by the field dependent Potekhin's opacity rather than the usual Kramers' opacity. The smooth transition from computing both (tabulated OPAL opacities added in reciprocal to the Potekhin opacity) can be seen.

Final bottom panel: The evolution of the luminosity, L , of the model as it cools. During the very early stages of cooling, luminosity falls rapidly, particularly in the regions where neutrino losses are most significant. The fiducial model cools rapidly below solar luminosity before gradually cooling to about $10^{-3} L_{\odot}$ on a Gyr timescale.

for the radius equation. As such, as $m \rightarrow 0$, or rather, as $m^{2/3} \rightarrow 0$,

$$\frac{m^{2/3}}{r^2} \rightarrow \left(\frac{4\pi\rho}{3}\right)^{2/3}. \quad (6.5)$$

This analysis raises an obvious problem. Because our earlier models have continuously increasing magnetic field density as a function of density (and hence, of radius) the underlying current sheath that exists in order to generate the field at this radius must support an infinite current density as $m^{2/3} \rightarrow 0$ ([Lander & Jones, 2009](#)). This is of course, unphysical. In order to alleviate this problem, we implemented a saturation radius, a fixed fraction of the total stellar radius within which the field density saturates. These models, presented and discussed in section 6.4.1, have zero magnetic field gradient as $m^{2/3} \rightarrow 0$ and, as such, have central magnetic fields that can be sustained by current sheaths supporting a finite current density. Having implemented this technique, we present in Figure 6.9 a series of Kippenhahn diagrams of the internal evolution of a super-Chandrasekhar mass ($1.6M_{\odot}$) highly magnetized white dwarf, where the use of a saturation radius as discussed allows this structure to exist without the requirement of an unphysical, infinitely dense current sheath. As such, we have presented here a series of models that are compatible with the super-Chandrasekhar mass structures proposed as progenitors for overluminous Type-Ia supernovae, with internal structures that require large, but physically plausible internal magnetic field configurations, without need for an unphysical current sheath configuration at increasingly smaller radii.

Chapter 7

Discussion and Conclusions

'Oh, hello... Come, sit with me, my fellow traveller. Let's sit together and watch the stars die.'

>Sure, why not.

Chert and the player,
Outer Wilds

In this chapter, we summarize all of the work undertaken over the course of this Ph.D. We discuss the aims and objectives of each project, the advancements made with regards to the methodologies employed to make progress on these topics and the results obtained. We describe the work in this dissertation in the context of the existing literature, as well as suggesting and discussing possible future work that could be undertaken to build upon what we have achieved here.

7.1 Literature assessment and details of computational methodologies

Throughout the first four chapters of this dissertation we presented a comprehensive outline of the physical and mathematical background of the field of stellar evolutionary astrophysics, beginning with a brief overview of the mathematical framework for stellar evolutionary codes in Chapter 1.

In Chapter 2, we provided a detailed and motivating discussion of the literature relating to Thorne-Żytkow Objects, one of the key focuses of this study. We discuss the works of TŻ, [Thorne & Żytkow \(1975\)](#) and [Thorne & Żytkow \(1977\)](#), the initial proposals for a new form of stellar structure, comprising of a giant- or supergiant-like envelope surrounding a neutron star core. Much of the work of TŻ is analytical in nature, where stellar structure calculations were performed, they were static in nature and made use of the Generate Outer

Boundary (GOB) program ([Paczyński, 1969](#)) rather than a Henyey-based envelope code. Their work was followed up by [Eich et al. \(1989\)](#); [Cannon et al. \(1992\)](#); [Cannon \(1993b\)](#) and [Podsiadlowski et al. \(1995\)](#), where STARS, or rather, a heavily modified iteration of that code, was used in order to compute evolutionary sequences of TŻO structures. The structures of TŻOs as computed by TŻ and those as computed by Cannon et al. are qualitatively similar but have some important differences between them. We describe these as the *canonical* TŻO models in sections 2.2.1 and 2.2.2, respectively. In brief, all of these models share key properties, the presence of a knee in the temperature–density profile at the base of the convective envelope, below which sits a radiative halo. In this region, the infalling material accreting in an Eddington-limited manner onto the neutron core gives up its gravitational potential energy. In both the models of TŻ and Cannon et al., there is a class of models (giants) wherein this form of energy release dominates the energy budget of the object. We describe the possible nucleosynthetic implications of the unique structures of these objects, in particular relating to the interrupted rapid proton process (irp) in section 2.3. This proton capture process was proposed by [Cannon \(1993b\)](#) as a solution to an issue that [Eich et al. \(1989\)](#) experienced in computing models of high mass TŻOs, namely the insufficiency of other nuclear burning mechanisms to satisfy the energy budgets of the objects in question. We outline some of the intrinsically hydrodynamical problems related to the evolution of TŻOs in section 2.4, with a brief discussion of the formation pathways of TŻOs in section 2.4.1 and of their deaths, and the possible observational implications thereof, in section 2.4.2.

In Chapter 3 we gave a brief overview of the phenomenon of very large magnetic field densities in compact objects. We discuss both highly magnetized white dwarfs and highly magnetized neutron stars. Specifically from the discussion of overly luminous type Ia supernovae and whether the progenitors of such objects could be white dwarfs existing above the Chandrasekhar mass, supported by magnetic pressure, we motivated the study of the structures of B-WDs. We noted, as did [Das & Mukhopadhyay \(2014\)](#) and others, that the decay of the magnetic field that supports the super-Chandrasekhar mass below the current mass of the B-WD in question could serve as the trigger for the deflagration that initiates the supernova in question. We discuss the behaviour of electrons and condensed matter in large magnetic fields and hence motivate the implementation of a prescription for magnetized white dwarfs in to STARS. Additionally discussed in section 3.3 are some of the relevant mechanisms by which neutrons can be generated in processes other than nuclear burning. This is of relevance for both the study of magnetized compact objects and for TŻOs.

In Chapter 4 we undertook a comprehensive overview of the relevant, for the purposes of our projects, details of the two one-dimensional, Henyey-based stellar evolution codes that we made use of throughout this dissertation, STARS and MESA. In section 4.1 we discussed in

general terms the fundamental integration technique that underpins both of these codes. In section 4.2 we discuss in more detail the novel features of STARS and in particular some of the modifications that have been made in order to facilitate the work undertaken on exotic stellar objects. This includes implementation of a core-envelope artifice, in order to connect the equation of state of the envelope to that of the neutron core, which we discussed in detail in section 4.2.2.1. We also implemented an expanded series of tables for opacities and thermal neutrino generation rates. This was required in order to cover the much wider range of temperatures and densities we encountered in the study of TŻOs. Additionally, modifications to implement the modified electron mass-based core-envelope artifice, routines to compute the opacity and chemical potentials in a neutron dominated environment and a series of convergence aids needed to compute such TŻO models were outlined in section 4.2.2.2. In section 4.3 we briefly discussed the Modules for Experiments in Stellar Astrophysics code (MESA), as well as motivating its use as a companion code to STARS.

7.2 New equilibrium structures for Thorne-Żytkow Objects

In chapter 5 we presented a new grid of envelope solutions for Thorne-Żytkow Objects. Having outlined the existing published models of TŻOs and discussed some of their possible limitations, in particular the nature of the interface between the neutron star core and the rest of the envelope in chapter 2, we here computed a grid of envelope models for TŻOs with a parameterized implementation of accretion on to the neutron core. In section 5.2 we presented a demonstrative grid of these models and discussed the implementation of a Cannon et al. accretion prescription, as mentioned. In section 5.2.1 we presented and analysed the results of these computations, summarizing the quantitative details in Table 5.1. In Figures 5.2 to 5.6 we showed the basic structural features of our new models and summarized the key photospheric, knee and maximal features of the models in Figure 5.7. We compared these models to the existing models of TŻOs and found that our models provide an additional series of solutions with a structure qualitatively similar to the existing supergiant-style solutions. The base of the convective envelope (the knee) in our models is located further away from the core, in terms of radius, by a factor of 10^4 to 10^5 and in terms of mass by a factor of 10 to 100. Unlike in previous models, the region below the base of the convective envelope, the halo, is always non-degenerate and, while our models' knees occur at higher densities than those of existing solutions, our peak halo densities are as much as 5 orders of magnitude smaller. The characteristic and differential planes of stellar structure were employed as an analysis tool throughout in sections 5.8 and 5.2.4.1, demonstrating the thermodynamic consistency of our solutions. In section 5.4 a point-by-point comparison to existing models of TŻO

envelopes was made and the limitations and caveats applicable to our models were discussed. Section 5.5 summarizes our key conclusions. In section 5.4.1 we discussed the differences between our series of models and those of TŻ, Cannon et al., Eich et al. (1989), Biehle (1991, 1994) and others. Our models agree, in broad, qualitative terms with these canonical models, sharing the key structural feature with all of these models, that is, the presence of a very sharp, in terms of density, transition from convective envelope to radiative halo at the knee. Additionally, our models, even those with accretion rate not in agreement with the Cannon et al. style rates are outwardly very similar to those of TŻ *etc.* We have M-type supergiant objects with very extended, diffuse and cool envelopes, with low effective temperatures and greatly reddened photospheres, lying even closer to a Hayashi track than candidate sAGB stars of similar masses (O’Grady et al., 2023). Internally, our models resemble most closely the supergiant-like solutions of TŻ & Cannon et al., with an envelope supported by the burning of nuclear fuel above the knee. We found, as did they, that hydrogen burning turns off sharply below the knee and a shell of helium burning in the radiative region below the knee. Despite these qualitative similarities, our models also show significant differences to the canonical models. They are much more expanded in terms of mass and radius, with the knee located considerably further out from the core. There is around $10^{-7} M_{\odot}$ of material located below our knees, whereas TŻ computed more like $10^{-10} M_{\odot}$ in their models. As a result, our models’ maximum temperatures, densities and hence electron degeneracy and plasma interaction parameters are considerably smaller. While our models, even at masses comparable to the giant-style solutions of TŻ, are supported primarily by nuclear burning, the region in the halo where the gravitational potential energy of the infalling material is more extended, and in fact, our halo is not isothermal, but increases in temperature with decreasing radius, and admits a density inversion near the core, driven by the helium burning shell. Concerned by both the possibility of instabilities, as were TŻ, and by the presence of such a density inversion, we undertook a series of validating tests. A simple analytical stability test for the presence of a vibrational instability in a radiative burning region was carried out, following the methodology of Dennis (1971) and Yoon et al. (2004). We found that our helium burning region does in fact admit a small amplitude oscillation for such a region as first described by Stothers & Wen Chin (1973) but is otherwise stable. In order to validate the assumption of a slow, near hydrostatic accretion on to the neutron core, the motivation for our use of a central boundary condition approach with an isolated neutron core, we recomputed two of our fiducial models with the hydrodynamical solver features of MESA enabled. This allowed for the computation of an acceleration term by assigning to each calculation point a cell-centered velocity. We found that at no point did the velocities of infalling material exceed around $10^{-2} \text{ cm s}^{-1}$, sufficiently slow to enable our earlier assumption to be safely

used. We tested the effects of varying accretion rates on the models in section 5.2.4 and found that the computed structures of the models at varying accretion rates could be well understood in our framework, even when the rate selected was not well physically motivated. Again, the characteristic plane of stellar evolution was then employed to explore and verify the thermodynamic consistency of the solutions, as before. We found that the topology of our solutions is independent of the accretion rate and is in fact consistent even when no accretion is permitted at all, raising the possibility that such a series of models could serve as the starting point for constructing models of other hypothetical astrophysical objects consisting of a compact object core, with a large diffuse, primarily convective envelope.

As we discussed in section 1.2, STARS and MESA serve as a useful pair of companion stellar evolution codes. In section 5.3 STARS was used to make models of TŻOs. This approach, where the entire core is to be directly modelled by altering the effective electron mass in the semi-analytical [Eggleton et al. \(1973\)](#) equation of state, carries with it a range of additional difficulties and complications. As we presented in section 5.3.1, the result of this investigation was a series of models of objects with cores, supported by degeneracy pressure, wherein the effective mass of the electron is between that of the electron, as in a white dwarf and that of the neutron, as in a neutron star. These objects behave as intermediate states between AGBs and TŻOs, as such, we have dubbed them hybrid-AGBs²¹. In these hybrid-AGBs, as we increase the maximum effective electron mass in the core, the degeneracy pressure support increases, allowing the core to grow more massive and hence, more compact. With a more massive and more compact core, the transition region from the core to the envelope became sharper, and the region in which nuclear burning occurs became smaller, and the burning more intense. In section 5.3.2 we presented the chemical structure of our hybrid-AGB models, which showed significant variation when compared to a normal AGB model of equivalent mass. Given the previously discussed difficulty in lifting the observational degeneracy between sAGB stars and TŻOs, and how anomalous surface abundances are likely the best tool for doing this, we show the surface abundances of these hybrid-AGB models in Figure 5.22. We further noted that, by employing the modifications made to STARS for the study of AGBs, we are likewise able to compute TDU events in our hybrid-AGBs, which allow the enrichment of their surfaces in s-process elements, as well as in the possible products of the ipr-process. We conclude our investigation in to TŻOs with a detailed discussion and comparison to previous work in section 5.4.1, and a broader conclusion in section 5.5.

²¹We settled on this name as a third option. I initially suggested “hyper-AGB”, but found that [Doherty et al. \(2014\)](#) had previously used this term to refer to thermally pulsating AGB-like stars that ignite neon off-centre in their cores. Rob Izzard suggested “über-AGB”, but was rejected for sounding too “heavy metal”. We finally settled on “hybrid-AGB”, as suggested by Anna Żytkow.

7.3 Super-Chandrasekhar mass, highly magnetized white dwarfs: possible overluminous SNe Ia progenitors

Motivated by the prospect of using overly massive white dwarfs as progenitors of observed overly luminous type Ia supernova, we undertook (Chapter 6) an investigation in to highly magnetized white dwarfs. We began with the an analytical prescription for the magnetic field density $B = \sqrt{\mathbf{B} \cdot \mathbf{B}}$ from [Gupta et al. \(2020\)](#); [Bhattacharya et al. \(2021\)](#) and [Mukhopadhyay et al. \(2021\)](#). This we implemented into the equation of state solving routines in STARS. The prescription was modified to allow for the use of a saturation radius in addition to the saturation density described by [Mukhopadhyay et al. \(2021\)](#). We made use of this saturation radius in order to alleviate the issue of unphysical current sheaths which arises when computing models with a non-zero central field gradient. We then computed the magnetic field contributions to the pressure and relativistic energy-density at each mesh point. We likewise modified the opacity routines to compute the magnetic field dependant Potekhin opacity ([Potekhin & Yakovlev, 2001](#); [Ventura & Potekhin, 2001](#)) which is expected to dominate at high field strengths. Additionally, a wide range of thermal neutrino generation mechanisms, as discussed in section 3.3, were implemented, in order to correctly capture the neutrino dominated cooling phase of these B-WDs, at early times. We produced a grid of models initially to validate the prescription. In Figure 6.1 we presented the mass–radius relationship for a series of B-WD models for a range of magnetic field parameters. We computed a mass–radius relationship that is in good agreement with the wholly analytical mass–radius curves computed by [Mukhopadhyay et al. \(2021\)](#). Most notably, as we showed in table 6.2, a series of models computed with field parameters $B = (10^7, 10^{14})\text{ G}$ admitted a super-Chandrasekhar maximum mass, of around 1.9 M_\odot supported solely²² by degeneracy and magnetic pressures. In Figures 6.2 and 6.3 we showed the internal density and temperature structures for two series of models, at two different fixed masses, one sub-Chandrasekhar mass (0.55 M_\odot) and one super-Chandrasekhar mass (1.60 M_\odot). The sub-Chandrasekhar mass models were computed at four different sets of magnetic field parameters, three non-zero, and one sufficiently large to greatly alter the density and temperature structures. The super-Chandrasekhar mass models were computed for three different sets of field parameters, all non-zero and all sufficiently large to admit supermassive solutions. In both cases we confirmed that such field configurations can indeed, as was expected, support super-Chandrasekhar mass white dwarf solutions.

²²Essentially zero thermal pressure support is present at luminosities as low as $L/L_\odot = 10^{-4}$ in comparison to the other sources of pressure support, but strictly speaking is non-zero at all finite temperature ([Fortin et al., 2018](#)).

A potential issue arose around the presence of a non-physical current sheath being implied in our model solution. We addressed and resolved this issue by the introduction of an aforementioned saturation radius, which serves as a model free parameter that can be tuned to produce a model that aims to reproduce observations, for example. The main benefit of this approach was that we were able to demonstrate that our earlier finding regarding the structure of highly magnetized super-Chandrasekhar mass white dwarfs remained valid, without the requirement for the presence of a non-physical current sheath at very small radii in the models. Our key results in this investigation were detailed in section 6.4.3. We found that the value of the saturation radius had a much smaller effect on the density profiles of the models of the same mass than B_0 . Indeed, different r_c were found to produce similar structures and cooling curves, further enabling the use of this as a tunable free parameter to fit observations. As an illustration, we found that an increase in the saturation radius of over 10x produced a difference in the central density of the model of less than 5 per cent. In Figure 6.9 we presented a number of detailed structure plots for the evolution and cooling of a specific super-Chandrasekhar mass model, with magnetic field strength, density, temperature, thermal energy release/loss, thermal neutrino losses and luminosity plotted as a function of radius and time, illustrating in detail the cooling evolution of an archetypal example of such a massive B-WD. Finally, we provided a more in depth discussion of these results in section 6.5, to which we particularly refer the reader for the discussion of the origin of such large magnetic fields in B-WDs, such as through the inheritance of a large progenitor fossil field.

7.4 Potential avenues for future work

Here we briefly discuss a few potential directions that could be taken to expand and develop on top of the work that has been presented in this dissertation, on both the topics of TŻOs and hybrid stars, as well as highly magnetized white dwarfs and other compact objects. Some of these possible research directions are relatively simple iterative improvements on the work presented here, while others are much more long term prospects that we shall discuss more in the abstract, rather than laying out specific research proposals.

7.4.1 TŻOs and other hybrid stars

The basic structure of a TŻO, whether they be the canonical models of TŻ, Cannon et al. *etc.* or the series of models we have presented in Chapter 5, are inherently challenging to compute numerically, or to understand analytically. A TŻO's structure covers an extremely wide range of densities and temperatures, from the cool, low-density diffuse envelopes to the extremely

centrally condensed neutron degenerate core. Models of these objects therefore must bring together all the relevant physics, in all of these regimes. The scope of this challenge becomes apparent when one considers the physical ingredients that are at play here, from intense nuclear burning in regions with very large local convective velocities to the equation of state of a neutron star. In short, a comprehensive understanding of these objects is to bring together a wide range of subjects that are still being hotly discussed and contested. Given the work we have presented, a very clear extension to this work would be the implementation of a fully up to date neutron star equation of state in to a Henyey-style evolution code such as MESA. This in itself would be a challenging task, even if a strongly preferred neutron star EoS were to emerge. Even so, converging full TŻOs models in this framework is expected to be difficult, for all of the reasons we have discussed throughout this dissertation. Given the nature of astrophysical neutron stars, it would be reasonable to assume that the neutron cores of TŻOs would be rotating. Indeed, it has been suggested that the gravitational wave emission from the spin-down of these neutron cores might well provide an observational signature of TŻOs ([DeMarchi et al., 2021](#)). Modelling TŻOs in a Henyey code more suited to handling rotation in a self-consistent manner, such as ROSE ([Potter et al., 2011](#)) would allow the interaction between the rapidly rotating and spinning down core and the diffuse envelope to be investigated. This being said, a more comprehensive look at the interaction between the rotating neutron core and the envelope will require the use of a two-dimensional Henyey-style code, as by [Li et al. \(2006\)](#) for example, but this would bring with it a suit of additional difficulties associated with such 2D codes.

Beyond the realm of the Henyey evolution code, two other promising avenues of research regarding TŻOs relate to hydrodynamic investigations of their formation and the use of population synthesis codes including grids of TŻO models to produce synthetic observables that may help to constrain population statistics for TŻOs. Further research on the first topic would make use of Smooth Particle Hydrodynamics (SPH) codes to investigate the common envelope phase that leads to the formation of a TŻO, as we discussed in section 2.4.1. Existing work on this topic ranges from early investigations of the prospect of the TŻO forming CEE event launching a jet, by [Chevalier \(1993\)](#), to modern simulations of neutron star CEE events by [Hirai & Podsiadlowski \(2022b\)](#).

Regarding the second research direction, another gap that exists in the literature relates to the self-consistent inclusion of ‘exotic’ stellar and stellar-like objects in rapid population synthesis codes. An interested prospect then is to investigate what proportion of XRBs might end up as TŻOs, or even if all neutron star companion XRBs could produce TŻOs. This investigation would require a self-consistent implementation of TŻOs in a binary population code, so as to produce a catalogue of synthetic observables, to be compared with

observations. The code `binary_c` (Izzard et al., 2006) already contains a simple treatment of TŻO populations, by flagging XRB systems that begin CEE in a manner consistent with TŻO formation channels. This allows for an estimate of TŻO populations but does not include any prescription for their evolution. Given the effects that TŻOs and their explosions (Moriya & Blinnikov, 2021) may have on, for example galactic chemical evolution, an evolutionary grid based approach, with proper interpolation in a model grid could provide the first, completely self-consistent inclusion of these objects in a binary population code.

7.4.2 Highly magnetized and supermassive compact objects

In this dissertation we have presented a series of models that supported the argument that super-Chandrasekhar mass B-WD structures could exist in equilibrium and cool over Gyr timescales. Given the timescales over which NS field decay mechanisms, primarily Ohmic decay and Hall drift operate, it is conceivable then that the analogous decay of the magnetic field in an overly massive B-WD could trigger a Type Ia supernova explosion at above the Chandrasekhar mass, once the maximum mass that the field configuration can support falls below the current mass of the object. This could provide a progenitor model for overly luminous Ia SNe. The main future directions for work on this topic would revolve around first refining the models of B-WD, with greater input from modern NS models, and secondly, much as with TŻOs, these novel models could be incorporated into rapid binary population synthesis codes. Given the discrepancies that still exist between observed Galactic Ia SNe rates and those predicted by population synthesis codes (see, e.g. Toonen et al. (2012) for further discussion) the implementation of such supermassive B-WDs into these codes could provide a solution. Naturally, an additional difficulty here arises in the modelling of the progenitors of the B-WDs themselves. This itself would require a better understanding of how large fossil fields or, more specifically, the inheritability of large fossil fields is distributed across a stellar population of white dwarf progenitors/progenitor systems.

Bibliography

- Andrássy R., Spruit H. C., 2013, A&A, 559, A122
- Arnett W. D., Meakin C., Viallet M., Campbell S. W., Lattanzio J. C., Mocák M., 2015, ApJ, 809, 30
- Arnett W. D., Meakin C., Hirschi R., Cristini A., Georgy C., Campbell S., Scott L., Kaiser E., 2018b, preprint, ([arXiv:1810.04653](https://arxiv.org/abs/1810.04653))
- Arnett W. D., Meakin C., Hirschi R., Cristini A., Georgy C., Campbell S., Scott L. J. A., Kaiser E. A., 2018a, preprint, ([arXiv:1810.04659](https://arxiv.org/abs/1810.04659))
- Arnett W. D., Meakin C., Hirschi R., Cristini A., Georgy C., Campbell S., Scott L. J. A., Kaiser E. A., 2018c, preprint
- Audouze J., Truran J. W., Zimmerman B. A., 1973, ApJ, 184, 493
- Bahcall J. N., 1964, ApJ, 139, 318
- Ball W. H., Tout C. A., Źytkow A. N., 2012, MNRAS, 421, 2713
- Bandyopadhyay D., Chakrabarty S., Pal S., 1997, Phys. Rev. Letters, 79, 2176
- Barkov M. V., Bisnovatyi-Kogan G. S., Lamzin S. A., 2001, Astron. Rep., 45, 230
- Bazán G., et al., 2003, 293, 1
- Beasor E. R., Davies B., Cabrera-Ziri I., Hurst G., 2018, MNRAS, 479, 3101
- Beaudet G., Petrosian V., Salpeter E. E., 1967, ApJ, 150, 979
- Begelman M. C., Rossi E. M., Armitage P. J., 2008, MNRAS, 387, 1649
- Bethe H. A., 1939, Phys. Rev., 55, 434
- Bhattacharya D., van den Heuvel E. P. J., 1991, Physics Reports, 203, 1
- Bhattacharya M., Mukhopadhyay B., Mukerjee S., 2018, arXiv:1810.07836 [astro-ph]
- Bhattacharya M., Hackett A. J., Gupta A., Tout C. A., Mukhopadhyay B., 2021, arXiv:2106.09736 [astro-ph]
- Biehle G. T., 1991, ApJ, 380, 167

- Biehle G. T., 1994, ApJ, 420, 364
- Bildsten L., 1997, arXiv:astro-ph/9709094
- Bisnovatyi-Kogan G. S., Lamzin S. A., 1984, SvA, 28, 187
- Boguta J., Bodmer A., 1977, Nuclear Physics A, 292, 413
- Böhm K.-H., 1963, ApJ, 138, 297
- Bondi H., 1952, MNRAS, 112, 195
- Boothroyd A. I., Sackmann I. J., 1992, ApJ Letters, 393, L21
- Boothroyd A. I., Sackmann I. J., 1999, ApJ, 510, 232
- Braaten E., Segel D., 1993, Phys. Rev. D, 48, 1478
- Braithwaite J., Spruit H. C., 2004, Nature, 431, 819
- Buchler J. R., Yueh W. R., 1976, ApJ, 210, 440
- Böhm-Vitense E., 1958, Z. Astrophys., 46, 108
- Cannon R. C., 1993a, Stars with Compact Cores, Ph.D Thesis
- Cannon R. C., 1993b, MNRAS, 263, 817
- Cannon R. C., 1993c, MNRAS, 263, 817
- Cannon R. C., Eggleton P. P., Zytkow A. N., Podsiadlowski P., 1992, ApJ, 386, 206
- Canuto V., 1970, ApJ, 159, 641
- Cassisi S., Potekhin A. Y., Pietrinferni A., Catelan M., Salaris M., 2007, ApJ, 661, 1094
- Cazzola P., De Zotti G., Saggion A., 1971, Phys. Rev. D, 3, 1722
- Chamel N., Mutafchieva Y. D., Stoyanov Z. K., Mihailov L. M., Pavlov R. L., 2016, Journal of Physics: Conference Series, 724, 012034
- Chatterjee D., Fantina A. F., Chamel N., Novak J., Oertel M., 2017, MNRAS, 469, 95
- Chevalier R. A., 1993, ApJ Letters, 411, L33
- Chevalier R. A., 2012, ApJ Letters, 752, L2
- Chornock R., et al., 2013, ApJ, 767, 162
- Chugunov A. I., Dewitt H. E., Yakovlev D. G., 2007, , 76, 025028
- Clayton D. D., 1983, Principles of Stellar Evolution and Nucleosynthesis. University of Chicago Press
- Collins C., Müller B., Heger A., 2018, MNRAS, 473, 1695

- Cooperstein J., 1988, Phys. Rev. C, 37, 786
- Cordes J. M., Wasserman I., 2016, MNRAS, 457, 232
- Cowling T. G., 1966a, QJRAS, 7, 121
- Cowling T. G., 1966b, Quarterly Journal of the Royal Astronomical Society, 7, 121
- Cox A. N., Stewart J. N., 1970, ApJ Supplement, 19, 243
- Crain R. A., et al., 2015, MNRAS, 450, 1937
- Cristini A., Meakin C., Hirschi R., Arnett D., Georgy C., Viallet M., Walkington I., 2017, MNRAS, 471, 279
- Cumming A., 2002, MNRAS, 333, 589
- Cyburt R. H., et al., 2010, ApJ Supplement, 189, 240
- Das U., Mukhopadhyay B., 2012, Phys. Rev. D, 86, 042001
- Das U., Mukhopadhyay B., 2014, Journal of Cosmology and Astroparticle Physics, 2014, 050
- DeMarchi L., Sanders J. R., Levesque E. M., 2021, ApJ, 911, 101
- Dearborn D. S. P., Lattanzio J. C., Eggleton P. P., 2006, ApJ, 639, 405
- Dennis T. R., 1971, ApJ, 167, 311
- Dexter J., Kasen D., 2013, ApJ, 772, 30
- Dingle R. B., 1957, Applied Scientific Research, Section B, 6, 225
- Doherty C. L., Gil-Pons P., Siess L., Lattanzio J. C., Lau H. H. B., 2014, MNRAS, 446, 2599
- Drewes M., McDonald J., Sablon L., Vitagliano E., 2021, arXiv:2109.06158 [astro-ph, physics:hep-ph]
- Eddington A. S., 1920, Nature, 106, 14
- Eddington A. S., 1930, MNRAS, 90, 279
- Eggenberger P., Meynet G., Maeder A., Hirschi R., Charbonnel C., Talon S., Ekström S., 2008, Ap&SS, 316, 43
- Eggleton P. P., 1971, MNRAS, 151, 351
- Eggleton P. P., Cannon R. C., 1991, ApJ, 383, 757
- Eggleton P. P., Faulkner J., Flannery B. P., 1973, A&A, 23, 325
- Eggleton P. P., Fitchett M. J., Tout C. A., 1989, ApJ, 347, 998
- Eich C., Zimmermann M. E., Thorne K. S., Zytkow A. N., 1989, ApJ, 346, 277

- Eldridge J. J., Tout C. A., 2004, MNRAS, 348, 201
- Everson R. W., MacLeod M., De S., Macias P., Ramirez-Ruiz E., 2020, ApJ, 899, 77
- Farmer R., Renzo M., Götberg Y., Bellinger E., Justham S., de Mink S. E., 2023, arXiv, p. arXiv:2305.07337
- Ferguson J. W., Alexander D. R., Allard F., Barman T., Bodnarik J. G., Hauschildt P. H., Heffner-Wong A., Tamanai A., 2005a, ApJ, 623, 585
- Ferguson J. W., Alexander D. R., Allard F., Barman T., Bodnarik J. G., Hauschildt P. H., Heffner-Wong A., Tamanai A., 2005b, ApJ, 623, 585
- Finlay P., et al., 2011, Phys. Rev. Lett., 106, 032501
- Flowers E., Itoh N., 1976, ApJ, 206, 218
- Flowers E., Itoh N., 1979, ApJ, 230, 847
- Fortin M., Taranto G., Burgio G. F., Haensel P., Schulze H.-J., Zdunik J. L., 2018, MNRAS, 475, 5010
- Fowler W. A., Hoyle F., 1964, ApJ Supplement, 9, 201
- Fricke K., 1968, Zeitschrift für Astrophysik, 68, 317
- Fu W., Wang G., Liu Y., 2008, ApJ, 678, 1517
- Fujimoto M. Y., 1982, ApJ, 257, 752
- Fuller G. M., Fowler W. A., Newman M. J., 1985, ApJ, 293, 1
- Gallino R., Arlandini C., Busso M., Lugaro M., Travaglio C., Straniero O., Chieffi A., Limongi M., 1998, ApJ, 497, 388
- Gao B., et al., 2021, Phys. Rev. Lett., 126, 152701
- Geppert U., Rheinhardt M., 2002, A&A, 392, 1015
- Gezari S., et al., 2009, ApJ, 690, 1313
- Ginzburg S., Fuller J., Kawka A., Caiazzo I., 2022, MNRAS, 514, 4111
- Glendenning N. K., 1982, Physics Letters B, 114, 392
- Glendenning N. K., 1985, ApJ, 293, 470
- Glendenning N. K., 1987, Zeitschrift für Physik A Hadrons and Nuclei, 327, 295
- Gnedin O. Y., Yakovlev D. G., 1995, Nucl. Phys. A, 582, 697
- Goerres J., Wiescher M., Rolfs C., 1989, ApJ, 343, 365
- Gold T., 1968, Nature, 218, 731

- Goldreich P., Reisenegger A., 1992, ApJ, 395, 250
- Goldreich P., Schubert G., 1967, ApJ, 150, 571
- Gordon M. S., Humphreys R. M., 2019, Galaxies, 7, 92
- Gough D., 1977, in Spiegel E. A., Zahn J.-P., eds, , Vol. 71, Problems of Stellar Convection. pp 15–56
- Graboske H. C., Harwood D. J., Rogers F. J., 1969, Phys. Rev., 186, 210
- Griffin S. M., Bedka K. M., Velden C. S., 2016, Journal of Applied Meteorology and Climatology, 55, 479
- Gupta A., Mukhopadhyay B., Tout C. A., 2020, MNRAS, 496, 894
- Haemmerlé L., Woods T. E., Klessen R. S., Heger A., Whalen D. J., 2018, ApJ Letters, 853, L3
- Hajyan G. S., Vartanyan Y. L., Grigoryan A. K., 1998, Astrophysics, 41, 349
- Hayashi C., Hōshi R., Sugimoto D., 1962, Prog. Theor. Phys. Supp., 22, 1
- Heger A., Woosley S., Baraffe I., Abel T., 2002, in Gilfanov M., Sunyeav R., Churazov E., eds, Lighthouses of the Universe: The Most Luminous Celestial Objects and Their Use for Cosmology. p. 369 ([arXiv:astro-ph/0112059](https://arxiv.org/abs/astro-ph/0112059))
- Henyey L. G., Wilets L., Böhm K. H., Lelevier R., Levee R. D., 1959, ApJ, 129, 628
- Henyey L. G., Forbes J. E., Gould N. L., 1964, ApJ, 139, 306
- Heyl J. S., Kulkarni S. R., 1998a, ApJ, 506, L61
- Heyl J. S., Kulkarni S. R., 1998b, ApJ, 506, L61
- Higgins E. R., Vink J. S., 2020, A&A, 635, A175
- Hirai R., Podsiadlowski P., 2022a, MNRAS, 517, 4544
- Hirai R., Podsiadlowski P., 2022b, MNRAS, 517, 4544
- Holmes J. A., Woosley S. E., Fowler W. A., Zimmerman B. A., 1976, Atomic Data and Nuclear Data Tables, 18, 305
- Howell S. B., 2006, Handbook of CCD Astronomy. Cambridge University Press
- Hoyle F., Lyttleton R. A., 1939, Mathematical Proceedings of the Cambridge Philosophical Society, 35, 592–609
- Hoyle F., Lyttleton R. A., 1941, MNRAS, 101, 227
- Hu R., Lou Y., 2010, in American Astronomical Society Meeting Abstracts #215. p. 300.07
- Hu K., Baring M. G., Wadiasingh Z., Harding A. K., 2019, MNRAS, 486, 3327

- Hubbard W. B., Lampe M., 1969a, ApJ Supplement, 18, 297
- Hubbard W. B., Lampe M., 1969b, ApJ Supplement, 18, 297
- Humphreys R. M., Davidson K., 1979, ApJ, 232, 409
- Hurley J. R., Tout C. A., Pols O. R., 2002, MNRAS, 329, 897
- Iben I. J., Renzini A., 1983, Annu. Rev. Astron. Astrophys., 21, 271
- Iglesias C. A., Rogers F. J., 1993, ApJ, 412, 752
- Iglesias C. A., Rogers F. J., 1996a, ApJ, 464, 943
- Iglesias C. A., Rogers F. J., 1996b, ApJ, 464, 943
- Iglesias C. A., Rogers F. J., 1996c, ApJ, 464, 943
- Inserra C., et al., 2018, MNRAS, 475, 1046
- Irwin A. W., 2004, The FreeEOS Code for Calculating the Equation of State for Stellar Interiors, <http://freeeos.sourceforge.net/>
- Irwin A. W., 2012, Astrophysics Source Code Library, p. ascl:1211.002
- Itoh N., Mitake S., Iyetomi H., Ichimaru S., 1983, ApJ, 273, 774
- Itoh N., Hayashi H., Nishikawa A., Kohyama Y., 1996a, ApJ Supplement, 102, 411
- Itoh N., Nishikawa A., Kohyama Y., 1996b, ApJ, 470, 1015
- Izzard R. G., Dray L. M., Karakas A. I., Lugardo M., Tout C. A., 2006, A&A, 460, 565
- Izzard R. G., Lugardo M., Karakas A. I., Iliadis C., Raai M. v., 2007, A&A, 466, 641
- Jermyn A. S., Schwab J., Bauer E., Timmes F. X., Potekhin A. Y., 2021, ApJ, 913, 72
- Jermyn A. S., et al., 2023, ApJ Supplement, 265, 15
- Jie J., Zhu C., Lv G., 2015, preprint, ([arXiv:1505.03182](https://arxiv.org/abs/1505.03182))
- Joyce M., Tayar J., 2023, Galaxies, p. arXiv:2303.09596
- Kantor E. M., Gusakov M. E., 2007, MNRAS, 381, 1702
- Keszthelyi Z., et al., 2022, MNRAS, 517, 2028
- Kippenhahn R., Thomas H. C., 1983, A&A, 124, 206
- Kippenhahn R., Weigert A., Hofmeister E., 1967, Methods in Computational Physics, 7, 129
- Kippenhahn R., Weigert A., Weiss A., 2012, Stellar Structure and Evolution
- Kippenhahn R., Weigert A., Weiss A., 2013, Stellar Structure and Evolution

- Kohyama Y., Itoh N., Obama A., Hayashi H., 1994, ApJ, 431, 761
- Konar S., 2017, J. Astrophys. Astron., 38, 47
- Kosvintsev Y. Y., Morozov V. I., Terekhov G. I., 1986, JETP Letters, 44, 571
- Kouveliotou C., et al., 1998, Nature, 393, 235
- Krolik J. H., 1984, ApJ, 282, 452
- Kudritzki R. P., Reimers D., 1978, A&A, 70, 227
- Kutschera W., 2013, International Journal of Mass Spectrometry, 349, 203
- Kutschera W., et al., 1984, Nuclear Instruments and Methods in Physics Research Section B: Beam Interactions with Materials and Atoms, 5, 430
- Landau L., 1938, Nature, 141, 333
- Lander S. K., Jones D. I., 2009, MNRAS, 395, 2162
- Lane H. J., 1870, AJS, s2-50, 57
- Langanke K., Martínez-Pinedo G., 2000, Nucl. Phys. A, 673, 481
- Langanke K., Martínez-Pinedo G., 2014, Nucl. Phys. A, 928, 305
- Langanke K., Martínez-Pinedo G., Zegers R. G. T., 2021, Rep. Prog. Phys., 84, 066301
- Larson R. B., Demarque P. R., 1964, ApJ, 140, 524
- Laslett L. J., 1949, Phys. Rev., 76, 858
- Leonard P. J. T., Hills J. G., Dewey R. J., 1994, ApJ Letters, 423, L19
- Levesque E. M., Massey P., Źytkow A. N., Morrell N., 2014, Proc. Int. Astron. Union, 9, 57
- Li L. H., Ventura P., Basu S., Sofia S., Demarque P., 2006, ApJ Supplement, 164, 215
- Lightman A. P., Zdziarski A. A., Rees M. J., 1987, ApJ, 315, L113
- Lopes I. P., Gough D., 2001, MNRAS, 322, 473
- MacDonald J., 2015, in 2053-2571, Structure and Evolution of Single Stars. pp 5–1 to 5–6
- MacLeod M., 2021, Bulletin of the AAS, 53
- Maeder A., Meynet G., 2012, Rev. Mod. Phys., 84, 25
- Marchant P., Pappas K. M. W., Gallegos-Garcia M., Berry C. P. L., Taam R. E., Kalogera V., Podsiadlowski P., 2021, A&A, 650, A107
- Marigo P., Girardi L., 2007, A&A, 469, 239
- Marigo, P. Chiosi, C. Kudritzki, R.-P. 2003, A&A, 399, 617

- Marigo P., Bressan A., Chiosi C., 1998, *A&A*, 331, 564
- Marques J. P., Monteiro M. J. P. F. G., Fernandes J., 2006, *MNRAS*, 371, 293
- Martin D., José J., Longland R., 2018, *Computational Astrophysics and Cosmology*, 5, 3
- McLaughlin M. A., et al., 2003, *ApJ Letters*, 591, L135
- McLaughlin M. A., et al., 2009, *MNRAS*, 400, 1431
- Mestel L., 1954, *MNRAS*, 114, 437
- Metzger B. D., 2012, *MNRAS*, 419, 827
- Meynet G., Maeder A., Mowlavi N., 2004, *A&A*, 416, 1023
- Miller Bertolami M. M. M., 2022, *A Red Giants' Toy Story*
- Miller A. A., et al., 2009, *ApJ*, 690, 1303
- Moriya T. J., 2018, *MNRAS Letters*, 475, L49
- Moriya T. J., Blinnikov S. I., 2021, *MNRAS*, 508, 74
- Mowlavi N., 1999, *A&A*, 344, 617
- Mukhopadhyay B., Bhattacharya M., Hackett A. J., Kalita S., Karinkuzhi D., Tout C. A., 2021, arXiv:2110.15374 [astro-ph]
- Nobili L., Turolla R., 1988, *ApJ*, 333, 248
- Norris T. L., Gancarz A. J., Rokop D. J., Thomas K. W., 1983, *Lunar and Planetary Science Conference Proceedings*, 88, B331
- O'Grady A. J. G., et al., 2020, *ApJ*, 901, 135
- O'Grady A. J. G., et al., 2023, *ApJ*, 943, 18
- Oda T., Hino M., Muto K., Takahara M., Sato K., 1994, *Atomic Data and Nuclear Data Tables*, 56, 231
- Odrzywołek A., 2007, *The European Physical Journal C*, 52, 425
- Ootes L. S., Page D., Wijnands R., Degenaar N., 2016, *MNRAS*, 461, 4400
- Oppenheimer J. R., Volkoff G. M., 1939, *Phys. Rev.*, 55, 374
- Oralbaev A., Skorokhvatov M., Titov O., 2016, *J. Phys. Conf. Ser.*, 675, 012003
- Ostriker J. P., Gunn J. E., 1969, *ApJ*, 157, 1395
- Otoniel E., Franzon B., Carvalho G. A., Malheiro M., Schramm S., Weber F., 2019, *ApJ*, 879, 46
- Pacini F., 1967, *Nature*, 216, 567

- Paczyński B., 1969, *Acta Astron.*, 19, 1
- Paczyński B., 1970a, *Acta Astron.*, 20, 47
- Paczyński B., 1970b, *Acta Astron.*, 20, 287
- Paxton B., Bildsten L., Dotter A., Herwig F., Lesaffre P., Timmes F., 2010, *ApJ Supplement*, 192, 3
- Paxton B., et al., 2013, *ApJ Supplement*, 208, 4
- Paxton B., et al., 2015, *ApJ Supplement*, 220, 15
- Paxton B., et al., 2018a, *ApJS*, 234, 34
- Paxton B., et al., 2018b, *ApJ Supplement*, 234, 34
- Paxton B., et al., 2019, *ApJ Supplement*, 243, 10
- Perrin, Jean 1919, *Ann. Phys.*, 9, 5
- Pethick C. J., 1992, *Rev. Mod. Phys.*, 64, 1133
- Pinheiro F. J. G., Fernandes J., 2013, *MNRAS*, 433, 2893
- Podsiadlowski P., 2007, *MNRAS*
- Podsiadlowski P., Cannon R. C., Rees M. J., 1995, *MNRAS*, 274, 485
- Pols O. R., Tout C. A., Eggleton P. P., Han Z., 1995, *MNRAS*, 274, 964
- Potekhin A. Y., 2014, *Phys.-Uspekhi*, 57, 735
- Potekhin A. Y., Chabrier G., 2010, *Contributions to Plasma Physics*, 50, 82
- Potekhin A. Y., Yakovlev D. G., 2001, p. 14
- Potter A. T., Tout C. A., Eldridge J. J., 2011, *MNRAS*, 419, 748
- Quimby R. M., et al., 2013, *ApJ Letters*, 768, L20
- Raihel C. A., Özel F., Psaltis D., 2019, *ApJ*, 875, 12
- Rauscher T., Heger A., Hoffman R. D., Woosley S. E., 2002, *ApJ*, 576, 323
- Ravlić A., Yüksel E., Niu Y. F., Colò G., Khan E., Paar N., 2020, *Phys. Rev. C*, 102, 065804
- Ray A., Kembhavi A. K., Antia H. M., 1987, *A&A*, 184, 164
- Renzini A., 1987, *A&A*, 188, 49
- Rogers F. J., Nayfonov A., 2002a, *ApJ*, 576, 1064
- Rogers F. J., Nayfonov A., 2002b, *ApJ*, 576, 1064

- Roxburgh I. W., 1998, in Chan K. L., Cheng K. S., Singh H. P., eds, Astronomical Society of the Pacific Conference Series Vol. 138, 1997 Pacific Rim Conference on Stellar Astrophysics. p. 411
- Rugel G., et al., 2009, Physical review letters, 103, 072502
- Sackmann I. J., Boothroyd A. I., 1999, ApJ, 510, 217
- Saslaw W. C., Schwarzschild M., 1965, ApJ, 142, 1468
- Saumon D., Chabrier G., van Horn H. M., 1995a, ApJ Supplement, 99, 713
- Saumon D., Chabrier G., van Horn H. M., 1995b, ApJ Supplement, 99, 713
- Scalzo R. A., et al., 2010, ApJ, 713, 1073
- Schatz H., Bildsten L., Cumming A., Wiescher M., 1999, ApJ, 524, 1014
- Schleicher D. R. G., Palla F., Ferrara A., Galli D., Latif M., 2013, A&A, 558, A59
- Schwarzschild M., 1958, Structure and Evolution of Stars. Princeton University Press
- Schwarzschild M., Härm R., 1958, ApJ, 128, 348
- Schwarzschild M., Härm R., 1965, ApJ, 142, 855
- Shapiro S. L., Teukolsky S. A., 1983
- Shaviv G., Salpeter E. E., 1973, ApJ, 184, 191
- Silverman J. M., et al., 2013, ApJ, 772, 125
- Sinha M., Mukhopadhyay B., Sedrakian A., 2013, Nuclear Physics A, 898, 43
- Stancliffe R. J., 2005, PhD thesis, University of Cambridge, UK
- Stancliffe R. J., Eldridge J. J., 2009, MNRAS, 396, 1699
- Stancliffe R. J., Tout C. A., Pols O. R., 2004, MNRAS, 352, 984
- Stancliffe R. J., Chieffi A., Lattanzio J. C., Church R. P., 2009, Publ. Astron. Soc. Aust., 26, 203
- Stothers R., Wen Chin C., 1973, ApJ, 182, 209
- Subramanian S., Mukhopadhyay B., 2015, MNRAS, 454, 752
- Sugimoto D., Fujimoto M. Y., 2000, ApJ, 538, 837
- Sugimoto D., Nomoto K., 1980, Space Sci. Rev., 25, 155
- Tabernero H. M., Dorda R., Negueruela I., Marfil E., 2021, A&A, 646, A98
- Terman J. L., Taam R. E., Hernquist L., 1995, ApJ, 445, 367

- Terreran G., et al., 2017, *Nat. Astron.*, 1, 713
- Thompson C., Duncan R. C., 1993, *ApJ*, 408, 194
- Thorne K. S., 1977, *ApJ*, 212, 825
- Thorne K. S., Źytkow A. N., 1975, *ApJ Letters*, 199, L19
- Thorne K. S., Źytkow A. N., 1977, *ApJ*, 212, 832
- Timmes F. X., 1999, *ApJ Supplement*, 124, 241
- Timmes F. X., Swesty F. D., 2000b, *ApJ Supplement*, 126, 501
- Timmes F. X., Swesty F. D., 2000a, *ApJ Supplement*, 126, 501
- Timmes F. X., Woosley S. E., Weaver T. A., 1995, *ApJ Supplement*, 98, 617
- Toonen S., Nelemans G., Portegies Zwart S., 2012, *A&A*, 546, A70
- Tout C. A., Aarseth S. J., Pols O. R., Eggleton P. P., 1997, *MNRAS*, 291, 732
- Tout C. A., Źytkow A. N., Church R. P., Lau H. H. B., Doherty C. L., Izzard R. G., 2014, *MNRAS Letters*, 445, L36
- Townsend R. H. D., Teitler S. A., 2013, *MNRAS*, 435, 3406
- Tutukov A., Yungelson L., 1979, *Mass loss and evolution of O-type stars : symposium no. 83..* D. Reidel
- Unno W., 1957, *ApJ*, 126, 259
- Vardya M. S., 1960, *ApJ Supplement*, 4, 281
- Ventura J., Potekhin A., 2001, p. 393
- Vervier J., 1968, *Nuclear Data Sheets Section B*, 2, 1
- Vogel P., Beacom J. F., 1999, *Phys. Rev. D*, 60, 053003
- Wallace R. K., Woosley S. E., 1981, *ApJ Supplement*, 45, 389
- Wallner A., et al., 2015, *Phys. Rev. Lett.*, 114, 041101
- Wasserburg G. J., Boothroyd A. I., Sackmann I. J., 1995, *ApJ Letters*, 447, L37
- Weaver T. A., Zimmerman G. B., Woosley S. E., 1978, *ApJ*, 225, 1021
- Webbink R. F., 1975, PhD thesis, University of Cambridge, UK
- Wickramasinghe D. T., Ferrario L., 2005, 334, 153
- Wiescher M., Görres J., Uberseder E., Imbriani G., Pignatari M., 2010, *Annu. Rev. Nucl. Part. Sci.*, 60, 381

- Woo J.-H., Demarque P., 2001, ApJ, 122, 1602
- Woods T. E., Heger A., Whalen D. J., Haemmerlé L., Klessen R. S., 2017, ApJ Letters, 842, L6
- Yahil A., van den Horn L., 1985, ApJ, 296, 554
- Yakovlev D. G., Levenfish K. P., 1995, A&A, 297, 717
- Yakovlev D. G., Pethick C. J., 2004, Annu. Rev. Astron. Astrophys., 42, 169
- Yakovlev D. G., Gnedin O. Y., Gusakov M. E., Kaminker A. D., Levenfish K. P., Potekhin A. Y., 2005, Nucl. Phys. A, 752, 590
- Yakovlev D. G., Haensel P., Baym G., Pethick C., 2013, Physics Uspekhi, 56, 289
- Yi S., Lee Y.-W., Demarque P., 1993, ApJ Letters, 411, L25
- Yong-quan Y., Ru-feng L., 1996, Chinese Astronomy and Astrophysics, 20, 321
- Yoon S. C., Langer N., van der Sluys M., 2004, A&A, 425, 207
- de Kool M., Ritter H., 1993, A&A, 267, 397

Appendix A

Analytical Derivations

In this appendix, we present and derive a number of analytical expressions that have been referred to and used, up until this point, without proof.

A.1 Contact between relativistic and standard stellar structure equations in the Newtonian limit

As presented in section 5.2.1.3 we find that the effects of GR corrections are minimal in the models that we consider. To ensure that the standard or corrected set of stellar structure equations we solve are consistent, we show here that the relativistic formulations of these equations by [Thorne \(1977\)](#) and [Thorne & Żytkow \(1977\)](#) reduce to the standard equations in the Newtonian limit, that is, where the relativistic correction factors are set to unity. In particular, we show that the $\varepsilon_{\text{grav}}$ formulation of [Paxton et al. \(2010\)](#) is consistent with the form of [Thorne & Żytkow \(1977\)](#), itself based on the consideration of stars with mass inflow through burning shells originally conducted by [Paczyński \(1970b\)](#). We define, following [Thorne \(1977\)](#), five dimensionless relativistic correction factors, \mathcal{R} , the redshift correction, \mathcal{V} , the volume correction, \mathcal{G} , the gravitational acceleration correction, \mathcal{E} , the energy correction

and \mathcal{H} , the enthalpy correction, as follows,

$$\mathcal{R} \equiv e^{\phi/c^2}, \quad (\text{A.1})$$

$$\mathcal{V} \equiv (1 - 2GM_{tr}/c^2r)^{-1/2}, \quad (\text{A.2})$$

$$\mathcal{G} \equiv \frac{1}{M_r}M_{tr} + 4\pi r^3 P/c^2, \quad (\text{A.3})$$

$$\mathcal{E} \equiv 1 + (\Pi - B)/c^2 = \rho_t/\rho, \quad (\text{A.4})$$

$$\mathcal{H} \equiv 1 + (\Pi - B + P/\rho)/c^2, \quad (\text{A.5})$$

where M_r is the rest mass, M_{tr} is the total mass, B is the binding energy of the nucleons, Π is the specific internal energy of the stellar material and ρ_t is the density of non-gravitational mass-energy, as

$$\rho (1 - B/c^2 + \Pi/c^2). \quad (\text{A.6})$$

The full set of relativistic structure equations produced is

$$\frac{dr}{dM_r} = \frac{1}{4\pi\rho\mathcal{V}}, \quad (\text{A.7})$$

$$\frac{dM_{tr}}{dM_r} = \frac{\mathcal{E}}{\mathcal{V}}, \quad (\text{A.8})$$

$$\frac{d\phi}{dM_r} = \frac{\mathcal{G}\mathcal{V}GM_r}{4\pi r^4\rho}, \quad (\text{A.9})$$

$$\frac{d(L_r\mathcal{R}^2)}{dM_r} = \mathcal{R}\epsilon_{\text{nuc,v}} + \mathcal{R}\dot{M} \left(\frac{d\Pi}{dM_r} - \left(\frac{P}{\rho^2} \right) \frac{d\rho}{dM_r} \right), \quad (\text{A.10})$$

$$\frac{dX_i}{dM_r} = -\frac{\mathcal{R}\alpha_i}{\dot{M}}, \text{ if radiative,} \quad (\text{A.11})$$

$$\frac{d\ln T}{dM_r} = \nabla \frac{\ln P}{dM_r}, \quad (\text{A.12})$$

$$\frac{dP}{dM_r} = -\mathcal{G}\mathcal{H}\mathcal{V} \left(\frac{GM_r}{4\pi r^4} \right), \quad (\text{A.13})$$

where \dot{M} is the rate of mass inflow through the base of the convective envelope and all other variables are as described in section 5.1.1. The velocity of mass inflow is simply $v_{\text{in}} \equiv -(\mathcal{V}/\mathcal{R})(\partial r/\partial t)_{M_r}$ and hence the rate of mass inflow is $\dot{M} = 4\pi r^2 \rho v_{\text{in}} \mathcal{R}$.

The luminosity produced by the release of gravitational potential energy can then be computed assuming that the rate of matter inflow is approximately constant and that the stellar structure

is stable on timescales long compared to the thermal timescale so that

$$\left(\frac{\partial}{\partial t} \right)_{M_r} = -\dot{M} \left(\frac{\partial}{\partial M_r} \right)_t, \quad (\text{A.14})$$

for all equations of stellar structure presented in an Eulerian frame by [Thorne \(1977\)](#). In effect, a d/dt term here vanishes because we claim that the rate at which the stellar structure changes, changing the rate of matter inflow is slow compared to the timescale on which matter flows towards the core. Then we note that

$$-\left(\frac{P}{\rho^2} \right) \frac{\partial \rho}{\partial M_r} = \frac{\partial \left(\frac{P}{\rho} \right)}{\partial M_r} - \frac{1}{\rho} \frac{\partial P}{\partial M_r}, \quad (\text{A.15})$$

and so, noting that the release of nuclear burning energy must be equivalent to the rate of change of the nuclear binding energy,

$$\varepsilon_{\text{nuc}} = \frac{1}{\mathcal{R}} \frac{\partial B}{\partial t}. \quad (\text{A.16})$$

Furthermore because, in moving matter, pressure transports energy, and given that the effective relativistic pressure is simply $\rho \mathcal{H} - \rho \mathcal{E}$, this generates a conservation law, first by defining a rate of change for luminosity with radial coordinate,

$$\begin{aligned} \frac{\partial}{\partial r} \left(\frac{\mathcal{R}^2 L_r}{c^2} \right) &= \\ -4\pi r^2 \rho \mathcal{V} \mathcal{R} \left(\left(\frac{\partial \mathcal{E}}{\partial t} \right)_{M_r} - \frac{P}{c^2} (\partial \rho / \partial t)_{M_r} \right). \end{aligned} \quad (\text{A.17})$$

Now we use equation (A.14) to convert to partial derivatives taken at fixed radial coordinate. The (relativistic) hydrostatic equilibrium and radiative energy transport equations then give

$$\begin{aligned} \frac{\partial}{\partial r} \left(\frac{\mathcal{R}^2 L_r}{c^2} \right) &= \\ -4\pi r^2 \rho \mathcal{V} \mathcal{R} \left(\left(\frac{\partial \mathcal{E}}{\partial t} \right)_r - \frac{P}{c^2} (\partial \rho / \partial t)_r \right) \\ + \left(\frac{\partial M_r}{\partial t} \right)_r \frac{\partial \mathcal{H} \mathcal{R}}{\partial r}. \end{aligned} \quad (\text{A.18})$$

Now, using equations (A.18) and (A.8), we can derive

$$\frac{\partial}{\partial r} \left(\left(\frac{\partial M_r}{\partial t} \right)_r \mathcal{H}\mathcal{R} \right) = \left(\frac{\partial M_r}{\partial t} \right)_r \frac{\partial \mathcal{H}\mathcal{R}}{\partial r} + 4\pi r^2 \mathcal{H}\mathcal{R} \left(\frac{\partial (\rho \mathcal{V})}{\partial t} \right)_r. \quad (\text{A.19})$$

And with

$$\frac{\partial (\mathcal{V}\mathcal{R})}{\partial r} = \frac{4\pi G r}{c^2} \rho \mathcal{H} \mathcal{V}^3 \mathcal{R}, \quad (\text{A.20})$$

and equation (A.19) we compute

$$\frac{\partial}{\partial r} \left(\left(\frac{\partial M_{tr}}{\partial t} \right)_r \mathcal{V}\mathcal{R} \right) = 4\pi r^2 \mathcal{R} \left(\rho \mathcal{H} \left(\frac{\partial \mathcal{V}}{\partial t} \right)_r + \mathcal{V} \left(\frac{\partial (\rho \mathcal{E})}{\partial t} \right)_r \right). \quad (\text{A.21})$$

Finally, we combine equations (A.18), (A.19) and (A.21) to derive our equation of mass-energy conservation

$$\frac{\partial}{\partial r} \left(\frac{\mathcal{R}^2 L_r}{c^2} - \left(\frac{\partial M_r}{\partial t} \right)_r \mathcal{H}\mathcal{R} + \left(\frac{\partial M_{tr}}{\partial t} \right)_r \mathcal{V}\mathcal{R} \right) = 0. \quad (\text{A.22})$$

Now, we can make use of this energy conservation expression and equation (A.15) to write an expression for gravitational energy release along with any non-convective nuclear energy generation, such as in the helium burning region in the halo of our models,

$$L_r = \frac{1}{\mathcal{R}^2} (\dot{M} c^2 \mathcal{H}\mathcal{R} + (\text{corr conv burn})), \quad (\text{A.23})$$

where (corr conv burn) is the redshift corrected energy release from nuclear burning in the convective envelope. This has no simple analytical form. In the Newtonian limit, this generates

$$L_r = \dot{M} \left(\Pi + \frac{P}{\rho} - B + \phi \right) + (\text{conv burn}), \quad (\text{A.24})$$

where removing the nuclear burning differential ($\Pi - B$), reduces to terms in $\partial s/\partial t$ alone, regenerating the Paxton et al. (2010) $\varepsilon_{\text{grav}}$ formulation, as,

$$\varepsilon_{\text{grav}} = -T \frac{ds}{dt} = -TC_P \left[(1 - \nabla_{\text{ad}\chi T}) \frac{d \ln T}{d \ln t} - \nabla_{\text{ad}\chi \rho} \frac{d \ln \rho}{d t} \right]. \quad (\text{A.25})$$

A.2 Magnetic field decay mechanisms for B-WDs

Here we present, derive and adapt formulae for magnetic field decay mechanisms that may operate in highly magnetized white dwarfs (Chapters 3 & 6). These, in general, in the way

presented here, are used to model the decay of the magnetic field of a neutron star. Each series of derivations is based on those performed by Bhattacharya et al. (2021), Hackett et al. (2023, in prep.), Goldreich & Reisenegger (1992), Geppert & Rheinhardt (2002), Cumming (2002) and Heyl & Kulkarni (1998b).

In the case of the non-inertial electric field in a neutron star, we can write the following (Goldreich & Reisenegger, 1992),

$$\vec{E} = \frac{\vec{j}}{\sigma_0} - \frac{\vec{v}}{c} \wedge \vec{B} + \left(\frac{m_p/\tau_{pn} - m_e^*/\tau_{en}}{m_p/\tau_{pn} + m_e^*/\tau_{en}} \right) \left(\frac{\vec{j} \wedge \vec{B}}{n_c e c} \right) + \frac{(\tau_{pn}/m_p) \nabla \mu_p - (\tau_{en}/m_e^*) \nabla \mu_e}{e(\tau_{pn}/m_p + \tau_{en}/m_e^*)}, \quad (\text{A.26})$$

where μ_i is the chemical potential of a species i , m_e^* is the effective inertia of the electron, as opposed to its effective mass, m_p is the mass of the proton, σ_0 is the electrical conductivity in the field-free case and τ_{ij} is the relaxation timescale assuming that thermal relaxation occurs only by means of collisions between species i and j . Given that μ_i is equal to the Fermi energy, plus the rest mass-energy, it is most convenient to think of it as being the effective mass of the species in question. In which case, Goldreich & Reisenegger (1992) write the equations of motion for the charged species, the protons and the electrons, as

$$m_p \frac{\partial \vec{v}_p}{\partial t} + m_p (\vec{v}_p \cdot \nabla) \vec{v}_p = -\nabla \mu_p - m_p \nabla \psi + e \left(\vec{E} + \frac{\vec{v}_p}{c} \times \vec{B} \right) - \frac{m_p \vec{v}_p}{\tau_{pn}} - \frac{m_p (\vec{v}_p - \vec{v}_e)}{\tau_{pe}}, \quad (\text{A.27})$$

and,

$$m_e^* \frac{\partial \vec{v}_e}{\partial t} + m_e^* (\vec{v}_e \cdot \nabla) \vec{v}_e = -\nabla \mu_e - e \left(\vec{E} + \frac{\vec{v}_e}{c} \times \vec{B} \right) - \frac{m_e^* \vec{v}_e}{\tau_{en}} - \frac{m_e^* (\vec{v}_e - \vec{v}_p)}{\tau_{ep}}, \quad (\text{A.28})$$

respectively, where the average velocity of the species i is \bar{v}_i , and τ_{ji} is again the thermal relaxation timescale for collisions with particle i impinged upon by particle j . Finally σ_B is the electrical conductivity at field density B and in the case of σ_0 , can be written as

$$\sigma_0 = n_c e^2 \left(\frac{1}{\tau_{ep}/m_e^*} + \frac{1}{\tau_{pn}/m_p + \tau_{en}/m_e^*} \right)^{-1}. \quad (\text{A.29})$$

We can now write a full time evolution equation for the magnetic field, with Faraday's law $\partial \vec{B} / \partial t = -c \nabla \times \vec{E}$, as

$$\frac{\partial \vec{B}}{\partial t} = -c \nabla \times \frac{\vec{j}}{\sigma_0} \quad (\text{A.30})$$

$$+ \nabla \times (\vec{v} \times \vec{B}) \quad (\text{A.31})$$

$$- \left(\frac{m_p/\tau_{pn} - m_e^*/\tau_{en}}{m_p/\tau_{pn} + m_e^*/\tau_{en}} \right) \nabla \times \left(\frac{\vec{j} \times \vec{B}}{n_c e} \right). \quad (\text{A.32})$$

Casting the field decay equation in this manner highlights the three decay mechanisms at play, ohmic decay on line one, ambipolar diffusion on line two and the Hall drift on line three. It is not trivial to implement this decay equation in a one dimensional stellar evolution code directly so we find a number of approximations to the decay timescales on which each process operates, so that they can in fact be implemented directly into such a code. To do this, we first partition the magnetic field, or rather, the magnetic force, \vec{f}_B into a divergence-free, solenoidal term \vec{f}_B^S and a curl-free, irrotational term, \vec{f}_B^{ir} . The degenerate ohmic decay timescale is then,

$$\tau_{\text{ohm}} = \frac{4\pi\sigma_0 L^2}{c^2}, \quad (\text{A.33})$$

where L^2 is the characteristic length scale over which the irrotational component of the magnetic force varies. It is however common, to state that L^2 is the characteristic length scale over which the field strength itself varies ([Das & Mukhopadhyay, 2012](#)). At lower field strengths, these two scales roughly coincide.

Appendix B

Nuclear reaction networks

Here we outline a selection of nuclear reaction networks we make use of in the STARS and MESA one-dimensional stellar evolution codes.

B.1 Networks – STARS

The Cambridge STARS code has always touted, as one of its defining features, the ability of the code to solve the structural, energy transport and chemical compositions equations simultaneously. So the nuclear network of the code consists of two completely separate, networks, a structural network, where the mass fractions of the structural elements are treated as structural variables (see section 4.2.1). As such, the energy released by the reactions involving these elements are treated fully self-consistently. Hence the elements considered are those for which their reactions contribute significantly to the overall energy budget of the star. The second network is the post-processing network. Here, the mass fractions of a much larger number of species are computed, at each timestep, *after* the structural computations have been completed. This allows a much larger network than the structural network because adding additional variables to the structural computations greatly increases the CPU time required to solve the structure at each timestep. The limitation here is that the energy that would be released from these reactions does not affect the structure of the model as it would in reality. Hence reactions that contribute significant energy must always be treated structurally.

B.1.1 The structural network

The structural network follows simultaneously the 20 reactions in table B.1. These reactions are largely as described by [Pols et al. \(1995\)](#) and [Stancliffe & Eldridge \(2009\)](#), where ^1H , ^4He , ^{12}C , ^{16}O , & ^{20}Ne are the species followed. Whereas [Pols et al. \(1995\)](#) make use of baryon

Table B.1 Nuclear reaction networks considered in STARS structural computations.

Reaction	Notes
$^1\text{H}(\text{p}, \beta^+ \nu)^2\text{H}(\text{p}, \gamma)^3\text{He}$	PP I/II/III
$^3\text{He}(^3\text{He}, 2\text{p})^4\text{He}$	PP I
$^3\text{He}(^4\text{He}, \gamma)^7\text{Be}$	PP I/II
$^7\text{Be}(\beta^-, \nu)^7\text{Li}(\text{p}, \alpha)^4\text{He}$	PP II
$^7\text{Be}(\text{p}, \gamma)^8\text{B}(\beta^+, \nu)^8\text{Be}^*(\alpha)^4\text{He}$	PP III
$^{12}\text{C}(\text{p}, \beta^+ \nu)^{13}\text{C}(\text{p}, \gamma)^{14}\text{N}$	CN Chain
$^{14}\text{N}(\text{p}, \beta^+ \nu)^{15}\text{N}(\text{p}, \gamma)^{16}\text{O}$	CNO
$^{14}\text{N}(\text{p}, \beta^+ \nu)^{15}\text{N}(\text{p}, \alpha)^{12}\text{C}$	CNO
$^{16}\text{O}(\text{p}, \beta^+ \nu)^{17}\text{O}(\text{p}, \alpha)^{14}\text{N}$	CNO
$^4\text{He}(\alpha)^8\text{Be}^*(\alpha, \gamma)^{12}\text{C}$	3α
$^{12}\text{C}(\alpha, \gamma)^{16}\text{O}$	3α
$^{14}\text{N}(\alpha, \gamma)^{18}\text{F}(\frac{1}{2}\alpha, \gamma)^{20}\text{Ne}$	<i>n.b.:</i> Fictitious Reaction ²³
$^{16}\text{O}(\alpha, \gamma)^{20}\text{Ne}$	3α
$^{20}\text{Ne}(\alpha, \gamma)^{24}\text{Mg}$	3α
$^{12}\text{C}(^{12}\text{C}, \alpha \gamma)^{20}\text{Ne}$	α process
$^{12}\text{C}(^{12}\text{C}, \gamma)^{24}\text{Mg}$	α process
$^{12}\text{C}(^{16}\text{O}, \alpha \gamma)^{24}\text{Mg}$	α process
$^{16}\text{O}(^{16}\text{O}, \alpha \gamma)^{28}\text{Si}(\gamma, \alpha)^{24}\text{Mg}$	α process
$^{20}\text{Ne}(\gamma, \alpha)^{16}\text{O}$	α process
$^{24}\text{Mg}(\gamma, \alpha)^{20}\text{Ne}$	α process

conservation in two different burning regimes to follow implicitly the abundances of ^{14}N and ^{24}Mg , we use this only for ^{24}Mg , choosing instead to evolve ^{14}N explicitly in order to make fewer assumptions about what burning processes operate in what density and temperature regimes, given our interest in computing structures of exotic stellar objects. Furthermore, [Pols et al. \(1995\)](#) consider the proton-proton chain reactions to be in equilibrium, hence, they follow ^3He and ^7Be abundances implicitly, we instead follow ^3He explicitly as did [Stancliffe & Eldridge \(2009\)](#), this allows a more realistic modelling of low-mass stars on the giant branch ([Dearborn et al., 2006](#)).

Table B.2 Chemical species considered in STARS post-processing computations.

	Post-Process			Structural
g	^{17}O	$^{26}\text{Al}^m$	^{56}Fe	^1H
n	^{18}O	$^{26}\text{Al}^g$	^{57}Fe	^3He
^2H	^{19}F	^{27}Al	^{58}Fe	^4He
^3He	^{21}Ne	^{28}Si	^{59}Fe	^{12}C
^7Li	^{22}Ne	^{29}Si	^{60}Fe	^{14}N
^7Be	^{22}Na	^{30}Si	^{59}Co	^{16}O
^{11}B	^{23}Na	^{31}P	^{58}Ni	^{20}Ne
^{13}C	^{24}Mg	^{32}S	^{59}Ni	
^{14}C	^{25}Mg	^{33}S	^{60}Ni	
^{15}N	^{26}Mg	^{34}S	^{61}Ni	

Table B.3 Radioactive Decays considered in STARS post-processing computations.

Unstable Species	$\tau_{1/2}$	Source
$^{26}\text{Al}^g$	0.72 Myr	Norris et al. (1983)
^{14}C	5730 yr	Kutschera (2013)
^{22}Na	2.6 yr	Laslett (1949)
$^{26}\text{Al}^m$	6 s	Finlay et al. (2011)
^{59}Fe	44.6 d	Vervier (1968)
^{60}Fe	2.26 Myr ²⁴	Kutschera et al. (1984) & Rugel et al. (2009)
^{59}Ni	0.075 Myr	Vervier (1968)
^0n	10.3 min	Kosvintsev et al. (1986)

B.1.2 Post-processing nuclear reaction network

In table B.2 the 46 chemical species whose abundances are solved for at each timestep in the full post-processing STARS nucleosynthesis code are listed. This corresponds to a requirement to solve an additional 46 second order differential equations at each point at each timestep (see section 4.2.1 for structural details). We note that the structural chemical variables, as discussed earlier, are recomputed at this stage, to act as a useful sanity check. Running a model with full post-processing then leads to very significant slowdown. Eight of the resultant nuclear reactions correspond to the decay of unstable particles, as in table B.3.

²³This reaction is unphysical, we burn ^{14}N to produce ^{20}Ne , rather than ^{22}Ne as occurs in reality ([Wiescher et al., 2010](#)). The discrepancy is small and deemed worthwhile in terms of saving an entire structural variable. Naturally, the full post-processing nucleosynthesis calculations account properly for this reaction.

²⁴[Kutschera et al. \(1984\)](#) provides $\tau_{1/2} = 1.5$ Myrs, while [Rugel et al. \(2009\)](#) computed $\tau_{1/2} = 2.26$ Myrs, which was supported in work by [Wallner et al. \(2015\)](#) & [Gao et al. \(2021\)](#). Given when these post-processing routines were first constructed, the earlier $\tau_{1/2}$ was originally used. This remained as the case until we updated it to use the [Rugel et al. \(2009\)](#) $\tau_{1/2}$ here.

We draw attention to our use of gallinos, artificial neutron sink particles that represent all neutron captures by heavy elements above ^{61}Ni . We follow the methodology of [Holmes et al. \(1976\)](#) and [Stancliffe \(2005\)](#) here by first including a sink reaction for light elements,



The cross-section for this reaction is computed as a simple average of the reaction rates of all the nuclei between ^{34}S and iron, as,

$$\sigma = \frac{\sum_{i=34}^{55} X_i \sigma_i}{\sum_{i=34}^{55} X_i}, \quad (\text{B.2})$$

where X_i represents the abundance of isotope i , and σ_i its associated cross-section. The heavy-element sink, or the s-process sink is very much analogous to the light-element sink, this time following the sink reaction,



with cross-section computed by the same averaging approach. We can make use of this heavy sink reaction to estimate the rate of the s-process nucleosynthesis, by making the assumption that ^{62}Ni decays to ^{61}Ni with the release of a gallino. These gallinos represent the wide range of s-process elements that we expect to be generated, but which our post-processing code does not follow explicitly.

B.2 Networks – MESA

A wide range of nuclear reaction networks are made available for use in the `net` module that is included in the MESA standard download and owes much of its existence to [Timmes \(1999\)](#). The standard `basic.net` network is very much analogous to the core structural nucleosynthesis network in STARS, and is comprised of ^1H , ^3He , ^4He , ^{12}C , ^{14}N , ^{16}O , ^{20}Ne and ^{24}Mg . A selection of extended nuclear networks is available and, if none are found to be sufficient, a custom network can be trivially constructed. Amongst many others, these include hot CNO reactions, the NaNe and MgAl cycles, networks for doing α -capture reaction chains, proton addition reactions, slow and rapid neutron captures as well as other heavy-ion capture reactions. In table B.4 we list a few of the most relevant nuclear networks of which we made use.

Table B.4 A sample of relevant MESA nuclear networks.

MESA network	Species	Notes
basic.net	^1H , ^3He , ^4He , ^{12}C , ^{14}N , ^{16}O , ^{20}Ne , ^{24}Mg	For low temperatures, ignoring advanced burning.
hot_cno.net	basic.net + ^{13}C , ^{15}N , ^{17}O , ^{18}O , ^{17}F , ^{18}F	β -limited CNO burning (Audouze et al., 1973).
co_burn.net	basic.net + ^{28}Si (see table B.5)	Includes C/O burning, alpha chain up to ^{28}Si .
approx21.net	co_burn.net + ^{32}S , ^{36}Ar , ^{40}Ca , ^{44}Ti , ^{48}Cr , ^{28}Si , ^{56}Cr , $^{52+54+56+}\text{Fe}$, ^{56}Ni	Includes also photodisintegration, proton and neutron reactions (+ decays), see Timmes & Swesty (2000b) & Weaver et al. (1978)
sagb_NeNa.net	hot_cno.net + ^2H , ^7Li , ^7Be , ^8B , ^7Li , $^{20-22}\text{Ne}$, $^{21-23}\text{Na}$	Includes relevant alpha chains for additional species, and NeNa cycle.
sagb_NeNa_MgAl.net	sagb_NeNa.net + $^{25-26}\text{Mg}$, $^{25-27}\text{Al}$	Includes relevant proton additions and weak decays for the MgAl cycle.

Table B.5 Details of the co_burn.net nuclear reaction network. All the basic.net reactions occur as before (see table B.4), hence we here present the additional reactions only

Reaction	Notes
$^{12}\text{C} + ^{12}\text{C} \rightarrow ^{20}\text{Ne} + ^4\text{He}$	Single combined rate – giving (approximately) correct energetics and desired inputs and outputs, but without intermediate products.
$^{12}\text{C} + ^{16}\text{O} \rightarrow ^{24}\text{Mg} + ^4\text{He}$	""
$^{12}\text{C} + ^{16}\text{O} \rightarrow ^{28}\text{Si}$	""
$^{16}\text{O} + ^{16}\text{O} \rightarrow ^{28}\text{Si} + ^4\text{He}$	""
$^{16}\text{O}(\gamma, p)^{15}\text{N}(p, \alpha)^{12}\text{C}$	Includes an auxiliary function for proton addition as $^{15}\text{N} + p \rightarrow ^{16}\text{O} + \gamma$
$^{16}\text{O}(\alpha, p)^{19}\text{F}(p, \gamma)^{20}\text{Ne}$	
$^{20}\text{Ne}(\gamma, p)^{19}\text{F}(p, \alpha)^{16}\text{O}$	
$^{20}\text{Ne}(\alpha, p)^{23}\text{Na}(p, \gamma)^{24}\text{Mg}$	
$^{24}\text{Mg}(\gamma, p)^{23}\text{Na}(p, \alpha)^{20}\text{Ne}$	
$^{24}\text{Mg}(\alpha, p)^{27}\text{Al}(p, \gamma)^{28}\text{Si}$	
$^{28}\text{Si}(\gamma, p)^{27}\text{Al}(p, \alpha)^{24}\text{Mg}$	

Given the importance of helium burning and α -chain reactions in our models of T $\ddot{\text{O}}$ s as presented in Chapter 5 in particular, we present the main helium burning network employed in table B.5. As we state there, the principle benefit of this over a larger helium burning network is a very significant decrease in the computational time needed to compute models. Recalling that Cannon (1993b) restricted himself, likewise for computational reasons, to a CNO cycle hydrogen burning network, we can achieve a similar speed-up while still exploring a much greater range of reactions.

B.2.1 Heger 2002-like adaptive nuclear network

In addressing the desire for having a larger nuclear network for the study of nucleosynthesis in T $\ddot{\text{O}}$ s / exotic stellar in general, we made use of the adaptive nuclear network in MESA, following Rauscher et al. (2002), and called Heger 2002-like by Paxton et al. (2010). As discussed by Rauscher et al. (2002), the adaptive network has access to the entire MESA nucleosynthesis network and then automatically adjusts the size of the network as model evolution progresses. As the presence, size and boundaries of convection regions cannot be arbitrarily predicted in advance, the network must be the same throughout the star. As a result, if the abundance (in mass fraction) of some isotope exceeds a certain minimum at any calculation point, then the neighbouring elements, the elements accessible by, for example, α -capture, as well as all isotopes that are accessible by a decay mode are added to the network,

along with the relevant reactions. Likewise, if the abundance of an isotope falls below some other given minimum, it is removed from the network, provided it is not itself part of a decay chain of a sufficiently abundant isotope. In order to prevent numerical instabilities, it is important to keep the minimum abundance to expand the network considerably (usually around 6 orders of magnitude) larger than the maximum abundance at which isotopes can be removed from the network. The network itself is solved for at each time step implicitly, with a sparse matrix inverter, again following the methodology of [Timmes et al. \(1995\)](#).

Appendix C

Commentary on Farmer et al. (2023)

Here we briefly discuss a recent preprint by [Farmer et al. \(2023\)](#) which is pertinent to our work. This work has only very recently been made publicly available and, while submitted, it has, as of now, yet to be accepted for publication and hence differences between the work as we discuss it here and the final published version may exist and may alter the nature of the discussion herein. We would strongly recommend that the reader make reference to the final published version of that work when it becomes available while perusing this appendix.

C.1 A brief overview of work in question

[Farmer et al. \(2023\)](#), (hereinafter F+23), produced a grid of evolutionary models of TŻOs, using MESA. They compute models with effective temperatures in the range $3.45 < \log(T_{\text{eff}}/\text{K}) < 3.65$ and with luminosities $4.85 < \log(L/L_{\odot}) < 5.5$. F+23 argue, as we do, that their models do not admit a mass gap in models, although they argue that this is due to the model evolving around a region of pair instability in the $\rho - T$ parameter space. They use the GYRE pulsation code ([Townsend & Teitler, 2013](#)) to compute adiabatic hydrostatic pulsations for the $l = 0$ radial pulsation mode, finding a fundamental above around 1000 d in all cases. As they state, these are very reminiscent of adiabatic pulsations in RSGs, driven by the opacity feature in the hydrogen ionization zone. They perform a nucleosynthetic computation with a 399 isotope network in order to derive a potentially observable signature of TŻOs, in particular, $^{44}\text{TiO}_2$ and ^{44}TiO .

C.1.1 A discussion of the modelling of TŻOs

F+23 describe, in section 2 of their paper, the procedure they followed to generate models of TŻOs. They begin by placing a set of central boundary conditions in order to simulate

the neutron core of the TZO. However, and crucially, while we place our central boundary condition at the surface of the neutron star itself, F+23 place the inner boundary at around 650 km above the core of the neutron star, assuming that the NS itself has a radius of around 10 km. This makes the underlying assumptions of their models very fundamentally different from ours. As they state, their inner boundary includes the neutron core, as does ours, but also includes the entire radiative region that exists below the knee. They assume that it occupies an insignificant radius and a negligibly small amount of mass. As is evident from F+23 figure 2, this places the inner-most calculation mesh point in their models in the convective envelope, above the base of the convective envelope. In stark contrast, our models account for and compute the majority of the radiative region below the knee. Because, as seen in our models, there is significant nuclear burning below the knee, as well as the fact the effectively all the gravitational potential energy of infalling envelope material is liberated *below* the knee, they are required to compensate for this by injecting energy at the inner-most calculation point, in the convective envelope, but above the knee itself. They set this luminosity to be equal to the Eddington luminosity of material accreting on to the neutron star,

$$L_{\text{Edd}} = L_{\text{knee}} = \frac{4\pi c G M_{\text{NS}}}{\kappa_c}, \quad (\text{C.1})$$

where they use κ_c , at opacity at the inner boundary, in the convective envelope above the knee as the opacity controlling the effective rate of accretion. Our accretion rate on to the neutron star, as computed in section 5.22, relies instead on the opacity at the base of the convective envelope, the knee. Given, as we show in Figure 5.5 and as [Cannon et al. \(1992\)](#); [Cannon \(1993b\)](#); [Biehle \(1994\)](#) etc. have shown, the opacity of the stellar material falls sharply specifically at the knee itself. This gives the F+23 approach an accretion rate around $10^{-8} M_\odot \text{ yr}^{-1}$, very much in the realm of accretion rates that we have considered, it raises a specific concern, namely, that while this gives a reasonable estimate for the accretion luminosity in a model, it does not account of the nuclear burning occurring below their inner boundary. As shown in Figure 5.3, we find that there is in fact a very significant amount of energy generation occurring via nuclear burning both at the knee itself, where hydrogen burning peaks and below which it drops off rapidly, and below the knee, in the radiative region, where helium burning begins and rapidly peaks. In section 2.4 of their work, F+23 state that once the local luminosity exceeds the local Eddington luminosity, then the envelope becomes convective and so when they assume that the neutron star accretes at the Eddington luminosity then their inner boundary condition should correspond to the base of the convective envelope but we note, as they do in section 3, that their models do not form a knee because they are injecting energy at the inner-most calculation point, which is in all

cases, in the convective envelope. In figure 13 of F+23, they present the density temperature profile of their models as a function of their ε_L factor, with which they scale the energy they inject at the inner-most calculation point, as a fraction of the Eddington luminosity. They state that the material below the knee moves to higher densities and temperatures increasing the nuclear burning rate to compensate. It would initially appear that making use of a ε_L factor equal to zero would be equivalent to the approach we have taken, of modelling the TZO down to the surface of the neutron star, including the radiative region, but if the radius boundary condition used is the same as before, regardless of ε_L , then this is more akin to the investigations we conducted in section 5.2.2. We might expect their models at low ε_L to behave somewhat like our models at $R_c = 500$ or 1000 km, as we present in Figures 5.9 and 5.11, the latter of which presents a 1000 km boundary condition. In contrast to their findings, the radiative region below our knee becomes isothermal and in fact does so because it becomes more and more degenerate. This endows those models with a particularly sharp knee, in contrast with the lack of knee in the equivalent F+23 models. We note that they state in the caption of Figure 13 that a model with ε_L set to exactly zero failed to evolve for 10^4 yr, whereas we were able to evolve such models, with a wide range of boundary conditions, for upwards of 10^6 yr. In section 2.4 of their work, F+23 state that their models have between 1700 and 2000 mesh points on average, whereas the majority of our models had in excess of an order of magnitude more mesh points. Furthermore, we altered the standard mesh point splitting/placing algorithm to give favourable weighting to $\log m$, temperature gradient (alongside the usual temperature weighting) and $\log r$, in order to resolve as well as possible the radiative region in our models. We suspect that this may have contributed to our ability to resolve this region with an inner boundary at much smaller radius than F+23.

C.1.2 Concerns regarding placing the inner boundary above the radiative zone

Given the internal structure that F+23 have modelled for their TZOs, we address here some concerns that arise, in particular with regards to placing the inner boundary in the convective envelope, above the radiative zone. The idea of modelling burning in a convective region by placing the inner boundary above a radiative region is very reminiscent of the large series of papers, principally lead by Paola Marigo, regarding the structure, evolution and nucleosynthesis of AGB and in particular TP-AGB stars. In earlier work on these objects, in particular in regards to burning and nucleosynthesis at the base of the convective envelope, for example by [Boothroyd & Sackmann \(1992\)](#) and [Wasserburg et al. \(1995\)](#), the envelopes of the TP-AGBs / RGBs were modelled directly but were coupled to an analytical prescription

for the core of the object. This approach proved fruitful for understanding say the CNO element balance on the first ascent of the giant branch (Boothroyd & Sackmann, 1999), as well as hot bottom burning and cool bottom processing processes in TP-AGBs (Marigo et al., 1998; Sackmann & Boothroyd, 1999) but has inherent limitations. Computing full models, where the complicated structure below the base of the convective envelope, that is the burning shells, radiative mantle and isothermal core, are treated self-consistently, such as by Marigo & Girardi (2007), lead to important differences between the two series of models. These differences can be more easily understood when one considers what placing an inner boundary in a convective region as opposed to a radiative region when the entropy is considered. Setting a hard, infinitely stiff inner boundary enforces $\partial S = 0$ at this point. Hence, the entire envelope structure differs. Namely, the density profile cannot be expected to be the same. Given the sensitivity of HBB, for example, to the local density, this notably alters the nucleosynthetic results. Given this, we must consider the nucleosynthetic results of F+23 in this context, which indeed they do in their section 8, where they note that making use of the diffusive transport of chemical species in MESA, as opposed to the two stream convective flow model by Cannon (1993b), may reduce nucleosynthetic yields of isotopes such as ^{44}Ti . We would add that a comparison between $\partial S = 0$ and $\partial S \neq 0$ inner boundary condition envelope models should also be taken into account.

Furthermore, in section 3.2, F+23 state that they believe that the observed anomalous chemical composition of HV 2112 (Levesque et al., 2014) in fact rules out the possibility of this star being a T $\ddot{\text{O}}$ on the basis that it is well fit otherwise by models of theirs at 5M_\odot total mass, with a 1.4M_\odot neutron core, and an initial metalicity of either $\log Z = -4$ or -3 , but that those models do not produce the chemical abundances observed in HV 2112. We would caution against ruling HV 2112 out as a candidate T $\ddot{\text{O}}$ on this basis alone. If the inner boundary of the model is placed in this case at 650km and, as such, the very hottest and most intensely burning region of the star is being simulated via the injection of energy at the inner most calculation point, then the region in which one might expect the most significant and hence most exotic nucleosynthetic processes to occur is in fact not being included in the nucleosynthesis calculation. Furthermore, we note that Tout et al. (2014) suggests that the anomalous chemical composition cannot, in fact, be entirely explained by nucleosynthesis in a T $\ddot{\text{O}}$. Rather, they suggest that, in particular, the abundance of calcium, specifically ^{40}Ca observed by Levesque et al. (2014), could be the result of the formation process of the T $\ddot{\text{O}}$ itself. Tout et al. (2014) note that the synthesis of calcium is the result of an alpha capture chain during the imminent pre-supernova stages of massive star evolution, specifically when photodisintegration of ^{28}Si and alpha capture to ^{56}Ni occurs. Therefore, it cannot be synthesized during the evolution of a T $\ddot{\text{O}}$ or a sAGB. They argue that while direct

accretion of calcium on to HV 2112 from the supernova of a companion is extremely unlikely and would require much fine tuning of orbital parameters *etc.*, calcium could be synthesized during the merging of the core of a giant star with the neutron star during the formation of the TŻO itself (see section 2.4.1). Considering the calculations performed by [Metzger \(2012\)](#) on nucleosynthesis expected during the accretion of a disc formed by a disrupted white dwarf on to a neutron star or black hole, [Tout et al. \(2014\)](#) argue that this mechanism, at play during the accretion of the disrupted core of the giant star on to the neutron star, can explain the calcium abundance in HV 2112.

C.2 A point-by-point comparison of conclusions derived

F+23 present 8 primary conclusions, which we shall compare point-by-point with our own results.

F+23 find that TŻO models evolve to lower luminosities and lower T_{eff} with time, existing between $\log T_{\text{eff}}$ around 3.47 to 3.6 and $\log L$ around 5.0 to 5.5. This is in agreement with the surface properties of the TŻO models we calculate in Chapter 5. However, the evolution of their surface properties with time is in disagreement with both our own results and with those of Cannon *etc.* We find, as presented in figure 5.1, that in all cases our models evolve towards higher luminosities. Although there are notable structural differences between the deep interiors of our models and those of Cannon’s, the qualitative similarities present themselves on the HR diagram because our model tracks lie, in most cases, parallel to theirs. In contrast, the F+23 models evolve along tracks moving in entirely the other direction. Again, as before, we attribute the differences in these evolutionary tracks to the boundary conditions in the F+23 paper, because both our models and those of Cannon’s contain a radiative region that is simulated, as opposed to integrated into a boundary condition. Although the extent of the deep interior of the models that we simulate differs greatly between our models and Cannon’s, we suggest that the key difference is indeed the simulation of the radiative halo that sits below the knee.

F+23 find no gap in the mass/luminosity parameter space where models can exist, as opposed to [Cannon et al. \(1992\)](#), but in agreement with [Cannon \(1993b\)](#), and with our own results that we do not find a mass gap in our model series.

F+23 use GYRE to compute adiabatic radial pulsation mode periods for their models, RSG-like pulsation periods and would expect HV 2112 to have a 1500 to 3000 day pulsation period if it is in fact a TŻO. We have not computed pulsation for our models but would indeed expect the envelopes of TŻOs, which are extremely RSG-like, to pulsate in this manner, driven by the opacity feature in the hydrogen ionization zone. Although we do not model

the pulsations themselves, our models do demonstrate the opacity feature in the envelope hydrogen ionization zone that we would expect to drive such pulsations.

They find that, if RSG pulsations drive much larger mass loss in comparison to wind mass-loss rates then the TŻO lifespans may only be 10^2 to 10^3 yr. Otherwise, based on a lifespan limited by the availability of nuclear fuel, they estimate a lifespan of between 10^4 yr and 10^5 yr, finding that the lifespan of the TŻO increases with increasing initial mass. We, by including the entire nuclear burning region, convective and otherwise, self-consistently find lifespans of above 10^6 yr. We do, as F+23 do, find that the lifespan of a TŻO increases with the initial mass of the object, as a result of a larger reservoir of available nuclear fuel in the envelope.

F+23, upon running nucleosynthetic computations, find similar enhancements in ipr-process elements (Rb, Sr, Y, Zr, Ru *etc.*) as reported by [Cannon \(1993b\)](#). We find these to be reasonable findings but again reiterate concern that by not modelling a significant portion of the region in which nuclear burning occurs we would not expect these nucleosynthetic computations to produce accurate abundances. They propose the use of oxide/dioxides of ^{44}Ti as an observational signature because fast convection would allow ^{44}Ti to be brought to the surface before decaying. There it would be sufficiently cool to form ^{44}TiO and $^{44}\text{TiO}_2$, which might be differentiable from molecules containing stable isotopes of titanium. TiO and TiO₂ are observed in abundance in the atmospheres of diffuse and cool stellar envelopes, in particular in RSGs and given, the outward RSG-like appearance of TŻOs, this molecular isotopic mass shifting would be the main detectable feature. While certainly a possible avenue, we remain concerned that the final say $^{44}\text{Ti} / ^{48}\text{Ti}$ ratio that F+23 compute, is influenced by the position of the inner boundary in the convective envelope in their models. We further note that, if s-process-like reactions occur in the radiative region of a TŻO, that the TiO lines may well be replaced with ZrO, as is observed in S stars ([Gallino et al., 1998](#)).